

THE UNIVERSITY
of ADELAIDE

CENTRE FOR AUTOMOTIVE
SAFETY RESEARCH

Alternative injury response functions for evaluating head accelerations, with application to pedestrian headform testing

A thesis submitted in fulfillment of the requirements for the degree of
Doctor of Philosophy
at
The University of Adelaide
Centre for Automotive Safety Research

by
Jeffrey Kym Dutschke

June 2012

Contents

Abstract **ix**

Declaration **xi**

Acknowledgments **xiii**

1 Introduction **1**
1.1 Introduction . . . 2
1.2 Safety testing . . . 3
1.2.1 Purpose of safety testing . . . 3
1.2.2 Properties of a test protocol . . . 4
Test conditions in the ANCAP head impact test . . . 4
Biofidelic surrogate . . . 5
1.3 Head injury . . . 6
1.3.1 Types and prevalence of head injury . . . 6
1.3.2 Measuring impacts that lead to head injury . . . 8
1.4 Injury Response Functions (IRFs) . . . 9
The Head Injury Criterion . . . 10
Other IRFs . . . 11
1.5 Consequences of safety testing . . . 12
1.6 Comparison of the IRFs . . . 13
1.6.1 Theoretical evaluation of the IRFs . . . 13
Effect of impact velocity and stopping distance . . . 13
Coefficient of restitution . . . 14
Effect of pulse shape . . . 14
1.6.2 Comparison of practical testing data . . . 15
1.7 Aims of the thesis . . . 15
1.8 Organisation of the thesis . . . 16
1.8.1 Preparatory information – Chapters 2 and 3 . . . 16
1.8.2 Theoretical pulse shape analysis – Chapters 4 and 5 . . . 17
Normalisation of the theoretical pulse shapes . . . 17

Comparison of the value of each IRF with each theoretical pulse shape . . . 18
Effect of impact velocity, headform stopping distance and coefficient of restitution . . . 18
1.8.3 Empirical pulse shape analysis – Chapters 6 and 7 . . . 19
Correlation of the data . . . 19
Effect of the threshold . . . 20
Comparison with rank correlation . . . 20
Investigation of pulse shapes with discrepant rankings 20
1.8.4 Concluding chapter – Chapter 8 . . . 21
1.9 Limitations of the thesis . . . 21

2 Injury Response Functions 23
2.1 Introduction . . . 24
2.1.1 Wayne State Tolerance Curve . . . 24
2.2 Injury Response Functions used in this thesis . . . 26
2.2.1 Head Injury Criterion . . . 26
2.2.2 3 millisecond clip . . . 27
2.2.3 Peak Acceleration . . . 28
2.2.4 Peak Virtual Power . . . 29
2.3 Injury Response Functions not examined in this thesis . . . 31
2.3.1 IRFs based on rotational acceleration . . . 31
Hybrid linear and angular acceleration IRFs . . . 32
2.3.2 IRFs based on finite element models . . . 33
2.3.3 IRFs based on lumped parameter models . . . 33
2.4 Concluding remarks . . . 34

3 Data 35
3.1 Introduction . . . 36
3.2 Test methods . . . 40
3.2.1 Apparatus . . . 40
The headforms . . . 40
Accelerometers . . . 42
Data Acquisition . . . 42
Firing Apparatus . . . 42
3.2.2 Test Procedure . . . 44
Test conditions . . . 44
Motion of the headform during free flight . . . 45
Normal impact velocity . . . 46
Acceleration . . . 47
3.3 Distributions of measured data . . . 47
3.3.1 Impact Speed . . . 47
3.3.2 Impact angle . . . 48
3.3.3 Impact velocity normal to the surface . . . 49

3.4 Retrospective Analysis . . . 51
3.4.1 Rotational dynamics of the headform . . . 51
3.4.2 Estimation of maximum stopping distance . . . 56
Calculation of deformation for the example test . . . 56
3.4.3 Estimation of coefficient of restitution . . . 56
3.5 Distributions of estimated data . . . 58
3.5.1 Stopping distance . . . 58
3.5.2 Coefficient of restitution . . . 60
3.6 Evaluation of each IRF . . . 61
3.6.1 HIC . . . 61
3.6.2 PVP . . . 63
3.6.3 3 millisecond clip . . . 63
3.6.4 Peak acceleration . . . 63
3.7 Descriptions of pulse shape . . . 66
3.7.1 Front and rear loaded pulse shapes . . . 66
3.7.2 Peaked and flat pulse shapes . . . 67
3.7.3 Pulse shapes with multiple peaks . . . 67
3.8 Summary and discussion . . . 70

4 The effect of a particular IRF on design decisions: analysis with theoretical test pulses 71
4.1 Introduction . . . 72
4.2 Pulse shapes used for analysis and a strategy for normalisation 74
4.2.1 Pulse shapes . . . 74
4.2.2 Normalising these pulse shapes . . . 74
Normalisation parameter — impact velocity . . . 76
Normalisation parameter — stopping distance . . . 78
4.3 Normalisation – no restitution . . . 79
Analytical values for impact velocity . . . 79
Analytical values for stopping distance . . . 80
4.3.1 The normalisation of pulse shapes that produce no rebound . . . 80
4.4 Normalisation of pulse shapes with rebound . . . 82
Expressions for impact velocity in terms of A, T, and R 84
Expressions for stopping distance in terms of A, T, and R . . . 85
4.4.1 The normalisation of pulse shapes for impacts with non-zero restitution . . . 90
4.5 The value of each IRF for each analytical pulse shape . . . 95
4.5.1 HIC . . . 95
4.5.2 PVP . . . 95
Half-sine pulse . . . 96
Triangular pulse . . . 96
Square pulse . . . 97

4.5.3 Peak acceleration . . . 98
4.5.4 3 millisecond clip . . . 98
Half-sine pulse . . . 99
Triangular pulse . . . 99
Square pulse . . . 99
4.5.5 Summary of analytical values of each IRF . . . 100
4.6 Evaluation of each IRF for the normalised pulse shapes . . . 100
4.6.1 HIC . . . 101
4.6.2 PVP . . . 103
4.6.3 Peak acceleration . . . 105
4.6.4 3 millisecond clip . . . 107
4.6.5 Combining the results . . . 111
4.7 Effect of IRF on design outcomes . . . 111

5 Relating each IRF to impact velocity, stopping distance, coefficient of restitution and pulse shape 115
5.1 Introduction . . . 116
5.2 Theory . . . 117
5.2.1 Effect of impact velocity and stopping distance on value of each IRF . . . 117
5.2.2 Effect of a coefficient of restitution on the value of each IRF . . . 119
Effect of a coefficient of restitution for the square pulse shape . . . 119
General expression for each IRF for the square pulse shape . . . 120
General expression for each IRF for half-sine and triangle pulse shapes . . . 121
Estimating the effect of the coefficient of restitution . 122
Estimating the effect of pulse shape . . . 122
5.2.3 A general expression for each IRF suitable for linear regression . . . 128
5.3 Data used in the linear regression . . . 129
Impact velocity . . . 129
Headform stopping distance . . . 130
Coefficient of restitution . . . 130
5.4 Linear regression of test data for each IRF . . . 130
5.4.1 HIC . . . 131
Difference between the predicted and obtained regression coefficients . . . 131
Differences between headforms . . . 133
Magnitude of the effect of the pulse shapes in the test data . . . 133
Independent effect of each regressor . . . 135

5.4.2 PVP . . . 137
5.4.3 Peak acceleration . . . 140
5.4.4 3 millisecond clip . . . 142
5.5 Discussion . . . 145
5.5.1 Interpretation of the coefficients predicted with the theory and obtained from the regression . . . 146
5.5.2 Context . . . 148

6 Quantification of the similarities between four IRFs 149
6.1 Introduction . . . 150
6.2 Comparison among IRFs using test data . . . 150
6.3 Dichotomous classification of tests into 'safe' and 'unsafe' categories using criteria formed with each IRF. . . . 153
6.3.1 Definition of a conservative criterion . . . 155
6.3.2 Conservative criteria compared with HIC>1000 . . . 156
6.4 Comparison among IRFs using ranked test data . . . 159
6.5 Comparison among IRFs using the ranked contribution of pulse shape to the IRF value of each test . . . 166
6.5.1 Rank correlation of stopping distance with pulse shape coefficient . . . 168
6.5.2 Rank correlation of pulse shape coefficients with IRF values . . . 170
6.5.3 Rank correlation among the pulse shape coefficients for each IRF . . . 172
6.6 Discussion . . . 175

7 Examination of discrepant pulse shapes in the test data 177
7.1 Introduction . . . 178
7.2 Identifying the tests with the most discrepant ranks of pulse shape coefficients . . . 179
7.3 Analysis of the discrepant pulse shapes between HIC and 3 millisecond clip . . . 180
7.3.1 Tests with a higher $\mathbb{P}_{\mathrm{HIC}}$ rank than $\mathbb{P}_{a_3}$ rank . . . 180
Tests with a narrow acceleration peak . . . 181
Tests with a double peak in acceleration . . . 188
7.3.2 Tests with a lower $\mathbb{P}_{\mathrm{HIC}}$ rank than $\mathbb{P}_{a_3}$ rank . . . 188
7.3.3 Analysis of the pulse shapes that are discrepant between $\mathbb{P}_{\mathrm{HIC}}$ and $\mathbb{P}_{a_3}$ . . . 192
7.4 Analysis of the discrepant pulse shapes between HIC and PVP 194
7.4.1 Tests with a higher $\mathbb{P}_{\mathrm{PVP}}$ rank than $\mathbb{P}_{\mathrm{HIC}}$ rank . . . 194
Pulse shapes with a late acceleration pulse . . . 199
Tests with a late rise in the acceleration . . . 199
7.4.2 Tests with a higher $\mathbb{P}_{\mathrm{HIC}}$ rank than $\mathbb{P}_{\mathrm{PVP}}$ rank . . . 200
7.4.3 Analysis of the differences between HIC_∞ and PVP . . . 203

7.5 Analysis of the discrepant pulse shapes between HIC and peak acceleration . . . 204
7.5.1 Tests with a higher $\mathbb{P}_{\text{HIC}}$ rank than $\mathbb{P}_{a_m}$ rank . . . 204
7.5.2 Tests with a lower $\mathbb{P}_{\text{HIC}}$ rank than $\mathbb{P}_{a_m}$ rank . . . 206
7.5.3 Analysis of the differences between HIC and peak acceleration . . . 212
7.6 Summary . . . 213

8 Discussion, recommendations and conclusions 217
8.1 Summary . . . 218
8.1.1 Theoretical examination of each IRF . . . 220
8.1.2 Effect of impact velocity, stopping distance and coefficient of restitution . . . 222
8.1.3 Effect of the IRF on the testing result . . . 224
Linear correlation . . . 225
'Safe' and 'unsafe' classification . . . 225
Rank correlation . . . 227
Rank correlation of pulse shape coefficients . . . 227
8.1.4 Comparison of individual discrepant tests . . . 227
8.2 Discussion . . . 229
8.2.1 Macroscopic view of the trends . . . 229
8.2.2 Microscopic view of the detail . . . 230
Influence of the differences . . . 231
8.2.3 Other factors to consider . . . 231
Choice of a threshold . . . 231
Choice of the physical testing parameters . . . 232
8.2.4 Summary . . . 233
8.3 Discussion of the limitations and future work . . . 234
8.4 Importance of this thesis for various stakeholders . . . 235
Regulatory and consumer testing organisations . . . 235
Design engineers . . . 236
Members of the public . . . 236
8.5 Conclusion . . . 236

A Test results 239

B Realistic pulse shapes 263
B.1 Deformation at the end of the impact is less than zero . . . 263
B.2 Peak acceleration occurs before time of maximum stopping distance. . . . 266

C Assumption that HIC_∞ and HIC_{15} are the same 269

D Comparison between rotational acceleration and linear acceleration based IRFs **275**
D.1 Peak rotational acceleration 276
D.2 Peak change in rotational velocity 279
D.3 Discussion 279

E Comparison of the PVP and HIP **283**

F Contingency tables **289**
F.1 HIC with PVP 290
F.2 HIC with 3 millisecond clip 292
F.3 HIC with peak acceleration 294

Bibliography **296**

Abstract

Impact testing of vehicles and helmets is performed under the specifications of a test protocol to ensure that regulatory standards and community expectations are met in terms of head injury safety. Impact severity is usually measured using the acceleration of the impactor (or dummy head) that is recorded during the impact. A specification that is defined in these testing protocols is the injury response function (IRF) that is used to summarise the magnitude of the recorded acceleration. There are various IRFs that can be chosen to summarise the acceleration data. This thesis examines several of these IRFs that are based on linear acceleration. The aim was to describe the differences between the IRFs and examine what differences might arise in the designs in response to the requirements of the IRF. There has historically been disagreement on the best way to assess injury risk, but the debate is only important to the extent that the design requirements are affected by the choice of IRF.

Four IRFs were examined in detail. These were the Head Injury Criterion (HIC), the Peak Virtual Power (PVP), the 3 millisecond clip (a_3) and the peak acceleration (a_m).

Simple acceleration pulse shapes were used to determine some of the properties of each of the IRFs. These included the role of the pulse shape, the stopping distance, the impact velocity and the coefficient of restitution on the value of each of the IRFs. The effect of the pulse shape on the value of the IRFs was examined using these simple pulse shapes that had been normalised for a constant impact velocity and stopping distance.

Equations predicting the value of each IRF were then derived that used the

stopping distance, the impact velocity and the coefficient of restitution as predictors.

The properties found using the simple pulse shapes were then examined using the real test data that included 247 tests obtained from a pedestrian testing protocol. The predictions of the equation for each IRF were compared to the test data using a linear regression. The remaining variation in the value of each IRF was attributed to the effect of the pulse shape.

In most cases, the measured relative severities of the impacts were not greatly affected by the choice of IRF, but there were some discrepancies. The characteristics of the pulse shapes that gave rise to these discrepancies were identified. These were identified by subtracting the effect of the stopping distance, the impact velocity and the coefficient of restitution from the value of the IRF for each test to determine an adjusted IRF value for each test. These adjusted IRF values were ranked and compared to determine the discrepant tests.

Differences in the magnitude of the effect of the pulse shape, the maximum stopping distance, the impact velocity and the coefficient of restitution on the value of each of the IRFs were found theoretically and these were verified in the experimental data.

The effect of the choice of threshold on determining the tests that were considered 'safe' and 'unsafe' was also examined. Sensitivity and Negative Predictive Value were used to determine thresholds that were conservative compared with HIC > 1000. The effect of the threshold was shown to be a very important parameter in a testing protocol.

It is concluded that there are some differences between the IRFs that were examined in detail. However, in general, the choice of IRF does not appear to greatly affect the ultimate design of crashworthy structures.

Declaration

This work contains no material which has been accepted for the award of any other degree or diploma in any university or other tertiary institution to Jeffrey K Dutschke and, to the best of my knowledge and belief, contains no material previously published or written by another person, except where due reference has been made in the text.

I give consent to this copy of my thesis, when deposited in the University Library, being made available for loan and photocopying, subject to the provisions of the Copyright Act 1968.

I also give permission for the digital version of my thesis to be made available on the web, via the University's digital research repository, the Library catalogue, and also through web search engines, unless permission has been granted by the University to restrict access for a period of time.

Jeffrey Dutschke
June 2012

Acknowledgments

I thank my supervisors Associate Professors Robert Anderson and Paul Hutchinson. Their encouragement for me to begin, change, persist with, and finish this thesis has been deeply appreciated. They are at this end of a long line of teachers I have had and to whom I am deeply indebted.

Thank you to Doctor Daniel Searson for his contributions to my working. Daniel shared his method and code for calculating the kinematics of the headform impacts described in Searson and Anderson (2008) with me and engaging in several enlightening discussions covering the various the topics of this thesis.

My thanks to the staff and students at CASR. I have appreciated your efforts in helping me to learn about academic research and road safety. In particular, Andrew van den Berg, Giulio Ponte, Daniel Searson and the others involved in performing the ANCAP pedestrian testing at the Centre for Automotive Safety Research impact lab. It was this data that I used in this thesis. Also to the Phd boys for their friendship and academic support.

Lastly, Mum, Dad and Amy. Thank you for your encouragement, support, assistance and love. You will be pleased to hear that I have submitted.

Chapter 1

Introduction

1.1 Introduction

Head injury is a sufficiently large problem in society that specific safety test protocols have been developed to ensure that the products that could contribute to this injury are developed with safety in mind. These test protocols commonly use a head-like surrogate to impact the structure being tested. The response of the surrogate to the impact is then measured and summarised to evaluate the safety of the product. The summary of the impact is made using an injury response function (IRF). For head injury, there are several IRFs that are commonly used test protocols, the most common of which is the Head Injury Criterion (HIC). The choice of IRF may lead to designs that favour the minimisation of the IRF under the specified test condition. If the IRF and the test condition accurately represent the average risk of the product in used, then the testing will have achieved its objectives. In the case of head injury, there is some dispute as to whether the objective of testing is adequately met. There has been historical disagreement about the most appropriate IRF to use (in terms of its predictive value) but less attention has been given to the effect that the choice of an IRF in a testing protocol has on the ultimate design of the given product. This thesis contributes to understanding this effect of the IRFs by evaluating the IRFs from a theoretical point of view and relating this to real data from a real test protocol.

In Australia in 2004-05 there were 25103 admissions to hospital for traumatic head injury. 40% of these admissions were the result of falls and 31% were as a result of a transportation incident (Helps et al., 2008, pg. 86). Among road users who are fatally injured, most of them have some type of head injury. McLean (1995) examined a sample of 414 fatally injured road users and an impact to the head was observed in 93% of these cases. Among pedestrians in that sample, 95% had an observed impact to the head. Of the 403 cases within this sample for whom a cause of injury could be clearly classified, brain injury was a cause of death in 55%. For pedestrians, brain injury was a cause of death for 53%.

A successful test protocol is a combination of several factors. These include a meaningful representation of an injury inducing situation, and a meaning-

ful method of measuring and assessing the injury risk associated with the product being tested. These are discussed in the coming sections.

1.2 Safety testing

1.2.1 Purpose of safety testing

Safety testing for head injury is done on a wide variety of products. Examples include the testing done for automotive safety, helmets and playground surfaces.

In each type of testing, the results of tests might either be used to certify the product as safe for use, as might be done in regulatory testing, or to rank the safety of the product relative to others, as might be done in consumer testing. Public safety is influenced by the results of this testing in various ways. In the case of regulatory testing for vehicles, it may be necessary to pass several tests before certification for sale is granted. Helmets passing a regulatory test may, for example, be authorised for sale and an Australian Standard sticker may be affixed to the helmet. In the case of consumer testing, a safety rating may be applied to the product. An example of this is the star rating system for new cars that is determined by the Australasian New Car Assessment Program (ANCAP).

One part of ANCAP is the pedestrian safety testing protocol. This testing protocol is identical to the pedestrian safety component of the European New Car Assessment Programme (Euro NCAP) (Euro NCAP, 2004). The object of this test protocol is to award safer vehicles more stars for pedestrian safety. An important component of the protocol is the safety offered by a vehicle to the head of a pedestrian who is hit (EEVC, 2003).

Safety testing is not the only way in which relative safety of a vehicle can be determined. For example, retrospective analysis of a large number of accidents can provide this information for safety. One example of this analysis, for Australian vehicles, was conducted by Newstead et al. (2012). However, information of this type is not available prior to sale or purchase of the new vehicle, and is therefore less able to inform consumers or assist a regulatory body certify the safety of new vehicles near the time of their release. Con-

sequently, the need for pre-sale information relating to safety makes safety testing important.

1.2.2 Properties of a test protocol

A test protocol provides the data to be able to effectively evaluate the safety of the product being tested. In terms of head injury safety there are several different types of test protocol that could be used. These include measuring a property of the product directly, such as the depth of an energy absorbing layer of material, or measuring the response of the product to an impact. The focus of this thesis is measuring the response of the product to an impact.

The factors that contribute to an impact testing protocol are those that make the test relevant to impacts that will occur while the product is in use. The relevance of the test protocol is achieved through having test conditions that are similar to those in real impacts, with a biofidelic surrogate to measure the response of a human in the impact and evaluating those measurements in a meaningful way. Each of these is defined as part of the test protocol, and determined through analysis of existing injury situations. For the test protocol used for the ANCAP pedestrian safety protocol these factors are discussed in (Glaeser, 1991). The test conditions and the biofidelic surrogate are discussed briefly here, as these are not the focus of thesis. The method of measuring and evaluating injury is discussed in more depth in Section 1.4.

Test conditions in the ANCAP head impact test

Detailed crash information as used to define the range of conditions seem in typical pedestrian crashes. Glaeser (1991) describes the conditions that were considered. These included the height and age of pedestrians that were hit and the velocity of the vehicles involved. Further analysis was conducted to determine the angle relative to the ground and the speed that the pedestrian's head was moving before being struck. The test conditions that were ultimately selected were values commonly found in these real impacts, where survivability was possible when appropriate design for safety was present.

Biofidelic surrogate

The human-like surrogates used in the test protocols described above are types of Anthropomorphic Test Device (ATD). An ATD is intended to replicate the response of the human subjected to the same impact forces. In a whole car test the ATD used represents a whole body, while in a pedestrian test the ATD represents only the head of a person. The most advanced ATDs have a geometry and mass that closely resembles that of a human and respond in the same way a human would when subjected to a load or impact (Mertz, 1993). These similarities between an ATD and its representative human are collectively known as its biofidelity. The main advantage of the use of an ATD is that tests performed with them are standardised and are repeatable across time and in different laboratories.

Each ATD contains sensors to measure its experience during the test. The information from the sensors is analysed and compared with pre-defined tolerance levels to determine the severity of the impact. Determining which of the mechanical parameters should be measured and their associated tolerance levels is the subject of biomechanical studies, some of which are described in the next section.

The ATD used in the ANCAP pedestrian head impact test protocol is a headform. Several other test protocols that focus on head injury also use a headform as the ATD. These include test protocols for occupant safety (Kaleto et al., 2007), pedestrian safety (EEVC, 2003), helmets (Newman, 1993) and playing surfaces (Standards Australia, 1996). This type of ATD is preferable in a test protocol where the effect of the remainder of the body would add variability to the results of the impact tests. Removing this variability permits the test equipment and test setup to be as simple as possible and have easily controlled initial impact conditions.

The ANCAP test protocol, and others like it, use featureless — almost spherical — headforms (EEVC, 2003). There are two headforms used in the ANCAP test protocol, one represents an adult head, the other represents a child head. The first headforms designed for this test protocol are described in Glaeser (1991).

The headform is propelled toward the vehicle structure and is in free-flight at the moment of impact. The headform used in pedestrian testing was subject to verification impacts conducted with post-mortem human subjects (Glaeser, 1991). The values of peak acceleration and three millisecond clip of linear acceleration along with the general acceleration pulse shape were compared with those results from the post-mortem tests and similar results were shown. No further comparisons were done; in particular, no comparisons with rotational acceleration were made. This headform is described in detail in Chapter 3.

1.3 Head injury

1.3.1 Types and prevalence of head injury

Head injury is a broad classification of a number of injuries that can occur to the head. Included are injuries to the head exterior, such as the scalp, through to injuries sustained in the brain. These might result from external factors, such as impact, or biological factors, such as a stroke. A traumatic head injury is one that occurs as a result of an impact to the head. The impact can either penetrate the skull bones or not. A non-penetrating impact is a blunt impact, and typically involves an impact with an object with a high mass and large impact surface. This type of impact to the head is most likely in vehicle accidents and falls. A penetrating impact is most likely to be due to impact with a high velocity low mass object, such as a gun bullet or piece of shrapnel. The head impacts that are considered in this thesis are those which are blunt in nature only.

The *International Statistical Classification of Diseases and Related Health Problems – 10th Revision* (World Health Organisation, 1992) provides one method of classifying disease and injury. Nine sections are related to head injury — S00–S09 — but just two sections are relevant for blunt trauma head injury. These are: S02 – Fracture to the skull and facial bones; and S06 – Intracranial injury. S02 includes different subclassifications for fractures of different (and multiple) bones in the head. S06 includes subclassifications including concussion (S06.0), diffuse and focal brain injury (S06.2, S06.3)

and traumatic haemorrhage in the epidural (S06.4), subdural (S06.5) and subarachnoid (S06.6) spaces.

Injury can occur in one or many of these structures at the same time. Concussion only (58%) was the most common condition for hospitalisation due to transport related head injuries in Australia in 2004-05 (Helps et al., 2008, pg 86). This was followed by intracranial injury (S06 excluding S06.0, 28%), skull fracture without any brain injury (8%) and skull fracture with concussion (6%). Among pedestrians requiring hospitalisation the distribution of these injuries show a much lower proportion of concussion only (32%) and a much higher proportion of intracranial injury (52%) (Helps et al., 2008, pg 88). The proportions of skull fracture without any brain injury (10%) and skull fracture with concussion (7%) for pedestrians were similar to those in the larger transportation sample.

It is generally accepted that fracture to the skull (ICD-10 S02) results from the ultimate strain limit of the skull being exceeded (Gurdjian et al., 1950; Kroman et al., 2011; Melvin and Evans, 1971; Yoganandan et al., 1995). These strains can come from static (crushing type) loadings or dynamic (impact type) loadings. When this strain exceeds the critical value for any of the bones, fracture can occur. Different bones in the skull have different breaking strains.

The mechanisms of brain injury have been shown to be also caused as strain in the various components of the brain exceed their own critical value (King et al., 2003; Ommaya et al., 1994). Injury to the various components manifest themselves with different clinical outcomes. For instance, oedema and haemorrhage can occur due to a rupturing of a blood vessel, while concussion and diffuse brain injury are damage of the neurons of the brain.

Concussion and diffuse brain injury are two important head injuries that are often considered. These are both injuries of the brain parenchyma (not the associated blood vessels or other components). It is known from studies of neurons that strain and strain rate are important factors in the incidence of this type of injury (Geddes et al., 2003; Geddes-Klein et al., 2006; LaPlaca et al., 1997) but strain and strain rate in tissue is difficult to measure in-vivo. Hardy et al. (2001) were able to obtain mechanical responses of human brain with a bi-planer x-ray technique in cadavers. More recently, Bayly

et al. (2005), Feng et al. (2010), and Sabet et al. (2008) have obtained strain patterns in living tissue using a tagged magnetic resonance imaging (MRI) technique for linear and rotational acceleration of the head. All of these techniques are limited to low severity impacts because of the difficulty in acquiring the data. The results of these experiments are still useful and the results of Hardy et al. (2001) have been used to verify finite element models of the human head (e.g. Kleiven, 2006; Takhounts et al., 2008). These finite element models have then been used to reconstruct injurious events and study the internal mechanical responses of the head or investigate situations in which a probability of head injury is present.

From the perspective of vehicle testing, however, the distinction between these different types of injury is likely not to be of primary importance. This is because it is possible for each of these injury types to the cause a range of injury consequences. These range from temporary and recoverable through to death. For instance, a skull fracture may be fatal or heal with no long term consequences, and a brain injury may result in a temporary concussion, mental impairment for life, or death. The challenge for design is to minimise the consequence of any injury that may occur, in addition to minimising the types of injuries that can occur.

1.3.2 Measuring impacts that lead to head injury

As it is difficult to directly measure the mechanisms of injury, surrogate measurements of injury mechanisms have been developed for the purpose of identifying injurious impacts. The main measures of impact severity are linear and angular acceleration (King et al., 2003). It has been suggested that linear accelerations are the main contributor to skull fracture and focal brain injuries while rotational accelerations are the main contributor of diffuse brain injury and some focal brain injuries (Hardy et al., 1994; Ommaya et al., 1994).

Rotational acceleration was the first quantity to be proposed (Holbourn, 1943) as a surrogate measure for brain injury risk. This was later shown, experimentally, to be the case (Ommaya and Hirsch, 1971). Furthermore it was also shown that the direction of the rotational acceleration was also

an important factor in the injury measured with rotational acceleration (Gennarelli et al., 1987).

In early experiments rotational acceleration was not as easily measured as was linear acceleration. Consequently rotational acceleration was ignored and linear acceleration was mechanical parameter that was measured instead in some early experiments of head injury tolerance (for example Got et al., 1978; Gurdjian et al., 1961). It was the results of these experiments that provided the data for the Wayne State Tolerance Curve (Gurdjian et al., 1966). It is this tolerance curve, and its use of linear acceleration, that is the basis for most of the IRFs currently used in safety testing. The Wayne State Tolerance Curve is discussed further in Chapter 2. At the time that these experiments were taking place, it was recognised that linear acceleration was the best available, but not the most ideal, measure for injury and was, in fact, a proxy for the actual mechanism of injury (Gadd, 1966).

Basic mechanics tells us that lessening impact force is likely to lessen all mechanical parameters individually thought to be implicated in several injury types. While it is possible to contrive impacts where, for example, rotational acceleration is uncorrelated with linear accelerations (for example in Kleiven, 2003) it is not established that such scenarios are important to average risk. It has also been shown in some realistic impact scenarios that rotational acceleration and linear acceleration are positively correlated (Funk et al., 2008). Considerable debate has occurred over the use of either linear acceleration or rotational acceleration as a proxy measurement for head injury risk (King et al., 2003) but this debate has yet to create change in test protocols which, as described in Chapter 2, continue to measure linear acceleration as their proxy for injury risk.

1.4 Injury Response Functions (IRFs)

The purpose of an IRF is to summarise the data collected during an impact into a single measure of impact severity. Typically, in an impact test, the acceleration of the head is measured during an impact as this is a proxy for the actual head injury mechanism, it is this acceleration that is summarised by the IRF. Alternatively, in a finite element model, the IRF could be a func-

tion of the strain measured in the brain. As such, an IRF is a mathematical construct that can be used to compare impact severities. Typically, because of the complexity of the data collected during an impact, an IRF is calculated numerically, evaluating a large portion of the impact to determine its value. In the case where acceleration is measured, it is the acceleration pulse shape which is evaluated.

The values of an IRF are not likely to be directly related to injury. In this sense the values of an IRF are ordinal. Ideally, different values of an IRF will reflect a difference in injury risk in a monotonically increasing (or decreasing) way. It is more realistic, however, due to variations in the population, that tolerance to impact will vary for individuals and those which are survivable for some may be lethal for others. A separate injury risk function is necessary to convert the value of the IRF to an expected average injury.

One type of injury risk function is a threshold. Values of the IRF below the threshold may be considered safe, with injury unlikely, and values that exceed the threshold may be considered to be unsafe, with injury likely.

In this thesis a distinction is made between an IRF and an injury criterion. The former is the summary that provides a indication of severity and can have many numerical values. The later compares this summary number with a threshold and has two outcomes, 'safe' or 'unsafe'.

One way of avoiding associating an IRF with injury risk is to rank results of multiple tests against each other. Results with a lower ranking would then have a lesser injury risk than those with a higher ranking, regardless of what the actual injury risk is.

The Head Injury Criterion

There is one main IRF that is used in most automotive test protocols (Simms and Wood, 2009, pg 77). It is called the Head Injury Criterion (HIC). It is used in the ANCAP pedestrian test protocol and also in many other non-automotive test protocols. It was proposed by Versace (1971). It is shown

in Equation (1.1).

$$\text{HIC} = \max \left[(t_2 - t_1) \left(\frac{\int_{t_1}^{t_2} a dt}{t_2 - t_1} \right)^{2.5} \right] \tag{1.1}$$

where a is the acceleration of the pulse shape in g and $t_1 < t_2$ are times in milliseconds during the impact pulse selected to maximise the value of HIC.

The HIC can be interpreted as the maximum value obtained when the average acceleration during a part of the pulse (between t_1 and t_2) is raised to the power of 2.5 and multiplied by the duration of the same part of the pulse. Consequently, for a flat pulse shape with acceleration A_s and duration T_s, $\text{HIC} = T_s \times A_s^{2.5}$. But this simplified example is rarely found in real impact conditions and whilst the value of HIC has been determined for several analytical pulse shapes (Chou and Nyquist, 1974) its value is usually determined numerically.

Whilst the HIC is widely used, it is also criticised (eg. Newman, 1980). The criticism is levelled at the quality of the data used to propose the HIC and the lack of consideration given to kinematics that are not associated with linear acceleration. For those reasons, it is generally acknowledged that the HIC may be replaced at some stage with a better IRF, when one is found (McLean, 1993).

A typical threshold used with the HIC to form an injury criterion is 1000. Values of HIC less than 1000 being considered 'safe' and values exceeding 1000 being considered 'unsafe'.

Other IRFs

In addition to the HIC there are other IRFs that have been used in mainstream test protocols. Reviews of the IRFs that had been adopted into automotive safety testing (Hess et al., 1980) and helmet safety test protocols (Newman, 1993) in addition to analysis of current test protocol showed that there are two other IRFs used frequently. These are the 3 millisecond clip (a_3) and the peak acceleration (a_m) IRFs. Each of these IRFs is used in test protocols that use subsystem headforms as their ATD.

In addition, other IRFs have been proposed which have not been adopted into a mainstream test protocol. A recent example is the Peak Virtual Power (PVP) IRF (Neal-Sturgess, 2002; Neal-Sturgess et al., 2001). The background and form of these IRFs is described in Chapter 2. Each of these IRFs; the HIC, a_3, a_m and PVP, is used for the same purpose – to summarise a pulse shape from an impact test so that it can be compared with other impact tests. The question is one regarding the IRF that best represents injury risk in a head impact.

1.5 Consequences of safety testing

To meet the safety levels specified and encouraged by the safety test protocol, designers might chose to modify their design to meet the particulars and peculiarities of a test protocol. For instance, in automotive safety several designers have approached a design modification with the test protocol in mind. For example Belingardi et al. (2009) and Liu et al. (2009) examined how bonnet design could be changed to meet the requirements of a pedestrian safety protocol, and He et al. (2000) examined the design methodology necessary to meet the requirements of the FMVSS 201 occupant protection standard. When designs are finalised with specific test protocol in mind there is a risk that the primary objective of meeting the requirements of the test protocol may not lead to the safest design. This might occur if some elements of the protocol are not well matched to real-world conditions, or are an incomplete representation of those conditions.

Relevant to this thesis is the question of the influence of the IRF on design. As was described earlier, several different IRFs have been developed and potentially any one of them could have been chosen as the IRF for a particular test protocol. Consequently, the optimum designs may be dependent on the choice of the IRF.

If the optimum design that emerges is a result of the choice of IRF, then the choice of the IRF would be an important determinant in the real safety of the products that are tested with those protocols. On the other hand, if the designs are insensitive to the choice of the IRF then that choice of IRF is not an important determinant in the real safety of the products that are tested.

Consequently, if designs are insensitive to the choice of the IRF, research does not need to focus on the differences in the IRFs or their shortcomings. An objective of this thesis is to investigate the properties of several IRFs to determine the effect that the choice of IRF could have on designs created with the requirements of a test protocol in mind.

1.6 Comparison of the IRFs

1.6.1 Theoretical evaluation of the IRFs

There are many factors that can influence acceleration measured during the test which, in turn, can then influence the value of the IRF. These include the impact velocity, the stopping distance of the headform during the impact, the coefficient of restitution of the impact and the effect of the form of the pulse shape. These factors have been more extensively researched for the HIC than for the other IRFs.

Effect of impact velocity and stopping distance

The value of an IRF changes with the impact parameters. For instance Lim et al. (1995) showed that the impact velocity, V, and the maximum deformation of the structure during the impact, the stopping distance, S, can strongly influence the value of the HIC, as shown in Equation (1.2).

$$\text{HIC} \propto V^4 S^{-1.5} \tag{1.2}$$

This equation was shown to be valid for impacts where the rebound velocity of the headform was negligible for several different theoretical pulse shapes. The constant of proportionality was determined by the pulse shape being evaluated.

Relationships between these impact parameters and the other IRFs, similar to the relationship shown in Equation (1.2), have not been published. These relationships are investigated in this thesis.

Coefficient of restitution

Bowman (1994) investigated the effect of the coefficient of restitution on the value of HIC and showed that a low value of coefficient of restitution was best for a low value of HIC. His analysis, however, was restricted to one specific theoretical pulse shape. This work has not been extended to evaluate the effect of coefficient of restitution on the other IRFs. In this thesis the concept of a variable value of coefficient of restitution is studied for a range of theoretical acceleration pulse shapes.

Effect of pulse shape

Chou and Nyquist (1974) analysed the HIC analytically with several theoretical pulse shapes including a square, triangle and half-sine pulse shape. For these pulse shapes they determined an analytical value of the HIC and important aspects of the pulse shapes such as change in velocity and stopping distance. They showed that the pulse shape can be influential on the value of the IRF. This theoretical work was extended by Hutchinson et al. (1998).

Other research has discussed the use of HIC and the pulse shapes that are optimal for it when it is used as an IRF. The optimal pulse shape is dependant on the parameters that are used to define what an ideal impact means. For instance Wu and Beaudet (2007) investigated the ideal pulse shape for HIC when a minimum stopping distance was required for a predetermined value of HIC. Similar work has not been completed for the other IRFs, but similar optimised pulse shapes could exist.

The designers' objective is to meet crashworthiness requirements of a protocol, as is measured by the operating IRF. In practice, this means reducing, to an acceptable level, the IRF measured in an impact with a known speed whilst utilising all the available deformation space of the vehicle as a stopping distance for the headform. Modifying the pulse shape can be used to assist in meeting this objective. In practice, the pulse shape can be modified by redesigning the impact structure. For example, modified materials or geometry can be used to change the pulse shape (Belingardi et al., 2009; Untaroiu et al., 2007).

1.6.2 Comparison of practical testing data

The effect the different IRFs have on the evaluation of test data has not been a focus in any research. In the development of a pedestrian test protocol Glaeser (1991) determined the value of HIC, a_3 and a_m for a small series of impact tests with a proposed headform. These results were not compared with each other except for evaluating the variance in results for each IRF.

The effect of IRF choice may or may not be of practical significance. For instance, even though two different IRFs may not be linearly correlated, there may be only a small difference between the ranking of test results with either IRF.

There is an opportunity to investigate the effect that different IRFs have in determining the measured safety of the products. Through this process the salient features of the different IRFs can be identified. In particular, this thesis is interested in the question of how alternative IRFs might encourage design in different directions in pedestrian safety testing. Specifically, the thesis seeks the pulse shapes and impact conditions favourable for various IRFs. This is done using analyses of idealised, theoretical pulse shapes and a series of 247 headform tests performed for the requirements of the Euro NCAP pedestrian safety test protocol (EEVC, 2003).

1.7 Aims of the thesis

The aims of this study were:

- To investigate the properties of HIC and three alternative IRFs using theoretical acceleration pulse shapes and to compare these to the known properties of HIC.
- To estimate theoretically, and measure experimentally, the magnitude of the effects of impact velocity, stopping distance and coefficient of restitution on the test result for the different IRFs.
- To consider the effects that the choice of IRF has for the testing result.

- To find and understand the impacts which give rise to discrepancies with alternative IRFs, and comment on the importance of the properties of those impacts.

1.8 Organisation of the thesis

The thesis has four main sections. In the first section some preparatory information is provided, necessary for the development of the remainder of the thesis. This includes a discussion of the IRFs that are used in the thesis. Information about the set of pedestrian headform tests used throughout the thesis is also presented.

In the second section some theory about each IRF is developed. This includes an analysis of pulse shape, as well as analysis of the effect of stopping distance, impact velocity and coefficient of restitution. In this section the effects of pulse shape, stopping distance, impact velocity and coefficient of restitution are considered to be inputs, which directly relate to the value of each IRF.

In the third section the pulse shapes from the pedestrian headform tests are evaluated with each IRF to understand the practical differences between each IRF. In this section the effects of pulse shape, stopping distance, impact velocity and coefficient of restitution are considered to be outputs of the test. Controlling for them allows the properties of the IRF to be examined in detail in real test data.

In the last section the thesis is summarised, main results are discussed, and conclusions and recommendations are made.

1.8.1 Preparatory information – Chapters 2 and 3

In Chapter 2 the IRFs that are used in this thesis are defined. These are HIC, PVP, a_m and a_3.

In Chapter 3 a total of 247 tests, with two different sized headforms, collected from ANCAP testing for pedestrian safety assessments are described. The consecutive series of tests were conducted between January 2006 and

February 2008. The methods used to measure test parameters, such as the impact velocity of the headform and an estimate of the headform stopping distance in each tests, are explained.

Some general information about the data set is provided in Chapter 3. The distributions of some results of the tests are provided. This includes distributions of measured and estimated parameters such as the angle of impact, impact velocity, stopping distance and coefficient of restitution as well as the distributions for each of the IRFs. These are provided so that the data set is fully characterised.

1.8.2 Theoretical pulse shape analysis – Chapters 4 and 5

In Chapter 4, several theoretical acceleration pulse shapes are described: a square, triangle and half-sine shape. Each pulse shape is described by its maximum acceleration amplitude, A, and its time duration, T. Several triangle pulse shapes are considered. Controlling the location of the apex of the pulse shape creates a pulse shape that varies from a front loaded pulse shape to a rear loaded pulse shape. Consequently there are a total of eight pulse shapes used in the analysis (square, half-sine and six triangle). The purpose of considering these theoretical pulse shapes is to examine how the pulse shape contributes to the value of the various IRFs being examined.

The theoretical pulse shapes selected do not directly represent any constitutive laws of impact mechanics. The purpose of studying them is to understand how each IRF measures each different type of pulse shape so that general conclusions about the IRFs may be made.

Normalisation of the theoretical pulse shapes

The pulse shape is not the only factor that contributes to the value of the IRF. Two physical properties of an impact that are relevant to an impact test protocol also contribute to the value of the IRF. They are the impact velocity and stopping distance of the impact. To isolate the pulse shape's effect on the value of the IRF from these physical factors, the theoretical pulse shapes were normalised so that they each had an identical impact velocity and stopping distance. This was achieved by calculating theoretically the impact

velocity and stopping distance for each pulse shape, for various coefficients of restitution. Each pulse shape was then forced to have the same impact velocity and stopping distance as a reference pulse shape for the purposes of normalisation.

Comparison of the value of each IRF with each theoretical pulse shape

The value of each IRF is calculated for each normalised theoretical pulse shape. Then, for each IRF its value for each pulse shape is compared. Important differences that are exposed between the IRFs are then identified and examined.

At the conclusion of Chapter 4 several properties of each IRF and how each IRF treats different pulse shapes will have been shown. These results will be utilised throughout the thesis to assist in the explanation of other results.

Effect of impact velocity, headform stopping distance and coefficient of restitution

In Chapter 5 the effect of the impact velocity, stopping distance and the coefficient of restitution on the value of each IRF is investigated. This is done by extending the results from Chapter 4 to determine the value of each IRF as a power function of the impact velocity, stopping distance and coefficient of restitution. It is shown that when there is no rebound velocity the other IRFs also have a relationship with impact velocity and stopping distance that is of the form shown in Equation (1.3).

$$\text{IRF} \propto V^m S^n \tag{1.3}$$

where m and n are constant for each IRF and independent of pulse shape.

For real impacts with a coefficient of restitution, R, it is further shown that, to a good approximation, the value of each IRF is also proportional to $(R+1)^q$ where q is constant for each IRF. Consequently, Equation (1.3) can be expanded to include the coefficient of restitution as shown in Equa-

tion (1.4).

$$\text{IRF} \propto (R+1)^q V^m S^n \tag{1.4}$$

The data described in Chapter 3, is used to investigate how well the variables of impact velocity, stopping distance and coefficient of restitution can predict the value of the IRF using Equation (1.4). The results show consistency between the theoretical predictions and the empirical values of each power function for each of the headform sizes used in the testing. However, as there is limited variability of the impact velocity and coefficient of restitution in the test data, the effect of these variables could not be completely explored empirically.

At the conclusion of Chapter 5 a thorough understanding of the effect of the physical properties of an impact on the value of each IRF will have been achieved. This understanding is used in subsequent chapters so that the pulse shape from the real tests can be considered in isolation from the dominating effects of these physical properties of impact velocity, stopping distance and coefficient of restitution.

1.8.3 Empirical pulse shape analysis – Chapters 6 and 7

The IRFs are applied to the test data, and the resulting measures of severity are compared in several ways. The comparisons are made on bases that are relevant in the context of vehicle safety testing where the objective is to either pass or fail a structure, or to rank structures in terms of their performance. These techniques are briefly introduced here.

Two different headforms were used in the generation of the test data. The data from each headform size are kept separate throughout the analysis.

Correlation of the data

Firstly, the value of each IRF for every test in the data set is compared with the other IRFs using a Pearson correlation. Because the impact velocity and the coefficient of restitution are tightly distributed in the dataset a high correlation between the IRFs is expected because the theoretical relationships

that were developed in previous chapters show that the value of each IRF is highly dependent on the headform stopping distance. These high correlation values between the IRFs are demonstrated empirically.

Effect of the threshold

Secondly, conservative thresholds for each IRF, compared with HIC = 1000 are found using analysis of contingency tables populated with tests from the data set. These conservative thresholds are then compared with thresholds for those IRFs that are available in the literature.

Comparison with rank correlation

Any implied relationship between the value of the IRF and injury risk can be removed when the tests are ranked according to the value of each IRF. (ie. from best to worst). Rank correlation is used to investigate how the ranking of tests differs according to the choice of IRF. A positive correlation is observed between the ranked data using each of the IRFs. Contributing to this correlation are common effects of impact velocity, stopping distance and coefficient of restitution.

Lastly, the effect that the pulse shape has on the value of the IRF is investigated using rank correlation. To isolate the effect of the pulse shape from the effect of impact velocity, stopping distance and coefficient of restitution, their influence on the IRF value is subtracted from the value of the IRF. The remainder is considered to the the pulse shape coefficient, $\mathbb{P}_{\text{IRF}}$. Each $\mathbb{P}_{\text{IRF}}$ is independent of impact velocity, stopping distance and coefficient of restitution. The correlation between the ranking of these pulse shape coefficients is lower than the correlation between the ranking of the values of each IRF. The correlation that remains is due to the effect of the pulse shape of each of the real tests.

Investigation of pulse shapes with discrepant rankings

In general, a positive correlation between each of the IRFs is shown. However, there are some discrepancies that are most obvious when the ranks of pulse

shape coefficient are examined. In Chapter 7 the pulse shapes of the tests for which alternate IRFs give different assessments to those made by HIC are investigated.

The features of the pulse shapes that contribute to their discrepant ranking with a pair of IRFs are discussed.

1.8.4 Concluding chapter – Chapter 8

A summary of the main findings of the thesis is provided in Chapter 8 and some of the major themes are discussed in a broader real-world context. The opportunity for future work stemming from the results of this thesis is also highlighted.

1.9 Limitations of the thesis

Discussions about alternative IRFs usually centre on biomechanics and biofidelity. These are not discussed in this thesis. Rather, the objective is to examine the influence that the IRF has on design within an established test protocol. To meet this objective, the properties of the IRFs themselves are studied, not the relationship of each IRF with injury. A recent study that examined the relationship between IRFs and injury was published by Marjoux et al. (2008).

The first major work understanding the determinants of the value of an IRF, that did not examine biofidelity, was by Chou and Nyquist (1974). It is the path established by Chou and Nyquist that this thesis explores, extending the results for HIC, developing results for the other IRFs, and making comparisons of these results.

Only IRFs that use linear acceleration as a basis for determining the severity of the impact are considered. The main reason for this limitation is that linear acceleration is the basis of the main head injury test protocols. These protocols include the Euro NCAP pedestrian head test protocol, various vehicle test protocols such as FMVSS 201 (2008) and FMVSS 208 (2008) and helmet test protocols such as NFPA 1971 (2007).

There are some testing environments proposed which consider both linear acceleration and rotational acceleration. The infrastructure required to perform the testing of impacts involving linear and angular accelerations is already available (Aare and Halldin, 2003) but it is still necessary to determine the appropriate standardised impact conditions that a test protocol using this infrastructure would use.

There are also IRFs that are determined from the outputs of a finite element model of the human head (Deck and Willinger, 2008). Typically these IRFs are based on strains measured in the modelled brain. These IRFs are not considered because of numerous other boundary conditions of the impact that must also be determined (such as the location of the impact on the head). These are not specified as part of current test protocols.

Chapter 2

Injury Response Functions

2.1 Introduction

There are several Injury Response Functions (IRFs) that can be used to summarise the risk of injury in an impact of a headform with a structure. Each has a mathematical definition that is used to summarise the kinematics measured by the headform. These mathematical definitions are presented in this chapter along with brief background information about each IRF. In Section 2.2 the IRFs evaluated in this thesis are presented and in Section 2.3 some of the IRFs that are not evaluated in this thesis are briefly presented for completeness.

In safety testing, on use of the IRF is to sort the more dangerous impacts from the less dangerous ones. A more difficult use of the IRF is to relate its value to injury risk. Some injury risk curves have been produced for use with the Head Injury Criterion (HIC) (Mertz et al., 1996). In most cases, IRFs have thresholds that are applied to delineate the tests that are considered 'safe' from the tests considered 'unsafe'.

2.1.1 Wayne State Tolerance Curve

According to Hess et al. (1980) the most influential piece of work that relates the kinematics of impact to head injury is the Wayne State University Tolerance Curve (WSTC). The curve that was introduced by Gurdjian et al. (1966) is shown in Figure 2.1. The WSTC is used to identify impacts that are 'dangerous to life' based on the magnitude and the duration of the effective acceleration to the head. The origins of the WSTC have been examined in many publications (for example SAE, 1980). The WSTC is based on results of experiments in which the heads of embalmed cadavers were impacted against an anvil; the acceleration and duration of the impact were measured and the presence or absence of skull fracture was noted (Lissner et al., 1960). These experiments were supplemented by others including experiments using direct application of air pressure on the brains of dogs (Gurdjian et al., 1953) and sled deceleration experiments using human volunteers (Stapp, 1961).

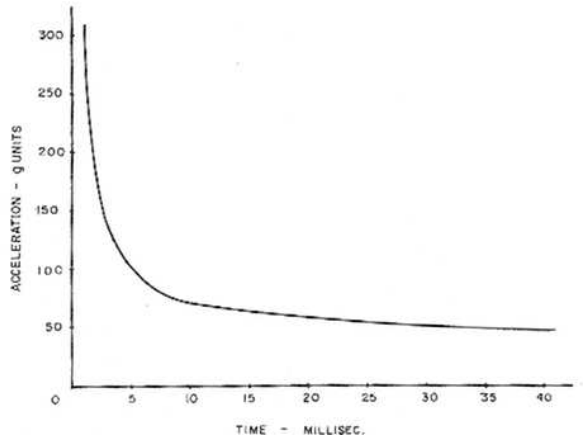

Figure 2.1: Wayne State Tolerance Curve (from Gurdjian et al., 1966). Impacts above the curve are considered unsafe.

The WSTC implies that an impact of high acceleration can be tolerated without injury provided that its duration is short, while an impact of low acceleration can be tolerated for a much longer time duration.

The data used as a basis for the WSTC has been criticised (Goldsmith, 1981; Newman, 1980). This criticism relates to the limited number of data points that were used and the relevance of the experimentation. In addition, the use of the WSTC for purposes other than frontal head impact was cautioned by those involved in its construction (Gurdjian et al., 1966).

The first versions of the WSTC appeared as interest in vehicle safety was growing. In 1968 the National Highway Traffic Safety Administration (NHTSA) was set up with the aim of, inter alia,reducing the injury associated with vehicle accidents. Due to the lack of any other definition of impact tolerance, the WSTC became written into mandatory testing protocol through various operationalisations of the curve. These operationalisations are the linear acceleration IRFs, and these are discussed in the following section.

2.2 Injury Response Functions used in this thesis

2.2.1 Head Injury Criterion

The Head Injury Criterion (HIC) is the IRF that has the most widespread use (Simms and Wood, 2009, pg 77). Its formulation is a result of analysis of the WSTC. Several sources document the creation of the HIC (e.g. Anderson and McLean, 2005; Hess et al., 1980; Newman, 1980; SAE, 1980). The main contributors to the definition of the HIC were Gadd and Versace. Their contributions are detailed below.

Gadd (1961, as stated in Hess et al., 1980) suggested that plotting the WSTC on logarithmic axes would result in a straight line as the boundary between impacts that were 'safe' and those that were 'unsafe'. This defined boundary could then be used to compare against acceleration pulse shapes. To make the comparison, a method of systematically evaluating the duration of the effective acceleration of the pulse shape was needed. Gadd (1966) suggested that the acceleration pulse shape, measured from an experiment, could be evaluated using the severity index, SI.

$$SI = \int_0^T a^n dt \tag{2.1}$$

Where t is time in seconds, T is the duration of the impact, a is the measured acceleration in g and n is a weighting factor which he suggested could be $n = 2.5$ based on the slope of the WSTC drawn on logarithmic axes. Using these values, an impact with a $SI > 1000$ was considered to have exceeded the boundary, and was therefore 'unsafe'.

While Gadd (1966) used the acceleration measured in the anterior-posterior direction of the skull, when the Severity Index was included in a Federal Motor Vehicle Safety Standard, the resultant acceleration, measured at the centre of the gravity of the head, was used in the calculation (SAE, 1980).

HIC was first described in a critical review of the severity index by Versace (1971). In that review it was shown that the severity index was mathematically illogical for all pulse shapes except a square pulse shape. This is because the WSTC uses 'average' acceleration as its ordinate axis. Versace

(1971) showed that $\left(\int a dt\right)^n = \int a^n dt$ only when a is a constant value. Versace (1971) proposed that a better operationalisation of the WSTC, which used an alternative definition of the 'average' acceleration that was defined in the WSTC. This alternative became known as the Head Injury Criterion when it was adopted into the FMVSS 208 in 1972 (Hess et al., 1980). The HIC function is:

$$\text{HIC} = \max \left[(t_2 - t_1) \left(\frac{\int_{t_1}^{t_2} a dt}{t_2 - t_1} \right)^{2.5} \right] \tag{2.2}$$

where a is the resultant acceleration in g at the centre of gravity of the head and $t_1 < t_2$ are times in milliseconds during the impact pulse selected to maximise the value of HIC.

The HIC can be modified by specifying a maximum duration of the evaluation window. The HIC_{15} has a maximum difference between t_1 and t_2 of 15 ms. The reason for limiting the HIC to a evaluation window of 15 ms was due to Hodgson and Thomas (1972) who noted that concussion only resulted from impacts with a short duration. The notation HIC_∞ is used in this thesis to indicate HIC without a restriction on the maximum difference between t_1 and t_2.

$\text{HIC} = 1000$ is the usual threshold applied in automobile safety testing with $\text{HIC} < 1000$ usually considered as an acceptable result. According to a meta-analysis performed by Prasad and Mertz (1985) this value of HIC indicates a 16% risk of life threatening brain injury.

2.2.2 3 millisecond clip

The 3 millisecond clip, or a_3, is the maximum acceleration that is sustained for a continuous period of 3 ms in an impact.

In Hess et al. (1980) the developments that contributed to the acceptance of this IRF are described as follows:

- Patrick et al. (1963) suggested that high acceleration peaks lasting longer than 1 ms should be avoided. In particular, a limit of 60 g to 80 g was considered the limit for a safe impact on a padded surface.

- In 1966 A Federal Motor Vehicle Safety Standard was issued, requiring, for instrument panels, that the deceleration of the prescribed headform not exceed 80 g for 1.0 ms or more.
- The Federal Motor Vehicle Safety Standard was then revised in 1967, after a 'request from petitioners', and the duration for which the acceleration could exceed 80 g was extended from 1.0 ms to 3.0 ms.

This IRF discounts accelerations that have a short duration,as these, according to the WSTC, have a lesser injury risk. Accelerations with a longer duration, however, are considered as they have a greater injury risk.

The 3 millisecond clip continues to be used, world wide, in various instrument panel test protocols (Boggess and Foreman, 2007). It is also used in several helmet impact test standards (Newman, 1993) such as NFPA 1971 (2007) used for fire helmet safety.

A typical a_3 threshold used as a criterion is 80 g (Boggess and Foreman, 2007; Hess et al., 1980). This threshold is applied for the variety of impact conditions used in those test protocols. In several of the helmet testing standards, however, the threshold is higher: up to 200 g (Newman, 1993).

Due to its definition, this IRF is meaningless for impacts that have a duration of less than 3 ms. For these impacts $a_3 = 0$ g. The 3 millisecond clip also dismisses features within pulse shapes that are very short in duration.

The 3 millisecond clip has been used to make comparisons between impacts with cadavers and with dummies or headforms. Got et al. (1978) demonstrated that the acceleration level that was present for a continuous period of 3 ms remained consistent between their experiments with the cadavers and with the dummies. Glaeser (1991) used it to show that the measurements made with headforms for a pedestrian test standard had a similar variability as measurements made using cadavers.

2.2.3 Peak Acceleration

The simplest summary of an acceleration pulse shape is a measure of the peak acceleration, a_m, attained during the impact. Gadd (1966), in the same manuscript that introduced the Severity Index, noted that up until the time

of his manuscript the peak of the acceleration pulse was "the most widely used rule of thumb measure" for evaluating impacts in the laboratory. This was because it is the simplest way of evaluating a pulse shape (Gadd, 1966).

The peak acceleration continues to be used in various helmet testing standards (Newman, 1993). Typical thresholds used with this IRF for helmet testing range between $a_m > 150\,\mathrm{g}$ and $a_m > 400\,\mathrm{g}$ with $a_m > 300\,\mathrm{g}$ being a typical threshold value.

2.2.4 Peak Virtual Power

Neal-Sturgess (2002) proposed a new IRF which he called Peak Virtual Power (PVP). The reasoning for the proposal was that other IRFs were based on empirical data, and this IRF was based on fundamental laws of thermodynamics subsequently applied to impact scenarios. The PVP was based on the principle of virtual power, described by Germain (1972, cited in Lemaitre and Chaboche 1994), and used for analysis of continuum mechanics. As such, the PVP is derived from the second law of thermodynamics using the Clausius-Duhem inequality. This derivation shows that injury is proportional to the rate of entropy production. Neal-Sturgess (2002) proposed that the peak value of the virtual power be used to identify the maximum rate of energy transfer, as this had been indicated, without proof, by Waller (1985) to be indicative of the severity of injury.

When the PVP was tested against crash databases with injury data, it was shown that the PVP was proportional to injury in many regions of the body (Neal-Sturgess, 2002). It was further demonstrated that the PVP and HIC were similar for simulations of impacts with a Hybrid III head. To date, the PVP has had only a small amount of rigorous analysis, and is not used in any test protocols. However, the mathematical derivation of injury potential it is a unique approach to the development of an IRF, and is consequently worthy of further analysis.

Newman et al. (2000b) also proposed an IRF that is similar to PVP, called Head Impact Power (HIP). HIP was based on the assumption that the dimensions of HICwere similar to that of the rate of change in energy with time, or power. As this quantity is a meaninful engineering quantity, it was

thought that using it in an IRF may lead to a better relationship with injury than exists with HIC.

The HIP uses linear and angular acceleration components split into the individual direction axes. Therefore its use with pedestrian headforms in their current configuration is not possible without substantial assumptions. The definition of HIP is shown in Equation (2.3).

$$\text{HIP} = \max \left[\sum_{i=x,y,z} C_i a_i(t) \int_0^t a_i dt + \sum_{j=x,y,z} W_j \alpha_j(t) \int_0^t \alpha_j dt \right] \tag{2.3}$$

where a_i is the linear acceleration measured in the i axis, α_j is the angular acceleration measured in the j axis, and t is the time in seconds. C_i and W_j are coefficients for each component. Newman et al. (2000b) suggested that $C_i = C$ be the mass of the head and W_j the the moment of inertia of the head in each axis.

Jiang et al. (2010) used HIP in their study and showed that it conforms to the principle of peak virtual power, or PVP.

A form of the PVP using only linear acceleration, that is similar to HIP is shown in Equation (2.4).

$$\text{PVP} = a(t^*) \int_0^{t^*} a(u)\, du \tag{2.4}$$

where t^* is the time that maximises the value of PVP. It is different from the HIP because the rotational components are not considered, the mass of the headform is not considered and the resultant acceleration is used for the calculation instead of acceleration in each orthoganal axis. This is the form of PVP used throughout this thesis because of its similarity with HIP. In Appendix E on page 283, a comparison between HIP and this PVP is made using the data described in Chapter 3. It is shown that there is strong agreement between these two IRFs.

Previously, DiLorenzo (1976) had suggested that power could be used as a predictor of injury. Both PVP and HIP are implementations of this idea.

The PVP is not in use in a testing protocol, nor does it have a threshold for injury. A threshold for HIP, however, was estimated by Marjoux et al. (2008)

using a finite element model. They estimated that HIP = 48 kW corresponds to a 50% probability of serious brain damage. This analysis in Appendix E is used when neccessary to suggest that the threshold of Marjoux et al. may be interpreted for the PVP also.

2.3 Injury Response Functions not examined in this thesis

There are several IRFs that are not examined in this thesis. Some of these IRFs are discussed briefly here. These IRFs can be divided into three different classes: those based on rotational acceleration, those based on finite element models, and those based on lumped parameter models. These IRFs are not examined because they are not based on measured linear acceleration pulse shapes which result from the impact tests currently performed.

2.3.1 IRFs based on rotational acceleration

Holbourn (1943) conducted experiments with a gel-filled head-shaped container and showed that strain could be generated in the brain tissue by rotational motion alone. Rotation has also been shown experimentally to contribute to brain injury (Ommaya and Hirsch, 1971). The direction of the angular motion has been found to be an important contributing factor to the level of injury found (Gennarelli et al., 1987).

Margulies and Thibault (1992) proposed injury tolerance limits for two IRFs based on rotational motion: peak angular acceleration and peak change in rotational motion. Despite this research, a single criterion for maximum rotational motion has not been generally accepted at this time (Simms and Wood, 2009, pg. 79) and none has been incorporated into any testing standards.

Hybrid linear and angular acceleration IRFs

In some IRFs linear and angular kinematics are considered at the same time. An example of this type of criteria is the HIP that was described in Section 2.2.4.

Angular kinematics have been used to extend the established IRFs that use linear acceleration to define alternative IRFs.

One of these is the Generalised Acceleration Model for Brain Injury Threshold (GAMBIT) (Newman, 1986).

$$G(t) = \left(\left(\frac{a(t)}{a_c} \right)^n + \left(\frac{\alpha(t)}{\alpha_c} \right)^m \right)^{\frac{1}{s}} \tag{2.5}$$

where a is the linear acceleration in g and a_c is a critical value of acceleration, and α is the angular acceleration with α_c a critical value in rad/s^2 and m, n and s as constants.

Different values can be selected for the constants and critical values. These create different 'isothresholds' of G. Newman (1986) suggested the simplest form shown in Equation (2.6) using the maximum values of a and α and $m = n = s = 1$.

$$G = \frac{a_m}{250} + \frac{\alpha_m}{10000} \tag{2.6}$$

Another IRF that combines linear and rotational kinematics is the strain IRF suggested by Aare et al. (2004). This IRF combines HIC with the peak change in angular velocity,$\Delta\ \omega$, and was derived from results of a finite element model of the head. The model calculated the strain, ϵ, in the brain tissue. A regression equation was solved to determine the coefficients k_1 and k_2 which are dependent on the impact direction. The final equation is shown in Equation (2.7).

$$\epsilon = k_1 \Delta\omega + k_2 \mathrm{HIC} \tag{2.7}$$

It is important to note that linear acceleration and angular acceleration are not independent quantities in real impacts. Funk et al. (2008) showed that linear acceleration could be systematically related to rotational acceleration

for various activities involving a direct force to the head including a soccer ball impact or a voluntary hand-to-head slap.

2.3.2 IRFs based on finite element models

Several finite element models of the human head have been made to study impact phenomena. Several of these were compared by Deck and Willinger (2009). Examples of the current finite element models were those described by Takhounts et al. (2003), Kleiven (2002) and Kang et al. (1997). The outputs of these models, which have been linked to injury in the brain were summarised by by Deck and Willinger (2008). They include the cumulative strain damage measure, dilatational damage measure, relative motion damage measure, strain rate, product of strain rate and strain, principal stress and Von-Mises stress, and skull strain energy.

2.3.3 IRFs based on lumped parameter models

Stalnaker et al. (1997, 1985) and Willinger et al. (1991) proposed and used IRFs based on lumped parameter models of the head. Lumped parameter models use masses, springs and dampers connected to each other in parallel or in series so that the frequency response of the head is mimicked by the model. They are similar to a finite element model in that the response of the model can be simulated with a computer but they are much simplified compared with a finite element model. The IRFs that were proposed include the New Mean Strain Criterion (Stalnaker et al., 1985) and the Translational Head Injury Model (Stalnaker et al., 1997).

The force-time measurements from an impact can be used as an input to these models and defined parameters measured from these models can then be used to estimate head injury potential.

2.4 Concluding remarks

The various IRFs that are available for use have been discussed in this chapter. They have been divided into those that are used in this thesis and those that are not used.

The IRFs that are used in the thesis are all based on linear acceleration, and have historical links to the WSTC and can be applied to measurements made in impact tests.

Chapter 3

Description of a set of data obtained from pedestrian headform testing

3.1 Introduction

The test data used in this study was collected for the pedestrian safety component of the Australasian New Car Assessment Program between January 2006 and February 2008. During this time, this assessment program was identical to version 4.1 of the Euro NCAP pedestrian test protocol (Euro NCAP, 2004). The Euro NCAP pedestrian test protocol has four sub-system test impactors, each of which is fired at a stationary vehicle for each impact test. Two of these impactors are headforms, respectively representing the head of a Child and an Adult. The others are an upper leg and a lower leg test. While the crashworthiness rating for each vehicle is based on the results of all the tests performed with all the sub-system impactors, the upper and lower leg tests were not considered in the analysis conducted in this thesis.

247 headform tests were conducted during this time. 139 of these were conducted with a smaller, Child, headform, and 108 were conducted with a heavier, Adult, headform. All of the valid tests that were conducted in the study period were included in the data set for analysis.

The headform test data was analysed retrospectively for the purposes of this study. Some of the data used needed to be estimated from the available data. This chapter will describe the data collected and the retrospective analysis performed for this study.

As an introduction to a single headform test, a series of frames from the high speed film of one test (21050701) are shown in Figure 3.1. Each frame is separated by 5 ms. The figure shows that a test consists of a headform being projected toward a structure on a vehicle. Upon contact the structure deforms. During the impact the headform rotates across the deformed surface of the bonnet. Accelerometers inside the headform are used to record the impact. The measured acceleration is then analysed for the purposes of evaluating the crashworthiness of that impact location.

In this Chapter the method for collecting the data is described, and distributions of the data are shown. This includes information about the methods used and data collected for each test in Section 3.2, and the methods used for retrospective analysis of the data in Section 3.4. Distributions for the



(a) -5 ms



(b) 0 ms — Contact begins



(c) 5 ms



(d) 10 ms

Figure 3.1: High speed film of test 21050701



(e) 15 ms



(f) 20 ms



(g) 25 ms



(h) 30 ms

Figure 3.1: High speed film of test 21050701(cont.)



(i) 35 ms



(j) 40 ms — Contact ends



(k) 45 ms



(l) 50 ms

Figure 3.1: High speed film of test 21050701(cont.)

measured data from every test are shown in Section 3.3 and the distributions of the data obtained retrospectively are shown in Section 3.5. The method for calculating each IRF is shown, along with the distributions of the IRFs, in Section 3.6. Where useful, the data from test 21050701 (shown in Figure 3.1) is used to illustrate the data that was collected. Finally some descriptive terms to describe the pulse shapes are illustrated in Section 3.7.

3.2 Test methods

All tests were performed according to the requirements of the Euro NCAP pedestrian test protocol. The Euro NCAP protocol describes the number and location of headform tests to be performed on each vehicle. Nominally, six tests with each headform size are conducted on each vehicle. These are spread across the likely impact zones for a pedestrian, as specified in the protocol.

The tests conducted with the child headform are conducted near the front of the vehicle, and the tests with the Adult headform are conducted further back. This reflects the difference in statures of the Child and Adult, and the resulting likely impact zones.

The location for the six tests with each headform are determined by the test laboratory according to the protocol. The structures that are chosen are those which are expected to be least crashworthy (when the acceleration is evaluated with HIC).

3.2.1 Apparatus

The apparatus specifications are described in EEVC (2003).

The headforms

Two headforms are used in the Euro NCAP (2004) test procedure. The Child headform has a mass of 2.5 kg, while the Adult headform has a mass of 4.8 kg. The Child headform is used in the test zones nearer to the front of

Table 3.1: Head form data (from EEVC, 2003).

NOTE:
These figures/tables/images have been removed
to comply with copyright regulations.
It is included in the print copy of the thesis
held by the University of Adelaide Library.

Figure 3.2: Child headform (from EEVC, 2003), dimensions in mm.

the vehicle (Note that these headforms have been superseded in the latest version of the protocol.)

The details of headform construction are shown in Table 3.1. A schematic of the Child headform is shown in Figure 3.2 and the Adult headform is shown in Figure 3.3.

NOTE:
This figure/table/image has been removed
to comply with copyright regulations.
It is included in the print copy of the thesis
held by the University of Adelaide Library.

Figure 3.3: Adult headform (from EEVC, 2003), dimensions in mm.

Accelerometers

The accelerometers are mounted in the headform such that their sensitive masses are located within a 10 mm spherical radius of the centre of gravity of the headform. The orientation of each accelerometer defines the three main reference axes, x, y and z. The orientation of each accelerometer, relative to the headform and to the the plane that is perpendicular to the ground when the headform is launched, is shown in Figure 3.4 .

Data Acquisition

The accelerometer signal was sampled at 50 kHz. The signal was processed according to the SAE J211 standard (SAE, 2003).

Firing Apparatus

The firing apparatus, or headform launcher, is designed to launch the headform at a desired angle and speed. It is powered by several elastic bands, and is electronically controlled. Firing speed control is obtained through

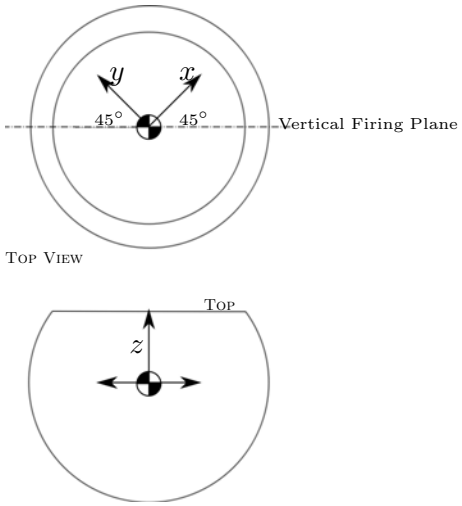

Figure 3.4: Orientation of the accelerometers in the headforms.



Figure 3.5: The firing apparatus.

the stretched length of the elastic bands prior to the firing time. The firing apparatus is shown in Figure 3.5.

The headform is pneumatically held in position on the carriage of the firing apparatus until the carriage is accelerated toward the end of the firing machine. The headform remains steady in the carriage throughout the acceleration phase of the carriage because of the inertial forces between the carriage and the headform. When the acceleration on the carriage ends, the headform is no longer attached to the carriage and begins its free motion toward the vehicle.

Table 3.2: Test Conditions for each headform.

Property	Headform	
	Child	Adult
Impact speed	$11.1 \pm 0.2\text{ms}^{-1}$	$11.1 \pm 0.2\text{ms}^{-1}$
∠Firing†	65°	50°

† measured relative to the ground

3.2.2 Test Procedure

Test conditions

The vehicle is manoeuvred so that the impact occurs at the selected location on the vehicle. The vertical flight plane of the headform, shown in Figure 3.4, is positioned so that it is parallel with the midline of the vehicle. The vehicle is then moved forward so that the headform strikes the intended impact location. The basic requirements of the test conditions are shown in Table 3.2.

A high speed camera capturing footage at 1000 Hz is positioned to film the impact. The camera is positioned to provide an uninterrupted view of the impact site without interfering with any of the objective measurement equipment. The camera does not provide any objective measurements and is used to review the impact if necessary.

The end of the firing apparatus is positioned as near as practicable to the testing location leaving room to measure the velocity of the headform and to ensure that the headform does not rebound back into the firing apparatus. The barrel of the firing apparatus is angled as given in Table 3.2. The effect of gravity is considered so that the first point of contact of the headform and the bonnet occurs within the 20 mm of the desired impact location. The effect of gravity on the motion of the headform is further discussed in the next subsection.

The impact speed is measured using a dual-laser speed measuring device (Anderson, 2005). The two lasers on the device are separated by a known distance and the speed of the headform is calculated from the time that the headform takes to interrupt each of laser paths in sequence. The speed

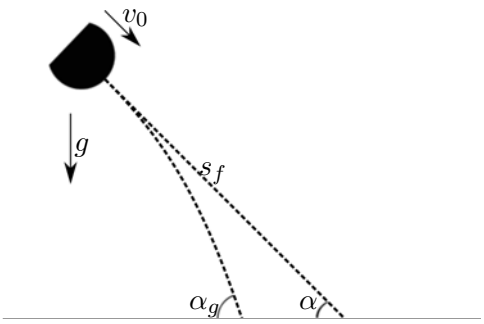

Figure 3.6: Effect of gravity on headform flight path.

gained by the headform due to gravity after passing through the measuring device is then added to the measured speed to determine the speed of the headform at impact.

Motion of the headform during free flight

During free flight the headform is free to accelerate with the effect of gravity. The action of gravity has two effects: the headform gains additional momentum through the gravitational acceleration, and the impact angle changes slightly. The additional momentum gained is calculated and added to the measured projectile speed as a routine part of the testing procedure to determine the final impact speed. However, the change in impact angle is not calculated as a routine part of the testing procedure. The impact angle is a necessary measurement to determine the deformation of the bonnet during the impact, as described in Section 3.5. A schematic showing the change in impact angle as a result of gravity is shown in Figure 3.6. At the instant of release from the carriage the headform has an trajectory that is the same as the firing angle of the launching machine. Without the assumption of gravity the impact angle is α, with the effect of gravity the impact angle is α_g.

The change in impact angle due to gravity can be calculated. The equation to determine the approximate new impact angle is shown in Equation (3.1).

$$\alpha_g = \arctan\left(\frac{v_0 \sin(\alpha) + g t_f}{v_0 \cos(\alpha)}\right) \tag{3.1}$$

Table 3.3: Striking angle, α_g, of headform for various flight distances, s_f.

Flight distance	Headform	
	Child	Adult
0.3 m	50.86°	65.57°
0.5 m	51.42°	65.93°
1.0 m	52.76°	66.79°

Where:
v_0 is the speed of the headform,
g is the acceleration due to gravity, and
t_f is the time the headform is in free flight.

The time in free flight can be approximated as the time taken for the headform to traverse the distance s_f shown in Figure 3.6 because the distance of the free flight is an estimated quantity. The approximation for the time in free flight is shown in Equation 3.2.

$$t_f \approx \frac{s_f}{v_0} \tag{3.2}$$

The striking angles for various flight distances of both headforms are shown in Table 3.3.

After discussion with the test engineers involved in the data collection, it was determined that a typical flight distance was 1 m for all tests. Consequently, with a headform speed of 11.1 m s^{-1} the Child headform impact angle increased from $\alpha = 50.0°$ to $\alpha_g = 52.76°$ and the Adult headform impact angle increased from $\alpha = 65.0°$ to $\alpha_g = 66.79°$. These adjustments to the impact angle are used in each of the calculations henceforth.

Normal impact velocity

The velocity of the headform at impact, normal to the impact surface, is an important parameter to estimate the maximum deformation of the structure during the impact. It is calculated from the angle of impact, $\theta(0)$ and the

impact speed.

$$V = v(0)\sin(\theta) \tag{3.3}$$

where $v(0)$ is the total impact speed and θ is the angle of impact.

The angle of impact, θ is equal to the flight angle, adjusted for gravity, plus the measured angle of the bonnet at the impact site. This was measured with a digital level with an accuracy of $\pm.1^\circ$.

Acceleration

The acceleration of the headform during the impact is measured by the triaxial accelerometer installed in each headform.

As an example, the filtered acceleration signals measured by each accelerometer along with the total resultant acceleration signal, for the test shown in Figure 3.1, is shown in Figure 3.7. The dominant signal is measured by the z-direction accelerometer. This accelerometer has its sensitive direction colinear with the direction of headform motion when the headform is launched.

The x-direction and y-direction accelerometers are angled at 45° to the plane of motion as was defined in Section 3.2.1. Consequently, any tests that occur on a smooth surface, as was the case in this test, produce acceleration measurements of a_x and a_y which are similar in magnitude but opposite in sign.

3.3 Distributions of measured data

3.3.1 Impact Speed

The impact speed is measured to an accuracy of $0.01\,\mathrm{m\,s^{-1}}$; later, for the purposes of the test being within the tolerance specified in the protocol, the speed is rounded to an accuracy of $0.1\,\mathrm{m\,s^{-1}}$. Figure 3.8 shows the cumulative distribution of the speed of the headform when impact occurred

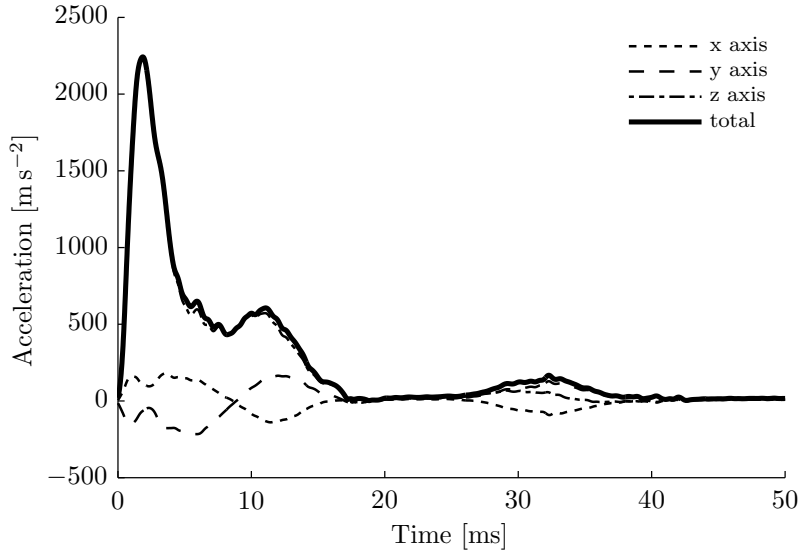

Figure 3.7: The measured acceleration from test 21050701. The z axis acceleration dominates the total acceleration so its data is mostly obscured by a plot of the resultant acceleration.

Table 3.4: Properties of the impact speeds (m s^{-1})

Headform	Child	Adult
Mean	11.07	11.10
Median	11.07	11.10
Std. Dev	0.06	0.07

for all tests with each headform. Table 3.4 summarises the impact speed data.

3.3.2 Impact angle

The impact angle is the sum of the angle of the bonnet at the impact location, measured with a digital level, and the flight angle of the headform at impact, described in Section 3.2.2. Figure 3.9 shows the cumulative distribution of the complementary impact angle for the tests performed with each headform. A complementary impact angle of 0° indicates that the velocity of the headform was perpendicular to the surface when impact occurred. The impact angle is solely dependant on the design of the vehicle as the trajectory of the headform relative to the ground is fixed by the test protocol.

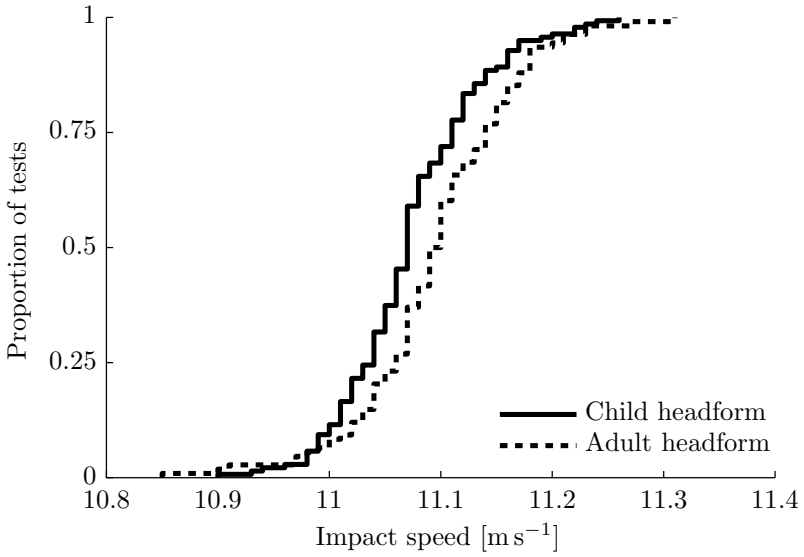

Figure 3.8: Cumulative distribution of impact speeds.

Table 3.5: Distribution of the normal impact velocity.

Headform	Child	Adult
Mean	10.33	10.77
Median	10.30	10.76
Std. Dev	0.57	0.19

95% of all tests with the Adult headform and 42% of tests with the Child headform had an impact angle which was within 20° of perpendicular. Consequently, more of the tests with the Child headform are 'glancing' impacts than the tests with the Adult headform. The differences in these distributions are due to the design of the vehicles included and the differences in firing angle of each headform.

3.3.3 Impact velocity normal to the surface

The normal impact velocity, V, is the velocity normal to the surface when impact occurs. Its distribution is shown in Figure 3.10. The Child headform has broader distribution of normal impact velocities because it has a larger range of impact angles.

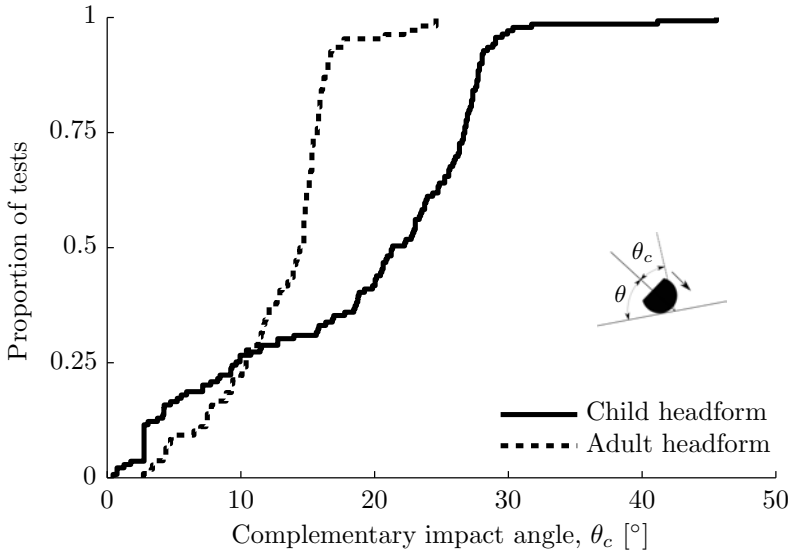

Figure 3.9: Cumulative distribution of complementary impact angle.

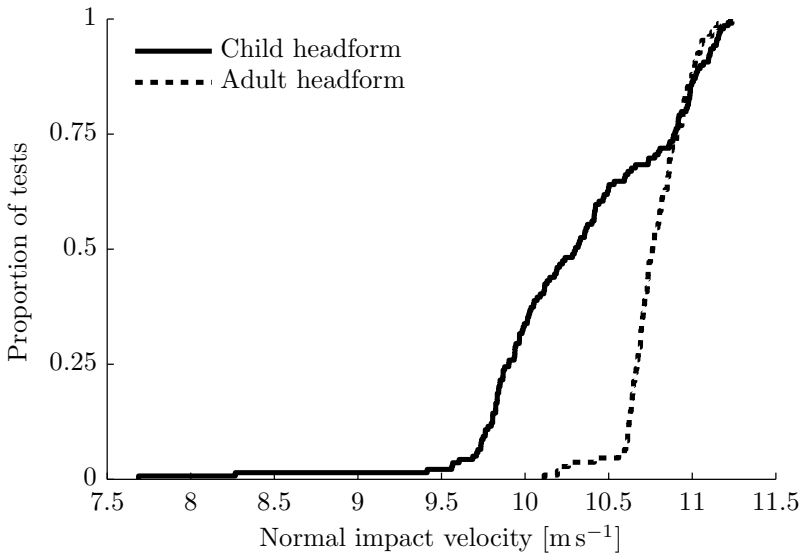

Figure 3.10: Cumulative distribution of the normal impact velocity, V.

3.4 Retrospective Analysis

Some of the features of the impact that can be clearly seen in the high speed film need to be estimated. These features include the displacement of the headform into the bonnet and the rotation of the headform throughout the impact.

This section describes a method to estimate the rotational kinematics and the normal and tangential acceleration of the headform during the impact using an iterative technique. From these estimates the displacement of the headform into the bonnet space can be estimated.

The displacement of the headform into the bonnet space during the impact is an important property for a vehicle designer to consider. It is possible to estimate this distance using the data available, and assumptions that can be made about the impact. A method for estimating these properties is discussed in this section.

3.4.1 Rotational dynamics of the headform

Searson and Anderson (2008) developed and applied a method for determining the angle of the headform relative to the bonnet throughout the impact. The method applies some simple assumptions to the motion of the headform and estimates the rotational motion of the headform in the plane of impact. These assumptions include that the impact can be modelled in two dimensions, and that the initial impact conditions are accurately measured. In addition, the method assumes that the rotation of the headform can be found by neglecting any sliding contact that occurs between the headform and the bonnet. This method is described here.

A two dimensional representation of the initial contact between the headform and the bonnet is shown in Figure 3.11. The figure shows the accelerations measured by each accelerometer, a_x, a_y and a_z, in this plane. Two additional accelerations, namely the acceleration normal to the impact surface, a_N, and the acceleration tangential to the impact surface, a_T, are also shown as is the angular acceleration of the headform, $\dot{\omega}$. Each arrow indicates the direction of positive values for each parameter.

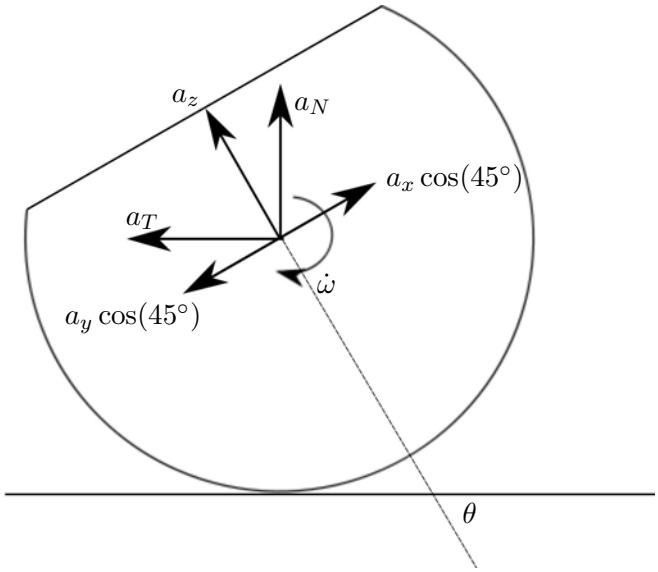

Figure 3.11: The direction of the accelerations measured at initial contact between the headform and the bonnet.

At the initial contact point, indicated by the subscript 0, the angle θ_0 is equal to the sum of the flight angle of the headform and the measured angle of the bonnet surface.

$$\theta_0 = \alpha_g + \measuredangle\text{bonnet} \tag{3.4}$$

The normal and tangential accelerations at the initial contact can be determined from the accelerations measured by the accelerometers.

$$a_{N0} = a_{z0} \sin(\theta_0) + a_{xy_0} \cos(\theta_0) \tag{3.5}$$

$$a_{T0} = a_{z0} \cos(\theta_0) - a_{xy_0} \sin(\theta_0) \tag{3.6}$$

where a_{xy} is the sum of acceleration measured by the x and y accelerometers in the plane of the impact, as indicated in Figure 3.11.

$$a_{xy} = \cos(45°)\,(a_x - a_y)$$

The angular acceleration of the headform can also be calculated at the point of contact assuming that the headform, with radius r, does not slide on the

bonnet.

$$\dot{\omega}_0 = \frac{a_{T0}}{r} \tag{3.7}$$

However, for the remainder of the impact the relative orientation of the headform and the bonnet is not measured and the angular acceleration is not known. The angle must be estimated as the impact progresses so that the displacement of the headform into the bonnet space can be obtained. This is done using an iterative technique where the normal and tangential acceleration and the angular position of the headform are determined and updated at each time step.

At each time step, indicated by a subscript j, the normal and tangential acceleration can be determined using the angle of the headform at that time step.

$$a_{Nj} = a_{zj}\sin(\theta_j) + a_{xy_j}\cos(\theta_j) \tag{3.8}$$

$$a_{Tj} = a_{zj}\cos(\theta_j) - a_{xy_j}\sin(\theta_j) \tag{3.9}$$

The angular acceleration of the headform can be determined at each time step using Equation (3.7).

$$\dot{\omega}_j = \frac{a_{Tj}}{r} \tag{3.10}$$

The angular position of the headform at the next time step can be calculated using a numerical integration method shown in Equations (3.11) and (3.12).

$$\omega_{j+1} = \omega_j + \dot{\omega}_j\Delta t \qquad \omega_0 = 0 \tag{3.11}$$

$$\theta_{j+1} = \theta_j + \omega_j\Delta t \qquad \theta_0 = \alpha_g + \measuredangle\text{bonnet} \tag{3.12}$$

where$\Delta\ t$ is the difference in time between each time step.

Equations (3.8) to (3.12) are cycled through iteratively to determine the normal and tangential accelerations and the angular position, velocity and acceleration at each time step measured by the triaxial accelerometer.

This method of calculating rotational motion is used for each test used in this thesis. Searson and Anderson (2008) compared their method to a simulation

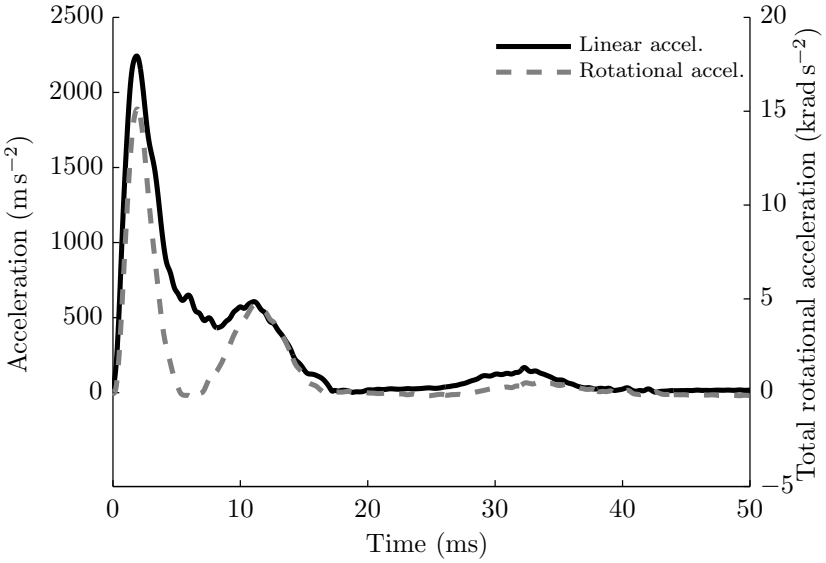

Figure 3.12: The derived rotational acceleration from test 21050701

using MADYMO software[1] and found consistent results between the actual kinematics and the estimation according to Equations (3.8) to (3.12).

The measured angular acceleration for this example test is shown in Figure 3.12 and the change in angular position is shown in Figure 3.13.

The rotational displacement of each test was verified for appropriateness in each test. For example, Figure 3.13 shows that after 20 ms the headform has rotated from an angle of 60.5° relative to the ground to an angle of 107.8° relative to the ground. Using the high speed footage of the impact the approximate magnitude of this rotation can be confirmed. The high speed footage cannot be used to accurately verify the rotation motion of the headform because it was filmed from a position that was not perpendicular to the headform flight plane. Figure 3.14 shows the headform prior to impact and the headform after 20 ms of contact. The change in angle in Figure 3.13 appears consistent with the change in angle in Figure 3.14.

[1]TNO Automotive Safety Solutions

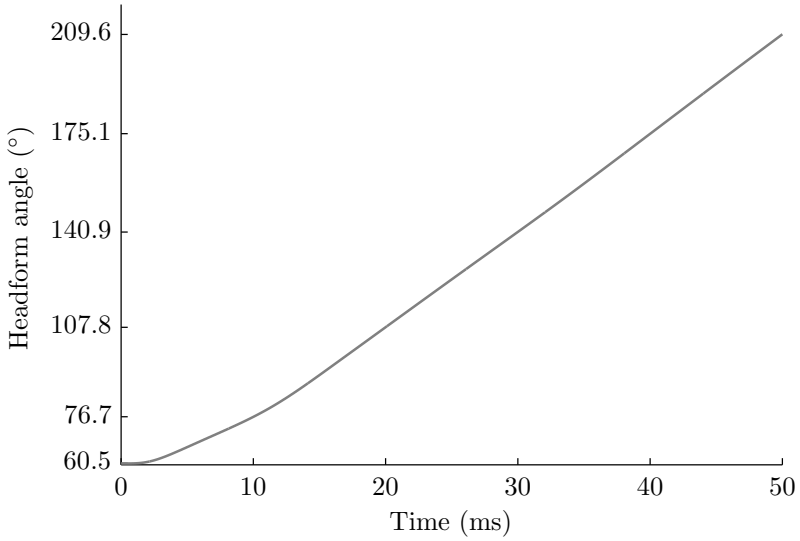

Figure 3.13: The derived rotational displacement from test 21050701. This can be compared to Figure 3.14.

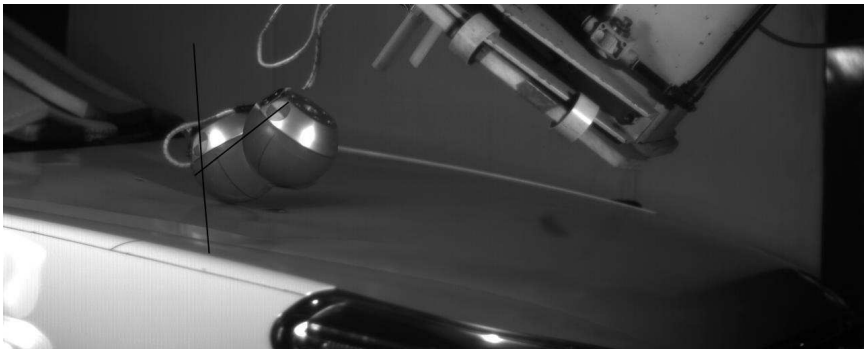

Figure 3.14: An overlay of the angle of the headform prior to initial impact and at 20 ms. The angle change, measured by the orientation of the target on the headform is also shown.

3.4.2 Estimation of maximum stopping distance

The method of Searson and Anderson (2008) generates the normal and the tangential components of acceleration. The normal acceleration that was calculated in Equation (3.8) can be integrated twice using the impact velocity normal to the impact surface into the bonnet, V, as an initial condition to determine the deformation, s, of the structure throughout the impact.

$$s(t) = \int_0^t \left[\int_0^t a_n(t).dt - V \right] .dt \tag{3.13}$$

This method of estimating the normal displacement was verified by Searson and Anderson (2008).

The time of initial contact was identified from inspection of the acceleration data.

The maximum deformation of the bonnet is the maximum absolute value obtained by Equation (3.13). This is the stopping distance for the test, because it is the distance required to bring the headform to a halt (normal to the bonnet surface) before it is accelerated out of the bonnet space again.

$$S = \max |s| \tag{3.14}$$

Calculation of deformation for the example test

The normal deformation of the headform in test 21050701 is shown in Figure 3.15. The figure shows that the maximum stopping distance occurs 11.1 ms into the impact. Figure 3.16 shows the resultant acceleration measured from the test plotted against the normal displacement. This figure shows that the maximum deformation coincided with the secondary acceleration peak that occurs at about 11 ms after the beginning of the impact.

3.4.3 Estimation of coefficient of restitution

The normal coefficient of restitution, R, is calculated as the ratio of the normal final velocity, V_T, out of the bonnet and the normal impact velocity, V, into the bonnet. The normal final velocity is calculated by integrating

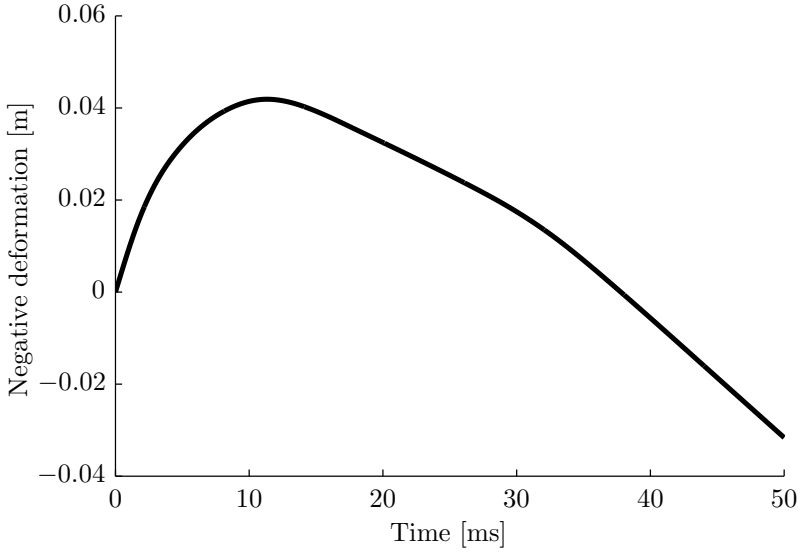

Figure 3.15: The derived displacement from test 21050701. Positive displacement indicates penetration into the bonnet structure.

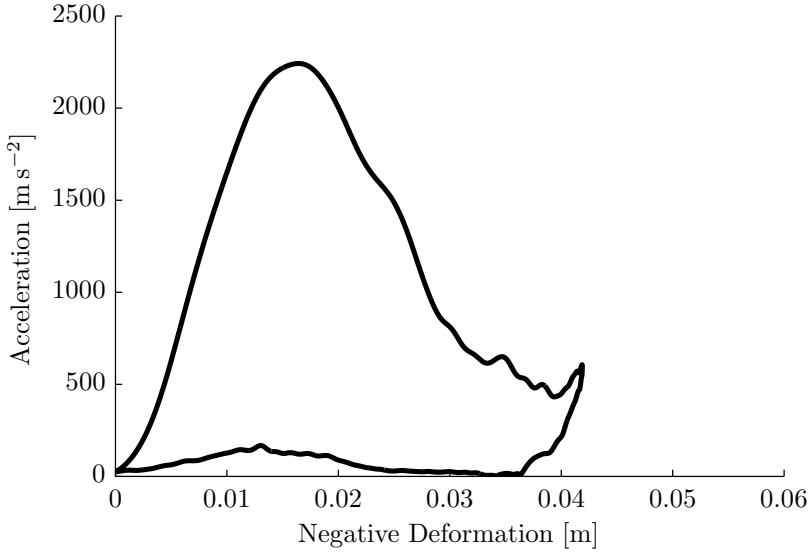

Figure 3.16: The total acceleration plotted against derived displacement from test 21050701

the normal acceleration once over the whole impact using the normal impact velocity as an initial condition.

$$R = \frac{V_T}{V} \tag{3.15}$$

The coefficient of restitution gives an indication of the energy absorbed by the bonnet during the impact.

3.5 Distributions of estimated data

3.5.1 Stopping distance

The distribution of the stopping distance, S, is shown in Figure 3.17. The headform stopping distance is the distance required to bring the headform to a stop before it is then accelerated away from the vehicle again. The tests with the Adult headform have a deeper stopping distance than the tests with the Child headform. This is because the Adult headform is heavier than the Child headform and therefore has a higher kinetic energy at impact.

The difference in stopping distance, as a conseqence of the difference in kinetic energy between the headforms can be explained using a linear elastic spring to model of impact. If the linear elastic spring has a stiffness κ, then the kinetic energy of a headform of mass M and speed V, can be related to the maximum stopping distance through the conservation of energy.

$$\frac{1}{2}MV^2 = \frac{1}{2}\kappa S^2 \tag{3.16}$$

Table 3.6: Distribution of the headform stopping distance.

Headform	Child	Adult
Mean	0.049	0.070
Median	0.049	0.069
Std. Dev	0.012	0.014

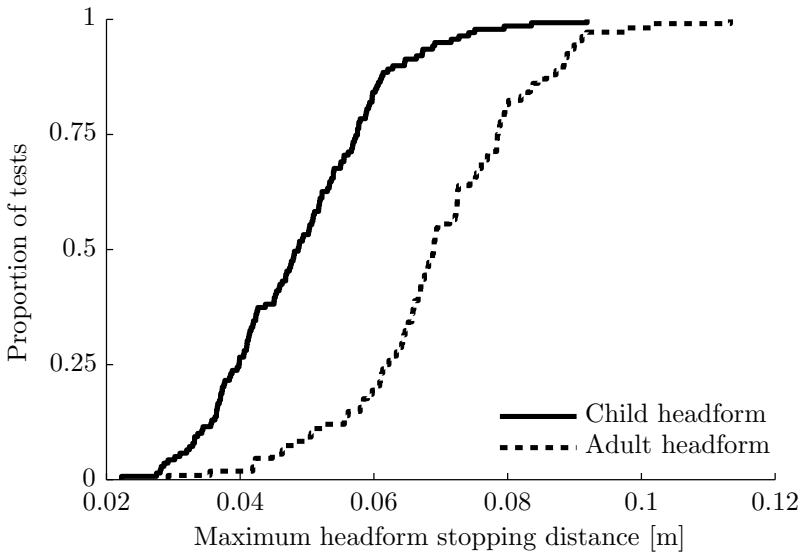

Figure 3.17: Cumulative distribution of the headform stopping distance (S).

The maximum headform stopping distance, therefore, is a function of the impact velocity, the mass of the headform and the stiffness of the impact surface.

$$S = V\sqrt{\frac{M}{\kappa}} \tag{3.17}$$

Taking the ratio of Equation (3.17) evaluated for the Child headform and Equation (3.17) evaluated for the Adult headform, a ratio of stopping distances for each headform on a common impact site can be derived.

$$\frac{S_C}{S_A} = \frac{V_C}{V_A}\sqrt{\frac{M_C\kappa_A}{M_A\kappa_C}} \tag{3.18}$$

Using typical median values from the data for normal impact velocity and the maximum headform stopping distance together with the mass of each headform, the ratio of the spring stiffness is nearly unity.

$$\sqrt{\frac{\kappa_A}{\kappa_C}} = 1.03 \tag{3.19}$$

Table 3.7: Normal coefficient of restitution.

Headform	Child	Adult
Mean	0.267	0.243
Median	0.272	0.252
Std. Dev	0.067	0.059

This indicates that most of the difference between the maximum headform stopping distance of each headform is due to the difference in kinetic energy of each headform prior to impact. In reality, the bonnet is not reasonably modelled as a linear elastic spring, because, it will be shown in the next section, the coefficients of restitution are much less than 1. This model does provide, however, a first order demonstration of the effect that the difference in kinetic energy has on the size of the stopping distance. Even though energy is not returned to the headform in an elastic manner, energy is absorbed (and then dissipated) by the impacted structure during the inbound phase of the impact. Other reasons for the difference could include the difference in size of each headform and the differences in vehicle construction of the zones that are tested with each headform.

3.5.2 Coefficient of restitution

The distribution of the coefficient of restitution is shown in Figure 3.18. The Shapiro-Wilk test shows that the coefficient of restitution is approximately normally distributed for each of the headform sizes. The summary statistics for each headform are shown in Table 3.7. The coefficient of restitution of those impacts with the heavier Adult headform is generally less than it is with the lighter Child headform.

One test has a coefficient of restitution that is approximately zero. Test 12090600 was on point C6D, near the edge line of the bonnet. Observation of the high speed film shows that its coefficient of restitution is approximately zero because at the conclusion of the impact the headform leaves the bonnet travelling parallel with the bonnet surface.

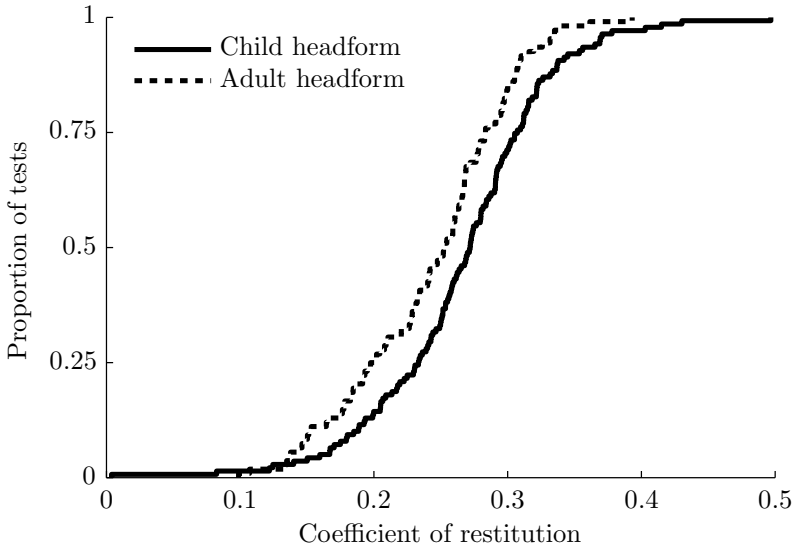

Figure 3.18: Cumulative distribution of the coefficient of restitution.

3.6 Evaluation of each IRF

In this section the method for evaluating each of the IRFs for each test is described. The distributions of the IRF value for the data set is also shown.

3.6.1 HIC

The HIC is calculated as

$$\text{HIC} = \max\left[(t_2 - t_1)\left(\int_{t_1}^{t_2} \frac{a(t)}{(t_2 - t_1)g}.dt\right)^{2.5}\right] \tag{3.20}$$

where t_1 and t_2 are two time points, selected so that the maximum of the function is found. A trapezoidal integration method is used to evaluate the integral of $a(t)$ for the calculation of HIC. The maximum value of HIC is found after evaluating the integral between every pair of t_1 and t_2.

Test 21050701 has a HIC severity of 1341 with $t_1 = 0.72$ ms and $t_2 = 3.90$ ms. The portion of test 21050701 that maximizes the HIC is shown as the shaded portion in Figure 3.19.

The distribution of HIC in the data set is shown in Figure 3.20.

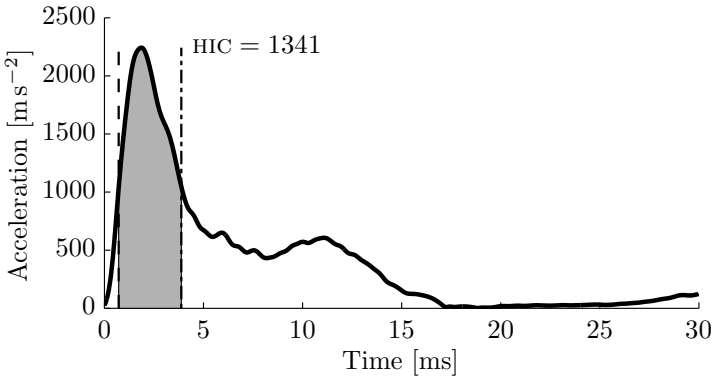

Figure 3.19: Evaluation of HIC for test 02050701.

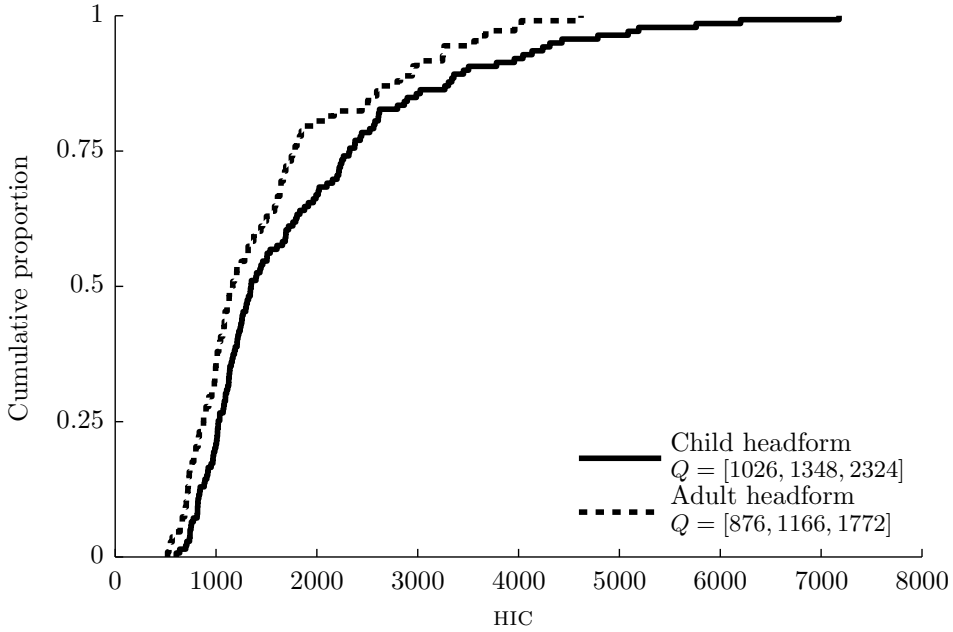

Figure 3.20: Cumulative distribution of tests evaluated with the HIC. The vector Q indicates the 25th, 50th and 75th percentile values of severity.

3.6.2 PVP

The PVP is determined by numerically integrating the acceleration from the start of the impact, and at each time point multiplying this by the acceleration at that time.

$$P(t) = a(t) \int_0^t a(u)du \tag{3.21}$$

The PVP is then the maximum value of $P(t)$ which occurs at $t = t^*$.

Figure 3.21 shows the value of $P(t)$ at each time step for this test. The PVP for this test is PVP $= 7.52\,\mathrm{kW\,kg^{-1}}$ which occurs at $t^* = 3.22\,\mathrm{ms}$.

The distribution of PVP in the data set is shown in Figure 3.22.

3.6.3 3 millisecond clip

The 3 millisecond clip indicates the value of acceleration that is exceeded for 3 consecutive milliseconds. The a_3 severity is evaluated at each discrete time point as shown in Equation (3.22) and adopts that discrete value of acceleration without interpolating between the data points.

$$a_3 = \max\left[a_3(t_i)\right] \tag{3.22}$$

where $a_3(t_i)$ is the minimum acceleration measured in the 3 ms time interval beginning with t_i.

Figure 3.23 shows the location where the 3ms severity is evaluated. The 3ms severity for this test is 114 g.

The distribution of a_3 in the data set is shown in Figure 3.24.

3.6.4 Peak acceleration

The value of the peak acceleration, a_m, follows from its intuitive definition: the peak acceleration measured during the impact. Typically, in head injury studies, the value of peak acceleration is quoted in multiples of the acceleration due to gravity ($9.81\ \mathrm{m\,s^{-2}}$). The peak acceleration for this test is

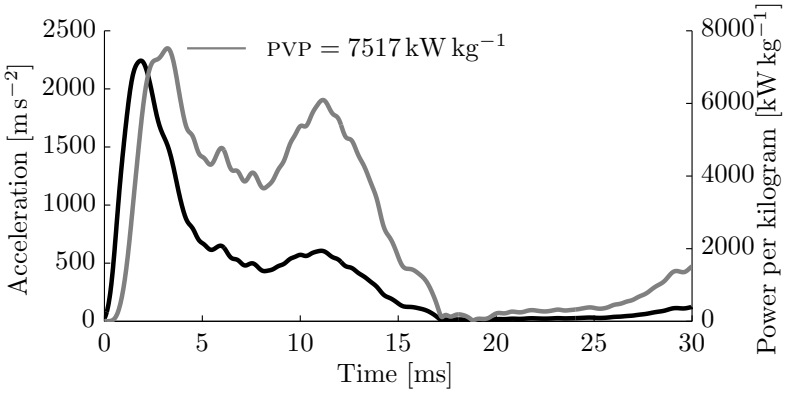

Figure 3.21: Evaluation of PVP of test 02050701.

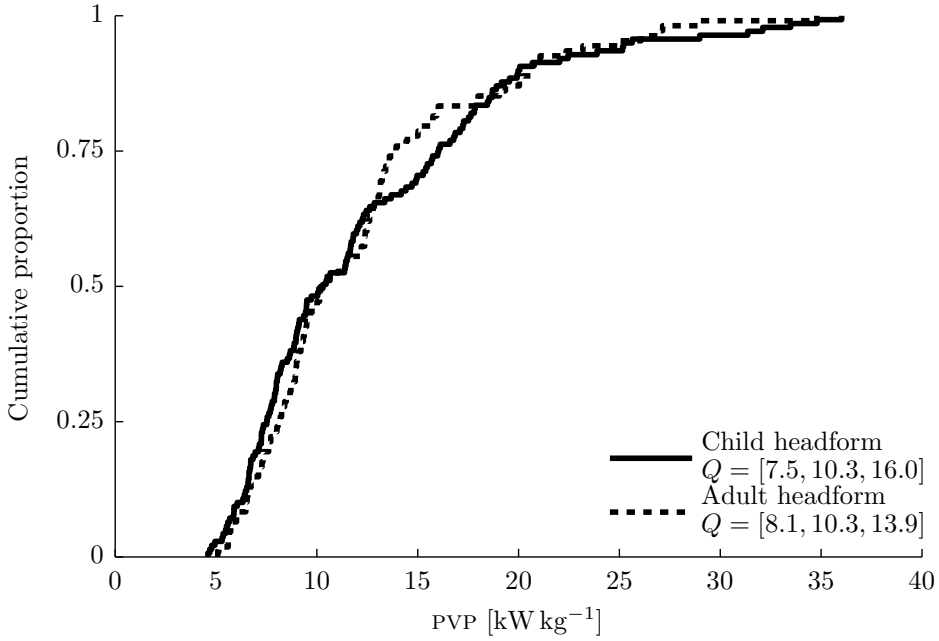

Figure 3.22: Cumulative distribution of tests evaluated with the PVP. The vector Q indicates the 25th, 50th and 75th percentile values of severity.

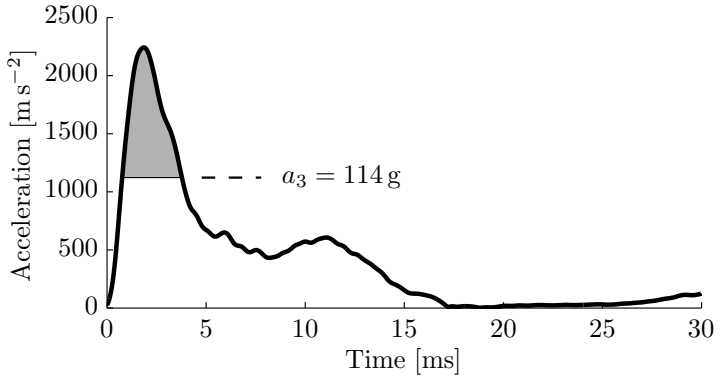

Figure 3.23: Evaluation of 3 millisecond clip of test 02050701.

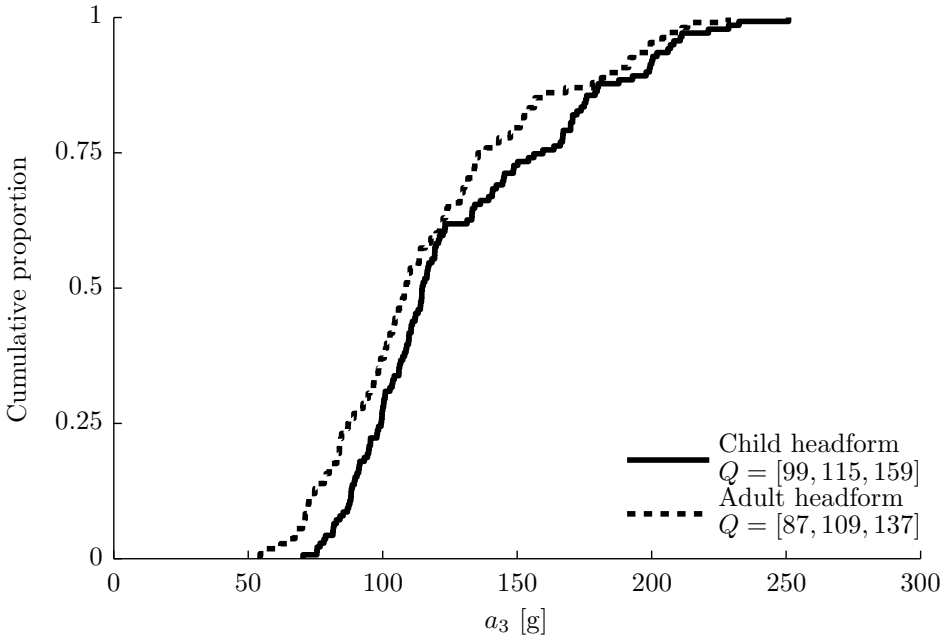

Figure 3.24: Cumulative distribution of tests evaluated with the 3 millisecond clip. The vector Q indicates the 25th, 50th and 75th percentile values of severity.

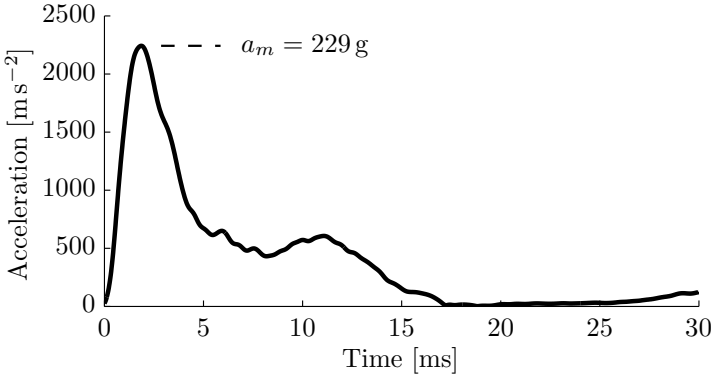

Figure 3.25: Peak Acceleration of test 02050701.

indicated in Figure 3.25. The formula used to measure the peak acceleration is shown in Equation (3.23).

$$a_m = \max\left[\frac{a(t_i)}{g}\right] \tag{3.23}$$

Test 21050701 has a peak acceleration value of 229 g which is equivalent $2242.5\,\mathrm{m\,s^{-2}}$.

The distribution of a_m in the data set is shown in Figure 3.26.

3.7 Descriptions of pulse shape

Several descriptive terms can be used to qualitatively describe pulse shapes. The descriptive terms used to describe some pulse shapes are explained here using example pulse shapes.

3.7.1 Front and rear loaded pulse shapes

Figure 3.27 shows the difference between a front loaded pulse shape and a rear loaded pulse shape. A front loaded pulse shape has most of the main acceleration components occurring early in the impact sequence. A rear loaded pulse shape has most of the main acceleration components occurring later in the pulse shape.

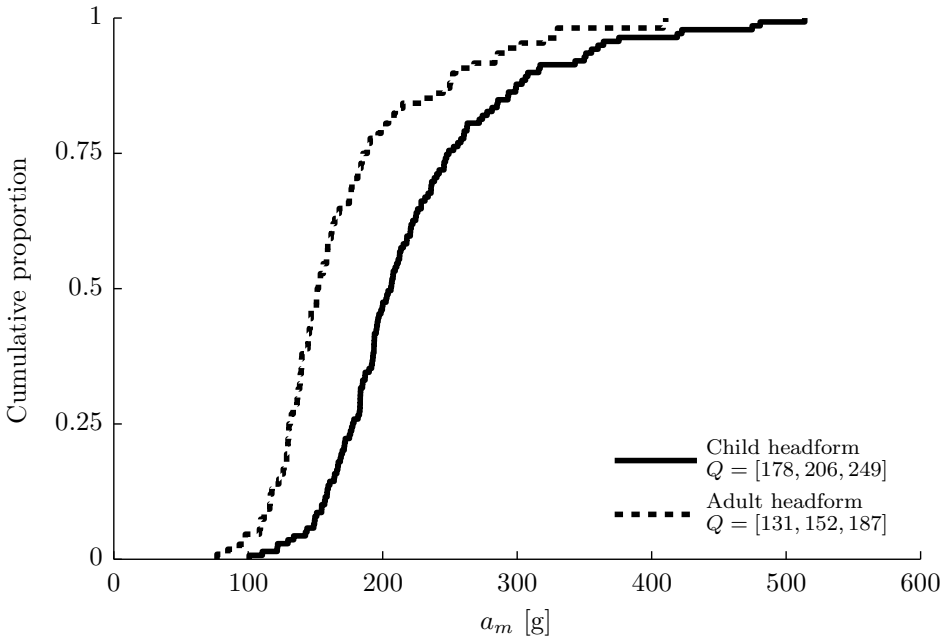

Figure 3.26: Cumulative distribution of tests evaluated with peak acceleration. The vector Q indicates the 25th, 50th and 75th percentile values of severity.

3.7.2 Peaked and flat pulse shapes

Figure 3.28 shows the difference between a peaked and a flat pulse shape. A peaked pulse shape includes most of the main acceleration components in a brief section of the acceleration pulse, while a flat pulse shape spreads the acceleration magnitude evenly over the duration of the impact.

3.7.3 Pulse shapes with multiple peaks

Figure 3.29 shows a pulse shape with multiple significant peaks in acceleration. Tests like this can arise because the headform 'bottoms out'. In these scenarios, the displacement of the headform is impeded by a rigid under-bonnet structure such as the engine. The first peak is due to the bonnet structure, the second peak is due to the rigid under-bonnet structure.

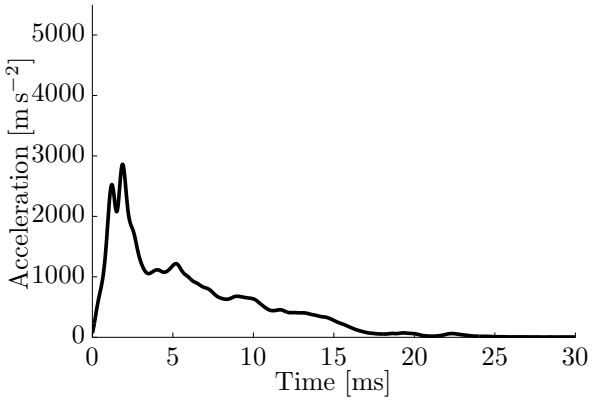

(a) Front loaded pulse shape. Test 020202020.

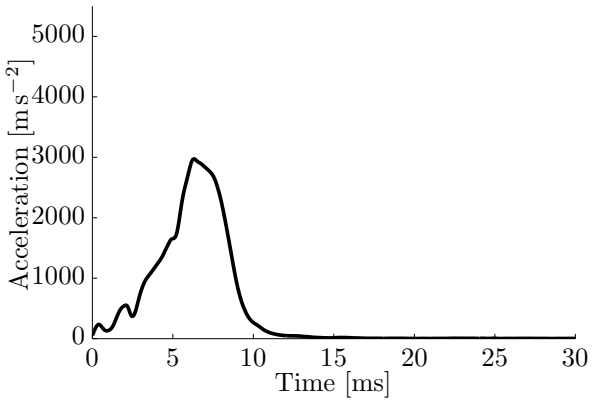

(b) Rear loaded pulse shape. Test 02020701.

Figure 3.27: Front and rear loaded pulse shapes.

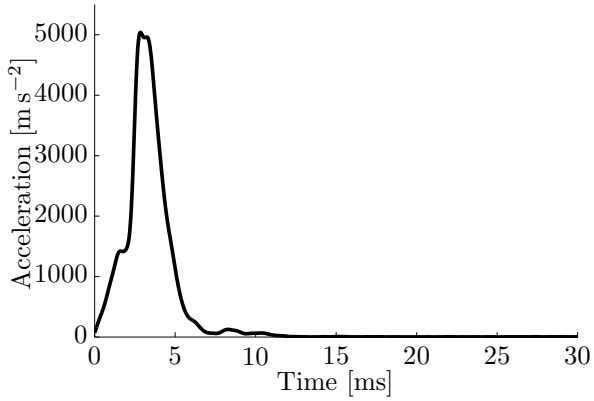

(a) Peaked pulse shape. Test 29010700.

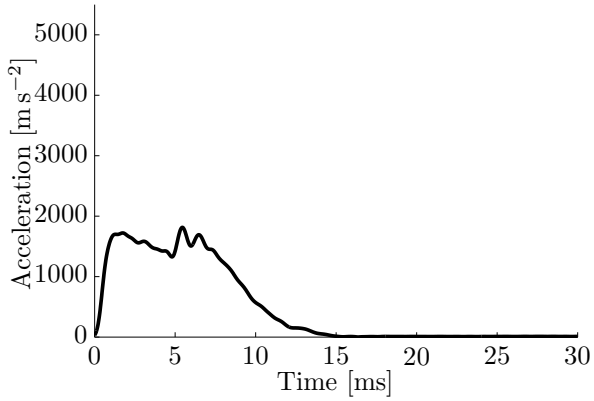

(b) Flat pulse shape. Test 30010702.

Figure 3.28: Peaked and flat pulse shapes.

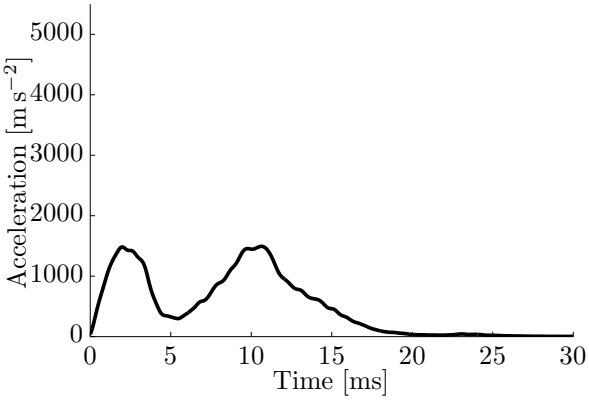

Figure 3.29: Pulse shape with multiple peaks.

3.8 Summary and discussion

The process of collecting and retrospectively analysing the data used in this thesis has been described in this Chapter. In addition the distributions of the data that was collected have been shown.

This data will be used in later chapters to examine some theoretical properties of the various IRFs, compare the IRFs, and find examples of differences between the IRFs.

A method for retrospective analysis, published previously (Searson and Anderson, 2008), has been used to estimate the rotational motion of a headform during an impact. This was shown, with an example, to give an approximate measure of the rotational motion of the headform. Consequently, the accuracy of the rotational motion of the headform is considered to be an estimation only. It is used, in conjunction with the linear accelerometers, to determine the normal component of acceleration, which in turn is integrated to obtain the stopping distance and coefficient of restitution. This method was shown to be appropriate for this purpose (Searson and Anderson, 2008).

Chapter 4

The effect of a particular IRF on design decisions: analysis with theoretical test pulses

4.1 Introduction

When a new design is subjected to a test protocol, an objective of the designer is to maximise its crashworthiness whilst conforming to any constraints placed on it. The performance of the design is evaluated using the IRF specified in the test protocol. The constraints that are placed on the design include the amount of deformation distance that is available to manage the energy of the impact and the velocity of the impactor.

The impact response of a design will produce a characteristic acceleration pulse shape. The pulse shape is the plot of resultant acceleration of the headform against time. This characteristic pulse shape depends on all aspects of the design including the material and geometry of the design. During the test there is a stopping distance that is required to bring the headform to rest. The stopping distance is the maximum deformation of the design during the test and is a function of the acceleration pulse shape and the impact velocity.

At the conclusion of the impact the headform will bounce away from the impact surface with a final velocity. The coefficient of restitution is the ratio of this final velocity and the impact velocity. The coefficient of restitution is a property of the impact and is, in part, determined by the properties of the design. If the final velocity is zero, the coefficient of restitution is zero. If the final velocity could be the same speed as the impact velocity, the coefficient of restitution is one.

For HIC, and for any other IRF that penalises high acceleration in a pulse shape, there are two competing considerations. Firstly, the acceleration must be kept as low as possible. Secondly, the acceleration needs to occur early in the impact so that the stopping distance is minimised. For example, Wu and Beaudet (2007) showed that there was an optimum pulse shape that minimised the deformation distance required whilst achieving a fixed value of HIC for a given impact velocity and negligible coefficient of restitution.

An acceleration pulse shape can be defined analytically. For example, Chou and Nyquist (1974) considered several pulse shapes, such as a square, half sine and triangular pulse shape in their analysis of HIC. These acceleration pulse shapes can be integrated once to determine their change in velocity.

Then, if the impact velocity is defined, the coefficient of restitution can also be determined and, after another integration, the stopping distance used to bring the impactor to rest can be determined. The analytical values of each IRF can also be determined analytically from such pulse shapes.

In this chapter eight pulse shapes are utilised to investigate each IRF considered in this thesis to show how each is affected by pulse shape. For each theoretical pulse shape the impact velocity will be normalised as will the stopping distance. This normalisation is done so that the different pulse shapes are considered unbiased by the effect of impact speed and stopping distance. Initially only pulse shapes with a coefficient of restitution of zero will be considered. Later, impacts with other values of coefficient of restitution are considered.

This chapter is arranged in the following way:

- In Section 4.2 the eight pulse shapes are defined and a strategy to normalise these by impact velocity and stopping distance is described.
- In Section 4.3 the pulse shapes are normalised when the coefficient of restitution is zero.
- In Section 4.4 the pulse shapes are normalised considering coefficients of restitution that are non-zero. Conditions that are necessary for a non-zero coefficient of restitution are also described.
- In Section 4.5 the analytical values of each IRF for each of the theoretical pulse shapes are determined. In the case of the HIC the results from Chou and Nyquist (1974) are used.
- In Section 4.6 the analytical values of each IRF are determined for each of the normalised pulse shapes. These values are compared with each other to show the effect that pulse shape has on the value of the IRF.
- In Section 4.7 the results of the analyses are discussed.

The results obtained in this chapter are used in the Chapter 5. In Chapter 5, the effect of the stopping distance, impact velocity and coefficient of restitution on the value of IRF will be investigated and quantified.

4.2 Pulse shapes used for analysis and a strategy for normalisation

4.2.1 Pulse shapes

Eight pulse shapes are used in this chapter. The eight pulse shapes are constructed from three general pulse shapes to produce a half-sine pulse, six triangular pulses and a square pulse. The six triangular pulse shapes differ from each other by the location of their apex. These pulse shapes were selected because they have been examined before and consequently analytical derivations of HIC are available (Chou and Nyquist, 1974). The definition of each pulse shape is shown in Table 4.1, and these pulse shapes are drawn in Figure 4.1. The acceleration, $a(t)$, is positive when acceleration of the impactor is directed away from the impact surface.

Each of the pulse shapes is described by two parameters: the value of the maximum acceleration, A_i, and the duration of the pulse, T_i, where i denotes the particular pulse shape. The triangular pulse also has a third parameter, k, for the skewness of the pulse that changes the location of the apex of the triangle from the start of the pulse (when $k = 0$) to the end of the pulse (when $k = 1$).

Throughout the chapter, acceleration is assumed to consist only of acceleration in one direction (normal to the impact surface). Consequently, this acceleration can be integrated once to determine the change in velocity normal to the surface and integrated twice to determine the distance normal to the surface on which the impact occurs. As a result, the acceleration and its integrated quantities can be considered to be scalar values.

4.2.2 Normalising these pulse shapes

As stated in the introduction, two normalising parameters are needed to compare the analytical pulse shapes in an unbiased way. These are the impact velocity and the stopping distance. In Chapter 5, it will be shown that an IRF can be expressed as a product of a function of velocity, stopping distance, and coefficient of restitution, and a function that is unique to each

Table 4.1: The definition of the pulse shapes used to analyse the IRFs.

Pulse	Equation
Half-sine	$a(t) = A_h \sin \frac{\pi}{T_h} t \quad 0 \leq t \leq T_h$
Triangular	$a(t) = \begin{cases} \frac{A_t}{kT_t} t & 0 \leq t \leq kT_t \\ \frac{A_t(T_t - t)}{T_t(1-k)} & kT_t < t \leq T_t \end{cases}$
Square	$a(t) = A_s \qquad 0 \leq t \leq T_s$

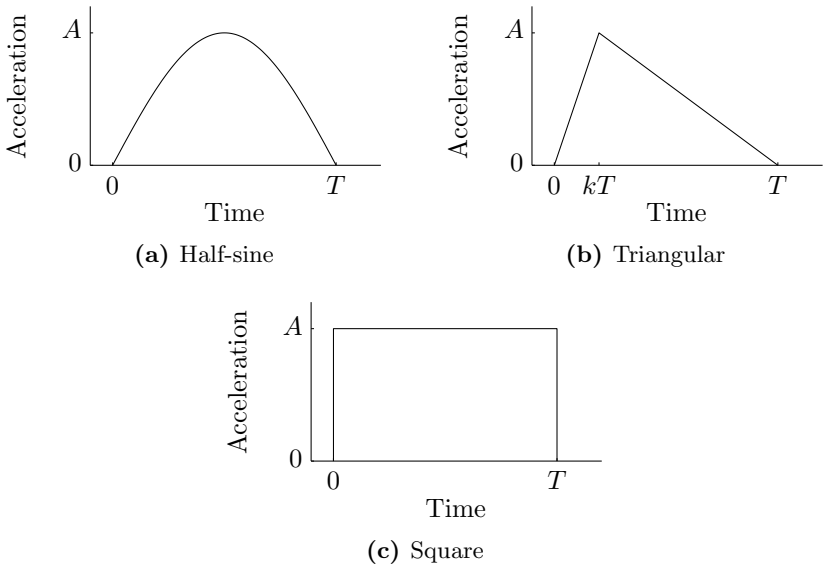

(a) Half-sine **(b)** Triangular **(c)** Square

Figure 4.1: Pulse shapes used.

pulse shape. It is the function that is unique to each pulse shape that is the focus of this chapter.

Normalisation, in this context, will mean defining a pulse shape that is constrained to produce the same deformation for given impact velocity, whatever the general shape of the pulse is. In so doing, the effect of pulse shape can be examined unencumbered by the effects of impact velocity or deformation.

These parameters for normalisation are chosen because the objective of this study is to determine how pulse shape affects the different IRFs being considered. Other authors have also normalised pulse shapes, but as their objectives differed, and their normalisation parameters were different. For example:

- Onusic (1995) normalised the pulse shapes by the signal size (a mathematical property of the pulse shape) and the duration of the pulse shape. The objective was to show if three pulse shapes had the same order or severity according to HIC and the Gadd Severity Index.
- Wu and Beaudet (2007) normalised the pulse shapes to have a constant value of HIC and a constant impact velocity. Their objective was to determine the minimum deformation distance that was required for a pulse shape.
- Lim et al. (1995) normalised the pulse shapes to have a constant impact velocity. Their objective was to determine the efficiency of the pulse shapes.

Normalisation parameter — impact velocity

For a given acceleration pulse shape, $a(t)$, of an impactor, its change in velocity is the integral of the acceleration from the beginning of the pulse at $t = 0$ to the end of the pulse at $t = T$.

$$\Delta v = \int_0^T a(t).dt \tag{4.1}$$

The velocity of the impactor normal to the impact surface at any time, $v(t)$, during the impact can also be determined.

$$v(t) = \int_0^t a(t).dt + v(0) \tag{4.2}$$

The initial velocity of the impactor, V is into the impact surface.

$$V = -v(0) \tag{4.3}$$

Consequently the velocity at any time during the impact is

$$v(t) = \int_0^t a(t).dt - V. \tag{4.4}$$

The change in velocity can be written as a combination of the final velocity of the impactor away from the impact surface and the impact velocity of the impactor into the surface.

$$\Delta v = \int_0^T a(t).dt \tag{4.5}$$

$$= v_T + V \tag{4.6}$$

Where $v_T = v(T)$ is the final velocity of the impactor away from the impact surface. Rearranging this equation to make V the subject the impact velocity is known for any change in velocity and final velocity.

$$V = \Delta v - v_T \tag{4.7}$$

$$V = \int_0^T a(t).dt - v_T \tag{4.8}$$

The coefficient of restitution, R, is defined in this thesis as the ratio of the final velocity and the impact velocity.

$$R = \frac{v_T}{V} \tag{4.9}$$

Because $v_T \geq 0$ is a positive velocity outwards from the bonnet and V is a

positive velocity into the bonnet and no energy is gained in an impact the coefficient of restitution has a value $0 \leq R \leq 1$.

The final velocity, v_T is assumed to be negligible in Section 4.3, consequently in that section $R = 0$. Later in the Section 4.4 when the final velocity is assumed to be non-zero the final velocity is a function of the coefficient of restitution.

Normalisation parameter — stopping distance

The second normalisation parameter is the stopping distance, S. The stopping distance is a positive value indicating the maximum deformation of the impacted surface during the impact. The deformation, s, of the impacted surface is a function of the acceleration pulse shape and the impact velocity.

$$s(t) = \int_0^t \left[\int_0^t a(t).dt \right] + V.dt \tag{4.10}$$

The stopping distance is the maximum absolute value of the deformation.

$$S = \max |s(t)| \tag{4.11}$$

$$= |s(\hat{t})| \tag{4.12}$$

Where $\hat{t}$ is a critical point that minimises Equation (4.10). $\hat{t}$ can be found when $t > 0$ and the solution to Equation (4.14) is found.

$$0 = \frac{d}{dt} s(t) \tag{4.13}$$

$$0 = \left[\int_0^{\hat{t}} a(t).dt \right] + V \tag{4.14}$$

.

When the coefficient of restitution is zero in the next section, $\hat{t} = T$, because $V = \Delta v - 0$. When the coefficient of restitution is non-zero, $0 < \hat{t} < T$.

Table 4.2: The impact velocity for the theoretical pulse shapes that produce no rebound.

Pulse	Impact velocity
Half-sine	$V_h = \frac{2}{\pi} A_h T_h$
Triangular	$V_t = \frac{1}{2} A_t T_t$
Square	$V_s = A_s T_s$

4.3 Normalisation of pulse shapes with no restitution

In this section, the pulse shapes are normalised for impact velocity and stopping distance with the condition that there is no rebound velocity. This condition is used for mathematical simplicity. This simplification was made by several authors including Wu and Beaudet (2007), Lim et al. (1995) and Chou and Nyquist (1974). It will be shown in Section 4.6 that this condition leads to the most crashworthy design according to most IRFs.

Initially the analytical values for the impact velocity and the stopping distance for each of the theoretical pulse shapes with the condition of no rebound are shown. Then the pulse shapes are normalised with a reference pulse shape (the square pulse shape). This is done to produce pulse shapes with identical stopping distance and identical impact velocity.

Analytical values for impact velocity

When the final velocity is zero the impact velocity, V, is equal to the change of velocity. The impact velocity for each pulse shape, when there is no rebound velocity, is shown in Table 4.2. These expressions come directly from the integral expression in Equation (4.8) The impact velocity for each pulse shape is a constant multiplied by AT with the constant determined by the pulse shape.

Table 4.3: The maximum stopping distance for the theoretical pulse shapes that produce no rebound.

Pulse	S
Half-sine	$S_h = \frac{1}{\pi} A_h \, T_h^2$
Triangular	$S_t = \frac{1+k}{6} A_t \, T_t^2$
Square	$S_s = \frac{1}{2} A_s T_s^2$

Analytical values for stopping distance

When the final velocity is zero, the maximum stopping distance occurs at $\hat{t} = T$.

$$S = \int_0^T \left[\int_0^t a(t).dt \right] + V.dt \tag{4.15}$$

The stopping distance for each pulse shape is given in Table 4.3. The table shows that the stopping distance for each pulse shape is a constant multiplied by AT^2. For the triangular pulse the stopping distance depends on the skewness of the pulse shape and values of A_t and T_t. Table 4.3 shows that the stopping distance of the triangular pulse shape increases as k increases. The triangular pulse shape with $k = 0.0$ has the lowest stopping distance of any pulse shape. This pulse shape was considered to be the most crashworthy of the simple pulse shapes evaluated by Wu and Beaudet (2007).

4.3.1 The normalisation of pulse shapes that produce no rebound

Each pulse shape, without any rebound, can now be normalised so that both the stopping distance and impact velocity is constant. The square pulse was chosen as the reference pulse.

Firstly, the pulses are normalised to have the same impact velocity. The procedure will be illustrated using the half-sine pulse shape as an example. The normalisation of the impact velocity is achieved by setting the ratio of the values for the impact velocity of the half-sine pulse and the impact

velocity of the square pulse to 1. The analytical values of the impact velocity of each were shown in Table 4.2.

$$1 = \frac{V_h}{V_{ref}} = \frac{V_h}{V_s} \tag{4.16}$$

$$1 = \frac{\frac{2}{\pi} A_h T_h}{A_{ref} T_{ref}} \tag{4.17}$$

$$1 = \frac{2}{\pi} \left(\frac{A_h}{A_{ref}} \right) \left(\frac{T_h}{T_{ref}} \right) \tag{4.18}$$

Secondly, the stopping distance of the half sine pulse is equalised with the stopping distance of the square pulse by setting the ratio of the stopping distance of each to 1. The analytical values of the stopping distance for each were shown in Table 4.3.

$$1 = \frac{S_h}{S_{ref}} \tag{4.19}$$

$$1 = \frac{\frac{1}{\pi} A_h T_h^2}{\frac{1}{2} A_{ref} T_{ref}^2} \tag{4.20}$$

$$1 = \frac{2}{\pi} \left(\frac{A_h}{A_{ref}} \right) \left(\frac{T_h}{T_{ref}} \right)^2 \tag{4.21}$$

Equations (4.18) and (4.21), can be solved simultaneously to determine the ratios of $\frac{A_h}{A_{ref}}$ and $\frac{T_h}{T_{ref}}$.

$$\frac{A_h}{A_{ref}} = \frac{\pi}{2} \qquad\qquad \frac{T_h}{T_{ref}} = 1 \tag{4.22}$$

A square pulse shape and a half sine pulse shape, with negligible final velocity, will have a common impact velocity and a common stopping distance when they have these ratios for A and T. The ratios for all pulse shapes are shown in Table 4.4.

The value of $\frac{A_i}{A_{ref}}$ indicates the peak acceleration of the pulse shape. Trivially, A_s has the lowest value of peak acceleration.

Table 4.4: Ratios for $\frac{A_i}{A_{ref}}$ and $\frac{T_i}{T_{ref}}$ for each pulse shape without rebound. The values for the reference pulse are italisised.

Pulse shape	$\frac{A_i}{A_{ref}}$	$\frac{T_i}{T_{ref}}$
Half-sine	$\frac{\pi}{2}$	1
Triangular	$\frac{4(1+k)}{3}$	$\frac{3}{2(1+k)}$
Square	*1*	*1*

The value of $\frac{A}{A_{ref}}$ in the case of a triangular pulse increases with increasing k. The value of $\frac{A}{A_{ref}}$ for the triangular pulse shape is greater than the value of $\frac{A}{A_{ref}}$ for the half sine pulse for values of k greater than $\frac{3\pi}{8} - 1$.

In Figure 4.2 the normalised pulse shapes are plotted. Rear loaded triangular pulse shapes (with high values of k) have shorter durations (T) than the other pulse shapes. Rear loaded triangular pulse shapes retard the velocity of the headform slowly at the beginning of the impact. As a result, the velocity remains high and the maximum stopping distance is reached in a short time. The symmetrical pulse shapes — the half-sine, the triangle with $k = 0.5$ and the square — have an impact duration ratio, $\frac{T}{T_{ref}}$, of 1.0.

These pulse shapes are also shown plotted against deformation in Figure 4.3.

4.4 Normalisation of pulse shapes with rebound

In the previous section the pulse shapes used were defined to have a rebound velocity of zero. Each pulse shape was normalised with a square reference pulse to have an identical impact velocity and an identical stopping distance. Then the normalised pulse shapes were plotted in two ways. The first showed the pulse shapes on axes of acceleration and time. The second showed the pulse shapes on axes of acceleration and deformation.

In a real test, however, the structure returns some of the energy of the impact to the headform. That is, the headform has a finite, non-zero, rebound velocity. In addition, the time of maximum deformation (stopping distance) occurs before the end of the impact. After the headform reaches this stopping distance, the structure rebounds towards its starting point.

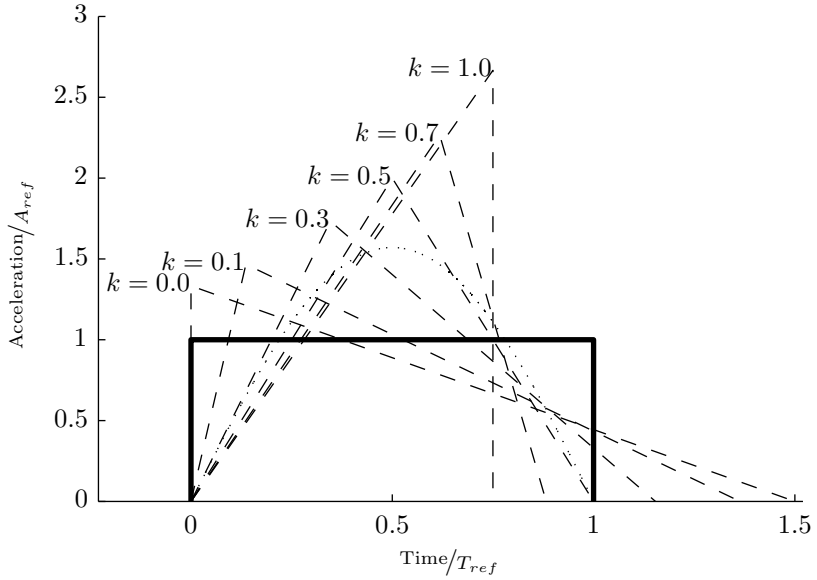

Figure 4.2: Pulse shapes, without rebound, normalised by impact velocity and stopping distance. The half-sine pulse is shown with the dotted line, the triangular pulses are shown with the dashed lines and the square, reference, pulse is shown with the thick solid line.

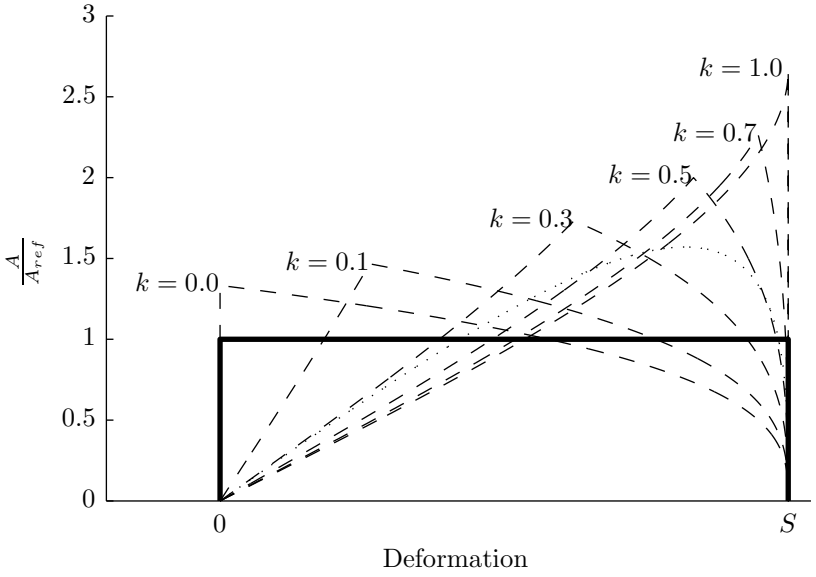

Figure 4.3: Pulse shapes, without rebound, normalised by impact velocity and stopping distance. The half-sine pulse is shown with the dotted line, the triangular pulses are shown with the dashed lines and the square, reference, pulse is shown with the thick solid line.

Pulse shapes that model a structure that returns some of the energy of an impact to a headform are considered in this section. A coefficient of restitution is used to find a general form of the results obtained in the previous section.

Bowman (1994) investigated the effect that the rebound velocity had on HIC values by varying the coefficient of restitution. His study, however, was limited to triangular impact pulse shapes where the time of the stopping distance coincided with the time of maximum acceleration. Because of the coincidence of the peak acceleration and stopping distance, the skewness of the triangular pulse shapes changed with the coefficient of restitution and this limited the usefulness of those results. In the present study the coefficient of restitution is applied independently of the pulse shape.

Applying the coefficient of restitution independently of the pulse shape is done for convenience to consider the effect of the coefficient of restitution. For a real structure, the coefficient of restitution is likely to be dependent on the pulse shape. In this scenario they are treated as independent parameters. This is able to be done because each pulse shape is defined analytically. They do not result from a contact model between the headform and the impacted surface.

As in the previous section, expressions for the impact velocity and stopping distance for each pulse shape is obtained. In this instance, however, the expressions are functions of A, T and the coefficient of restitution, R.

Expressions for impact velocity in terms of A, T, and R

The analytical value of the impact velocity is defined using the coefficient of restitution, R. This was introduced in Equation (4.9), as the ratio of the final velocity and the impact velocity.

$$R = \frac{v_T}{V} \tag{4.23}$$

Using this definition of coefficient of restitution, the impact velocity can be determined from the Equation (4.8) which relates the impact velocity, the

Table 4.5: The impact velocity for the theoretical pulse shapes with rebound allowed. The impact velocity is equal to the product of a constant, A, T and $\frac{1}{1+R}$.

Pulse	Impact velocity
Half-sine	$V_h = \frac{2}{\pi}\frac{A_h T_h}{1+R}$
Triangular	$V_t = \frac{1}{2}\frac{A_t T_t}{1+R}$
Square	$V_s = \frac{A_s T_s}{1+R}$

change in velocity and the final velocity.

$$V = \frac{\int_0^T a(t)dt}{1+R} \tag{4.24}$$

The impact velocities for each pulse shape, for values of $R \geq 0$ are shown in Table 4.5. Each impact velocity is a constant multiplied by AT where the constant is due to the pulse shape and is a function of $(1 + R)$.

Expressions for stopping distance in terms of A, T, and R

The analytical value of the stopping distance for each pulse shape is found by evaluating Equation (4.14) to determine the time that the maximum deformation occurs. Equation (4.10) is then evaluated at $t = \hat{t}$ to find the expression for the stopping distance. Because the impact velocity is a function of the coefficient of restitution, the stopping distance will also be a function of the coefficient of restitution.

The theoretical pulse shapes that are modelled should be physically realistic. To be so, the acceleration on the headform at any value of displacement during the inbound phase of the impact, $a|_{s,\text{inbound}}$, should be less than, or equal to, the acceleration of the headform at the same amount of displacement during the outbound phase of the impact, $a|_{s,\text{rebound}}$.

$$a|_{s,\text{inbound}} \geq a|_{s,\text{rebound}} \tag{4.25}$$

This constraint ensures that the design returns no more energy to the headform at all levels of displacement than was absorbed during the inbound phase of the impact.

The condition for a physically realistic pulse shape in Equation (4.25) is written in the displacement domain, but the acceleration is measured in the time domain. There are two conditions placed on the acceleration in the time domain. The first condition is that the bonnet must be in compression while the headform is accelerated away from the bonnet. The second condition is that the peak acceleration must occur at, or before, the time that the headform reaches its maximum displacement, $\hat{t}$.

The first condition says that the bonnet must be in compression throughout the impact. Without it, the bonnet would be accelerating the headform after the bonnet has returned *beyond* its natural position. For the bonnet to be in compression, the displacement, s, must be negative throughout the impact. Only those impacts that are have a negative displacement at the end of the impact, that is, at $t = T$, will satisfy this condition because the acceleration is always positive, the initial velocity, $v(0) = -V$, is negative, and the initial impact occurs at a displacement equal to 0.

Mathematically this condition can be written by forcing Equation (4.10), evaluated at $t = T$, to represent the value of displacement and the end of the impact, to be less than or equal to 0.

$$0 \geq s(T) \tag{4.26}$$

$$0 \geq \int_0^T \left[\int_0^t a(t).dt \right] - V\,.dt \tag{4.27}$$

By substituting pulse shape functions of $a(t)$ from Table 4.1 and values of V from Table 4.5 into Equation (4.27) the range of values that result in physical pulse shapes can be found. The half-sine and square pulse shapes are simple to evaluate. Equation (4.26) is satisfied for all possible values of R ($0 \leq R \leq 1$) for these pulse shapes. For the triangular pulse shape the solution is obtained in parts. Starting with Equation (4.27) and substituting in the appropriate values of a and V, an equation for the range of values

Table 4.6: The time, from the beginning of the pulse shape, at which the peak deformation of the impact occurs.

Pulse	Equation
Half-sine	$T\frac{2}{\pi}\arcsin\left(\sqrt{\frac{1}{R+1}}\right)$
Triangular	$T-T(1-k)\sqrt{\frac{R}{(R+1)(1-k)}}$
Square	$T\frac{1}{R+1}$

can be found. After some algebra, shown in Appendix B.1, the range of triangular pulse shapes that satisfy Equation (4.26) can be found.

$$R \leq \frac{k+1}{2-k} \tag{4.28}$$

The second condition for a physically realistic pulse shape is that peak in acceleration is coincident with, or occurs before, the time of the peak deformation of the impact. If this does not occur, the acceleration at some time during the rebound phase of the impact is higher than the acceleration on the inbound phase. Mathematically, this constraint can be expressed by forcing the time of the maximum acceleration t^*, to be less than, or equal to, the time of the peak deformation, $\hat{t}$.

$$t^* \leq \hat{t} \tag{4.29}$$

For the square pulse, t^* is all values of t; for the half sine pulse, $t^* = \frac{T}{2}$; and for the triangular pulse, $t^* = kT$. The time of the stopping distance can be determined by substituting the appropriate functions of $a(t)$ and V into Equation (4.13) and solving for $\hat{t}$. The time of the stopping distance for each of the pulse shapes is shown in Table 4.6.

Equation (4.29) is satisfied for all values of R for the half-sine and square pulse shapes. Equation (4.29) is satisfied for only some values of R for the triangular pulse. The derivation for the triangular pulse shapes with an apex in acceleration that occurs at or before the time of the maximum displacement is shown in Appendix B.2. The condition for the triangular

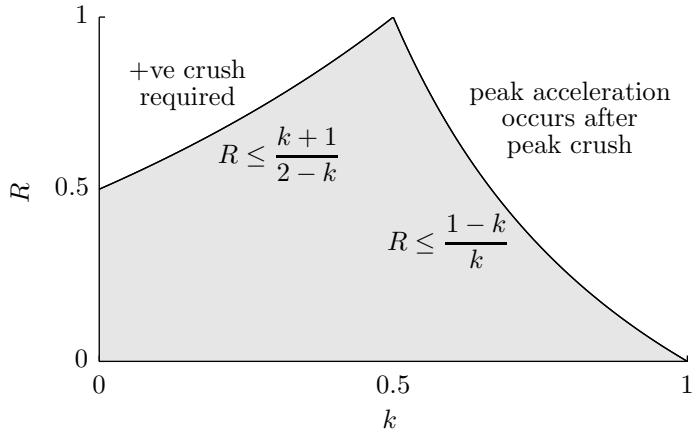

Figure 4.4: Conditions for a physically realistic triangular pulse shape. Pulses with with values of k and R in the shaded zone are physically possible.

pulse shapes is shown in Equation (4.30).

$$R \leq \frac{1-k}{k} \tag{4.30}$$

The two physical constraints on a triangular pulse shape are defined in Equations (4.28) and (4.30). These two constraints are visualised in Figure 4.4. The figure shows, in the shaded area, all values of k and R for triangular pulse shapes that result in physically realistic impact conditions. Only the symmetrical triangular pulse is physically possible for all values of R while all other triangular pulse shapes are only possible for some constrained values of R.

This preliminary work means that the stopping distance for each pulse shape can be calculated by using Equation (4.10) evaluated at the times shown in Table 4.6. The value of the stopping distance, S, for each pulse shape is shown in Table 4.7. The expressions in Table 4.7 have been evaluated for some specific coefficients of restitution and in the case of the triangular pulses, the skewness value, in Table 4.8. The data in the first column of this table are the same as the data in Table 4.3. The stopping distance decreases as the coefficient of restitution increases for all pulse shapes. As the skewness of the triangle increases, the stopping distance becomes greater.

Table 4.7: The maximum stopping distance for the theoretical pulse shapes with rebound allowed. The maximum stopping distance is equal to the product of a constant, A and T^2, with the constant being a non-linear function of R.

Pulse	Stopping distance
Half-sine	$S_h = \frac{2\sqrt{R}-2(R-1)\csc^{-1}(\sqrt{R+1})}{\pi^2(R+1)} A_h T_h^2$
Triangular†	$S_t = \frac{\left(1+k-2R+Rk+2R(1-k)\sqrt{\frac{R}{(R+1)(1-k)}}\right)}{6R+6} A_t T_t^2$
Square	$S_s = \frac{1}{2(R+1)^2} A_s T_s^2$

† Valid only when $R \leq \frac{k+1}{2-k}$ and $R \leq \frac{1-k}{k}$.

Table 4.8: The maximum stopping distance for different pulse shapes with rebound allowed, evaluated at discrete values of R.

Pulse Shape		Coefficient of restitution				
		0.00	0.25	0.50	0.75	1.00
Half-sine	$\times A_h T_h^2$	0.3183	0.2157	0.1601	0.1251	0.1013
Triangular $k = 0.0$	$\times A_t T_t^2$	0.1667	0.0965	0.0642		
Triangular $k = 0.1$	$\times A_t T_t^2$	0.1833	0.1116	0.0775		
Triangular $k = 0.3$	$\times A_t T_t^2$	0.2167	0.1416	0.1037	0.0806	
Triangular $k = 0.5$	$\times A_t T_t^2$	0.2500	0.1711	0.1287	0.1018	0.0833
Triangular $k = 0.7$	$\times A_t T_t^2$	0.2833	0.1997			
Triangular $k = 1.0$	$\times A_t T_t^2$	0.3333				
Square	$\times A_s T_s^2$	0.5000	0.3200	0.2222	0.1633	0.1250

4.4.1 The normalisation of pulse shapes for impacts with non-zero restitution

The pulse shapes with a finite coefficient of restitution can be normalised using the values in Tables 4.5 and 4.8 in a similar way as they were normalised for the pulse shapes without restitution in Section 4.3. Each of the pulse shapes is normalised so that it has the same impact velocity and stopping distance as a reference pulse. Again, the square pulse, generated from an impact with zero restitution, is used as the reference pulse.

For example, the half-sine pulse with a coefficient of restitution of 1 can be normalised with the reference pulse (the square pulse with $R = 0$). Firstly, this is done by normalising the impact velocity of the half sine pulse with $R = 1$ to the reference square pulse.

$$1 = \frac{V_h\Big|_{R=1}}{V_{ref}\Big|_{R=0}} = \frac{V_h}{V_s} \tag{4.31}$$

$$1 = \frac{\frac{2A_hT_h}{\pi(R+1)}\Big|_{R=1}}{A_{ref}T_{ref}} \tag{4.32}$$

$$1 = \frac{\frac{2A_hT_h}{\pi(1+1)}}{A_{ref}T_{ref}} \tag{4.33}$$

$$1 = \frac{1}{\pi}\left(\frac{A_h}{A_{ref}}\right)\left(\frac{T_h}{T_{ref}}\right) \tag{4.34}$$

Secondly, this is done by normalising the stopping distance of the half sine pulse with $R = 1$ with the reference square pulse.

$$1 = \frac{S_h\Big|_{R=1}}{S_{ref}\Big|_{R=0}} \tag{4.35}$$

$$1 = \frac{-0.1013A_hT_h^2}{-\frac{1}{2}A_{ref}T_{ref}^2} \tag{4.36}$$

$$1 = \frac{2}{\pi}\left(\frac{A_h}{A_{ref}}\right)\left(\frac{T_h}{T_{ref}}\right)^2 \tag{4.37}$$

Equations (4.34) and (4.37) can be solved simultaneously to determine the values of $\left(\frac{A_h}{A_{ref}}\right)$ and $\left(\frac{T_h}{T_{ref}}\right)$.

$$\frac{A_h}{A_{ref}} = 2 \qquad \frac{T_h}{T_{ref}} = 1.571 \tag{4.38}$$

Ratios at discrete values of R are presented here because the general analytic solution is unwieldy.

This process of evaluating the ratios, $\frac{A_h}{A_{ref}}$ and $\frac{T_h}{T_{ref}}$, can be repeated for each specific pulse shape and for several values of coefficient of restitution. The ratio of the amplitudes for each specific pulse shapes is shown in Table 4.9 and the ratio of the durations is shown in Table 4.10. The values with a coefficient of restitution of zero are identical to those calculated from the expressions in Table 4.4.

These pulse shapes are plotted against time in Figure 4.5 and against the displacement in Figure 4.6. When the pulse shapes are drawn against displacement in this way, the path taken by the half sine pulse shape is: ; the path taken by the triangular pulse shapes is: ; and the path taken by the square pulse shape is: . When drawn in this way, these paths are similar to the pulse shapes that are seen in real testing (for example see Figure 3.16 on page 57 or Figure 13 in Wu and Beaudet (2007)).

The eight pulse shapes have now been normalised so that they have the same impact velocity and stopping distance over a discrete range of coefficients of restitution. In the next section the analytical values of each IRF for each pulse shape are found. Then the eight pulse shapes can be evaluated using each of the IRFs so that the effect of the pulse shape and coefficient of restitution on each IRF can be investigated.

Table 4.9: Ratio of A_i and A_{ref}. The reference pulse is italicised.

Pulse Shape	Coefficient of restitution				
	0.00	0.25	0.50	0.75	1.00
Half-sine	1.571	1.663	1.777	1.891	2.000
Triangle $k = 0.0$	1.333	1.206	1.155		
Triangle $k = 0.1$	1.467	1.395	1.395		
Triangle $k = 0.3$	1.733	1.770	1.866	1.975	
Triangle $k = 0.5$	2.000	2.139	2.316	2.495	2.667
Triangle $k = 0.7$	2.267	2.496			
Triangle $k = 1.0$	2.667				
Square	*1.000*	1.000	1.000	1.000	1.000

Table 4.10: Ratio of T_i and T_{ref}. The reference pulse is italicised.

Pulse Shape	Coefficient of restitution				
	0.00	0.25	0.50	0.75	1.00
Half-sine	1.000	1.181	1.326	1.454	1.571
Triangle $k = 0.0$	1.500	2.073	2.598		
Triangle $k = 0.1$	1.364	1.792	2.150		
Triangle $k = 0.3$	1.154	1.412	1.608	1.772	
Triangle $k = 0.5$	1.000	1.169	1.295	1.403	1.500
Triangle $k = 0.7$	0.882	1.002			
Triangle $k = 1.0$	0.750				
Square	*1.000*	1.250	1.500	1.750	2.000

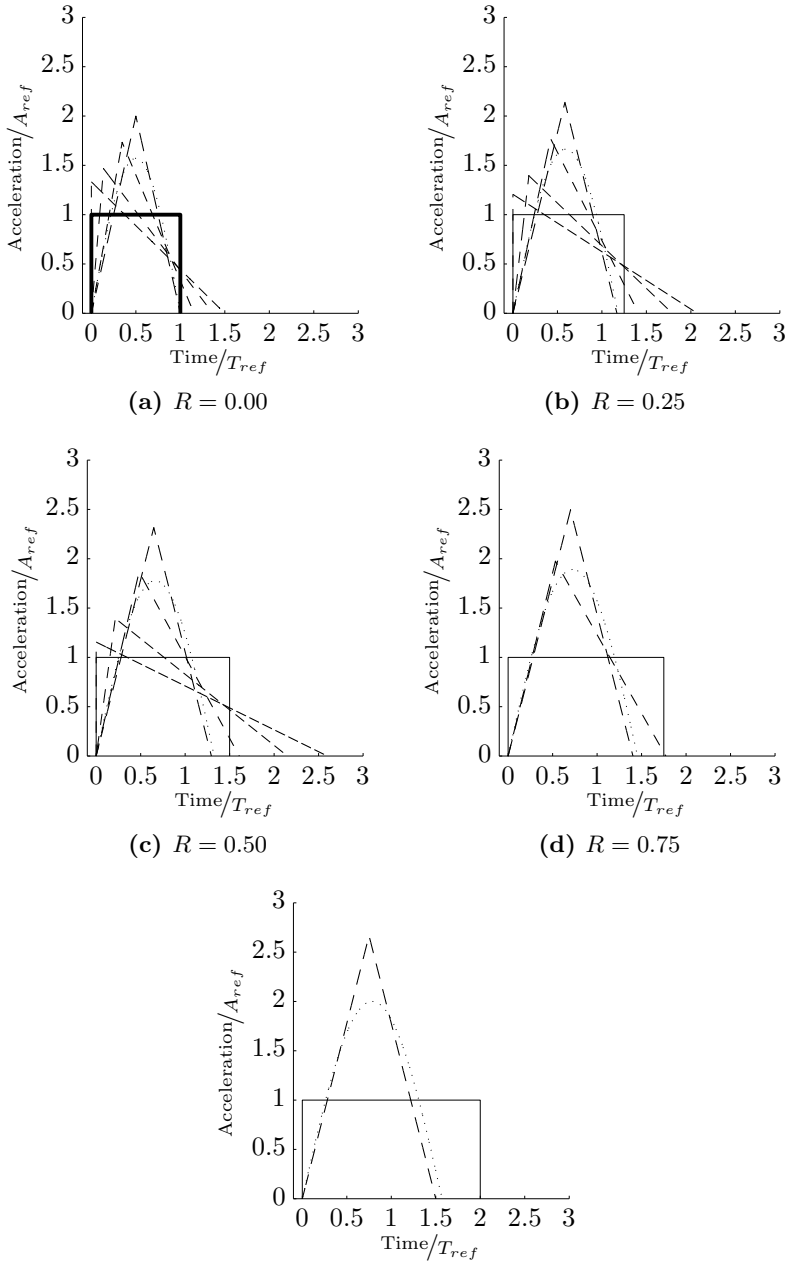

(a) $R = 0.00$ **(b)** $R = 0.25$

(c) $R = 0.50$ **(d)** $R = 0.75$

(e) $R = 1.00$

Figure 4.5: Normalised pulse shapes. Each pulse shape shown has the same impact velocity and stopping distance. Square pulses are shown with a solid line, half-sine pulses are shown with a dotted line and triangular pulses are shown with a dashed line. The reference pulse has the thickest line in (a).

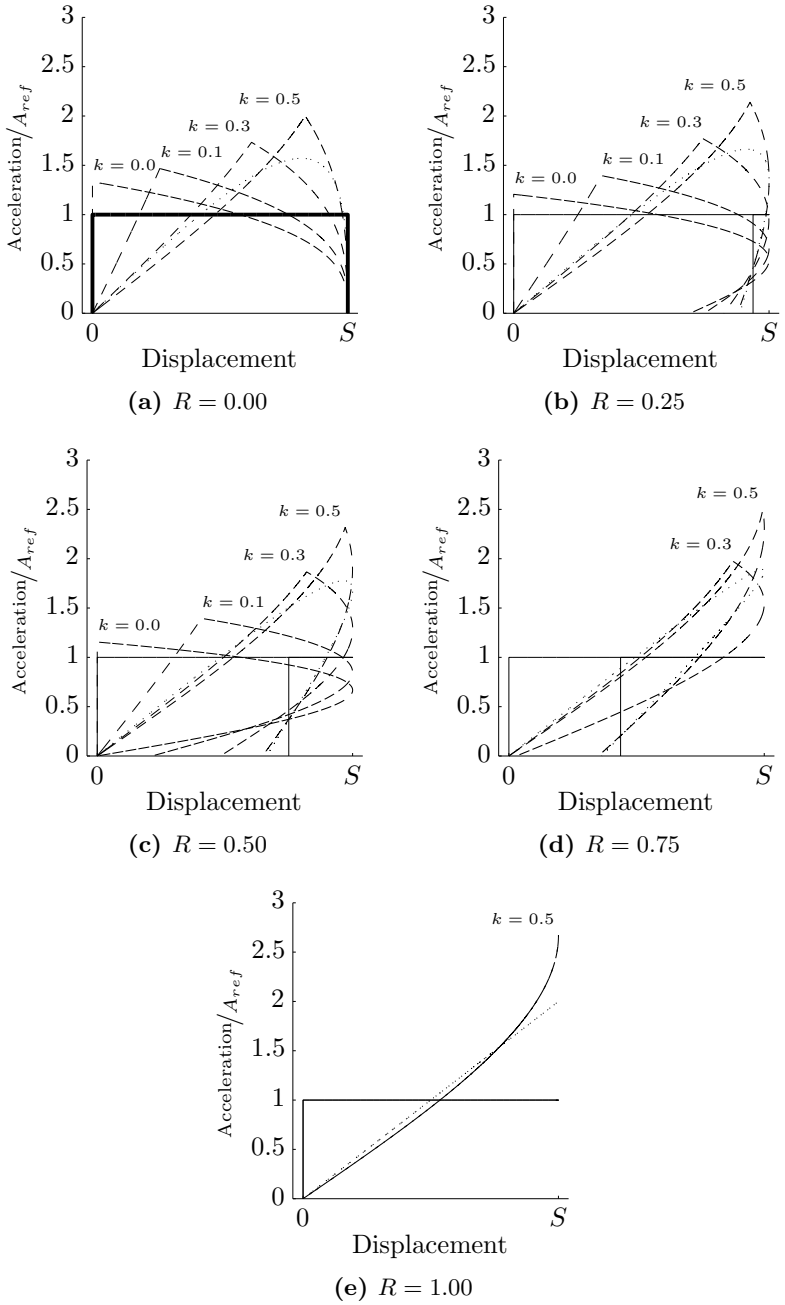

(a) $R = 0.00$ **(b)** $R = 0.25$

(c) $R = 0.50$ **(d)** $R = 0.75$

(e) $R = 1.00$

Figure 4.6: Normalised pulse shapes shown in the acceleration and displacement domain. Each pulse shape shown has the same impact velocity and stopping distance. Square pulses are shown with a solid line, half-sine pulses are shown with a dotted line and triangular pulses are shown with a dashed line. The reference pulse has the thickest line in (a).

4.5 The value of each IRF for each analytical pulse shape

In this section the analytical value of the IRF is obtained for each of the pulse shapes in terms of A and T. Throughout this section A_i is assumed to be measured in meters per second squared and T_i is assumed to be measured in milliseconds and the constant g will be used to represent an acceleration equivalent to gravity. Expressions for the value of each IRF for each pulse shape are collected in Table 4.11.

4.5.1 HIC

The value of the HIC IRF for each analytical pulse shape used in this chapter has been described previously in Chou and Nyquist (1974) and these are shown in Table 4.11. In this chapter the HIC_∞ form of the HIC is used instead of the HIC_{15}. This is so that the confounding factors associated with the duration of the HIC evaluation window do not need to be considered. Most of the actual impact pulses have a HIC evaluation window that is less than 15 ms (see in Chapter 6).

4.5.2 PVP

The expression for PVP is

$$\text{PVP} = a(t^*) \int_0^{t^*} a(u)du \tag{4.39}$$

where t^* maximises the value of PVP.

The location of t^* is located at one of the critical points of the expression $a(t) \int_0^t a(t)dt$. This can be found by setting the first derivative of the expression to zero.

$$0 = \frac{d}{dt}\left[a(t) \int_0^t a(u)du\right] \tag{4.40}$$

Equation (4.40) can be rewritten as shown in Equation (4.41).

$$0 = a^2(t) + \frac{d}{dt}[a(t)] \int_0^t a(u).du \tag{4.41}$$

Solving this equation for $t = t^*$ will determine the value of t^* that maximises the value of PVP in Equation (4.39). Equation (4.41) also implies that the location of the PVP will occur when the value of acceleration is decreasing with time (or $\frac{d}{dt}[a(t)] < 0$). This is because $a^2(t)$ and $\int_0^t a(u).du$ are both greater than zero, as a result the product of $\frac{d}{dt}[a(t)]$ and $\int_0^t a(t).dt$ must be less than zero. This means that the PVP will be found at, or after the apex of the triangular pulse, after the peak of the half-sine pulse, and at the end of the square pulse. The specific locations for each pulse shape are now discussed in turn.

Half-sine pulse

The time of the maximum of PVP for the half-sine pulse is determined using the Equation (4.41). Solving this equation with the appropriate value of $a(t)$ for the half-sine pulse shows that the PVP of the half sine pulse occurs after two-thirds of the pulse duration.

$$t_h^* = \frac{2T_h}{3} \tag{4.42}$$

The half-sine pulse then has a value of PVP calculated using Equation (4.44).

$$\text{PVP}_h = \frac{2}{\pi} A_h^2 T_h \sin\left(\frac{\pi t_h^*}{T_h}\right) \sin\left(\frac{\pi t_h^*}{2T_h}\right)^2 \tag{4.43}$$

$$\text{PVP}_h = \frac{3\sqrt{3}}{4\pi} A_h^2 T_h \tag{4.44}$$

Triangular pulse

Equation (4.41) is evaluated for a triangular pulse to determine the time of the maximum PVP for this pulse shape. The solution has to take into

account the discontinuity in the derivative of acceleration that occurs at the peak of the acceleration. Therefore, two equations for the location of the PVP are found for the triangular pulse. The location of the PVP is either at, or after, the apex. If the apex occurs early in the impact pulse (within the first two-thirds of the impact pulse duration) then the location of the PVP is after the apex. Otherwise, it coincides with the apex.

$$t_t^* = \begin{cases} T_t \left(1 - \frac{\sqrt{1-k}}{\sqrt{3}}\right) & 0 \leq k \leq \frac{2}{3} \\ kT_t & \frac{2}{3} < k \leq 1 \end{cases} \tag{4.45}$$

The maximum value of the PVP for the symmetrical triangular pulse shape occurs at $t_t = 0.592T$ which is after the apex of the pulse. The symmetrical triangular pulse shape and the half sine pulse shape are both symmetrical pulse shapes. The time of maximum PVP for the symmetrical triangular pulse shape is earlier in the impact sequence than for the half-sine pulse shape.

The PVP for the triangular pulses is given by the expression in Equation (4.46) and is plotted in Figure 4.7.

$$\text{PVP} = \begin{cases} \frac{\sqrt{3}}{9\sqrt{1-k}} A_t^2 T_t & 0 \leq k \leq \frac{2}{3} \\ \frac{k}{2} A_t^2 T_t & \frac{2}{3} \leq k \leq 1 \end{cases} \tag{4.46}$$

Square pulse

The derivative of the acceleration of the square pulse is 0 for most of its duration. The only time where it is less than 0 is at the end of the pulse, at $t^* = T$. As a result the PVP of the square pulse will occur at that location. The value of the PVP for the square pulse is then the product of the square of the acceleration and the duration.

$$\text{PVP} = A^2 T \tag{4.47}$$

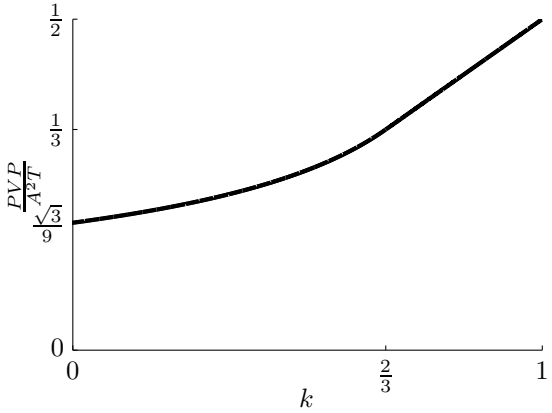

Figure 4.7: Value of PVP for triangular waveforms with amplitude A, duration T, and an apex at kT. See Equation (4.46) for equation of the line.

The value of the PVP for each of these pulse shapes is summarised in Table 4.11.

4.5.3 Peak acceleration

The peak acceleration for each of these theoretical pulses is the value of the coefficient A divided by the acceleration due to gravity. Table 4.11 also shows the value of the a_m for each of the pulse shapes.

4.5.4 3 millisecond clip

The value of the a_3 IRF is always less than or equal to the peak acceleration value. As the duration of the pulse increases the width of the pulse shape increases near the location of the peak acceleration. Consequently the value of the a_3 approaches the value of the peak acceleration as the pulse shape becomes longer in duration.

The a_3 IRF is not comparable with other IRFs for very short impacts of less than 3 ms in duration. That is because for all these impacts with durations less than 3 ms the 3 millisecond clip is equal to 0.

The value of the a_3 IRF for each of the pulse shapes is calculated in the following paragraphs and summarised in Table 4.11.

Half-sine pulse

The half-sine is a symmetrical pulse so the value of the 3 millisecond clip can be found by evaluating the equation of the pulse 1.5 ms prior to the point of peak acceleration. The value of a_3 for pulse shapes with $T_h \geq 3$ ms with T_h measured in milliseconds is calculated below.

$$a_3 = \frac{A_h}{g} \cos\left(\frac{1.5\pi}{T_h}\right) \tag{4.48}$$

Triangular pulse

The technique of similar triangles can be used to determine the value of the a_3 IRF for the triangular pulse. The triangles $\overline{OA'T}$ and $\overline{I'A'J'}$ in Figure 4.8 are similar, with I' and J' located at the value of a_3 and separated by 3 ms.

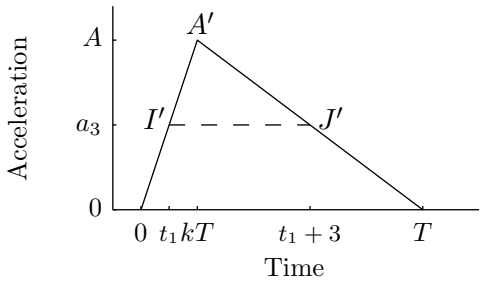

Figure 4.8: Triangular pulse shape

Using the similar triangles relationship, the a_3 takes the value shown in Equation (4.49).

$$a_3 = \frac{A_t}{g}\left(1 - \frac{3}{T_t}\right) \tag{4.49}$$

The a_3 value for this pulse is 0 for all pulses that have a duration less than or equal to 3 ms.

Square pulse

Provided the duration of the pulse is more than three milliseconds the value of a_3 for the square pulse is the same as the value of the peak acceleration.

Table 4.11: Values of HIC, PVP, a_m and a_3 IRFs for various analytical pulse shapes. The HIC values are derived from Chou and Nyquist (1974).

Pulse	HIC	PVP	a_m	a_3($^{\curlywedge}$)
Half-sine	$\frac{0.4146}{g^{2.5}} {A_h}^{2.5} T_h$	$\frac{3\sqrt{3}}{4\,\pi} A_h^2\, T_h$	$\frac{A_h}{g}$	$\frac{A_h}{g} \cos\left(\frac{[1.5\,\mathrm{ms}]\pi}{T_h}\right)$
Triangular	$\frac{0.2464}{g^{2.5}} {A_t}^{2.5} T_t$	$\frac{\sqrt{3}}{9\sqrt{1-k}} A_t^2 T_t$ (†) $\frac{k}{2} A_t^2 T_t$ (‡)	$\frac{A_t}{g}$	$\frac{A_t}{g}\left(1 - \frac{[3\,\mathrm{ms}]}{T_t}\right)$
Square	$\frac{1}{g^{2.5}} {A_s}^{2.5} T_s$	$A_s^2 T_s$	$\frac{A_s}{g}$	$\frac{A_s}{g}$

$^{\dagger} 0 \leq k \leq \frac{2}{3}$, $^{\ddagger} \frac{2}{3} \leq k \leq 1$, $^{\curlywedge}\ T_i > 3\,\mathrm{ms}$

4.5.5 Summary of analytical values of each IRF

The analytical values of each IRF for each of the pulse shapes is shown in Table 4.11.

In Table 4.11 each IRF is a power function of A and T. Velocity is also a power function of A and T (Table 4.5), as is the stopping distance (Table 4.7). Each IRF can be expressed as a power function of velocity and stopping distance, with the pulse shape and the coefficient of restitution, R, also relevant. In Chapter 5 these power functions will be developed and compared with the data collected in tests with vehicles.

4.6 Evaluation of each IRF for the normalised pulse shapes

The expression for each IRF for each pulse shape in Table 4.11 is in terms of the absolute value of each A and each T. The values of A and T for the pulse shapes normalised for identical impact velocity and stopping distance are in terms of a square, reference pulse, with zero coefficient of restitution (that is $\frac{A}{A_{ref}}$ and $\frac{T}{T_{ref}}$). Consequently, the value of each IRF, for each pulse shape, will be calculated relative to the value of that IRF for the reference pulse shape.

For example, using the expressions for HIC in Table 4.11, the value of the HIC for the half-sine pulse shape, relative to the value of HIC for the reference pulse shape (square with $R = 0$) is shown in Equation (4.50).

$$\frac{\text{HIC}_h}{\text{HIC}_{ref}} = \frac{0.4146\left(\frac{A_h}{g}\right)^{2.5} T_h}{\left(\frac{A_s}{g}\right)^{2.5} T_s} \tag{4.50}$$

$$= 0.4146\left(\frac{A_h}{A_s}\right)^{2.5}\left(\frac{T_h}{T_s}\right) \tag{4.51}$$

where the ratios $\frac{A_h}{A_{ref}}$ and $\frac{T_h}{T_{ref}}$ for the half-sine pulse shape at each value of coefficient of restitution can be found in Tables 4.9 and 4.10.

The ratio of HIC for the half-sine pulse shape (with $R = 0$) and the HIC for the reference square pulse shape is found to be 1.282.

This means that a half-sine acceleration pulse with a coefficient of restitution of zero will have a HIC value that is 1.282 times the value of HIC for a square pulse shape with a coefficient of restitution of zero when they have a common impact velocity and stopping distance. It follows that a design using the half sine pulse will become more crashworthy according to HIC if it is redesigned to have a square pulse shape, provided that the stopping distance remains unchanged for a given impact velocity.

The relative performances of the various pulse shapes for each IRF are now considered.

4.6.1 HIC

The dependence of HIC on pulse shapes and coefficient of restitution is shown in Figure 4.9. In this and in following figures the square reference pulse is always shown with the filled black square marker.

For the pulse shapes shown, the HIC is minimised when the pulse is triangular with $k = 0.0$ and $R = 0$. For triangular pulses, the HIC increases as the value of k increases. The square pulse generates a higher HIC than the triangular pulse when $k = 0.1$ but a lower HIC than the triangular pulse when $k = 0.3$. A half-sine pulse produces a lower HIC than a symmetrical triangular pulse shape.

As the coefficient of restitution increases, the HIC of each pulse shape increases. A higher coefficient of restitution means the structure is dissipating

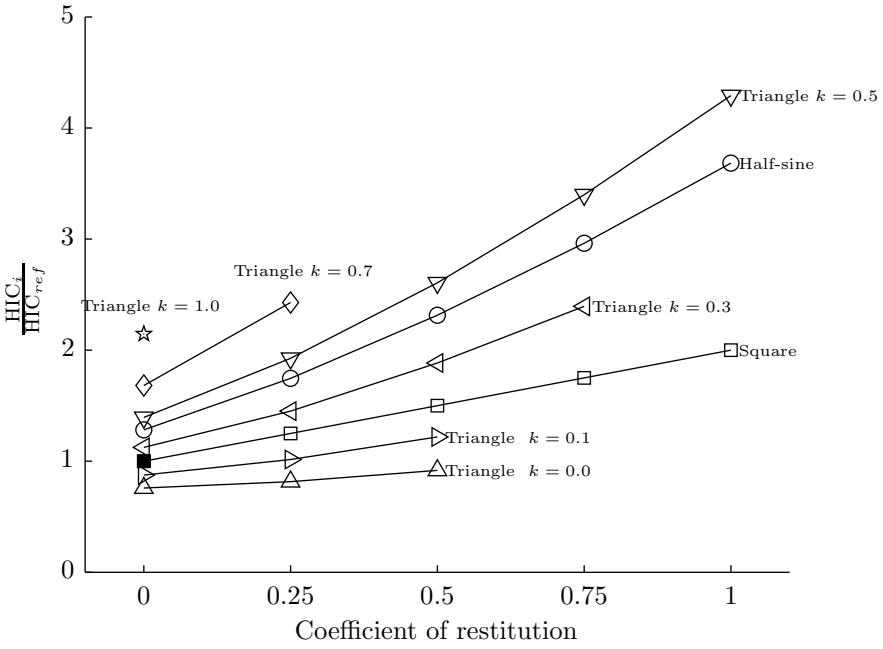

Figure 4.9: HIC value of each pulse shape compared with the HIC of the reference pulse shown with the black filled square marker. The stopping distance and the impact speed have constant values for each pulse shape.

less of the impact energy and the headform undergoes a larger change in velocity. Chou and Nyquist (1974) showed that the HIC was proportional to the square of the change in velocity. As the coefficient of restitution increases, the change in the velocity becomes higher and the HIC increases.

The graph shows that a poorly designed structure — one with a high value of HIC — can be improved in two ways when there is a fixed stopping distance and the impact velocity remains constant. The value of HIC can be reduced either by reducing the coefficient of restitution of the structure and/or changing the pulse shape of the structure. For instance, a structure that has a triangular pulse shape with $k = 0.3$ and a coefficient of restitution of 0.5 can be improved by lowering the coefficient of restitution to 0.25 or by changing the structure so that it has a square acceleration pulse shape or by doing both at the same time. Each will result in a structure that has a lower HIC.

Wu and Beaudet (2007) ordered their pulse shapes from the pulse shape that required the least stopping distance to the one that required the most stopping distance. This order was the ramp-down triangular pulse ($k = 0$), the square pulse, the half sine pulse, the isosceles triangle ($k = 0.5$) pulse and finally the ramp-up triangular pulse ($k = 1.0$). This order represents the crashworthiness of each of the pulse shapes in that study. This ordering is also found in the present study. The present study confirms these earlier results. A pulse shape with a short stopping distance for a particular value of HIC will also have a lower value of HIC when the crush distance is fixed.

These earlier results have been confirmed by this analysis, and they have been extended by including the coefficient of restitution of the structure. These results show that a decrease in the coefficient of restitution can, in some cases, reduce the HIC more than a change in the pulse shape.

4.6.2 PVP

The normalised pulse shapes were evaluated according to PVP and the results are shown in Figure 4.10.

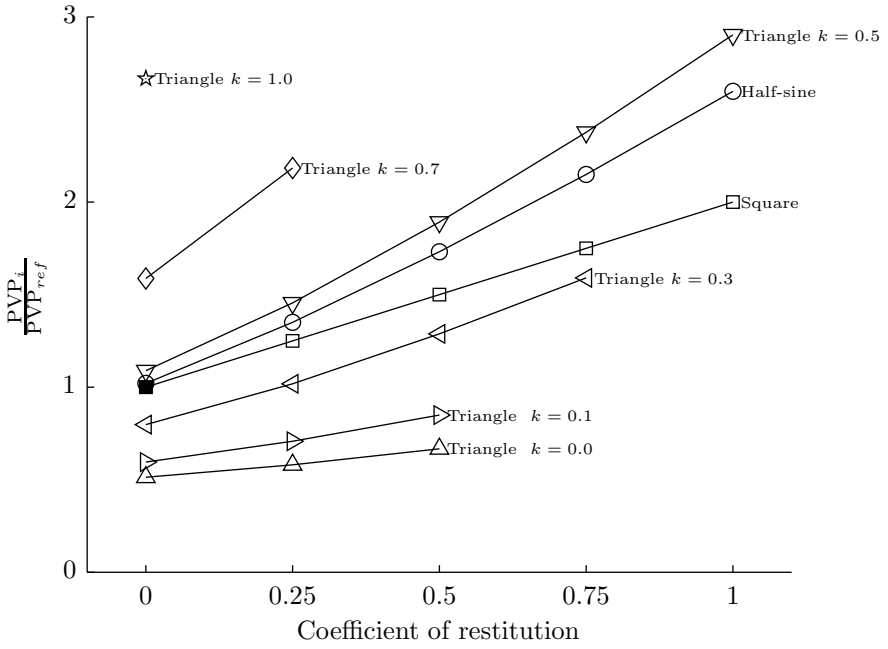

Figure 4.10: PVP value of each pulse shape compared with the PVP of the reference pulse shown with the filled marker. The stopping distance and the impact speed have constant values for each pulse shape.

Similar to the results for the HIC function, the front loaded triangular pulse shapes produced the lowest PVP. The triangular pulse shapes have higher values of PVP as the value of k increases.

At any given value of R the ranking of the pulse shapes with the PVP is the same as at any other value of R. But this order is slightly different from the order that was found for the HIC. In particular, the PVP of the square pulse is higher than the PVP of a triangle with $k = 0.3$ which is the reverse of the order when these pulse shapes were evaluated with HIC.

The implication for this is that the order of pulse shapes for the PVP is different from the order of pulse shapes for the HIC. And so a designer who is seeking to improve a design could settle on a different pulse shape if the PVP were used as the objective IRF instead of the HIC.

4.6.3 Peak acceleration

Figure 4.11 shows the relationship for the a_m IRF for the different pulse shapes.

The square pulse square pulse generates the lowest value of a_m, regardless of R. This is because the square pulse has the lowest value of peak acceleration. The triangular pulse with $k = 0.0$ generates the lowest value of a_m of the triangular pulse shapes and the a_m value increases as the value of k increases.

Highly front loaded pulse shapes with a low coefficient of restitution have higher a_m values than similar pulse shapes with a higher coefficient of restitution. These pulse shapes and their respective peaks in acceleration were shown in Figure 4.5 and quantified in Table 4.9. A decrease in a_m is associated with an increase in coefficient of restitution in these pulse shapes because of the normalisation undergone. For a consistent stopping distance and impact velocity, with an increase in coefficient of restitution, these pulse shapes become longer in duration but lower in peak acceleration. With these changes the average acceleration during the inbound phase of the impact increases, because the acceleration at the maximum stopping distance is greater, despite the decrease in peak acceleration. This effect, while present in the other pulse shapes, is not as pronounced because a greater portion of those pulse shapes is associated with increasing (or constant) acceleration

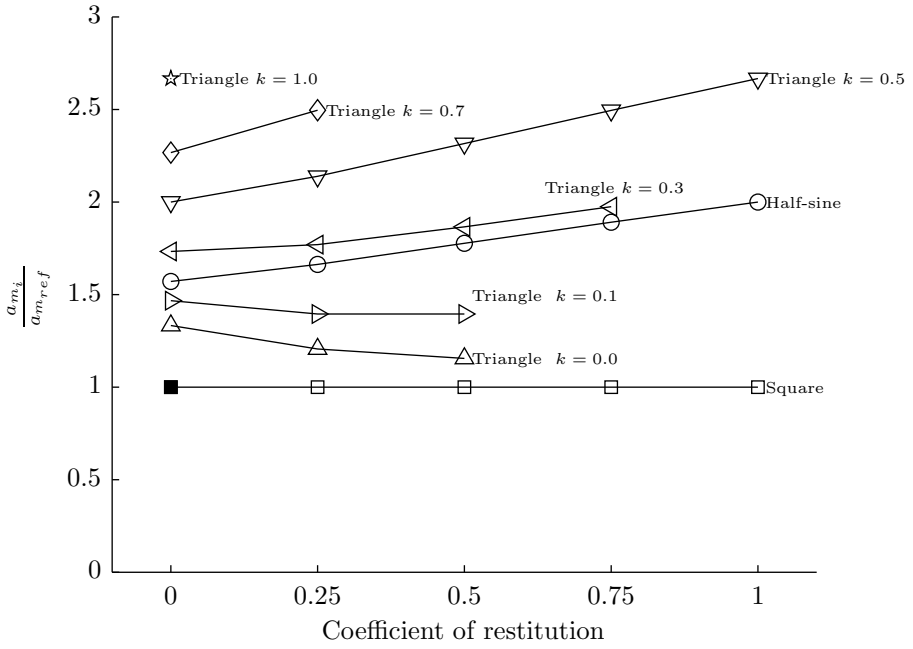

Figure 4.11: a_m value of each pulse shape compared with the a_m of the reference pulse shown with the black filled square marker. The stopping distance and the impact speed have constant values for each pulse shape.

during the inbound phase of the impact. This decrease in a_m with increase in coefficient of restitution is inconsistent with the other results presented for the HIC and PVP IRFs. The values of the HIC and PVP always decreased as the value of the coefficient of restitution decreased. For the a_m this is not always the case. Consequently, the use of a_m as an objective for optimising a structure could result in structures that dissipate less of the impact energy being considered more crashworthy than structures that dissipate more of the impact energy. As a result, structures might be designed differently than they might be when a minimised HIC or PVP is the objective.

4.6.4 3 millisecond clip

Unlike the previous IRFs, the relative value of the 3 millisecond clip IRF is dependent on the duration of the pulse. For instance, the value of a_3 for the half-sine pulse shape is proportional to $\cos\left(\frac{1.5\pi}{T_h}\right)$ where T_h is measured in milliseconds. Consequently, the values of this IRF need to be calculated for different durations of the reference square pulse shape. This is done in Figures 4.12 through to 4.16 where the square reference pulse has a duration of 20 ms, 10 ms, 6.67 ms, 5 ms, and 4 ms respectively.

In each figure, each pulse has a constant value of the ratio of the impact velocity and the stopping distance. The ratio of these two quantities can be taken to determine a characteristic property of each of the pulse shapes in the figure. This ratio is introduced as the the velocity-stopping distance ratio, VSDR. The ratio is used later in the thesis to aid the analysis of the a_3 IRF. This ratio has dimensions of $^1/_{\text{Time}}$. Each figure refers to a specific VSDR: $100\,\text{s}^{-1}$, $200\,\text{s}^{-1}$, $300\,\text{s}^{-1}$, $400\,\text{s}^{-1}$ and $500\,\text{s}^{-1}$.

An impact will have a high VSDR if the impact velocity is large compared with the stopping distance and these impacts will have a short impact duration. A low VSDR will result if the impact velocity is small compared with the stopping distance and these impacts will have a long duration. Using some typical values, an impact that has an initial velocity of $11.1\,\text{m}\,\text{s}^{-1}$ and a VSDR of $200\,\text{s}^{-1}$ will have a stopping distance depth of 5.55 cm. For comparison, the data used in this thesis have a mean VSDR of $198\,\text{s}^{-1}$, and range between $95\,\text{s}^{-1}$ and $435\,\text{s}^{-1}$.

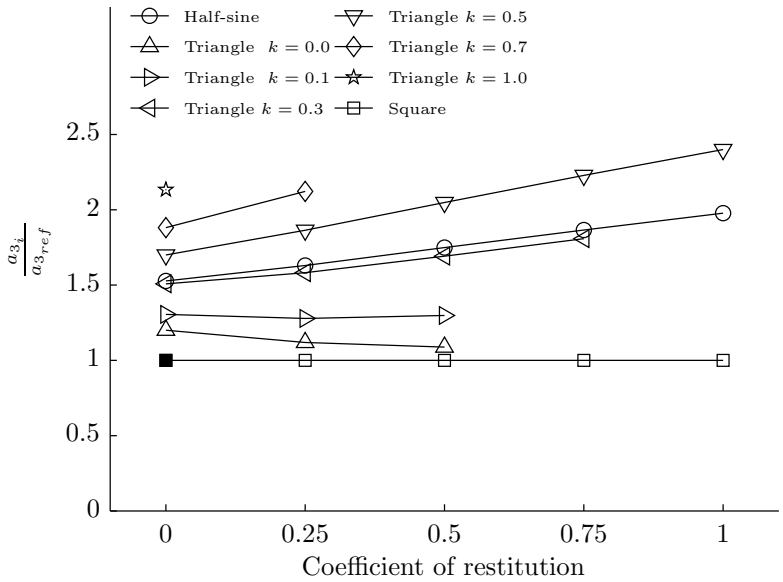

Figure 4.12: 3 millisecond clip value of each pulse shape compared with the 3 millisecond clip of the reference pulse shown with the filled marker. VSDR $= 100\,\mathrm{s}^{-1}$. The stopping distance and the impact speed have constant values for each pulse shape.

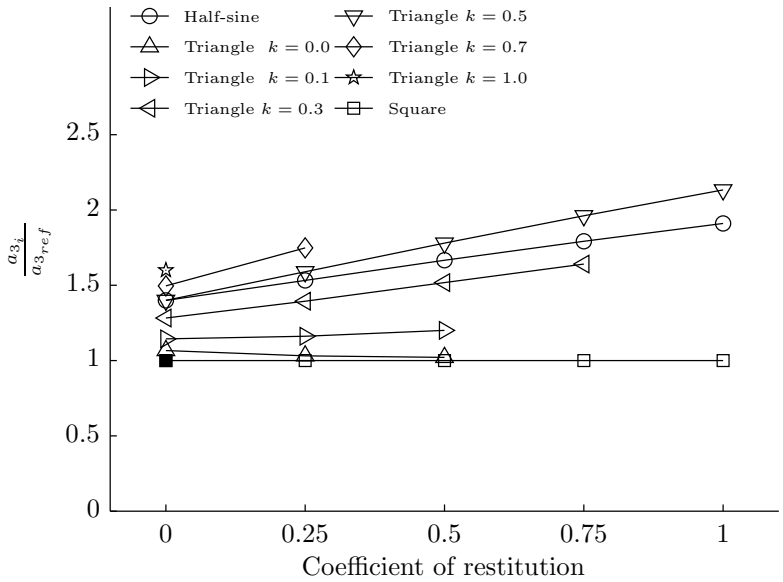

Figure 4.13: 3 millisecond clip value of each pulse shape compared with the 3 millisecond clip of the reference pulse shown with the filled marker. VSDR $= 200\,\mathrm{s}^{-1}$. The stopping distance and the impact speed have constant values for each pulse shape.

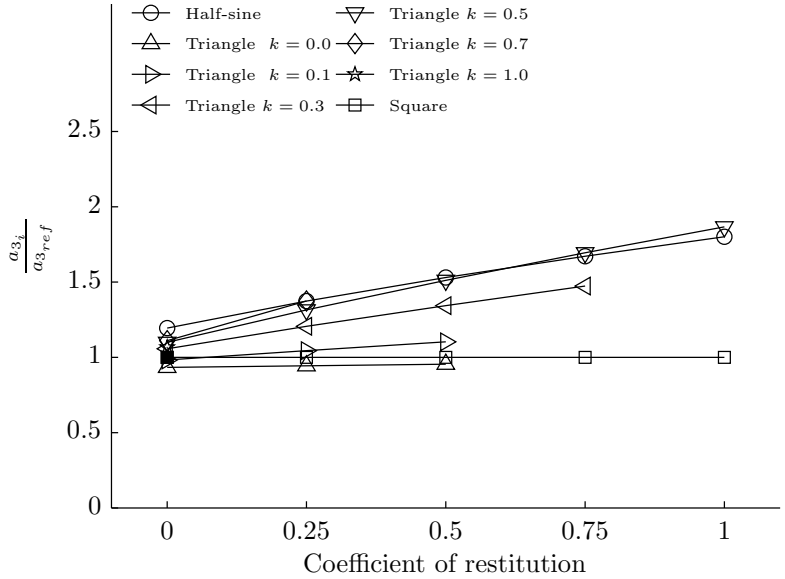

Figure 4.14: 3 millisecond clip value of each pulse shape compared with the 3 millisecond clip of the reference pulse shown with the filled marker. VSDR $= 300\,\mathrm{s}^{-1}$. The stopping distance and the impact speed have constant values for each pulse shape.

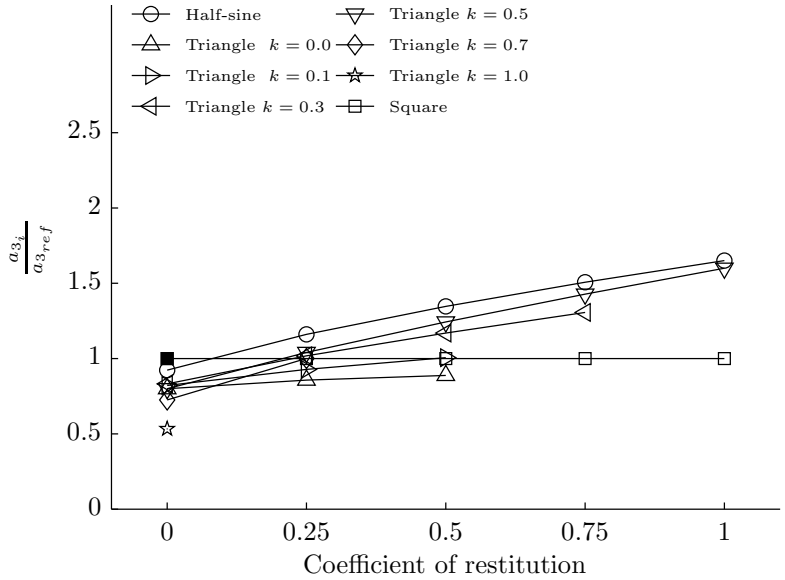

Figure 4.15: 3 millisecond clip value of each pulse shape compared with the 3 millisecond clip of the reference pulse shown with the filled marker. VSDR $= 400\,\mathrm{s}^{-1}$. The stopping distance and the impact speed have constant values for each pulse shape.

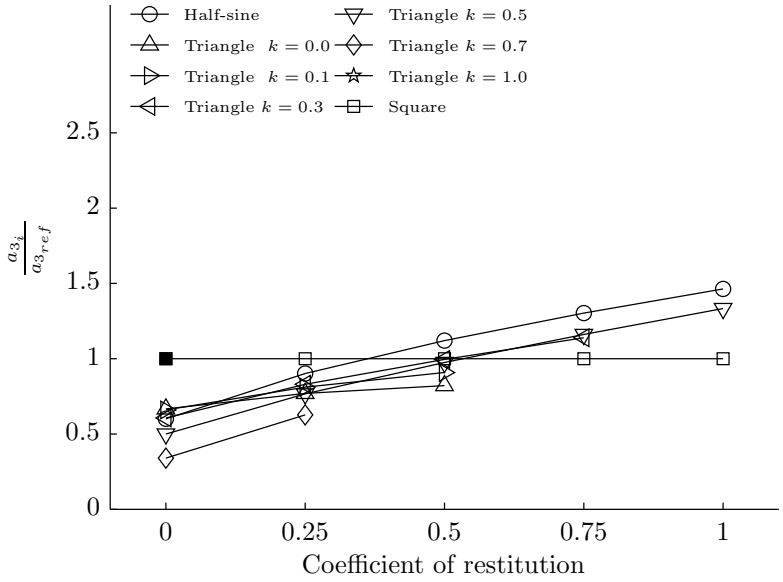

Figure 4.16: 3 millisecond clip value of each pulse shape compared with the 3 millisecond clip of the reference pulse shown with the filled marker. VSDR = $500\,\mathrm{s}^{-1}$. The triangular pulse with $k = 1$ has a duration that is less than 3 ms and therefore does have a value. The stopping distance and the impact speed have constant values for each pulse shape.

These results show that the pulse shape with the lowest value of a_3 is dependent on the VSDR. A square pulse produces the lowest a_3 for low VSDR impacts. For pulse shapes with a high VSDR, a rear loaded triangular pulse shape ($k = 1.0$) has the lowest value of a_3 when the coefficient of restitution is low.

When the VSDR is low, such as in Figure 4.12, a_3 is similar to the a_m with respect to the pulse shapes that produce the lowest values. These pulse shapes have a long duration, and so, the maximum acceleration is a little higher than the maximum acceleration sustained for 3 ms. As with the a_m the relationship between a_3 and the coefficient of restitution is inconsistent across the pulse shapes, indicating again, that if two structures were to be tested with this IRF then, in some circumstances, the structure which dissipated the least energy could be considered to be the more crashworthy of the two.

When the VSDR is high, such as in Figure 4.16, the most crashworthy pulse shape depends on the value of the coefficient of restitution. Rear loaded tri-

angular pulse shapes are more crashworthy when the coefficient of restitution is low, while front loaded triangular pulse are more crashworthy when the value of coefficient of restitution is high. This occurs because the triangular pulse shape has a duration dependent on the value of k. If the duration of the pulse shape is 3 ms in duration the value of a_3 will be 0. As the pulse duration increases, the value of a_3 becomes nearer to the value of a_m.

4.6.5 Combining the results

The results from the analysis of all IRFs can be combined. The ratios of the value of the IRF for each pulse shape and the value of the IRF for the reference square pulse shape are shown in Figure 4.17. Each subfigure shows the pulse shapes with coefficients of restitution equal to zero and 0.25.

In Figure 4.17 the pulse shape with the lowest value of the normalised IRF, $\frac{\text{IRF}}{\text{IRF}_{ref}}$ may be interpreted as the pulse shape that is most crashworthy. The front loaded triangular pulses are more crashworthy than the other triangular pulse shapes for most IRFs and coefficients of restitution. The front loaded triangular pulse shape is the most crashworthy in most scenarios. When this is not the case, the square pulse shape is the most crashworthy. The square and front loaded triangular pulse shapes are more crashworthy than the others because they each have an early peak in the acceleration. This early peak in acceleration retards the speed of the impactor quickly. This means the remaining deformation distance can be traversed slowly, and at a low level of acceleration. This low level of acceleration is rewarded with low values of each IRF.

4.7 Discussion of effect of the choice of IRF on design outcomes

In this analysis, analytical pulse shapes with a range of coefficients of restitution were normalised so that their impact velocity and their stopping distance were identical. These normalised pulse shapes were then evaluated with four IRFs to determine the effects the pulse shape and the coefficient of restitution have on the value of each IRF.

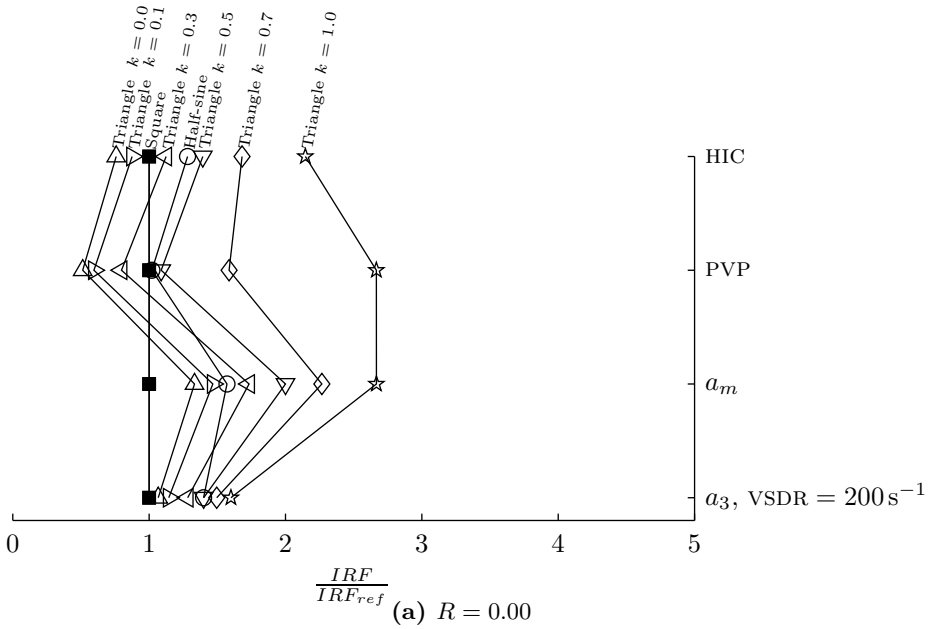

(a) $R = 0.00$

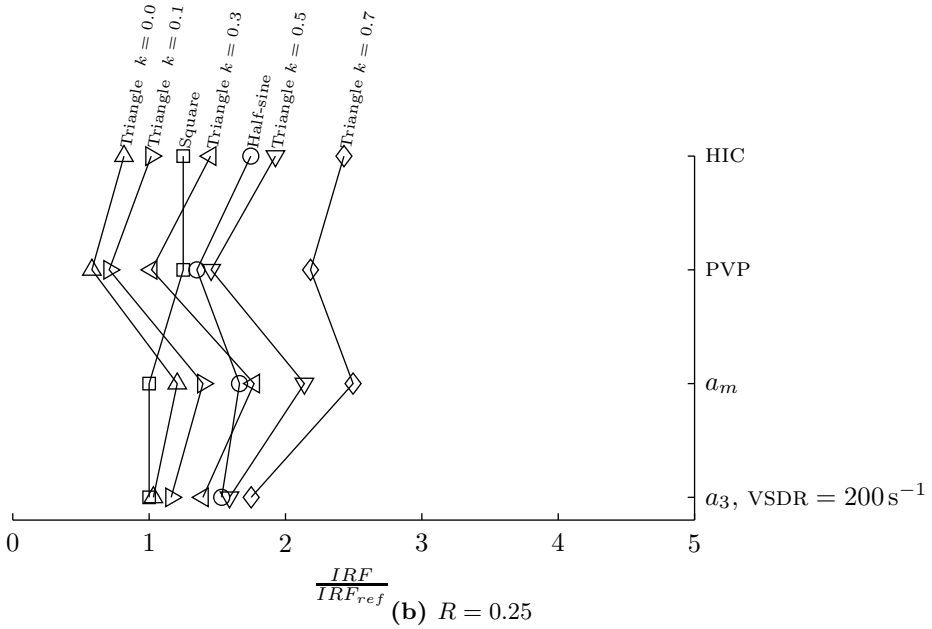

(b) $R = 0.25$

Figure 4.17: Ratio of crashworthiness of each pulse shape compared for each IRF at two values of coefficient of restitution. The pulse shapes with the highest crashworthiness are on the left side of the figure. The reference pulses are shown as the filled black squares in (a).

The approach taken was similar to that used in previous studies; certain impact parameters were held constant while the details of the structural response varied, as represented by the different pulse shapes and coefficients of restitution.

With respect to the structures that are subjected to impact testing for pedestrian safety, differences in impact pulse shape may result from the use of:

- different materials (Belingardi et al., 2009; Schwarz et al., 2004; Shahbeyk et al., 2003),
- deformable bonnet mounts (Pinecki and Zeitouni, 2007), or
- the distribution of the bonnet ribs (Liu et al., 2009; Schwarz et al., 2004; Untaroiu et al., 2006).

Of the pulse shapes used in the analysis, the triangular pulse with $k = 0.0$ was the most crashworthy pulse according to HIC, PVP and, under some conditions, the a_3 IRF. The square pulse was most crashworthy for the a_m and for the a_3 under some other impact conditions, while other triangular pulse shapes were the most crashworthy for the remaining test conditions for the a_3 IRF.

In general, two phenomena were common irrespective of the choice of IRF:

- the crashworthiness of a pulse shape increased as the coefficient of restitution decreased; and
- the front loaded triangular pulse shapes were more crashworthy than other pulse shapes.

However, in some cases, a_m and a_3 contradicted the above statements. Sometimes, when the a_m and a_3 IRFs were used to assess the pulses, more crashworthy values of these IRFs were achieved as the coefficient of restitution increased. Sometimes the front loaded triangular pulse shapes appeared less crashworthy than other triangular pulse shapes. These trends were inconsistent with the bulk of other results where more crashworthy results were related to lower values of k and lower values of R.

Broadly, this analysis has shown that a design that dissipates more of the impact energy through a lower coefficient of restitution will tend to appear more crashworthy irrespective of the IRF that is used. The exception to

this is the front loaded triangle pulse shapes evaluated with the a_m and a_3 IRFs. This analysis has also shown that lower peak accelerations also appear more crashworthy irrespective of the assessment function. Often, these lower peak accelerations can be achieved by front loading the pulse. The two design goals of decreasing the coefficient of restitution, and front-loading the impact, are strategies that would be common to assessment procedures even if different IRFs were used. The exception would be for specific scenarios related to the particular requirements of the a_m and a_3 IRFs.

These observations are relevant to the question: How would the ultimate design of a structure be influenced by the particular form of the IRF that is used to assess it? Based on the forgoing results, the answer would be that there would be minimal, if any, change in the ultimate design. For the practitioner interested in designing a structure to meet a design constraint, whilst minimising the value of an IRF, he or she should aim to make the structure dissipate as much energy at the lowest possible level of acceleration. Changing the pulse shape is one way of achieving this goal. Further redesigns resulting in lower acceleration levels, and lower coefficients of restitution will continue to improve the crashworthiness of the structure, irrespective of the IRF considered.

Chapter 5

Relating each IRF to impact velocity, stopping distance, coefficient of restitution and pulse shape

5.1 Introduction

In this chapter it will be shown that each IRF used in this thesis can be written as a power function of the impact velocity, headform stopping distance and coefficient of restitution. The effect of the pulse shape will be a constant in these power functions. From these power functions the relative influence of those components can be evaluated.

Lim et al. (1995) previously observed that the HIC IRF can be written as a power function of the impact velocity and stopping distance but they did this only in the case where an impact has a coefficient of restitution of zero. This work has not been extended to other IRFs nor for other values of the coefficient of restitution. Importantly, it is shown in this chapter that the different IRFs are all affected in a qualitatively similar (but not quantitatively identical) way by changes in impact velocity and the stopping distance.

The power functions are then compared with the results of a linear regression: the values of each IRF are regressed on the impact velocity, stopping distance and coefficient of restitution from the set of headform impact test data described in Chapter 3.

There are differences between the theoretical and the empirical relationships. These differences arise because the actual acceleration pulse shapes differ from the idealised acceleration pulse shapes used to derive the theory. The idealised pulse shapes are less complex than the pulse shapes from the real data.

This chapter is arranged in the following way:

- The theory developed in the previous chapter is extended to show that each IRF can be written as a power function of impact velocity, stopping distance and coefficient of restitution.
- A linear regression of each IRF on these factors in the test data is performed and the results are compared with the theory, and
- The implications of these results are discussed.

5.2 Theory

5.2.1 Effect of impact velocity and stopping distance on value of each IRF

In Chapter 4, several theoretical pulse shapes, i, were defined by the peak acceleration A_i and their duration T_i. These pulse shapes included a half-sine, a square, and several triangle pulses. Each pulse shape had an initial velocity, V_i, that could be written as a product of A_i and T_i and a pulse shape function, $\nu_i(R)$ (a function of the coefficient of restitution R) in the following form (Table 4.5 on page 85 shows expressions for some specific cases).

$$V_i = \nu_i(R) A_i T_i \tag{5.1}$$

The stopping distance of the headform, S_i, for each pulse shape can also be written in a similar way (Table 4.7 on page 89 provides some expressions for some specific cases).

$$S_i = \eta_i(R) A_i T_i^2 \tag{5.2}$$

Here, $\eta(R)$ is a value that is a function of R that is specific for each pulse shape. Because each expression contains A_i and T_i raised to some power, both can be considered power functions of A and T.

Furthermore, each of the IRFs used in Chapter 4 can also be written as power functions of A and T (Table 4.11 on page 100 provides the expressions for each IRF).

$$IRF_{i,j} = \lambda_{i,j} A_i^{\alpha_j} T_i^{\beta_j} \tag{5.3}$$

In this expression, j indicates a parameter that has a unique value for each IRF and λ is a numerical constant for each pulse shape, i, and IRF, j.

Because Equations (5.1) to (5.3) can all be written as power functions of A and T, they can be combined so that each IRF is written as a power function

of the impact velocity and stopping distance. This is done in Equation (5.4).

$$IRF_{i,j} = \Lambda_{i,j}(R)\, V_i^{m_j}\, S_i^{n_j} \tag{5.4}$$

Here m and n are constants determined for each IRF and$\Lambda_{i,j}$ is a function of R, determined for each IRF and each pulse shape.

The values of m_j, n_j and$\Lambda_{i,j}$ can be found by substituting the values from Equations (5.1) through to (5.3) into Equation (5.4).

$$\lambda_{i,j} A_i^{\alpha_j} T_i^{\beta_j} = \Lambda_{i,j} \left(\nu_i A_i T_i\right)^{m_j} \left(\eta_i A_i T_i^2\right)^{n_j} \tag{5.5}$$

Their values are:

$$m_j = 2\alpha_j - \beta_j \tag{5.6}$$

$$n_j = -\alpha_j + \beta_j \tag{5.7}$$

$$\Lambda_{i,j} = \frac{\lambda_{i,j}}{(\nu_i)^{m_j} (\eta_i)^{n_j}} \tag{5.8}$$

Lim et al. (1995) calculated the values of m and n in the case of HIC for some simple pulse shapes. These values are independent of pulse shape. The values of m and n for the HIC and each of the other IRFs are shown in Table 5.1.

Table 5.1: Indices of Equation (5.4) for each IRF.

IRF	m	n
HIC	4	-1.5
PVP	3	-1
a_m	2	-1
a_3	2	-1

Table 5.1 shows the relationship each IRF has with the impact velocity and stopping distance given by the values of m and n. The values of m range between 2 and 4, while the values of n are between -1.5 and -1. The relationship between each IRF and impact velocity and stopping distance is qualitatively similar however because m is positive and n is negative in every case.

Table 5.2: Table of$\Lambda_{i,j}$ for each pulse shape i, where the coefficient of restitution is zero

IRF	Half-sine	Triangle	Square
$\Lambda_{i,\mathrm{HIC}}$	1.5039×10^{-3}	$(k+1)^{1.5} \times 0.8899 \times 10^{-3}$	1.1730×10^{-3}
$\Lambda_{i,\mathrm{PVP}}$	0.510131	$\frac{4\sqrt{3}\,(k+1)}{27\sqrt{1-k}}$ † $\frac{2\,k\,(k+1)}{3}$ ‡	$\frac{1}{2}$
Λ_{i,a_m}	$\frac{\pi}{4g}$	$\frac{2(k+1)}{3g}$	$\frac{1}{2g}$
Λ_{i,a_3} *	0.07133	$0.01359(k+1)(4-k)$	0.0509684

† $0 \leq k \leq \frac{2}{3}$
‡ $\frac{2}{3} < k \leq 1$
* $\mathrm{VSDR} = 200\,\mathrm{s}^{-1}$

The value of$\Lambda_{i,\mathrm{HIC}}$ was calculated by Lim et al. (1995), but only for some pulse shapes and only when the coefficient of restitution is zero. Values have not previously been obtained for the other IRFs. The values for the IRFs arising from Equation (5.8) for pulse shapes with zero restitution are shown in Table 5.2. In the case of the a_3, only the results for an impact with a velocity-stopping distance ratio (VSDR) equal to $200\,\mathrm{s}^{-1}$ are shown.

5.2.2 Effect of a coefficient of restitution on the value of each IRF

Effect of a coefficient of restitution for the square pulse shape

In general, when $R > 0$, the analytical expression for Λ for each pulse shape is cumbersome and is concise only for a square pulse. The expression for $\Lambda_{s,\mathrm{HIC}}$, when $R > 0$, can be found by substituting the values of V and S for the square pulse from Tables 4.5 and 4.7 on page 89 into Equation (5.8).

Table 5.3: Values of$\Lambda_{s,j}$ for the square pulse shape provided its duration is more than 3 ms.

IRF	$\Lambda_{s,j}$
HIC	$\frac{1}{2^{1.5}g^{2.5}}(R+1)$
PVP	$\frac{1}{2}(R+1)$
a_m	$\frac{1}{2g}$
a_3	$\frac{1}{2g}$

$$\Lambda_{s,\text{HIC}} = \frac{\frac{1}{g^{2.5}}}{\left(\frac{1}{1+R}\right)^4 \left(\frac{1}{2(R+1)^2}\right)^{-1.5}} \tag{5.9}$$

$$\Lambda_{s,\text{HIC}} = \frac{1}{2^{1.5}g^{2.5}}(R+1) \tag{5.10}$$

Equation (5.10) shows that the$\Lambda_{s,\text{HIC}}$ is a numerical value multiplied by the coefficient $(R+1)$.

The expressions for$\Lambda_{s,j}$ for PVP, a_3 and a_m were calculated in a similar way. These expressions are shown in Table 5.3. The table shows that the $\Lambda_{s,\text{HIC}}$ and the$\Lambda_{s,\text{PVP}}$ are linear functions of $(R+1)$ while Λ_{s,a_3} andΛ_{s,a_m} are not functions of R. For the purposes of establishing an equation suitable for regression it is assumed thatΛ_{s,a_3} andΛ_{s,a_m} are functions of $(R+1)$ with a coefficient of 0.

General expression for each IRF for the square pulse shape

The expressions for$\Lambda_{s,j}$ are all of the form

$$\Lambda_{s,j} = e^{p_j}(R+1)^{q_j} \tag{5.11}$$

with $q = 1$ for HIC and PVP and $q = 0$ for a_3 and a_m. This can be used in Equation (5.4) to show that a general power function for the value of each IRF with a square pulse shape is

$$IRF_j = e^{p_j}(R+1)^{q_j}\, V^{m_j}\, S^{n_j} \tag{5.12}$$

with m and n the values shown in Table 5.1.

It would be convenient if Equation (5.12) were true for all pulse shapes and IRFs, but even if it were an approximation of the relationship then a regression using test data could be performed using it. Because of this, the applicability of this expression with the other theoretical pulse shapes defined in the previous chapter is investigated.

General expression for each IRF for half-sine and triangle pulse shapes

The expression for$\Lambda_{i,j}$ for the half-sine and triangle pulse shapes that were examined in the previous chapter is cumbersome, but it can be obtained using the symbolic toolbox in Matlab[1]. For example, the value of $\Lambda_{h,\mathrm{HIC}}$ for the half-sine pulse, obtained using this method, is given by the following, non-linear, expression.

$$\Lambda_{h,\mathrm{HIC}} = \frac{0.4146\pi(R+1)^{2.5}\left(\sqrt{R}-(R-1)\arcsin\left(\sqrt{\frac{1}{(R+1)}}\right)\right)^{3/2}}{4g^{2.5}\sqrt{2}} \quad (5.13)$$

These expressions for$\Lambda_{i,j}$ do not provide a simple form of the relationship of$\Lambda_{i,j}$ with $(R+1)$.

The general expression shown in Equation (5.11) will be valid for other pulse shapes if a plot of $\log(\Lambda_{s,j})$ against $\log(R+1)$ is linear. This linear relationship can be demonstrated by taking logarithms of both sides of Equation (5.11).

$$\log(\Lambda_{i,j}) = p_j + q_j \log(R+1) \quad (5.14)$$

The analytical expressions for $\log(Lambda_{i,j})$, obtained from the symbolic toolbox in Matlab, are plotted in Figures 5.1 to 5.4. It is apparent that, in every case, the relationships are approximately linear, especially when only small ranges of $\log(R+1)$ are examined. Thus, Equation (5.14) may be used to approximate the relationship between$\Lambda_{s,j}$ and $(R+1)$. Consequently, the expression for the value of every IRF in terms of R, S and V, shown in

[1] Mathworks inc.

Table 5.4: Indices of Equation (5.15).

IRF	m	n	q
HIC	4	-1.5	1
PVP	3	-1	1
a_m	2	-1	0
a_3	2	-1	0

Equation (5.12), can be considered as approximately valid for all theoretical pulse shapes. The expression is

$$IRF_j \approx e^{p_j}(R+1)^{q_j}\,(V)^{m_j}\,(S)^{n_j} \tag{5.15}$$

The value of m and n have been determined analytically for each IRF and are independent of pulse shape. The value of q is not independent of pulse shape. For the square pulse shape, its value has been determined analytically.

Estimating the effect of the coefficient of restitution

The gradient of the lines in Figures 5.1 to 5.4 are, in each case, similar to the gradient of the line for the square pulse shape. Some of the gradients are steeper than the gradient of the square pulse shape, and others are shallower. Because of this variation, for the purposes of estimating the value of q in the expression in Equation (5.15) the values obtained for the square pulse shape are used.

The indices for the expression in Equation (5.15) are summarised in Table 5.4.

Estimating the effect of pulse shape

One parameter in Equation (5.15) has not yet been investigated. This is the value of p for each pulse shape. The value of p can be determined from Figures 5.1 to 5.4. The effect of the VSDR on the value of p must also be considered, in addition to the effect of the pulse shape, for the a_3, as this can have a large effect on the value of the a_3 for each pulse shape. The values of $\log(\Lambda)$ for two triangle pulse shapes at various VSDR values are shown in Figure 5.5.

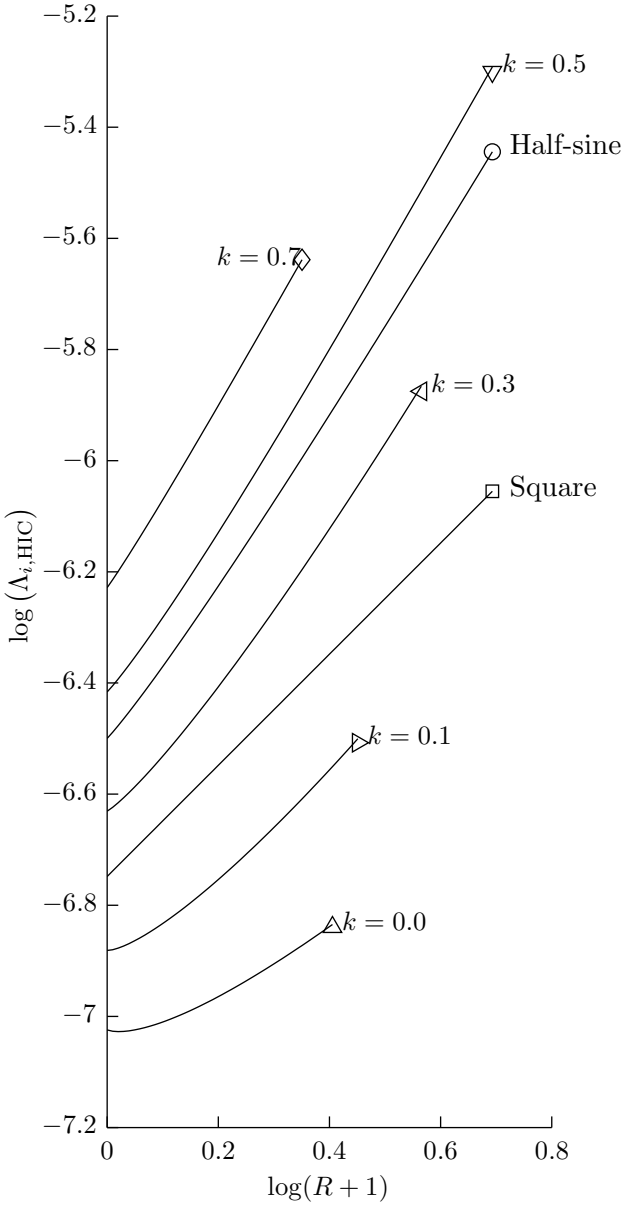

Figure 5.1: Effect of $\log(R+1)$ on the value of $\log(\Lambda_{i,\mathrm{HIC}})$. The square pulse is marked with a square marker, The half-sine pulse is marked with a circle marker, the other lines are for triangle pulse shapes with an apex at $t = kT$. The stopping distance and impact speed are at a fixed value.

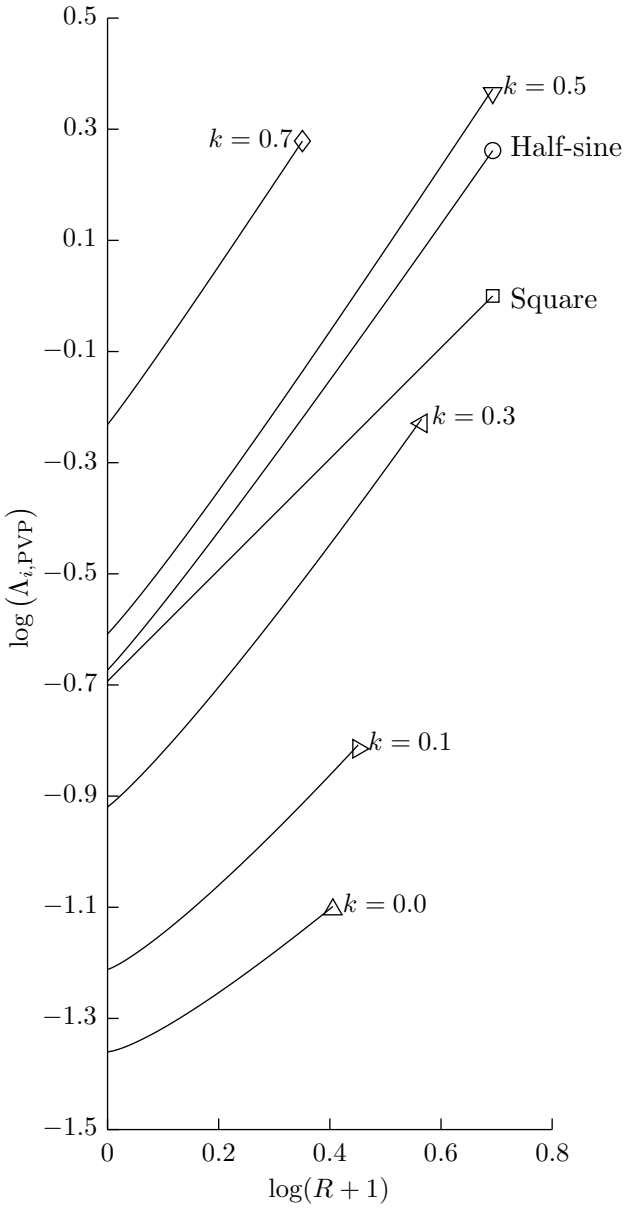

Figure 5.2: Effect of $\log(R+1)$ on the value of $\log(\Lambda_{i,\mathrm{PVP}})$. The square pulse is marked with a square marker, The half-sine pulse is marked with a circle marker, the other lines are for triangle pulse shapes with an apex at $t = kT$. The stopping distance and impact speed are at a fixed value.

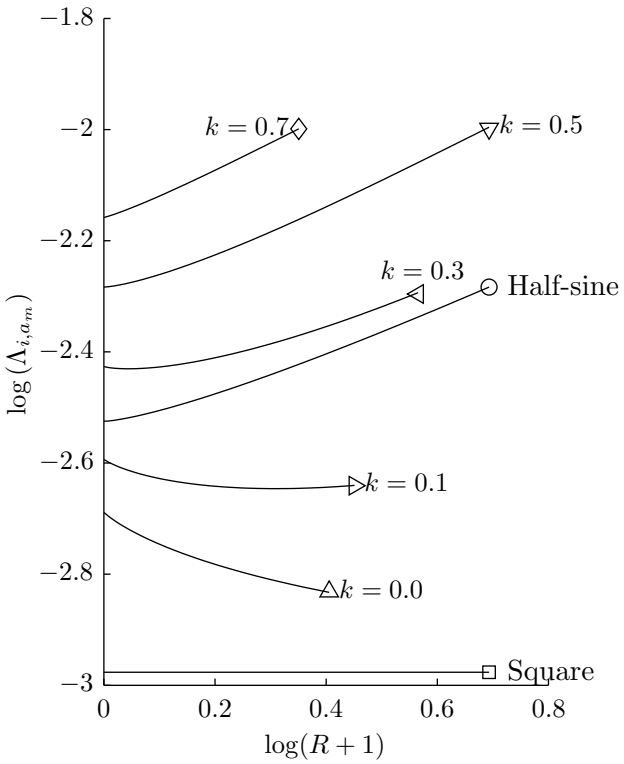

Figure 5.3: Effect of $\log(R+1)$ on the value of $\log(\Lambda_{i,a_m})$. The square pulse is marked with a square marker, The half-sine pulse is marked with a circle marker, the other lines are for triangle pulse shapes with an apex at $t = kT$. The stopping distance and impact speed are at a fixed value.

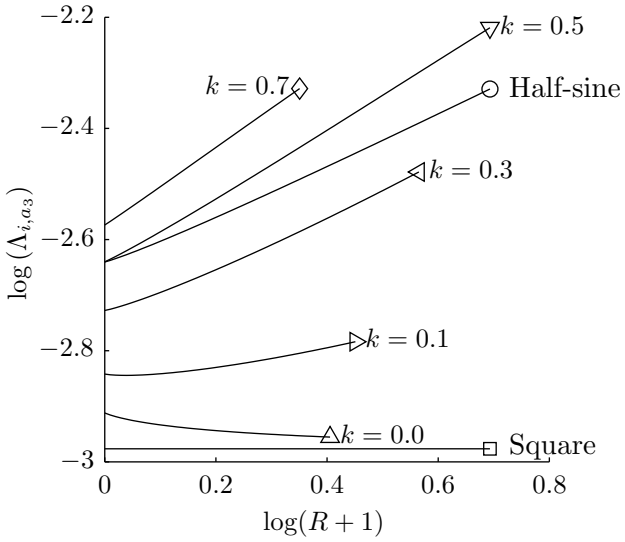

Figure 5.4: Effect of $\log(R+1)$ on the value of $\log(\Lambda_{i,a_3})$ for impacts with a VSDR of $200\,\mathrm{s}^{-1}$. The square pulse is marked with a square marker, The half-sine pulse is marked with a circle marker, the other lines are for triangle pulse shapes with an apex at $t = kT$. The stopping distance and impact speed are at a fixed value.

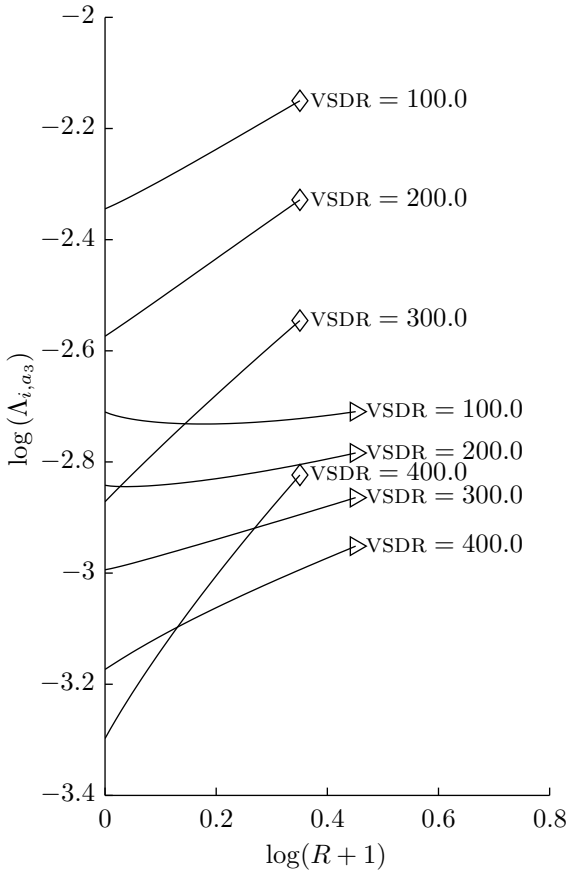

Figure 5.5: Effect of $\log(R+1)$ on the value of $\log(\Lambda_{i,a_3})$ at different values of VSDR. The triangle with $k = 0.1$ is shown with the right pointing marker, and the triangle with $k = 0.7$ is shown with the diamond marker. The range in $\log(\Lambda_{i,a_3})$ is larger than shown in Figure 5.4.

Table 5.5: Difference in $\log(\Lambda)$ at $R = 0$ between pulse shapes with the most extreme values of $\log(\Lambda)$ in Figures 5.1 to 5.3 and 5.5. For HIC and PVP these pulse shapes are the triangle pulse shapes with $k = 0$ and $k = 0.7$, for a_m these pulse shapes are the square pulse shape and the triangle pulse shapes with $k = 0.7$, and for a_3 the pulse shapes are the most extreme shown in Figure 5.5.

IRF	$\log(\Lambda_i)$ Range
HIC	0.796
PVP	1.133
a_m	0.818
a_3	0.953

Of additional interest is the range of the value of p for each IRF with these analytical pulse shapes. This gives an impression of the effect a pulse shape change has on the value of each IRF. This can be approximated as the range in$\Lambda_{\ i}$ between the most extreme pulse shapes at a coefficient of restitution of zero. This data can be found by evaluating the relevant components of Table 5.2 and, in the case of the a_3 read from Figure 5.5. It is summarised in Table 5.5. This information will be used to show that the unexplained variation in the regression can be attributed to the effect of pulse shape.

5.2.3 A general expression for each IRF suitable for linear regression

The logarithm of Equation (5.15) is taken to provide a linear equation suitable for linear regression.

$$\log(\text{IRF}_j) \approx p_j + q_j \log(R+1) + m_j \log(V) + n_j \log(S) \tag{5.16}$$

Using the known values of each IRF for each test, along with the values of R, V and S for these tests, the values of q, m_j and n_j can be obtained for real data using linear regression. These can be compared with the values of q_j which were estimated from the analytical pulse shapes, and m_j and n_j that were determined exactly for the analytical pulse shapes. These values that were estimated and determined were summarised in Table 5.4.

5.3 Data used in the linear regression

247 tests collected as part of a routine testing procedure for a consumer performance testing regime were described in Chapter 3. To summarise these, 108 of the tests were done using a larger, 4.8 kg, Adult headform and 139 tests were done using a smaller, 2.5 kg, Child headform. All tests were performed on vehicle structures that could be struck by a pedestrian's head. This data will be used to test whether the values of m, n and q in Equation (5.16), obtained from regression, are as predicted by the theory.

The data for the two headform sizes are kept separate. This is because each headform size has a unique distribution of stopping distance. If both headform sizes have similar results during the regression then this offers additional confidence in the accuracy of the result of the regression.

To use this data, measurements are needed from each test: the impact velocity, the stopping distance, the coefficient of restitution and the value of each IRF. These will be described in turn.

Impact velocity

The impact velocity is the velocity of the headform, normal to the impact surface, just prior to impact as this is the only velocity that contributes to the stopping distance of the test. This velocity was calculated to include the additional energy gained by the headform due to gravity and the change in impact angle induced by gravity. The cumulative distribution of the impact velocity was given in Figure 3.10 on page 50. The smaller and lighter Child headform has the larger range of normal impact velocities, ranging from approximately $9.5\,\mathrm{m\,s^{-1}}$ to $11.1\,\mathrm{m\,s^{-1}}$ with a standard deviation of $0.64\,\mathrm{m\,s^{-1}}$. The Adult headform has the narrower range of normal impact speeds ranging from approximately $10.5\,\mathrm{m\,s^{-1}}$ to $11.1\,\mathrm{m\,s^{-1}}$ with a standard deviation of $0.21\,\mathrm{m\,s^{-1}}$.

Both ranges of normal impact speeds are narrow as a proportion of their absolute value, with the Adult headform data narrower than the Child headform data. Consequently a regression performed with this data is unlikely to provide useful results about the influence of impact speed on the value

of the IRF. The results of a regression seeking an estimate for the effect of impact speed, particularly one using the Adult headform data, should therefore be treated with caution.

Headform stopping distance

The stopping distance of the test is the maximum displacement of the headform in the normal direction. This data was calculated by assuming that the rotational motion of the headform could be determined from the linear accelerometers as described in Section 3.4. The distribution of the data for the stopping distance was shown in Figure 3.17 on page 59.

The stopping distance data has a wider range than the impact velocity data and this wider range occurs for both headform sizes. Consequently, this data is more likely to provide results that confirm the theory developed for the relationship of the stopping distance on the value of each of the IRFs than the impact velocity data.

Coefficient of restitution

The distribution of the coefficient of restitution was shown in Figure 3.18 on page 61 and described in Table 3.7. Like the impact velocity data, this data is also narrowly distributed and so is unlikely to yield useful results in the regression,and the results relying on this information for an estimate of the effect of coefficient of restitution should also be treated with caution.

5.4 Linear regression of test data for each IRF

The linear least squares regression of Equation (5.16) is used for each of the IRFs using the data described. The computer program R (R Development Core Team, 2010) was used to perform each regression. The coefficients obtained by the regressions are compared with the predicted coefficients that were shown in Table 5.1.

Table 5.6: Results from regression of $\log(\text{HIC}) \sim p + n\log(S) + m\log(V) + q\log(R+1)$.

	Predicted	Estimate	95% CI
	Child Headform		
Intercept		-9.5	$(-11.5, -7.6)$
$\log(S)$	$\mathbf{-1.5}$	-1.8	$(-1.9, -1.6)$
$\log(V)$	**4**	4.9	$(4.1, 5.7)$
$\log(R+1)$	**1**	0.5	$(-0.4, 1.3)$
	Residual standard error: 0.25		
	Adult Headform		
Intercept		-16.4	$(-24.8, -8.0)$
$\log(S)$	$\mathbf{-1.5}$	-1.9	$(-2.2, -1.6)$
$\log(V)$	**4**	7.7	$(4.2, 11.1)$
$\log(R+1)$	**1**	1.1	$(-0.2, 2.4)$
	Residual standard error: 0.32		

The residual standard error is used to determine the goodness of fit of each regression model. The residual standard error is equal to $\sqrt{\frac{SSE}{df}}$, where SSE is the sum of squared errors and df is the number of degrees of freedom.

5.4.1 HIC

The results of the regression of Equation (5.16) for the HIC IRF with each headform size are shown in Table 5.6. The table shows the 95% confidence interval for the coefficients of each parameter used in the regression. The coefficient of the impact velocity is steeper than the expected value, especially for the Adult headform. The coefficient for the stopping distance is also steeper (in a negative sense) for both headform sizes than the expected value of -1.5. The confidence interval of the coefficient of $\log(R+1)$ includes the value 1 for both headforms, although its range is broad.

Difference between the predicted and obtained regression coefficients

The theoretical coefficients for the impact velocity and stopping distance are outside the confidence intervals of the coefficients obtained from the regression. A plausible explanation for this difference in coefficients is the

variation of the pulse shapes in the data set. The pulse shapes used to develop the theory are less complex than the pulse shapes in the real data.

The analytical acceleration pulse shapes considered in Chapter 4 all contained just one peak in the acceleration. This compares with the acceleration pulse shapes from the real data which can have multiple peaks in the acceleration pulse and multiple zones of increasing and decreasing acceleration. An example of such a test with multiple peaks in the acceleration was shown in Chapter 3 in Figure 3.29 on page 69.

With the analytical pulse shapes, the impact velocity contributes exclusively to the creation of a single peak in acceleration, and the stopping distance is an exclusive parameter resulting from that single peak in acceleration. Furthermore, each IRF is evaluated in the neighbourhood of this single peak in acceleration. When multiple peaks exist, then these exclusivity assumptions valid for the analytical pulse shapes do not necessarily hold.

Consider, for instance, the example test from Chapter 3 (21050701) which has multiple peaks in the acceleration. In this test there are three notable features.

1. Figure 3.19 on page 62 shows that the window of evaluation of the HIC for this test is concentrated only around the main peak in the acceleration. The second peak in this case does not influence the value of the HIC.

2. Some of the impact velocity must be absorbed by the structure to generate this second peak. This means that some of the impact velocity is not being considered in the evaluation of the HIC for this test.

3. Figure 3.15 on page 57 shows that the stopping distance for this test occurs at approximately 12 ms into the impact; that is, coinciding with the second peak in acceleration.

Consequently, because of the secondary peak in this example test: the impact velocity is higher than would be predicted by the value of HIC, and the headform stopping distance is higher than would be predicted by the value of HIC. Many tests in the data set have a secondary peak in acceleration.

Kerkeling et al. (2005) described the physical mechanisms that generated these pulse shapes with a larger primary acceleration peak and a later sec-

ondary, less substantial, acceleration peak. The primary acceleration peak is due to the active mass of the bonnet that must be accelerated in the initial phase of the impact. The later peak is due to the stiffness of the structure.

These tests influence the coefficients found from the regression. In Figure 5.6 the effect that additional impact velocity and stopping distance, that is not accounted for in a single peak in acceleration, have on the regression coefficients is shown.

When additional impact velocity and stopping distance are present in an impact then the slopes of the regression lines are steeper. This provides a possible explanation for the difference between the coefficients obtained from the regression and the coefficients predicted by the theory.

The results of the regression in Table 5.6 show, for both headforms, that the coefficients for impact velocity and stopping distance, have steeper values than those predicted by the theory. As a result, the values of the coefficients obtained for the regression, while not quite the values predicted by the theory, are reasonable given that the real pulses differ from the theoretical pulses used to derive the theory.

Differences between headforms

The 95% confidence interval for the coefficient of $\log(V)$ in Table 5.6 is wider for the Adult headform than for the Child headform. This is because the range in the impact velocity data for the Adult headform is smaller than that for the Child headform. As such, the estimate of the coefficient value of $\log(V)$ for the Child headform is more reliable than it is for the Adult headform.

Magnitude of the effect of the pulse shapes in the test data

The results in Table 5.6 also show the residual standard error of the regression. 68% of the residual errors exist within a range of twice the standard error and 95% exist inside a range of four times the residual standard error. Twice the residual standard error is 0.5 for the Child headform and 0.6 for the Adult headform while four times the residual standard error in these

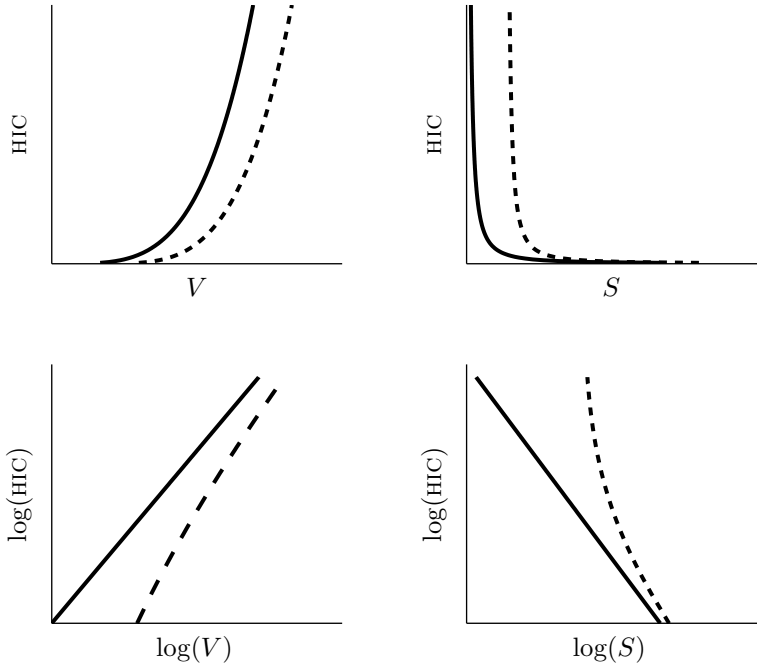

(a) Impact velocity. **(b)** Stopping distance.

Figure 5.6: Effect of (a) additional velocity and (b) additional stopping distance on the value of the regression coefficients. The upper graphs show, with a solid line, the data predicted by the theory. The dotted line shows the same data with a a small constant added to simulate the effect of additional impact velocity or stopping distance. The lower figures show the same data plotted on a logarithmic scale. The dotted line, on the logarithmic scale, has a steeper slope than the solid line for both the velocity and stopping distance.

regressions is 1.0 for the Child headform and 1.3 for the Adult headform. This range can be interpreted as the range of the variability of log(HIC) that is not explained by the effect of impact velocity, headform stopping distance and coefficient of restitution.

A main contributor to this variability is the pulse shapes in the real data. In Table 5.5 the range of $\log(\Lambda)$ for the theoretical pulse shapes was estimated as 0.8. The range estimated by the regression is close to the range suggested by the theoretical data. This means that most of the unexplained variability of log(HIC) can be attributed to the effect of the pulse shape.

Independent effect of each regressor

The effect of each regressor can be examined independently. Equation (5.16) is rearranged so that, in turn, each predictor is separate from other parameters. For example, the log of stopping distance can be separated from the other predictors as is shown in the following equation.

$$\log(S) \sim \log(\text{HIC}) - 4\log(V) - \log(R+1) \tag{5.17}$$

Both sides of this equation are shown in Figure 5.7(a).

A similar separation is shown for the stopping distance and coefficient of restitution in Equations (5.18) and (5.19) and in Figures 5.7(b) and 5.7(c) respectively.

$$\log(V) \sim \log(\text{HIC}) + 1.5\log(S) - \log(R+1) \tag{5.18}$$

$$\log(R+1) \sim \log(\text{HIC}) - 4\log(V) + 1.5\log(S) \tag{5.19}$$

Table 5.7 shows the coefficients of a regression of HIC adjusted for impact velocity and coefficient of restitution as was expressed in Equation (5.17). The effect of stopping distance remains steeper than that predicted by the theory. This difference remains as a result of the difference in pulse shapes used in the theory and those found in the data set.

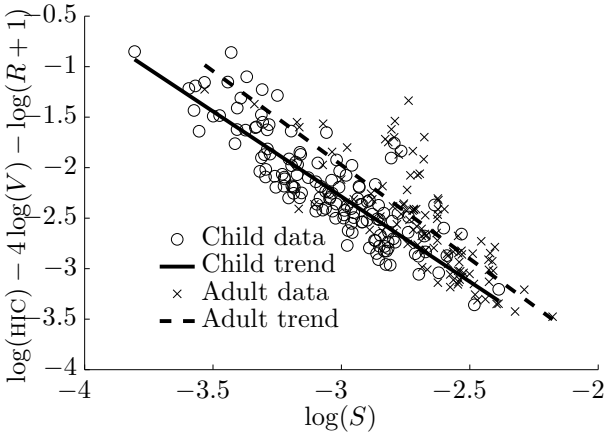

(a) Stopping distance

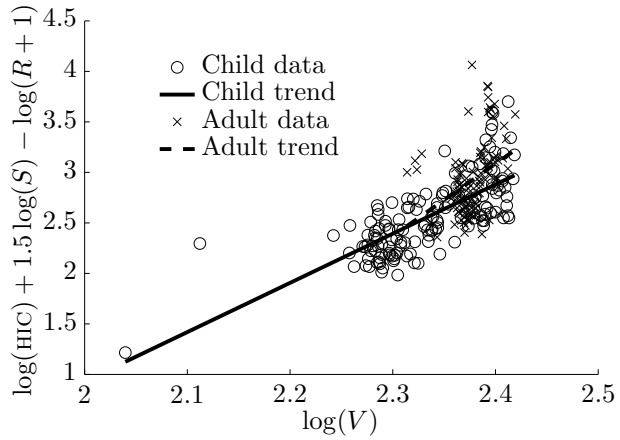

(b) Impact Velocity

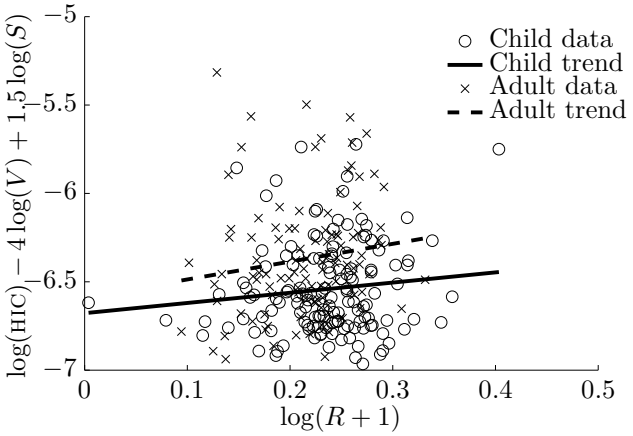

(c) Coefficient of restitution

Figure 5.7: Independent effect of each regressor for HIC adjusted for the effect of the other regressors.

Table 5.7: Results from regression of $\log(\text{HIC}) - 4\log(V) - \log(R+1) \sim p + n\log(S)$.

	Predicted	Estimate	95% CI
	Child Headform		
Intercept		-7.3	$(-7.9, -6.8)$
$\log(S)$	$\mathbf{-1.5}$	-1.7	$(-1.9, -1.5)$
	Residual standard error: 0.26		
	Adult Headform		
Intercept		-7.6	$(-8.3, -6.8)$
$\log(S)$	$\mathbf{-1.5}$	-1.9	$(-2.1, -1.6)$
	Residual standard error: 0.32		

5.4.2 PVP

The results of the regression for the PVP are shown in Table 5.8. The coefficient of the log of the stopping distance, n_j, is expected to be -1, the coefficient of the log of impact velocity is predicted to be 3 and the coefficient for the log of $(R+1)$ is predicted to be about 1.

As was the case for the regression with HIC, the coefficients obtained from the regression of the experimental data with PVP are steeper for both the impact velocity and stopping distance than is predicted by the theory. The

Table 5.8: Results from regression of $\log(\text{PVP}) \sim p + n\log(S) + m\log(V) + q\log(R+1)$.

	Predicted	Estimate	95% CI
	Child Headform		
Intercept		-5.3	$(-7.7, -3.0)$
$\log(S)$	$\mathbf{-1}$	-1.2	$(-1.4, -1.0)$
$\log(V)$	$\mathbf{3}$	4.6	$(3.7, 5.5)$
$\log(R+1)$	$\mathbf{1}$	1.2	$(0.1, 2.2)$
	Residual standard error: 0.30		
	Adult Headform		
Intercept		-7.3	$(-15.6, 1.0)$
$\log(S)$	$\mathbf{-1}$	-1.3	$(-1.6, -1.0)$
$\log(V)$	$\mathbf{3}$	5.4	$(2.0, 8.9)$
$\log(R+1)$	$\mathbf{1}$	0.5	$(-0.8, 1.8)$
	Residual standard error: 0.32		

Table 5.9: Results from regression of $\log(\text{PVP}) - 3\log(V) - \log(R+1) \sim p + n\log(S)$.

	Predicted	Estimate	95% CI
	Child Headform		
Intercept		-1.5	$(-2.1, -0.8)$
$\log(S)$	$\mathbf{-1.0}$	-1.2	$(-1.4, -0.9)$
	Residual standard error: 0.31		
	Adult Headform		
Intercept		-1.5	$(-2.3, -0.8)$
$\log(S)$	$\mathbf{-1.0}$	-1.3	$(-1.6, -1.0)$
	Residual standard error: 0.32		

reason for this can also be shown using the example test. Figure 3.21 shows that the PVP occurs about 4 ms after the start of the impact. This is well before the secondary peak in acceleration at 12 ms, where a less substantial peak in the PVP occurs. Less substantial peaks like these were not considered in the theoretical data.

In Table 5.3$\Lambda_{s,\text{PVP}}$ was shown to be proportional to $(R+1)$. There is no evidence in this data set to refute this theoretical claim.

95% of the residuals lie within 1.2 for the Child headform tests and within 1.3 for the Adult headform tests. These are very similar to the estimated range of $\log(\Lambda_{i,\text{PVP}})$ from the analytical pulse shapes in Table 5.5.

Figure 5.8 shows the effect of stopping distance, impact velocity and coefficient of restitution on the PVP, adjusted for the effect of the other regressors, in a similar way to that shown for HIC previously.

Table 5.9 shows the coefficients of the regression of PVP adjusted for impact velocity and coefficient of restitution with stopping distance. The predicted value for the coefficient is included in the confidence interval for each headform size.

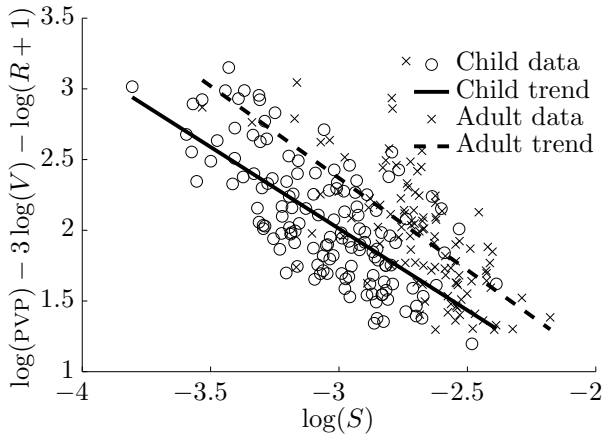

(a) Stopping distance

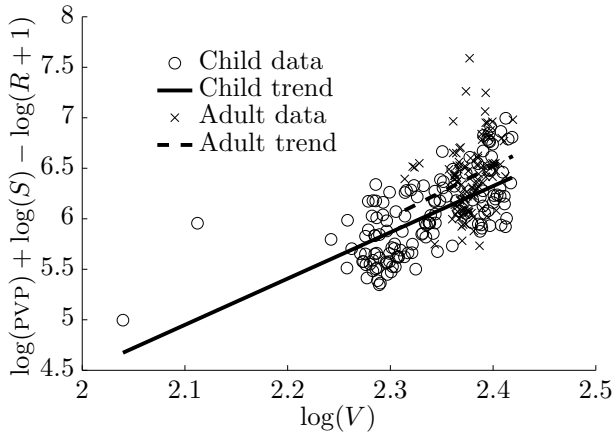

(b) Impact Velocity

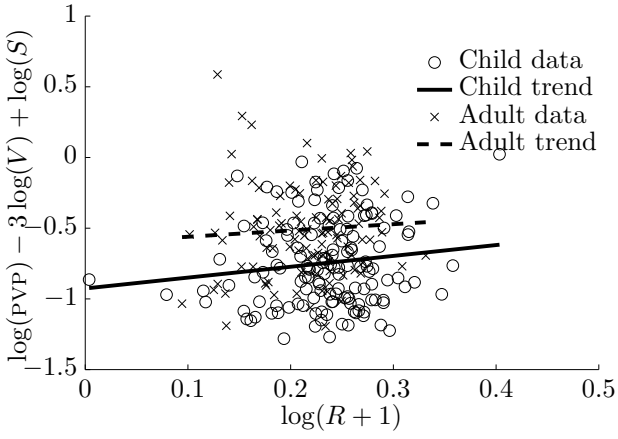

(c) Coefficient of restitution

Figure 5.8: Independent effect of each regressor for PVP adjusted for the effect of the other regressors.

5.4.3 Peak acceleration

The results of the regression for the peak acceleration are shown in Table 5.10.

Both results show the effect of stopping distance is similar to that predicted by the theory. Both include the predicted value inside the confidence interval. The Adult headform's coefficient of $\log(S)$ is steeper than the predicted value of 1. The Child headform's coefficient is shallower than the predicted value. Both include the predicted value inside the confidence interval, however. The Adult headform's coefficient of $\log(V)$ is steeper than the predicted value of 2 while the Child headform's coefficient is shallower than the predicted value.

Figure 5.9 shows the effect of stopping distance, impact velocity and coefficient of restitution on the a_m, adjusted for the effect of the other regressors.

Table 5.11 shows the regression of the stopping distance with the a_m adjusted for impact velocity (coefficient of restitution is predicted to not have an effect on the a_m). The expected value of the coefficient of log of stopping distance lies within the confidence interval of the regression.

Table 5.10: Results from regression of $\log(a_m) \sim p + n\log(S) + m\log(V) + q\log(R+1)$.

	Predicted	Estimate	95% CI
	Child Headform		
Intercept		-1.0	$(-2.5, 0.5)$
$\log(S)$	$\mathbf{-1}$	-0.9	$(-1.0, -0.7)$
$\log(V)$	**2**	1.6	$(1.0, 2.2)$
$\log(R+1)$	**0**	-0.2	$(-0.9, 0.4)$
	Residual standard error: 0.19		
	Adult Headform		
Intercept		-4.0	$(-9.4, 1.3)$
$\log(S)$	$\mathbf{-1}$	-1.1	$(-1.3, -1.0)$
$\log(V)$	**2**	2.6	$(0.4, 4.8)$
$\log(R+1)$	**0**	-0.6	$(-1.4, 0.2)$
	Residual standard error: 0.21		

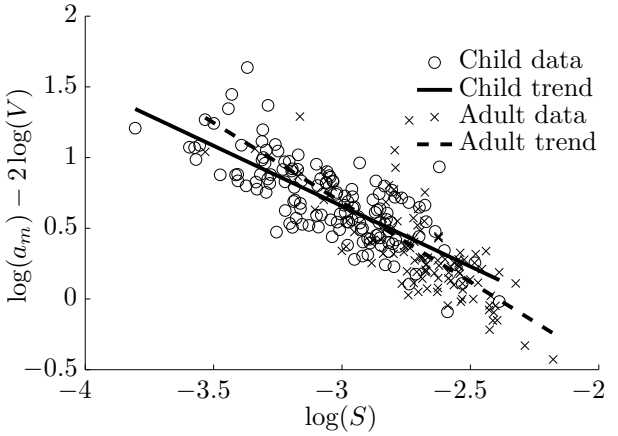

(a) Stopping distance

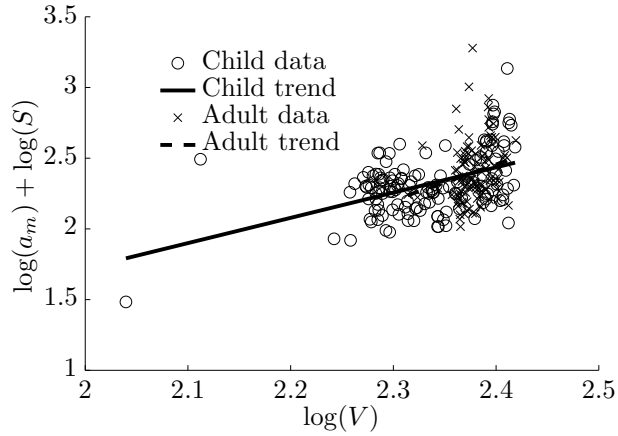

(b) Impact Velocity

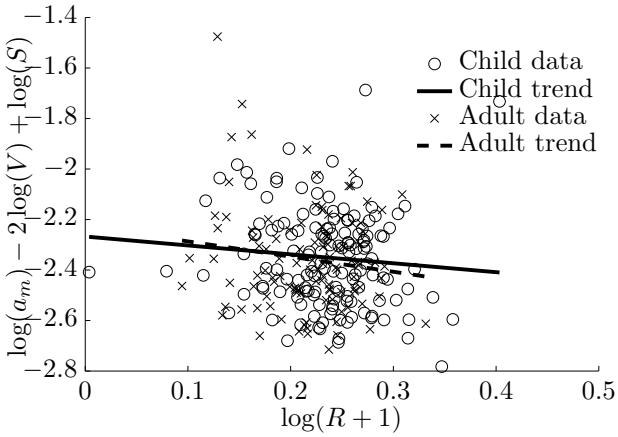

(c) Coefficient of restitution

Figure 5.9: Independent effect of each regressor on a_m adjusted for the effect of the other regressors.

Table 5.11: Results from regression of $\log(a_m) - 2\log(V) \sim p + n\log(S)$.

	Predicted	Estimate	95% CI
	Child Headform		
Intercept		-1.9	$(-2.3, -1.5)$
$\log(S)$	$\mathbf{-1.0}$	-0.9	$(-1.0, -0.7)$
	Residual standard error: 0.19		
	Adult Headform		
Intercept		-2.7	$(-3.2, -2.2)$
$\log(S)$	$\mathbf{-1.0}$	-1.1	$(-1.3, -0.9)$
	Residual standard error: 0.21		

The regression shows that the coefficient of the log of $(R + 1)$ is less than zero with both headform sizes. From Figure 5.3 it was predicted that the slope of the $(R+1)$ would be about zero because many lines had a negligible slope. The confidence interval for these results include this zero value but have a best estimate that is negative. This negative regression coefficient provides some evidence to confirm the finding of the previous chapter that the a_m could encourage the design of structures with a higher coefficient of restitution.

The interval covered by 95% of the residuals is approximately equal to 0.8 for both headforms. This is about the same as the range suggested in Table 5.5. This indicates that the variation in the data can be adequately explained by the pulse shape variation.

5.4.4 3 millisecond clip

The results of the regression for the a_3 IRF is shown in Table 5.12 and the effect of the independent regressors are shown graphically in Figure 5.10.

The coefficient of $\log(S)$ for the Adult headform matches the slope predicted by the theory. For the Child headform the coefficient is shallower than predicted.

Table 5.12 shows that the coefficient of $\log(R + 1)$ is a little greater than zero for both headforms. However, The predicted value is within the range of the confidence interval for both headforms.

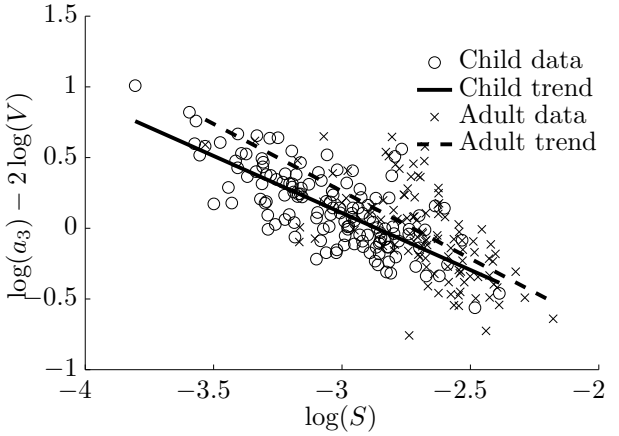

(a) Stopping distance

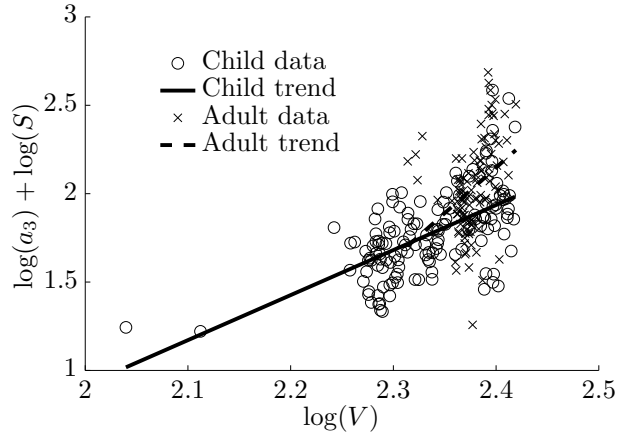

(b) Impact Velocity

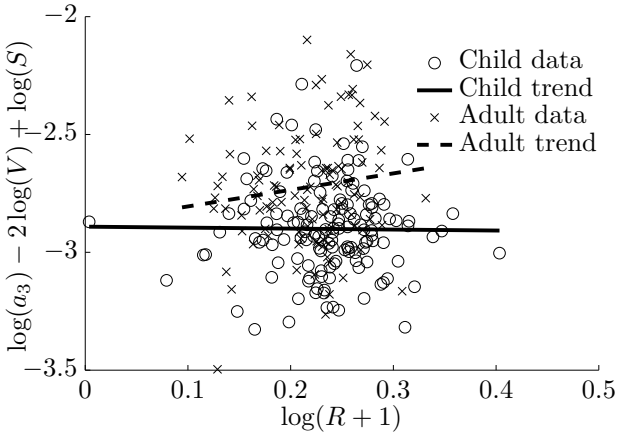

(c) Coefficient of restitution

Figure 5.10: Independent effect of each regressor for a_3 adjusted for the predicted effect of the other regressors.

Table 5.12: Results from regression of $\log(a_3) \sim p + n\log(S) + m\log(V) + q\log(R+1)$.

	Predicted	Estimate	95% CI
	Child Headform		
Intercept		-3.6	$(-5.0, -2.1)$
$\log(S)$	$\mathbf{-1}$	-0.8	$(-0.9, -0.7)$
$\log(V)$	**2**	2.5	$(1.9, 3.1)$
$\log(R+1)$	**0**	0.4	$(-0.2, 1.0)$
	Residual standard error: 0.19		
	Adult Headform		
Intercept		-10.6	$(-16.9, -4.2)$
$\log(S)$	$\mathbf{-1}$	-1.0	$(-1.2, -0.8)$
$\log(V)$	**2**	5.3	$(2.6, 7.9)$
$\log(R+1)$	**0**	0.8	$(-0.2, 1.7)$
	Residual standard error: 0.24		

Table 5.13: Results from regression of $\log(a_3) - 2\log(V) \sim p + n\log(S)$.

	Predicted	Estimate	95% CI
	Child Headform		
Intercept		-2.3	$(-2.7, -1.9)$
$\log(S)$	$\mathbf{-1.0}$	-0.8	$(-0.9, -0.7)$
	Residual standard error: 0.19		
	Adult Headform		
Intercept		-2.6	$(-3.2, -2.0)$
$\log(S)$	$\mathbf{-1.0}$	-1.0	$(-1.2, -0.7)$
	Residual standard error: 0.25		

The interval covered by 95% of the residuals is about 0.8 for the Child headform tests and about 1.0 for the Adult headform tests. These are a similar size as the range suggested in Table 5.5 which was found after considering the effect of different pulse shapes and various VSDR values.

The effect of stopping distance on the value of a_3 adjusted for impact velocity and coefficient of restitution is shown in Table 5.13. For the Adult headform the coefficient obtained from the regression is the same as predicted by the theory but for the Child headform the coefficient is shallower than predicted by the theory.

Table 5.14: Summary of data predicted from theory (bold) and obtained from regressions.

IRF	Headform	Coefficients $\log(V)$ m		$\log(S)$ n		$\log(R+1)$ q	
HIC	Child	**4**	4.9	**−1.5**	−1.8	**1**	0.5
	Adult		7.7		−1.9		1.1
PVP	Child	**3**	4.6	**−1**	−1.2	**1**	1.2
	Adult		5.4		−1.3		0.5
a_m	Child	**2**	1.6	**−1**	−0.9	**0**	−0.2
	Adult		2.6		−1.1		−0.6
a_3	Child	**2**	2.5	**−1**	−0.8	**0**	0.4
	Adult		5.3		−1.0		0.8

5.5 Discussion

In this chapter power functions have been developed from the simple analytical pulse shapes used in Chapter 4. The theory relates the value of an IRF to the impact velocity, stopping distance and coefficient of restitution by the power function shown in Equation (5.20).

$$IRF_j \approx e^{p_j}(R+1)^{q_j}\,(V)^{m_j}\,(S)^{n_j} \tag{5.20}$$

The indices of the impact velocity, stopping distance and coefficient of restitution were predicted for each IRF based on the analytical pulses used to develop the theory. The logarithm of the power function was taken so each power function could be evaluated using a linear least squares regression with the test data used throughout this thesis. As a result the indices become coefficients and these coefficients indicate the slope of the regression line. Table 5.14 summarises the predicted indices and the regression coefficients obtained in this chapter for each of the IRFs.

Because of the limited range in the data for impact velocity and coefficient of restitution, the effect of these parameters should be considered with more caution than is given to the estimated effect of stopping distance.

5.5.1 Interpretation of the coefficients predicted with the theory and obtained from the regression

The negative value for the coefficient of $\log(S)$ shows that a softer bonnet — one that has allows a greater stopping distance — generally results in a lower value of an IRF than a bonnet that is stiffer. This negative value has been confirmed by the empirical data. The empirical data has a negative value for each of the IRFs and not just the HIC.

The positive value for $\log(V)$ shows that an impact with a higher impact velocity will result in a higher IRF value. This increase is greater for HIC than for the other IRFs.

For the HIC and the PVP the empirical regression has shown that decreasing the structure's coefficient of restitution will improve the crashworthiness of the structure. This is because the coefficient of $\log(R+1)$ is positive as was predicted in the previous chapter. The evidence in this chapter also suggests that an increase in the coefficient of restitution may reduce the value of the a_m. These regression coefficients are similar to the results of the previous chapter, particularly the result that suggests that the use of the a_m IRF may encourage designs that dissipate less of the energy of the impact.

The residual variation in the data is adequately explained by the variation in acceleration pulse shapes. The range of this variation was similar to the theoretical pulse shapes range for the HIC, PVP and a_m IRFs. The range of this variation found in the regression for the a_3 was larger than expected from the theoretical pulse shapes. The type of pulse shapes that cause this variation in the regression results will be shown in Chapter 7.

There were differences between the coefficients predicted by the theory and the coefficients obtained from the regression. It was shown, with an example, that a likely explanation for these differences are the differences between the pulse shapes used to derive the theory and the pulse shapes found in the data set. Each analytical pulse shape contained only one peak in the acceleration. The real pulse shapes, on the other hand, contain many peaks in the acceleration. These multiple peaks can decrease the value of the IRF while maintaining their impact velocity and stopping distance values. As a

result, the coefficients for the impact velocity and stopping distance both have steeper slopes than predicted by the theory.

In this data set the impact velocity was changed only by the different angles of the hoods relative to the firing angle. Consequently, a design that is angled further from the perpendicular to the firing angle of the test condition will have a lower IRF value than a bonnet that is angled nearer to the perpendicular of the firing angle because the impact velocity is slower. The effect of changing the bonnet angle is amplified for the HIC compared with the other IRFs because it has the highest coefficient of $\log(V)$. As a result, a change in angle alters the value of the HIC more than it alters the value of the other IRFs. Alternatively, in a scenario where the impact speed can be managed as part of the design process (such as in a full scale impact test with a restrained occupant) a reduction in impact speed would be treated more favourably by the HIC than by the other IRFs.

Practically speaking, a designer would need to be aware of the difference between the coefficients obtained from the theoretical analysis and the coefficients obtained from the empirical analysis. If the design is being assessed with HIC, the empirical analysis shows a lesser increase in stopping distance is required in a practical design to lower the tested value of HIC than is evident from the theoretical analysis. This is also the case for designs being assessed with PVP, but is not necessarily the case for designs being assessed with a_3 or with a_m.

These results have implications for the question, how would the ultimate design of a structure be influenced by the particular form of the IRF that is used to assess it. In this chapter all the IRFs encourage designs where the impact velocity is low, and all encourage designs where the stopping distance is as large as possible. In this sense, the ultimate design, when assessed by any of the IRFs, will have a stopping distance that is as large as possible. In addition, if the impact velocity can be modified by the design, then this will be lowered as far as possible for the ultimate design. It is likely that the ultimate design will also have a low coefficient of restitution. This is unless it is being assessed with the a_m in which case a slight increase in coefficient of restitution could be advantageous. But, as was shown in the previous chapter, this peculiar result for the a_m may only be relevant when considering front loaded pulse shapes. Consequently, the evidence in

this chapter suggests that the ultimate design will not change greatly if any one of the IRFs is used as the assessment tool.

5.5.2 Context

In the previous chapter, similarities between the different IRFs were shown with theoretical pulse shapes. In this chapter a theoretical model of the expected value of an IRF was constructed from these theoretical pulse shapes and this model was tested with empirical data. After testing the theoretical model with the empirical data the similarities between the IRFs have been confirmed. The value of the IRFs increases as the impact velocity increases and their value decreases as the stopping distance increases.

Now that the similarities between the IRFs have been established, it is valuable to consider the differences among the IRFs. In particular, it is worth considering those tests which would be considered to be crashworthy with one IRF and not crashworthy with another.

Looking ahead in this thesis, the theoretical model developed in this chapter will provide a useful method of critically examining those tests with dissimilar crashworthiness measurements when they are evaluated with different IRFs. In the next two chapters the extent of the similarities among the various IRFs will be examined and then the differences among the IRFs for the specific pulse shapes will be shown.

Chapter 6

Quantification of the similarities between four IRFs

6.1 Introduction

In this chapter, the test data are evaluated using the four linear acceleration based IRFs, the results of which allow these IRFs to be compared with each other. The IRFs are compared in several ways.

1. In Section 6.2 the IRF values are compared as untransformed data points. The Pearson correlation coefficient is used to quantify the association among the IRFs.
2. In Section 6.3 the tests are dichotomised into 'safe' and 'unsafe' according to criteria formed with each of the IRFs. These are then compared to the threshold HIC = 1000.
3. In Section 6.4 the tests are ranked according to the value of each IRF. The rankings according to each IRF are compared.

The rank correlation method invites the effect of pulse shape to be studied more closely. The contribution of pulse shape to the value of the IRF for each test is found and investigated in Section 6.5.

The chapter focuses on the collected data using the tests performed with each headform in separate groups. Individual tests are not the focus of this chapter because these are examined in Chapter 7.

Whilst not the focus of this thesis, a short discussion comparing these linear acceleration based IRFs with two rotational acceleration based IRFs is provided in Appendix D. These are not discussed here because of the limitations associated with that data, as detailed in the Appendix.

6.2 Comparison among IRFs using test data

A usual first step when examining related data, is to cross plot the data and determine the Pearson correlation coefficient so that the relationship between the values of each measured variable can be quantified. In this section the relationship between each pair of IRFs is quantified.

Figures 6.1 and 6.2 contain cross plots of HIC_∞, PVP, a_3 and a_m for all tests with the Child headform and the Adult headform respectively.

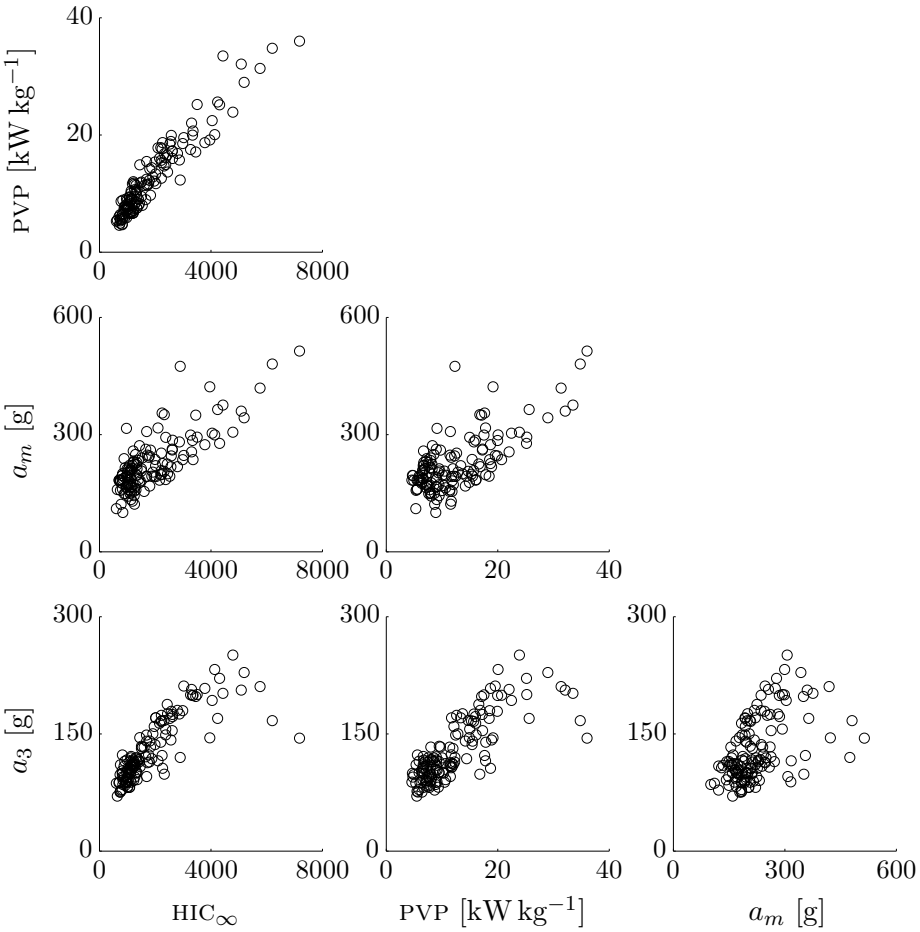

Figure 6.1: Cross plots of HIC$_\infty$, PVP, a_3 and a_m for all 139 tests with the Child headform.

Table 6.1: Square of Pearson correlation coefficients (r^2) of cross plots shown in Figure 6.1.

	HIC$_\infty$	PVP	a_m
PVP	0.9074		
a_m	0.6450	0.5036	
a_3	0.6691	0.6282	0.2628

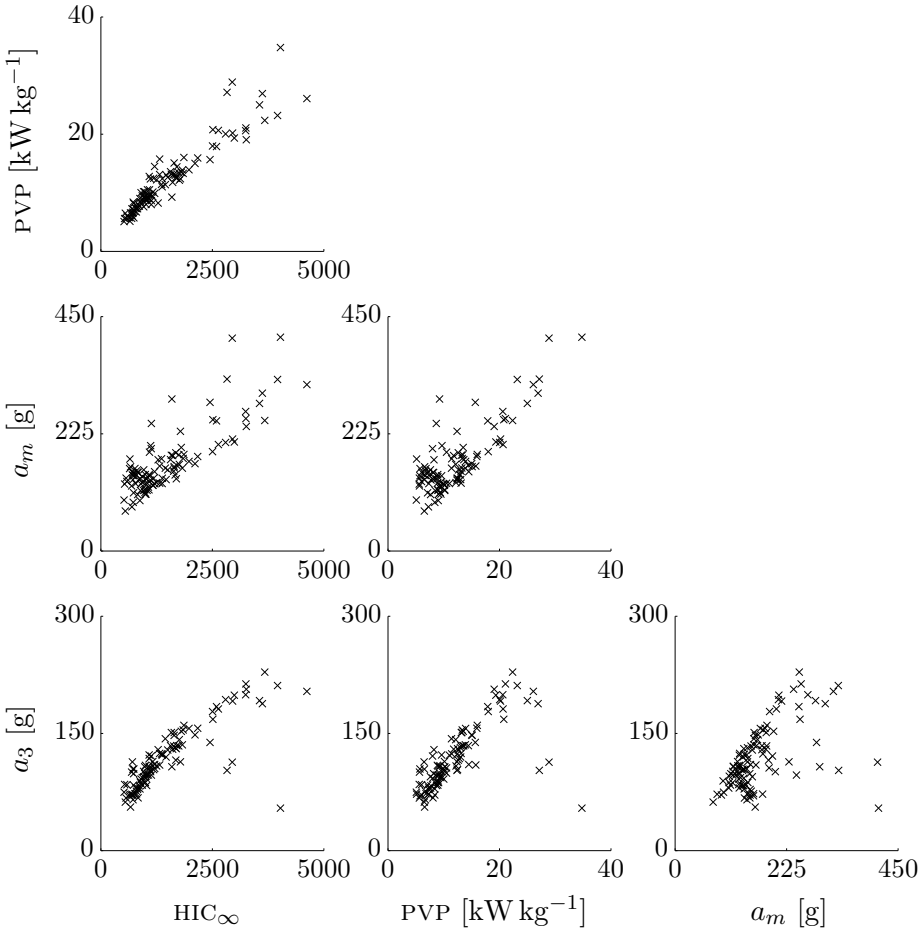

Figure 6.2: Cross plots of HIC$_\infty$, PVP, a_3 and a_m for all 108 tests with the Adult headform.

Table 6.2: Square of Pearson correlation coefficients (r^2) of cross plots shown in Figure 6.2.

	HIC$_\infty$	PVP	a_m
PVP	0.8865		
a_m	0.6889	0.6774	
a_3	0.6666	0.4764	0.2632

The HIC_{∞} (without a restriction in evaluation window size) is used instead of the HIC_{15} because, as shown in Appendix C, there is negligible difference between these in this data set.

Tables 6.1 and 6.2 show the square of the Pearson correlation coefficient for the tests with the Child and Adult headforms respectively. All the correlations are positive and statistically significant ($p < .001$). The positive correlations are expected because each IRF has a negative relationship with stopping distance and a positive relationship with impact velocity (See Chapter 4).

The square of the correlation coefficient for each pair of IRFs is similar for each headform size. The HIC and PVP have the highest correlation while the a_m and a_3 have the lowest correlation.

6.3 Dichotomous classification of tests into 'safe' and 'unsafe' categories using criteria formed with each IRF.

In this section, the data are examined by considering whether tests results satisfy criteria for being considered 'safe', in that they have a value that is less than a threshold for an IRF, or whether the test results fail those criteria and are hence considered 'unsafe'. This is particularly important in regulatory testing where it is critical to accurately determine the status of a structure; because if it is found to be 'unsafe' then its certification for use or sale within a jurisdiction should be withheld.

The combination of an IRF and a threshold for that IRF, together, form a criterion. The threshold used with the HIC_{15} IRF for the Euro NCAP test protocol (under which these data were collected) is $\text{HIC}_{15} = 1000$. An impact that occurs at $\text{HIC} = 1000$ is estimated to equate to a 16% probability of fatal injury (Prasad and Mertz, 1985). Tests with $\text{HIC}_{15} > 1000$ are considered 'unsafe'. In Appendix C it is shown that there were no tests with both $\text{HIC}_{15} < 1000$ and $\text{HIC}_{\infty} > 1000$, so the criteria of $\text{HIC}_{\infty} > 1000$ and $\text{HIC}_{15} > 1000$ are identical in this data set. An alternative criterion

Table 6.3: Contingency table $IRF1 > x$ and $IRF2 > y$.

		$IRF1 > x$ (*Reference criterion*)		*Total*
		Safe	Unsafe	
$IRF2 > y$	Safe	a	b	$a + b$
	Unsafe	c	d	$c + d$
Total		$a + c$	$b + d$	$a + b + c + d$

might simply be a different threshold for HIC, such as $\text{HIC}_\infty > 1700$; or it might use a different IRF such as $a_3 > 80\,\text{g}$.

In this section, alternative criteria using the other IRFs are compared with a HIC > 1000 reference criterion using the data described in Chapter 3 using the results obtained from contingency tables. Comparisons between criteria other than HIC > 1000 are not investigated as the primary objective was to examine how a change in criterion from HIC > 1000 would influence the fail/pass assessment of the tests. The data were collected to be examined with this criterion, and it is appropriate to compare the other criteria to this. This method of comparison can be adopted for other data, perhaps using a different base criterion, as appropriate for that data.

An example contingency table, using $IRF1 > x$ and $IRF2 > y$ as criteria, is shown in Table 6.3. The table is populated with $a + b + c + d$ tests, each of which has been classified with the two criteria.

In Table 6.3 there are four possible classifications for a test:

- 'safe' & 'safe';
- 'safe' & 'unsafe';
- 'unsafe' & 'safe';
- 'unsafe' & 'unsafe'.

The tests that are 'safe' & 'unsafe' or 'unsafe' & 'safe' are those where the IRF criteria are discordant. The number, and location, of these tests is important. These are the tests that are assessed differently using the respective criteria. In the example table there are b tests considered 'unsafe' by only $IRF1 > x$, and c tests are considered 'unsafe' with $IRF2 > y$ only.

6.3.1 Definition of a conservative criterion

Of particular interest is the threshold of an alternative IRF that is conservative relative to a reference criterion. A conservative criterion is more likely to err toward categorising a test as 'unsafe' when the reference criterion has categorised it 'safe', than to err toward categorising a test as 'safe' when the reference criterion has categorised it 'unsafe'. A conservative criterion could be considered to be at least as effective for safety as the reference criterion because 'unsafe' tests with the reference criterion are unlikely to be categorised as 'safe' with the alternate criterion.

Referring to the categories in Table 6.3, if b is a high number and c is a low number, relative to the number of tests in both a and d, then $IRF1 > x$ is more likely to declare that a test is 'unsafe' than $IRF2 > y$, and thus $IRF1 > x$ is a more conservative criterion. Alternatively, if c is a high number and b is low, relative to the number of tests in a and d, the opposite is the case and $IRF2 > x$ is an anti-conservative criterion.

Four common statistics can be used to determine if the number of tests in b and c, relative to the number of tests in a and d suggest that that $IRF1 > x$ is a more conservative criterion than $IRF2 > y$. These statistics are the sensitivity, specificity, positive predictive value (PPV) and negative predictive value (NPV). Relative to the categorisations made by the criteria $IRF1 > x$, these are defined using the numbers of tests that occur in each of the categories in Table 6.3 (Loong, 2003).

$$\text{Sensitivity} = \frac{d}{b+d} \tag{6.1}$$

$$\text{Specificity} = \frac{a}{a+c} \tag{6.2}$$

$$\text{PPV} = \frac{d}{c+d} \tag{6.3}$$

$$\text{NPV} = \frac{a}{a+b} \tag{6.4}$$

95% confidence interval limits for each of these statistics can be determined using the Wilson score method incorporating continuity correction (Newcombe, 1998).

These common statistics, can be used to help determine a conservative criterion relative to the HIC > 1000 reference criterion.

The sensitivity indicates the probability that the alternative criterion, $IRF2 > y$, simultaneously identifies a test as 'unsafe' when the reference criterion, $IRF1 > x$, has done so. The specificity indicates the probability that the alternative criterion and the reference criterion simultaneously identify a test as 'safe' when the reference criterion has done so. For this analysis, one condition necessary for the alternative criterion to be considered conservative compared with the reference criterion is for the sensitivity to be not less than the specificity.

$$\text{Sensitivity} \geq \text{Specificity} \tag{6.5}$$

The PPV indicates the probability that a test categorised as 'unsafe' with the alternative criterion is also categorised as 'unsafe' with the reference criterion. The NPV indicates the probability that a test categorised as 'safe' with the alternative criterion is also categorised as 'safe' with the reference criterion. A high value of NPV indicates that the alternative criterion is more likely to classify a test as 'unsafe' than the reference criterion. A second condition for the alternative criterion to be considered conservative, relative to the reference criterion, is that the NPV is not less than the PPV.

$$\text{NPV} \geq \text{PPV} \tag{6.6}$$

6.3.2 Conservative criteria compared with HIC>1000

From the 139 Child headform tests in the data set, 29 (26.9%) are considered 'safe' using HIC > 1000, and 38 (35.2%) of the 108 Adult headform tests are considered 'safe'.

The highest threshold value for each of the alternative IRFs that results in a conservative criterion compared with HIC > 1000 for the data sets with each headform is shown in Table 6.4. These are the maximum thresholds where the expressions in Equations (6.5) and 6.6 are true. The contingency tables examining the data at these thresholds are shown in Appendix F.

Table 6.4: Summary of thresholds of each IRF that are conservative compared with HIC > 1000 in the data set of each headform.

Alternative IRF	Headform	Conservative threshold	Sens.	Spec.	PPV	NPV
PVP	Child	$6.6\,\mathrm{kW\,kg^{-1}}$	0.99	0.62	0.91	0.95
	Adult	$8.7\,\mathrm{kW\,kg^{-1}}$	0.94	0.76	0.88	0.88
a_3	Child	81.6 g	0.99	0.21	0.83	0.86
	Adult	95.2 g	0.96	0.79	0.89	0.91
a_m	Child	121 g	1.00	0.07	0.80	1.00
	Adult	126 g	0.94	0.34	0.73	0.76

Also shown in Appendix F is the value of Sensitivity, Specificity, PPV and NPV at each threshold of each alternate IRF.

The thresholds for each IRF are different for the data from the tests with each headform. This captures differences between the headforms (mass and size) and impact conditions (impact angle, and distribution of impact speeds) as well as differences between the structures that are tested by the different headforms.

The specificity is very low for the criteria with the a_m and a_3. This reflects the moderate correlation coefficient between the HIC and these IRFs shown in the previous section. Many more tests are needed to be categorised as 'unsafe' with these alternate criterion than with the reference criterion for the alternate criterion to be considered conservative.

The thresholds found for conservative criteria with each alternate IRF can be compared with the commonly applied thresholds for those IRFs.

As mentioned in Chapter 2, typical threshold for a_m range between $a_m = 150\,\mathrm{g}$ and $a_m = 400\,\mathrm{g}$. The conservative thresholds for a_m, identified in Table 6.4, are both substantially less than these commonly applied thresholds.

Typical thresholds mentioned in Chapter 2, for the a_3 range between $a_3 = 80\,\mathrm{g}$ and $a_3 = 200\,\mathrm{g}$. $a_3 = 80\,\mathrm{g}$ is more conservative than the values shown in Table 6.4, however these values are quite similar.

The PVP does not have a commonly applied threshold. However, the Head Impact Power (HIP) IRF has been studied and estimations of thresholds of

injury have been proposed. In Appendix E the HIP is shown to be closely related to PVP in this data set:

$$\text{PVP} \approx \text{HIP} \div \text{Mass} \tag{6.7}$$

where the mass is the mass of the headform under consideration. Consequently, the thresholds proposed by other authors for HIP can be translated to their equivalent PVP values using this relationship and from there can be compared with the conservative thresholds shown in Table 6.4.

In a study that reconstructed 61 real world accidents Marjoux et al. (2008) determined that HIP = 45 kW resulted in a 50% probability of severe neurological injuries. In the same paper HIC = 1032 was also shown to have a 50% probability of severe neurological injuries. In another study that reconstructed impacts involving American footballers, Newman et al. (2000b) found that HIP = 12.8 kW predicted 50% of Mild Traumatic Brain Injuries and equated this to HIC = 240. Both of these were found using a head mass of 4.5 kg (Marjoux et al. using a finite element model and Newman et al. using a modified Hybrid III dummy head and neck) which has a smaller mass than the 4.8 kg Adult headform. Using the assumption that the PVP and the HIP are related through the headform mass, Equation (6.7) can be used to find that the equivalent values of PVP for those values of HIP are $10\,\text{kW}\,\text{kg}^{-1}$ for the Marjoux et al. (2008) study and $2.84\,\text{kW}\,\text{kg}^{-1}$ for the Newman et al. (2000b) study.

The PVP $= 2.84\,\text{kW}\,\text{kg}^{-1}$ threshold is for a much lower injury severity than is considered for HIC = 1000, so it will not be considered further. The PVP $= 10\,\text{kW}\,\text{kg}^{-1}$ is higher than the thresholds considered conservative in Table 6.4, and thus would not be considered to be a conservative threshold.

The difference between the published thresholds and those that are identified as being conservative highlight one way that the choice of IRF can be important in a test protocol. The threshold chosen to accompany the IRF can have a strong influence on the designs that are classified as 'safe'. If the criterion set for a test protocol is too lenient, for example using a_m equal to 300 g or 400 g as a criterion in the Euro NCAP test protocol, then the expectation arising for impact protection will be lower than with a criterion with more stringent requirements. An inappropriate selection of the thresh-

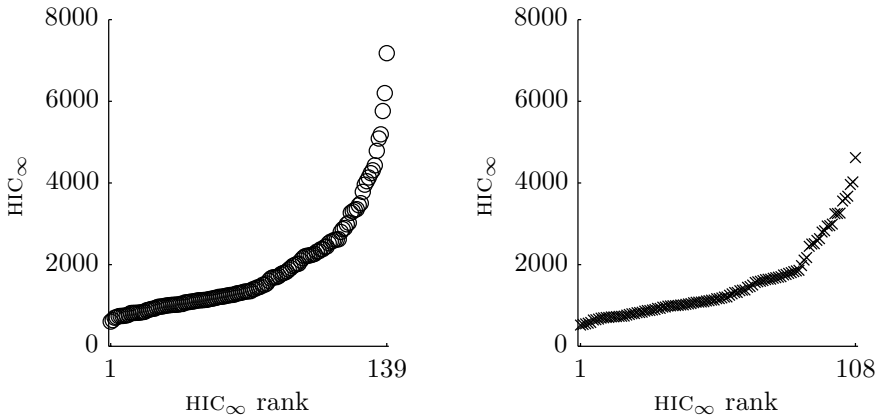

(a) Tests with Child headform **(b)** Tests with Adult headform

Figure 6.3: Rank and value of HIC_∞ for each test.

old can change the target that is set for 'safety'. It is important that the criterion used in a test protocol is set on the basis of biomechanical evidence.

6.4 Comparison among IRFs using ranked test data

A third way to examine the results of a test is to consider that test relative to all other tests in the data set. This can be done by considering the ranking of each test according to its crashworthiness with each IRF. After ranking, each test is either more crashworthy (with a lower rank) or less crashworthy (with a higher rank) than every other test in the data set. This removes the non-linearity that the correlation of the non-ranked data had in Section 6.2. In addition, it removes any implied relationship with injury that a value of each might have.

Figures 6.3, 6.4, 6.5 and 6.6 show, for each headform size, the relationship between the rank and the value of each test assessed using the HIC_∞, PVP, a_m, and a_3.

The rank-ordered data for one IRF can be correlated with rank-ordered data for the other IRFs. The cross plots of the ranked data for each pair of IRFs for Child headform tests is shown in Figure 6.7. The Spearman rank cor-

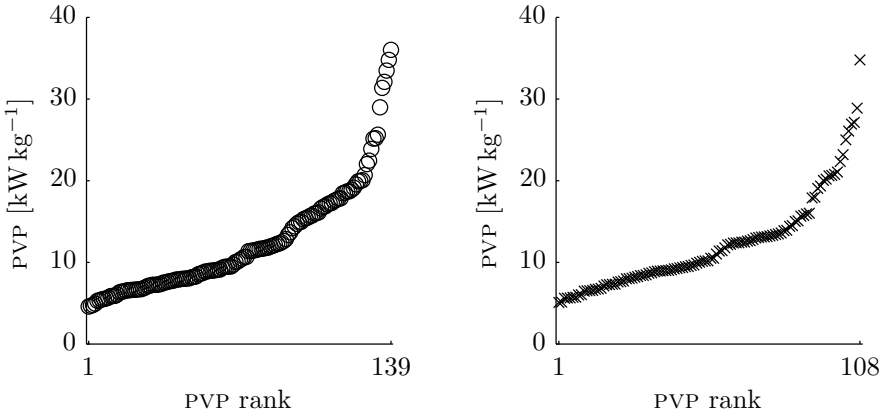

(a) Tests with the Child headform **(b)** Tests with the Adult headform

Figure 6.4: Rank and value of PVP for each test.

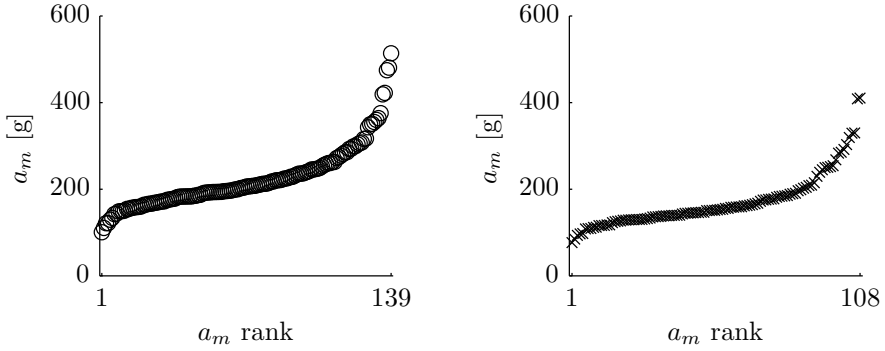

(a) Tests with the Child headform **(b)** Tests with the Adult headform

Figure 6.5: Rank and value of a_m for each test.

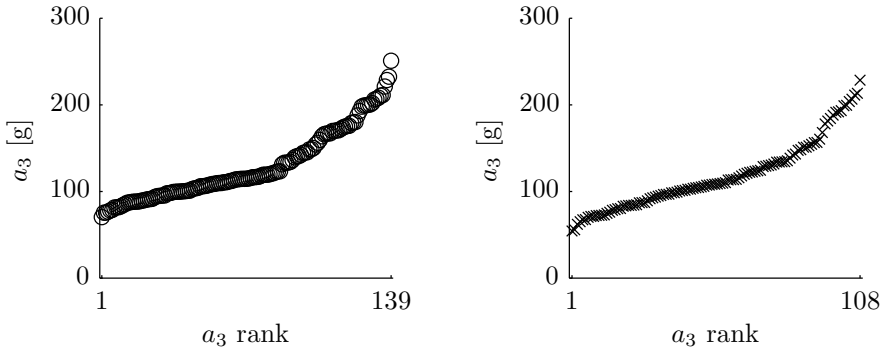

(a) Tests with the Child headform **(b)** Tests with the Adult headform

Figure 6.6: Rank and value of a_3 for each test.

relation coefficients, ρ, for each pair of ranked data is shown in Table 6.5. Similarly, Figure 6.8 and Table 6.6 show the cross plots of ranks and Spearman correlation coefficients for the Adult headform tests evaluated for each IRF.

Figures 6.7 and 6.8 illustrate the general positive agreement between the rankings assigned by each IRF. All associations are statistically significant ($\rho > 0.326$ implies $p < .001$ when there are more than 100 data points (Zar, 1972)). A positive correlation is expected because of the positive correlation shown in Section 6.2. This in turn is due to the association of each IRF with the headform stopping distance, impact velocity and coefficient of restitution.

The value of the correlation coefficient of each pair of IRFs is similar for both headform sizes. Notably, the a_m IRF is least correlated with the other IRFs. This shows the emphasis that other IRFs place on the peak value of acceleration is small.

Ranking the data emphasises the similarities between the various IRFs and does this without referring to the scale of the IRFs determined by the absolute values of each IRF. Elimination of the scale from the data allows the data to be analysed without reference to the probability of injury, or any other interpretation of the scale. This data shows that the ranking of crashworthiness of two structures is likely to be maintained when the ranking is evaluated by any one of the IRFs shown. Consequently it is a powerful method for analysis in the present context.

The positive correlation shown in this analysis suggests that the choice of available IRFs has a second order effect on the qualitative analysis of the relative safety of one structure compared with another. The difference in stopping distance and impact velocity, and to a lesser extent, coefficient of restitution, are the first order effects on the relative design performance of the impacted structure.

Consequently, the rank correlation of headform stopping distance and each IRF may show that headform stopping distance is, itself, an adequate measure of crashworthiness. Cross plots of the rank of test IRF values with the rank of headform stopping distance of each Child headform test is shown in Figure 6.9. Figure 6.10 shows the same for each Adult headform test.

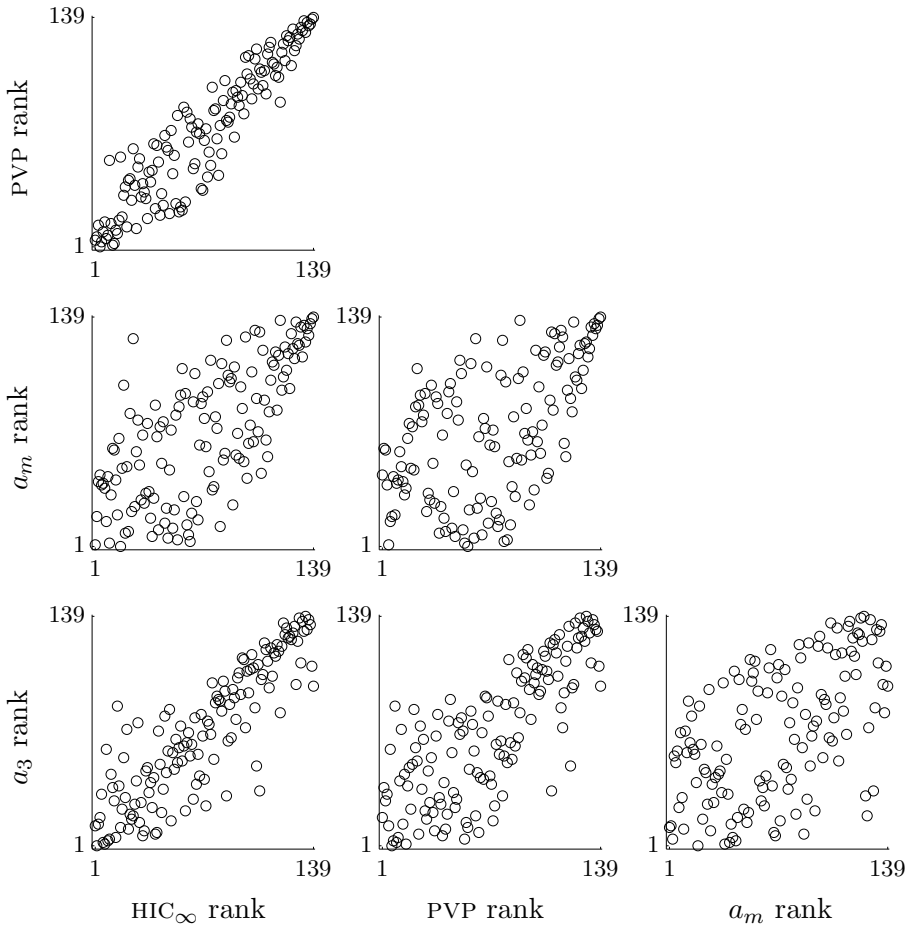

Figure 6.7: Cross plots of HIC$_\infty$ rank, PVP rank, a_3 rank and a_m rank for all 139 tests with the Child headform.

Table 6.5: Spearman (ρ) rank correlation coefficient of cross plots shown in Figure 6.7.

	HIC$_\infty$	PVP	a_m
PVP	0.9286		
a_m	0.7013	0.5529	
a_3	0.8718	0.7886	0.5543

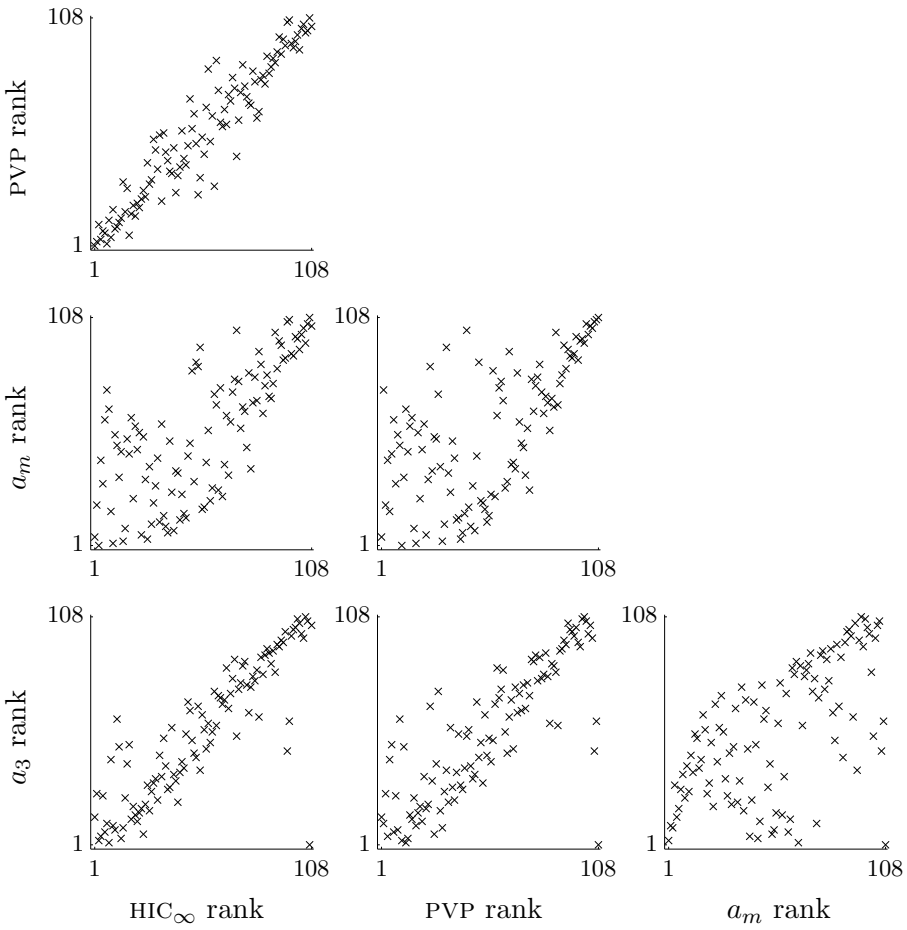

Figure 6.8: Cross plots of HIC$_\infty$ rank, PVP rank, a_3 rank and a_m rank for all 108 tests with the Adult headform.

Table 6.6: Spearman (ρ) rank correlation coefficient of cross plots shown in Figure 6.8.

	HIC$_\infty$	PVP	a_m
PVP	0.9482		
a_m	0.7322	0.6408	
a_3	0.8601	0.8107	0.5980

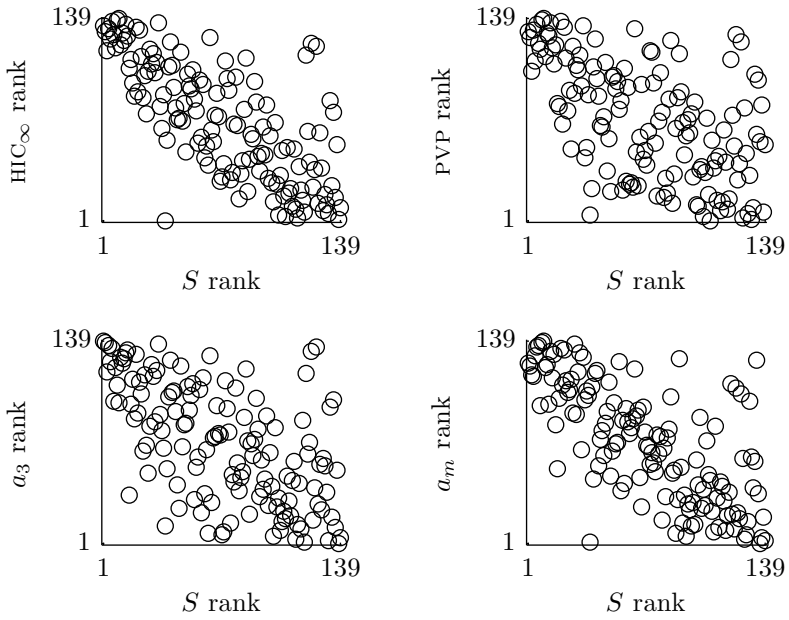

Figure 6.9: Cross plots of the rank of IRF value with rank of stopping distance for all tests with the Child headform.

Table 6.7 shows the Spearman rank correlation coefficients for each of these cross plots. All correlation coefficients are negative and statistically significant and have magnitudes comparable to the correlation coefficients shown in Tables 6.5 and 6.6.

The consequence of the negative correlation between the stopping distance and each IRF is that a structure with a large stopping distance is likely to be considered safer than another structure with a smaller stopping distance, regardless of the IRF that is being used to measure the safety. On the other hand, the correlation coefficient is not high and this is due to the effects such as bottoming out occurring. For instance, a test that bottoms out could have a a high rank for the IRF (ie. be uncrashworthy) because of a high acceleration and have a large stopping distance (because it has a soft bonnet). Consequently, the use of headform stopping distance as a method for evaluating the injury risk posed by a structure is not perfect and does not adequately account for injury risk as is proposed in the Wayne State Tolerance Curve.

Notwithstanding the effect of the threshold that was discussed in the pre-

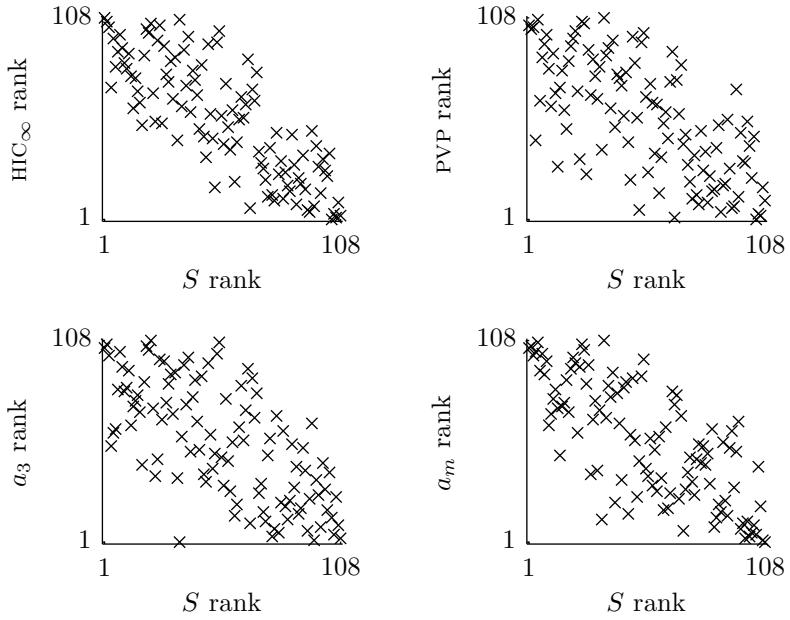

Figure 6.10: Cross plots of the rank of IRF value with rank of stopping distance for all tests with the Adult headform.

Table 6.7: Spearman rank correlation coefficients of the cross plots shown in Figures 6.9 and 6.10.

	Spearman ρ	
	Child headform	Adult headform
HIC_∞ with S	-0.7333	-0.8110
PVP with S	-0.5652	-0.6847
a_3 with S	-0.5936	-0.6790
a_m with S	-0.7003	-0.7460

vious section, this result lays the foundation of one conclusion of this thesis that the IRF choice used as a tool for evaluating an impact is not especially critical when determining the order of crashworthiness. This is because, to a large extent, each IRF is an approximate measure of stopping distance.

However, the IRF also examines other aspects of the acceleration pulse shape that are not directly related to stopping distance. The effect of impact velocity and coefficient of restitution are not easily examined in this data set because of the small range of values they have in the data set. The effect of pulse shape on the outcome of each IRF can be examined. This is examined in the next section.

6.5 Comparison among IRFs using the ranked contribution of pulse shape to the IRF value of each test

As suggested in the previous chapter, the impact velocity, stopping distance and coefficient of restitution explain much of the value of each IRF. The remaining contribution to the value of each IRF is the form of the pulse shape. The contribution of the pulse shape to the value of the IRF can be found by subtracting the contribution of the impact velocity, stopping distance and coefficient of restitution from the value of the IRF.

The contributions of the impact velocity, stopping distance and coefficient of restitution on the value of each IRF were predicted from theory and obtained from linear regression in Chapter 5. An estimate for the pulse shape coeffi - cient can be obtained by subtracting the predicted effect of impact velocity and coefficient of restitution and the effect of stopping distance obtained from regression from the value of each IRF. The predicted effect of impact velocity and coefficient of restitution are used, instead of the values obtained from regression, because the contributions obtained from the regression for these parameters needs to be treated with caution due to the small variation in those data. The equations to estimate the pulse shape coefficient are shown in Equations (6.8) to (6.11), where $\mathbb{P}_{\text{IRF}}$ indicates the test pulse shape coefficient to each IRF, and n is the coefficient obtained from regression of the stopping distance with each IRF adjusted for the predicted effect

of impact velocity and coefficient of restitution.

$$\mathbb{P}_{\text{HIC}} = \exp\left(\log(\text{HIC}_\infty) - 4\log(V) - n\log(S) - \log(R+1)\right) \tag{6.8}$$

$$\mathbb{P}_{\text{PVP}} = \exp\left(\log(\text{PVP}) - 3\log(V) - n\log(S) - \log(R+1)\right) \tag{6.9}$$

$$\mathbb{P}_{a_3} = \exp\left(\log(a_3) - 2\log(V) - n\log(S)\right) \tag{6.10}$$

$$\mathbb{P}_{a_m} = \exp\left(\log(a_m) - 2\log(V) - n\log(S)\right) \tag{6.11}$$

The value of n is different for each IRF and each headform. Table 6.8 shows the values that are used for each headform size and IRF. These values were obtained from the regressions detailed in Tables 5.7, 5.9, 5.11 and 5.13.

Table 6.8: Coefficients of stopping distance, n, found from regression, necessary to determine $\mathbb{P}_{\text{IRF}}$ in Equations (6.8) to (6.11).

	Headform	
IRF	Child	Adult
HIC	-1.7	-1.9
PVP	-1.2	-1.3
a_3	-0.8	-1.0
a_m	-0.9	-1.1

Each test has a unique pulse shape coefficient for each IRF, $\mathbb{P}_{\text{IRF}}$. For the tests with each headform these unique values can be ranked. These ranked values of test pulse shape coefficients can then be cross plotted and correlated with ranked values of other parameters of each test. This is done in the coming subsections.

First, the ranks of pulse shape coefficients will be cross plotted with the ranks of stopping distance to show that the stopping distance does not have a residual effect on the pulse shape coefficient. Then the ranks of pulse shape coefficient for each IRF will be cross plotted with the ranks of value of that IRF. Finally, the ranks of pulse shape coefficient for each IRF will be cross plotted with the ranks of pulse shape coefficient for all other IRFs.

Before further analysis was completed, however, the effect of the coefficient of stopping distance on the ranking of the pulse shape coefficient was investigated. The rankings of the pulse shape coefficient were calculated using the values shown in Table 6.8 and using values that were a distance of one standard error, positive and negative, from this value. The Spearman rank

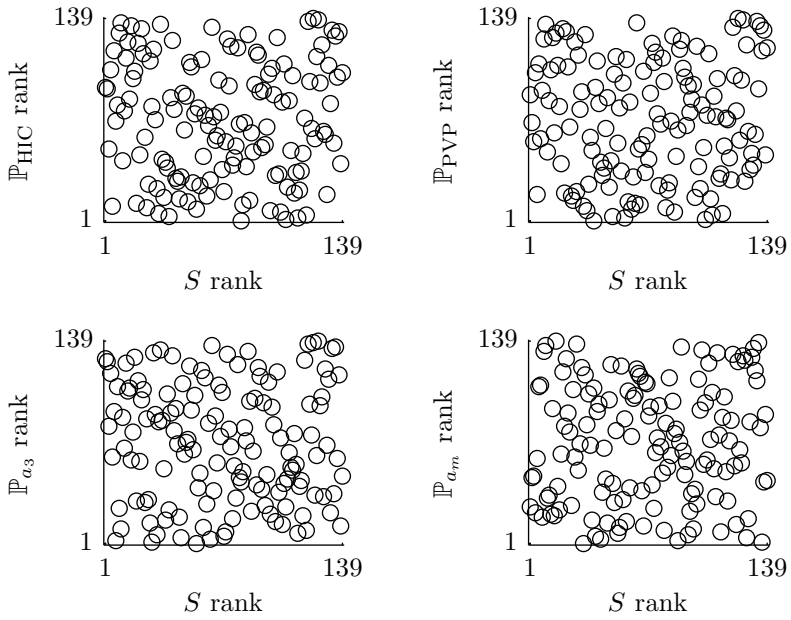

Figure 6.11: Cross plots of the ranks of pulse shape coefficient with ranks of stopping distance for all tests with the Child headform.

correlation coefficients between these rankings was greater than 0.95 for each IRF. Consequently, the rankings determined using the values in Table 6.8 were considered insensitive to reasonable variation in the coefficient assigned to the effect of stopping distance.

6.5.1 Rank correlation of stopping distance with pulse shape coefficient

The ranks of pulse shape coefficient are cross plotted with the ranks of stopping distance in Figure 6.11 for the Child headform tests and in Figure 6.12 for the Adult headform tests. Table 6.9 shows the Spearman rank correlation coefficients for each of these cross plots. None of the correlations are statistically significant ($p < 0.001$). This shows that the effect of the headform stopping distance has been effectively removed from the pulse shape coefficient of each test. The absence of correlation is expected because the pulse shape coefficients are no longer functions of the headform stopping distance and so should disassociate from the value of the headform stopping distance.

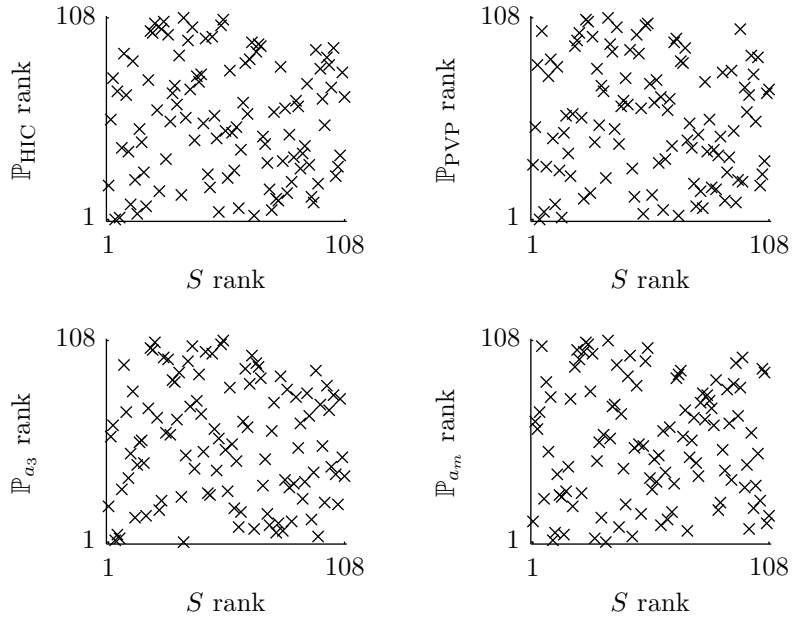

Figure 6.12: Cross plots of the ranks of pulse shape coefficient with ranks of stopping distance for all tests with the Adult headform.

Table 6.9: Spearman rank correlation coefficients of the cross plots shown in Figures 6.11 and 6.12.

	Spearman ρ	
	Child headform	Adult headform
$\mathbb{P}_{\mathrm{HIC}}$ with S	−0.0052	−0.0539
$\mathbb{P}_{\mathrm{PVP}}$ with S	0.0211	−0.0943
$\mathbb{P}_{a_3}$ with S	−0.0490	−0.0638
$\mathbb{P}_{a_m}$ with S	0.0715	−0.0085

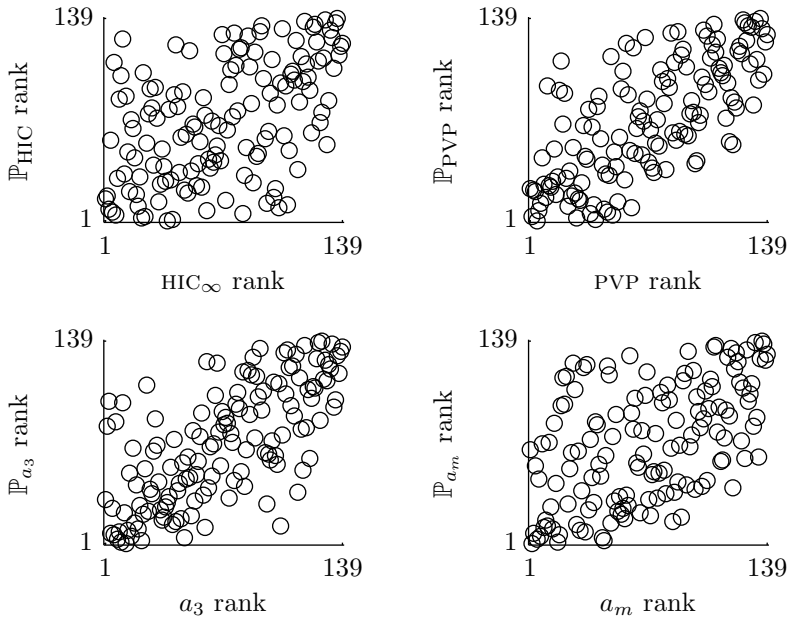

Figure 6.13: Cross plot of ranks of pulse shape coefficient for each IRF with ranks of IRF value. Child headform tests.

6.5.2 Rank correlation of pulse shape coefficients with IRF values

In Figure 6.13 the ranks of pulse shape coefficient are cross plotted with the ranks of IRF value for the tests with the Child headform. The cross plots using the Adult headform tests are shown in Figure 6.14. The Spearman rank correlation coefficient of each of the cross plots is shown in Table 6.10. Each is significantly positively correlated. This correlation is not due to the headform stopping distance as this was previously shown to be uncorrelated with the pulse shape coefficient for each IRF. It is instead due to the effect of pulse shape. Tests with a high value of an IRF have a pulse shape that makes a strong contribution to this value, irrespective of the effect of impact velocity, stopping distance or coefficient of restitution.

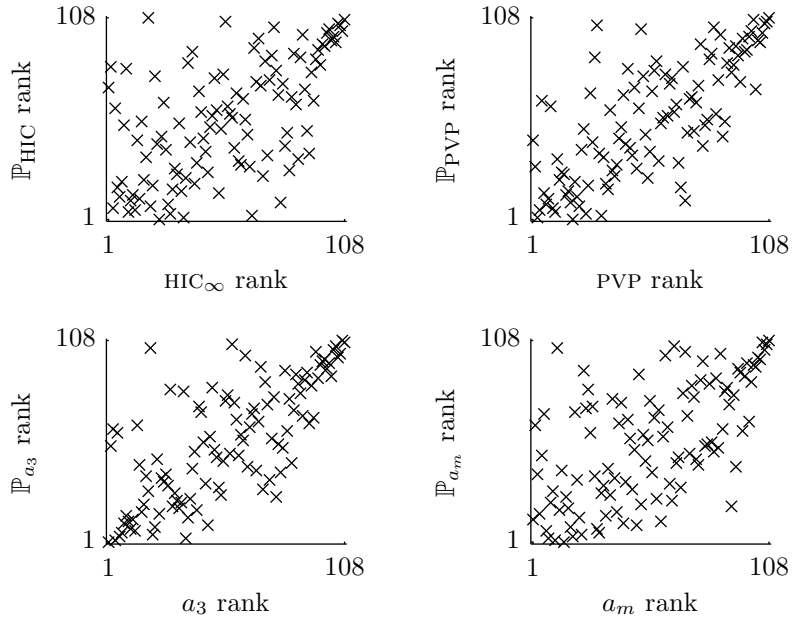

Figure 6.14: Cross plot of ranks of pulse shape coefficient for each IRF with ranks of IRF value. Child headform tests.

Table 6.10: Spearman rank correlation coefficients of cross plots shown in Figures 6.13 and 6.14.

	Spearman ρ	
	Child headform	Adult headform
HIC_∞ with $\mathbb{P}_{\text{HIC}}$	0.4968	0.5725
PVP with $\mathbb{P}_{\text{PVP}}$	0.7143	0.7421
a_3 with $\mathbb{P}_{a_3}$	0.6960	0.7298
a_m with $\mathbb{P}_{a_m}$	0.5219	0.6075

6.5.3 Rank correlation among the pulse shape coefficients for each IRF

The cross plots of rank of pulse shape coefficient for each IRF is shown in Figure 6.15 for the Child headform tests and Figure 6.16 for the Adult headform tests. Tables 6.11 and 6.12 show the Spearman rank correlation coefficients for each of the cross plots.

The clearest association shown in the cross plots is the positive and significant correlation between $\mathbb{P}_{\text{HIC}}$ ranks and the $\mathbb{P}_{\text{PVP}}$ ranks. This demonstrates that the most crashworthy pulse shapes according to HIC tend to be the pulse shapes that are most crashworthy according to PVP. This positive and significant correlation is also generally true for all of the correlations between the ranks of $\mathbb{P}_{\text{HIC}}$, $\mathbb{P}_{\text{PVP}}$ and $\mathbb{P}_{a_3}$, although for the other pairs of ranks the correlations are weaker. This shows that the IRF is important in distinguishing between the pulse shapes that are crashworthy and those that are not.

The cross plots involving the ranks of $\mathbb{P}_{a_m}$, on the other hand, are not significant, and in the case of the Child headform data, negative correlations with other $\mathbb{P}_{\text{IRF}}$ ranks are being induced. This shows that it is quite likely that a crashworthy pulse shape according to a_m may be considered uncrashworthy according to another IRF. Consequently, the acceleration pulse shapes for designs produced for assessment with a_m may be quite different from the acceleration pulse shapes produced for designs intended for assessment with other IRFs.

The pulse shapes with the most discrepant ranks between $\mathbb{P}_{\text{HIC}}$ and the other $\mathbb{P}_{\text{IRF}}$, including between the $\mathbb{P}_{\text{HIC}}$ and $\mathbb{P}_{a_m}$ are found and described in the next chapter. The reasons for the discrepancies in rank will be elucidated for these tests.

It should be noted, however, that these differences between the IRFs were substantiated only after the effects of stopping distance, impact velocity and coefficient of restitution were subtracted from the value of each IRF. Consequently the relative importance of these differences, compared with the similarities arising from the effects of stopping distance and impact velocity should not be over emphasised.

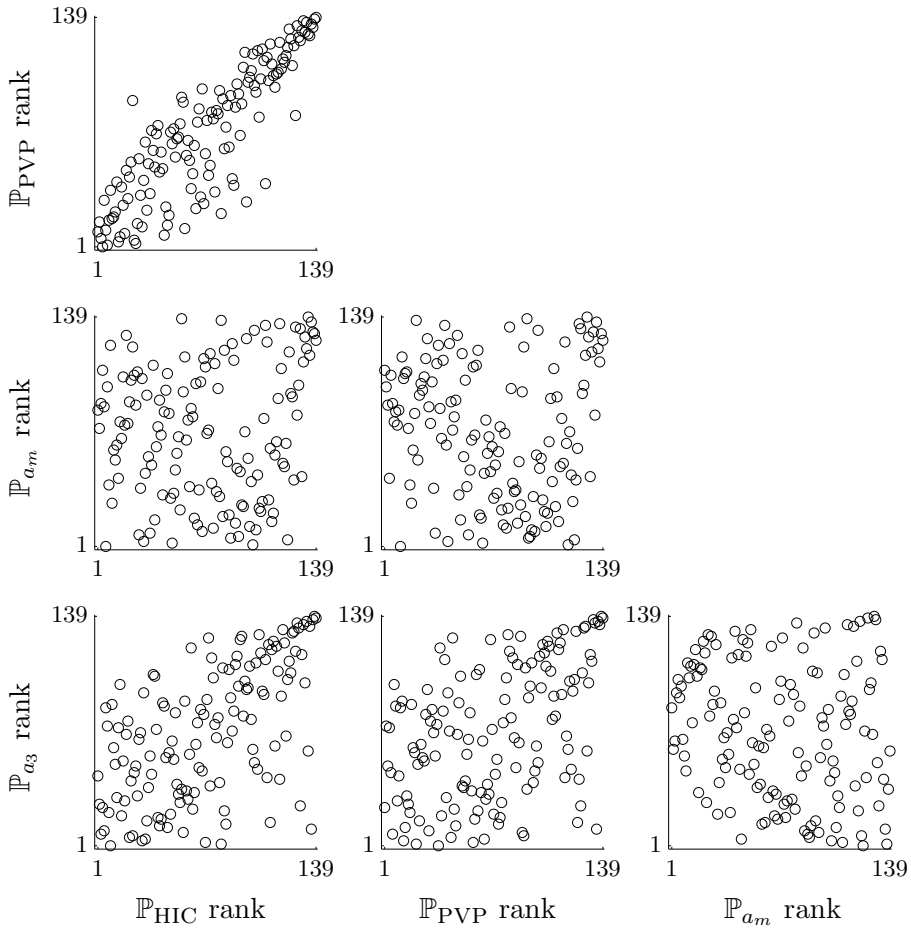

Figure 6.15: Cross plots among each $\mathbb{P}_{\text{IRF}}$ rank for tests with the Child headform.

Table 6.11: Spearman ρ rank correlation coefficient for the cross plots shown in Figure 6.15.

	$\mathbb{P}_{\text{HIC}}$	$\mathbb{P}_{\text{PVP}}$	$\mathbb{P}_{a_m}$
$\mathbb{P}_{\text{PVP}}$	0.8592		
$\mathbb{P}_{a_m}$	0.1208	-0.0454	
$\mathbb{P}_{a_3}$	0.5846	0.4459	-0.1670

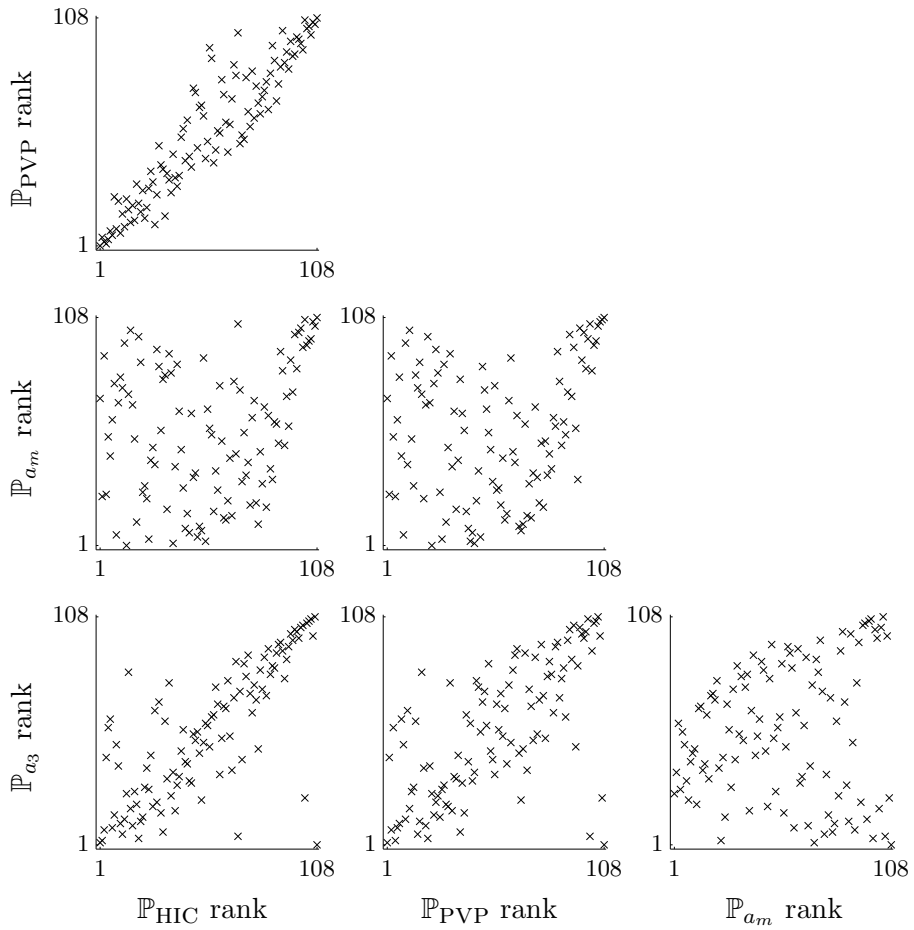

Figure 6.16: Cross plots among each $\mathbb{P}_{\text{IRF}}$ rank for tests with the Adult headform.

Table 6.12: Spearman ρ rank correlation coefficient for the cross plots shown in Figure 6.16.

	$\mathbb{P}_{\text{HIC}}$	$\mathbb{P}_{\text{PVP}}$	$\mathbb{P}_{a_m}$
$\mathbb{P}_{\text{PVP}}$	0.9299		
$\mathbb{P}_{a_m}$	0.2469	0.2398	
$\mathbb{P}_{a_3}$	0.7534	0.6584	0.1401

6.6 Discussion

The results of this chapter show that the four IRFs considered treat impact severity similarly. This was shown most clearly in Section 6.4 where the ranking of tests results was positively correlated and statistically significant for all pairs of IRFs. This analysis might quell debate about the preferential use of one IRF over another in test protocols. As a consequence, unless there is clear biomechanical evidence to the contrary, the choice of an IRF should not be over emphasised when the objective is to increase the crashworthiness of the structures being tested. This is because any choice from IRFs considered in this chapter will give a similar picture of the relative crashworthiness of the structures being tested.

With the similarities between the IRFs that are based on linear acceleration in mind, it would be unwise for one IRF to be replaced with another in a test protocol, especially if a change in threshold is implied, without first predicting what the effect this change may have on what is considered safe. This is because the choice of the threshold is paramount in determining how conservative the alternative criterion will be in comparison to the initial criterion. The analysis in Section 6.3 has shown that the choice of the threshold is very important in determining if the alternate criterion is more or less conservative than the original reference criterion. Importantly, the values of the Sensitivity, Specificity, PPV and NPV can be determined for alternate criteria from contingency tables constructed from real test data. These can be used to give an indication of how conservative the alternate criterion is. If the interests of safety are paramount, then the Sensitivity of the alternate criterion should be greater than the Specificity, and the NPV should be greater than the PPV to ensure a conservative approach to any change in criterion.

While this analysis and discussion has focused on the similarities between the various IRFs, which is dominated by effects of stopping distance, impact velocity and coefficient of restitution, it is clear from the less than perfect correlation that there is still variation in the order of crashworthiness established by each IRF. It was shown that a source of this variation is the contribution of the pulse shape to the value of each IRF. This was investigated using the pulse shape coefficient for each IRF.

The pulse shape coefficient was determined by subtracting, from the value of the IRF, the effects of impact velocity and coefficient of restitution (both predicted from theoretical analysis), and the effect of stopping distance (obtained from regression).

The pulse shape coefficient for each test with each IRF was cross plotted with the other pulse shape coefficients to show how differently each IRF treats different pulse shapes. It was shown that some pairs of IRFs (in particular HIC and PVP) rank pulse shapes similarly, while other pairs (in particular a_m with any other IRF) rank pulse shapes quite differently.

These differences, whilst negligible compared with the amount of available and utilised stopping distance in the structure, still show differences between the various IRFs that may be of importance. These differences are discussed in the next chapter using individual tests from the data set.

Chapter 7

Examination of discrepant pulse shapes in the test data

7.1 Introduction

In the previous chapter the rank of crashworthiness was used to show the association among the alternative IRFs. In a general sense, a change in crashworthiness, measured by one IRF would have a similar positive or negative change in crashworthiness when measured with an alternative IRF. It has been shown that much of this similarity can be attributed to the effects of impact velocity, stopping distance and, to a lesser extent, coefficient of restitution. The remaining, complicated, component that has not been examined in the test data is the effect of the pulse shape.

In this chapter, it shall be posited that the pulse shapes of the tests with the highest differences in the ranks of the IRF pulse shape coefficient, $\mathbb{P}_{\text{IRF}}$, are the most informative tests to study the differences between the IRFs. This is because the effect of the stopping distance, impact velocity and coefficient of restitution has been factored out of the values of the IRF pulse shape coefficient, and any remaining differences are due to the pulse shape and the way that these are evaluated by the IRFs. As a consequence, the tests with the most discrepant rankings according to the pulse shape coefficient, will show the types of pulse shapes that are evaluated most differently with each IRF.

The equations to calculate $\mathbb{P}_{\text{IRF}}$ for each test were shown in the previous chapter in Equations (6.8) to (6.11). In general the pulse shape coefficient is calculated by removing the effects of the impact velocity, coefficient of restitution and stopping distance from the value of the IRF.

The discrepant tests between the HIC_∞ and each of the other IRFs are considered in this chapter. Features common to each of these discrepant tests are found and explored in the whole data set, where appropriate. These differences can highlight some important aspects of these IRFs including the way they measure real pulse shapes. These differences cannot be easily explored using theoretical pulse shapes.

When the discrepant pulse shapes are evaluated in the context of the theoretical results obtained in earlier chapters, the features of each pulse shape that influence the crashworthiness with each IRF, can be identified. This is

often sufficient to determine why a test has a lower pulse shape coefficient than another.

7.2 Identifying the tests with the most discrepant ranks of pulse shape coefficients

Tests that have discrepant ranks of pulse shape coefficient for two IRFs are those that, once removed from the data set, increase the value of the Spearman rank correlation coefficient of all tests that remain in the data set. The most discrepant test is the one which, after its removal, increases the value of the Spearman rank correlation coefficient by the highest amount. There may be several tests that, when removed, increase the value of the Spearman rank correlation coefficient by the same amount and when this occurs they are all considered equally discrepant. The order of discrepancy is the order of the tests that are most discrepant and these can be obtained by successively removing each of the tests that are the most discrepant in the remaining data set.

A Matlab program was written to find the order of discrepancy of the tests in the data set so that they could be used for analysis. From each data set the 10 most discrepant tests were identified. These 10 tests were then sorted into two categories defined by the $\mathbb{P}_{\text{IRF}}$ with the higher rank.

This process of determining the most discrepant tests in the data set was chosen because it could be implemented readily. Other methods, such as identifying the tests with the greatest difference in pulse shape coefficient rank, could have been used instead. The important part of this chapter, however, is to identify some discrepant tests and then use those tests to improve the understanding of the theoretical basis for each IRF and how the IRFs relate to the vehicle structures. The method used achieves this.

The tests with minimal discrepancy are not able to contribute to improving the theoretical understanding of each IRF. Their minimal discrepancy could be due to several factors including actually being a non-discrepant test or having neighbours that are so discrepant that the test is forced to have minimal discrepancy by default. These minimally discrepant tests are not considered in this chapter.

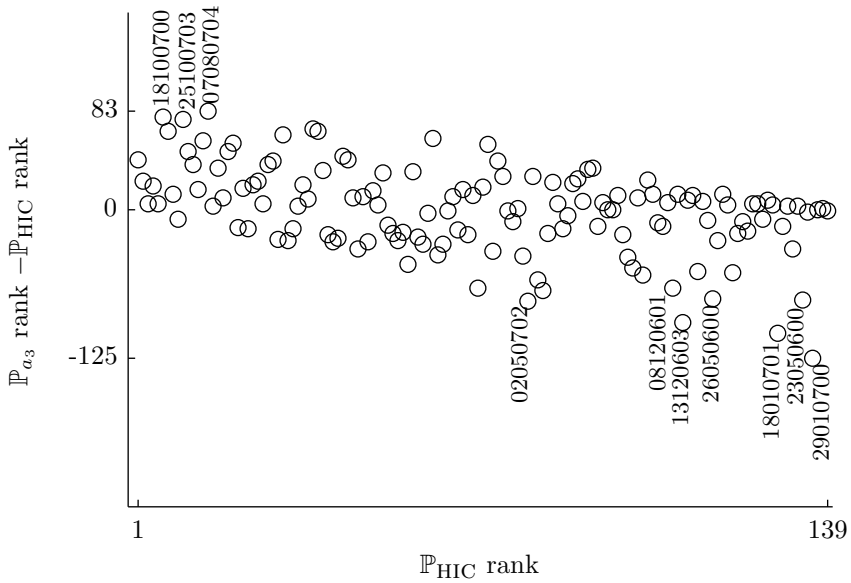

Figure 7.1: Child headform tests with discrepant ranking between $\mathbb{P}_{\mathrm{HIC}}$ and $\mathbb{P}_{a_3}$.

7.3 Analysis of the discrepant pulse shapes between HIC and 3 millisecond clip

The tests identified as being discrepant between the ranks of $\mathbb{P}_{\mathrm{HIC}}$ and the ranks of $\mathbb{P}_{a_3}$ are shown in Figure 7.1 and Figure 7.2. In each figure the difference in pulse shape coefficient rank is cross plotted against the rank of $\mathbb{P}_{\mathrm{HIC}}$. In subsection 7.3.1 the tests with a high $\mathbb{P}_{\mathrm{HIC}}$ rank and a low $\mathbb{P}_{a_3}$ rank are investigated and in subsection 7.3.2 the tests with a low $\mathbb{P}_{\mathrm{HIC}}$ rank and a high $\mathbb{P}_{a_3}$ rank are investigated. The tests investigated are those labeled in Figures 7.1 and 7.2.

7.3.1 Tests with a higher $\mathbb{P}_{\mathrm{HIC}}$ rank than $\mathbb{P}_{a_3}$ rank

The pulse shapes within the top ten most discrepant tests, and with $\mathbb{P}_{a_3}$ ranked higher than $\mathbb{P}_{\mathrm{HIC}}$, are shown in Figure 7.3 and Figure 7.4. Figure 7.3 shows the tests performed with the Child headform and Figure 7.4 shows the tests performed with the Adult headform. In the figures the gray vertical lines indicate the limits of the HIC evaluation window. The gray horizontal

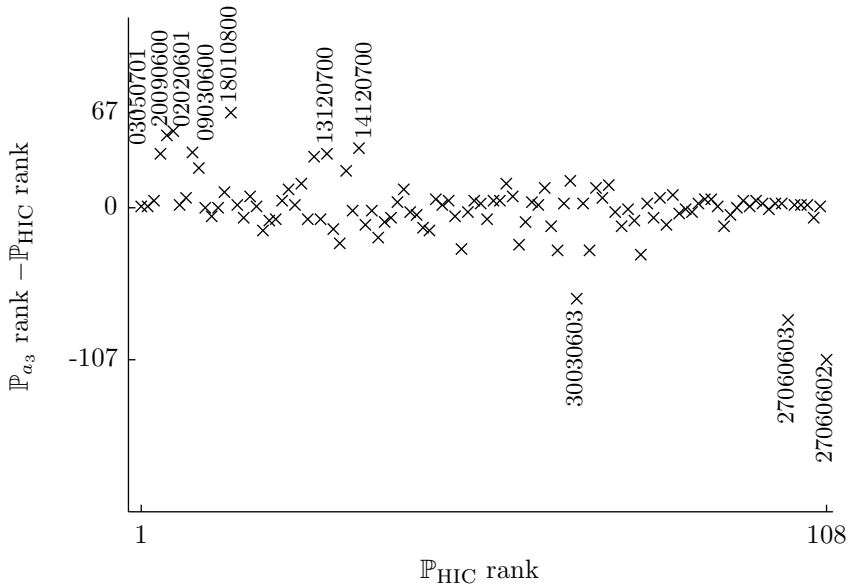

Figure 7.2: Adult headform tests with discrepant ranking between $\mathbb{P}_{\text{HIC}}$ and $\mathbb{P}_{a_3}$.

line is 3 ms in length and indicates the place and level where a_3 IRF is evaluated. Table 7.1 summarises the important features of each test shown.

Table 7.1 shows that there are two main reasons why a pulse shape has a lower ranking with $\mathbb{P}_{\text{HIC}}$ than with $\mathbb{P}_{a_3}$. One is that a narrow acceleration peak with a duration less than 3 ms is present. These narrow acceleration peaks have a high average acceleration but due to their narrowness the level of the acceleration exceeded for the entire 3 ms duration is low. The other reason for the discrepancy in ranking is a pulse shape with two narrow acceleration peaks, each with a duration less than 3 ms separated by a narrow acceleration trough, is present. These pulse shapes have a high acceleration averaged across both peaks, but because of the trough, the acceleration that is exceeded for the entire 3 ms duration is low. These two main reasons for difference are discussed in detail presently.

Tests with a narrow acceleration peak

14 tests in the data set have a HIC_∞ evaluation window less than 3 ms in duration. 11 of the tests are with the Child headform, and three are with

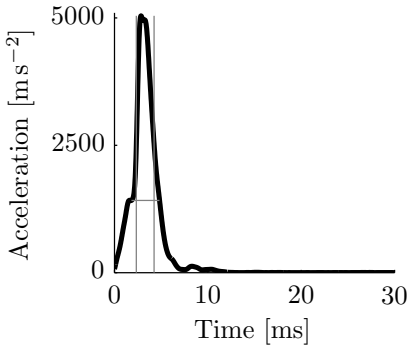

(a) Test 29010700 (C5D), HIC_∞ = 7178 (136), a_3 = 144.6 g (11).

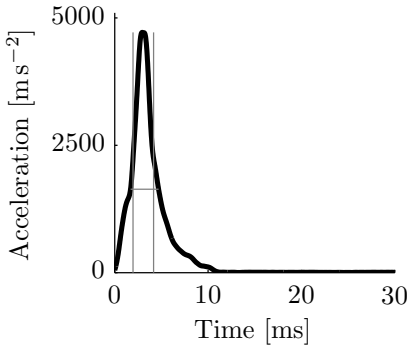

(b) Test 18010701 (C2C), HIC_∞ = 6201 (129), a_3 = 167.0 g (25).

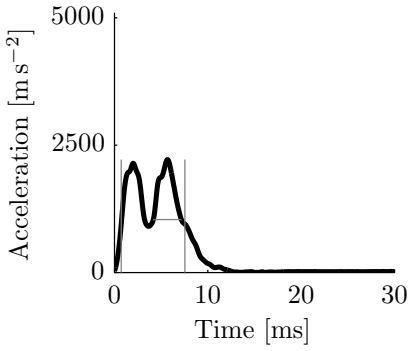

(c) Test 13120603 (C1B), HIC_∞ = 2264 (110), a_3 = 106.0 g (15).

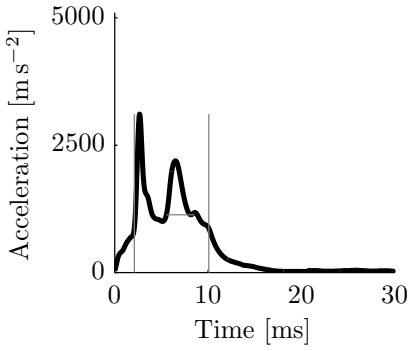

(d) Test 26050600 (C3B), HIC_∞ = 2100 (116), a_3 = 115.6 g (41).

Figure 7.3: Child headform tests where $\mathbb{P}_{\text{HIC}}$ rank is higher than $\mathbb{P}_{a_3}$ rank. The number in brackets () indicates the $\mathbb{P}_{\text{IRF}}$ rank value. Continued on the facing page.

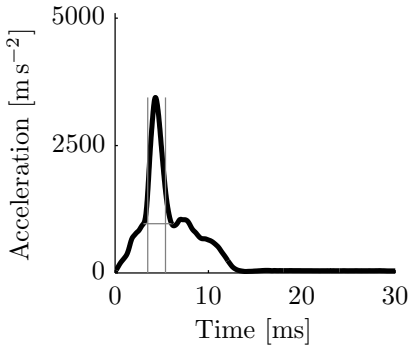

(e) Test 23050600 (C1D(d)),
HIC_∞ = 2326 (134), a_3 = 98.5 g (58).

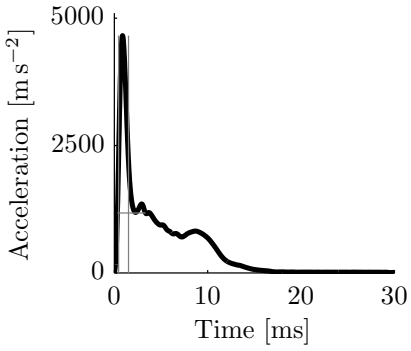

(f) Test 02050702 (C6A),
HIC_∞ = 2897 (79), a_3 = 119.9 g (2).

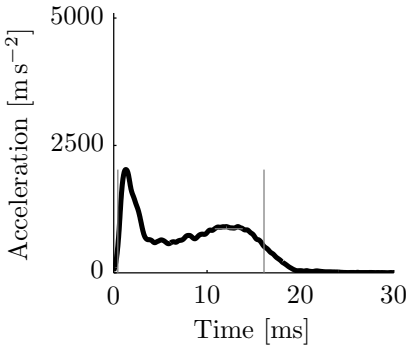

(g) Test 08120601 (C3B),
HIC_∞ = 1137 (107), a_3 = 88.2 g (42).

Figure 7.3: Child headform tests where $\mathbb{P}_{\text{HIC}}$ rank is higher than $\mathbb{P}_{a_3}$ rank. The number in brackets () indicates the $\mathbb{P}_{\text{IRF}}$ rank value.

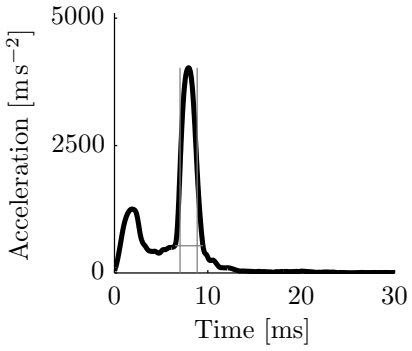

(a) Test 27060602 (A3D), HIC_∞ = 4026 (108), a_3 = 54.4 g (1).

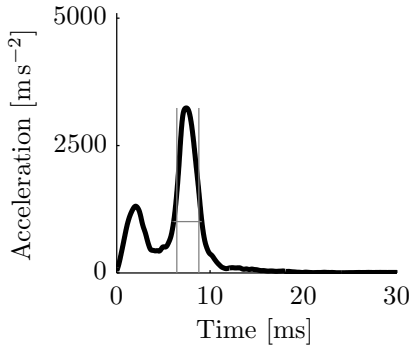

(b) Test 27060603 (A2D), HIC_∞ = 2829 (102), a_3 = 102.7 g (23).

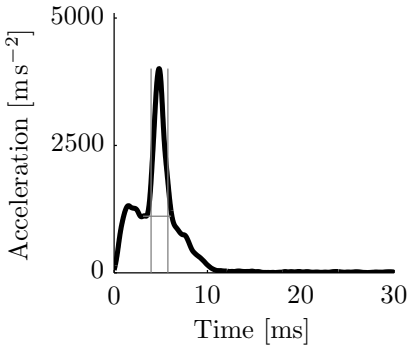

(c) Test 30030603 (A3A), HIC_∞ = 2946 (71), a_3 = 113.2 g (5).

Figure 7.4: Adult headform tests where $\mathbb{P}_{\text{HIC}}$ rank is higher than $\mathbb{P}_{a_3}$ rank. The number in brackets () indicates the $\mathbb{P}_{\text{IRF}}$ rank value.

Table 7.1: Tests that have a higher ranking of $\mathbb{P}_{\text{HIC}}$ than ranking of $\mathbb{P}_{a_3}$.

Test	Impact structure	Comment
	Child headform tests	
29010700	Above radiator support rail	Narrow peak
18010701	Above radiator support rail	Narrow peak
13120603	Above suspension strut	Double narrow peak
26050600	On wiper pivot	Double narrow peak
23050600	In-front of brake master cylinder	Narrow peak
02050702	Above plenum	Narrow peak
08120601	Above firewall	Narrow peak
	Adult headform tests	
27060602	Above intake manifold	Narrow peak
27060603	Above intake manifold	Narrow peak
30030603	Above air intake	Narrow peak

the Adult headform. Figure 7.5 shows how the difference in ranking with the $\mathbb{P}_{a_3}$ and $\mathbb{P}_{\text{HIC}}$ changes as the HIC_∞ evaluation window changes. All structures with a HIC_∞ evaluation window shorter than 3 ms have an $\mathbb{P}_{a_3}$ rank higher than their $\mathbb{P}_{\text{HIC}}$ rank. A transition occurs at about a HIC_∞ evaluation window length of 3 ms. As the HIC_∞ evaluation window becomes longer than 3 ms, tests have a lower $\mathbb{P}_{a_3}$ rank than $\mathbb{P}_{\text{HIC}}$ rank. These tests are discussed in the next section. The differences in rank of the tests with long HIC_∞ windows (> 6 ms) are evenly distributed around zero difference in rank.

Details of the acceleration pulses of the 14 tests with a HIC_∞ window that is less than 3 ms are shown in Figure 7.6. There are differences between the tests with the Child headform (shown in black) and the Adult headform (shown in grey and marked with an *). The narrow peak in acceleration occurs near the start of the impact in the Child headform tests and later in the impact for the Adult headform tests. The Child headform tests shown are conducted near the front of the bonnet, and in this region there are stiff under-bonnet structures that are near to the bonnet surface such as a radiator support rail. These interact with the deformation of the bonnet early in the impact and result in a short acceleration peak. The Adult headform tests shown have under-bonnet structures that are further away

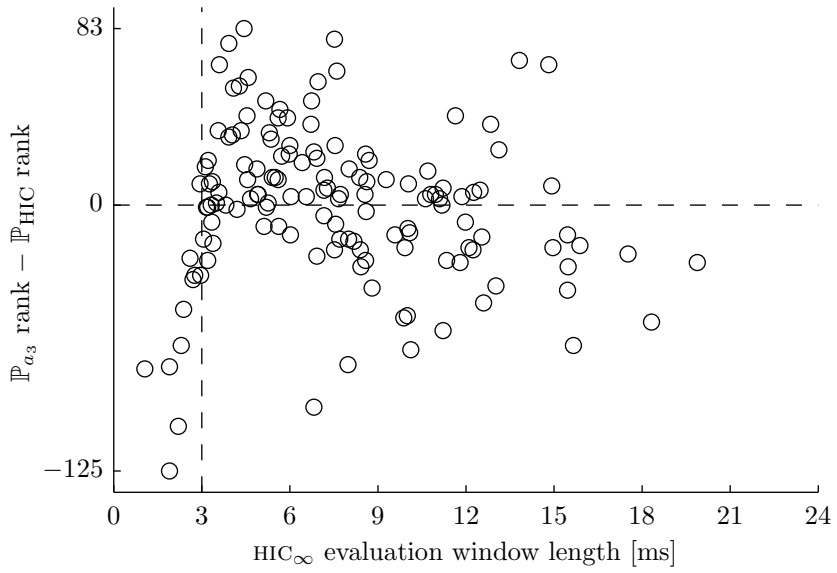

(a) Child headform tests.

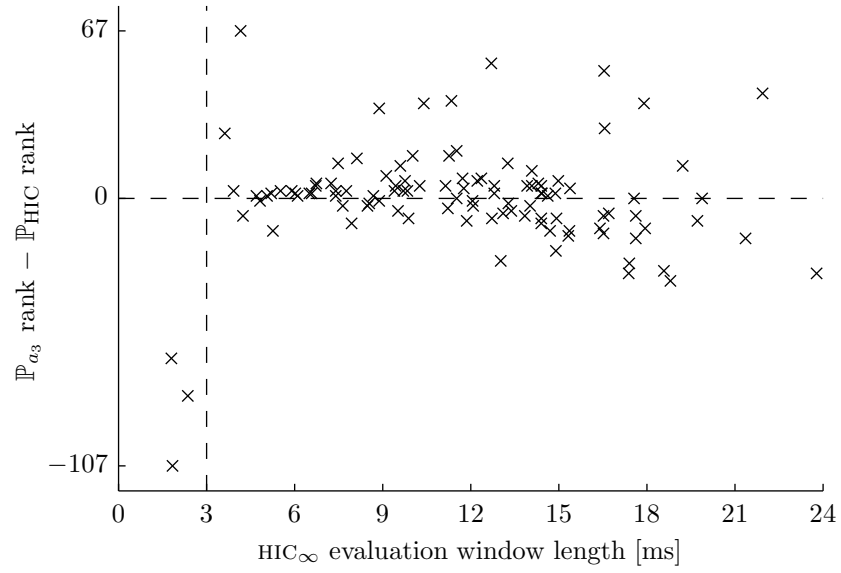

(b) Adult headform tests.

Figure 7.5: Graph of tests with the 4.8kg headform comparing the difference in rank between $\mathbb{P}_{\text{HIC}}$ and $\mathbb{P}_{a_3}$ and the time of calculation of the HIC_∞.

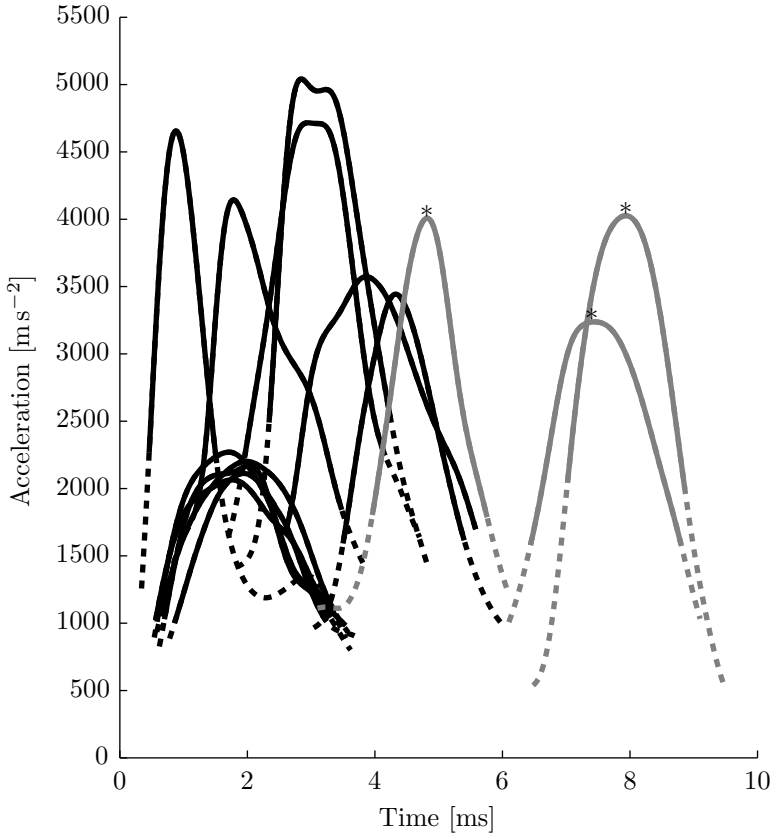

Figure 7.6: The 14 tests that have a HIC_∞ evaluation window that has a duration that is less than 3 ms. The portion of the test inside the HIC_∞ evaluation window is shown with the solid line, the dashed line indicates the limit of the a_3 3 ms window. Both headform masses shown (black are Child headform tests, the grey, starred tests are the Adult headform tests). For clarity, the remainder of the acceleration measured for each test that is not included in the a_3 IRF window is removed.

from the bonnet (such as the air intake manifold). This extra distance causes the impact with this secondary structure to occur later in the impact. Despite these differences, the main effect is a very narrow acceleration pulse that has a high ranking with $\mathbb{P}_{\text{HIC}}$ and a low ranking with $\mathbb{P}_{a_3}$.

Tests with a double peak in acceleration

The other test type shown amongst the discrepant tests has a double peak in the acceleration. Both peaks are included in the HIC_∞ evaluation window. Generally, these tests strike a primary structure and then a stiff secondary structure (bottoming out). Test 13120603 in Figure 7.3(c) is an example of such a test. This test was aimed just above a suspension strut. The high speed film of this test shows the bonnet readily deform before the headform is retarded by an under-bonnet structure. It is these under-body structures that influence the test and create the second peak in acceleration.

Importantly, the low value of the a_3 occurs because the two peaks in the acceleration are both narrow. Neither of them has a duration of more than 3 ms so the maximum acceleration that is sustained for 3 ms is located at their base.

7.3.2 Tests with a lower $\mathbb{P}_{\text{HIC}}$ rank than $\mathbb{P}_{a_3}$ rank

The tests with a lower ranking with $\mathbb{P}_{\text{HIC}}$ than with $\mathbb{P}_{a_3}$ are shown in Figure 7.7 and in Figure 7.8. Figure 7.7 shows the tests with the Child headform and Figure 7.8 shows the tests with the Adult headform. Table 7.2 summarises the important characteristics of the tests. There is one common feature to all these pulse shapes. That is the value of the a_3 is very near the value of the maximum acceleration. This manifests itself in two ways. There are the pulse shapes with a wide peak in acceleration. They have a HIC_∞ evaluation window that is a little longer than 3 ms. These tests contrast with the narrow peaks discussed in the previous section. Secondly, the other pulse shapes are triangle pulse shapes with an early peak in the acceleration followed by a gradual reduction in the acceleration as time progresses. These triangle tests were shown in Chapter 4 to be ideal for a low HIC_∞ with minimum stopping distance. There are several consequences of these types of pulse shapes that are discussed in this section.

The difference between the rankings of $\mathbb{P}_{a_3}$ and $\mathbb{P}_{\text{HIC}}$ are plotted against the difference between the value of a_3 and mean value of acceleration during the 3 ms window of a_3, in Figure 7.9. There is a trend suggesting that the measured acceleration is only slightly greater than the a_3 value for tests with

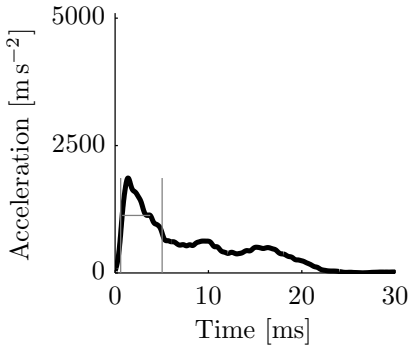

(a) Test 07080704 (C1B(b)), HIC_∞ = 908 (15), a_3 = 115.0 g (98).

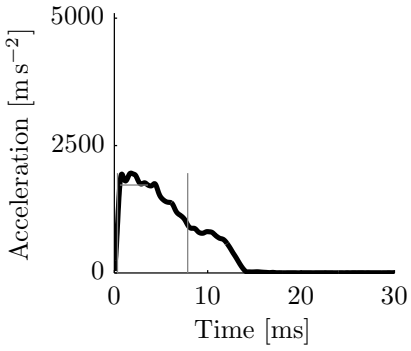

(b) Test 18100700 (C1D), HIC_∞ = 2443 (6), a_3 = 175.8 g (84).

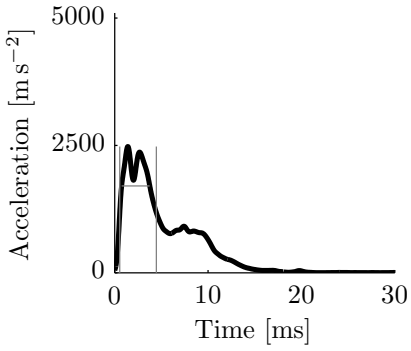

(c) Test 25100703 (C3D), HIC_∞ = 2220 (10), a_3 = 173.8 g (86).

Figure 7.7: Child headform tests where $\mathbb{P}_{\text{HIC}}$ rank is lower than $\mathbb{P}_{a_3}$ rank. The number in brackets () indicates the $\mathbb{P}_{\text{IRF}}$ rank value.

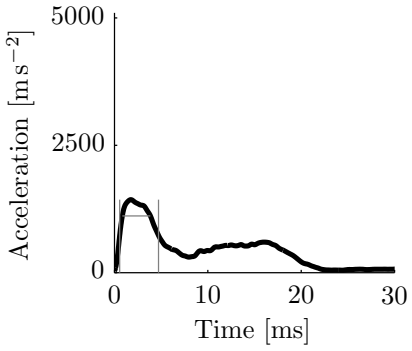

(a) Test 18010800 (A4D(cd)), HIC_∞ = 706 (20), a_3 = 113.6 g (82).

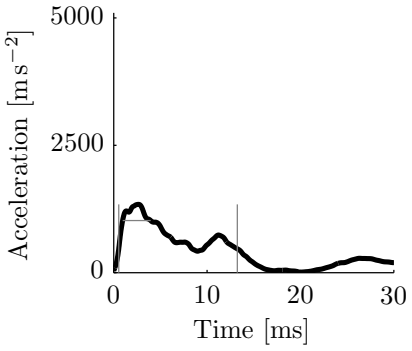

(b) Test 02020601 (A3C), HIC_∞ = 718 (7), a_3 = 104.3 g (60).

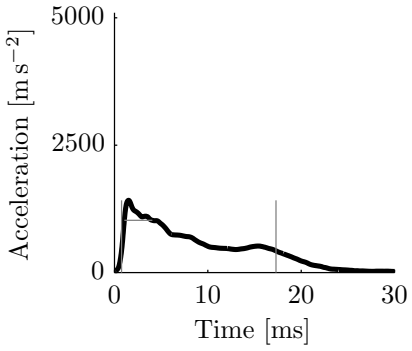

(c) Test 20090600 (A2B), HIC_∞ = 740 (6), a_3 = 104.6 g (56).

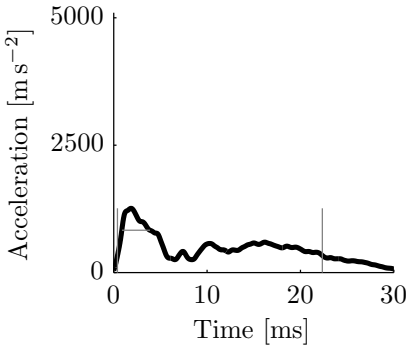

(d) Test 14120700 (A2D(cd)), HIC_∞ = 533 (10), a_3 = 84.7 g (77).

Figure 7.8: Adult headform tests where $\mathbb{P}_{\text{HIC}}$ rank is lower than $\mathbb{P}_{a_3}$ rank. The number in brackets () indicates the $\mathbb{P}_{\text{IRF}}$ rank value. Continued on the facing page.

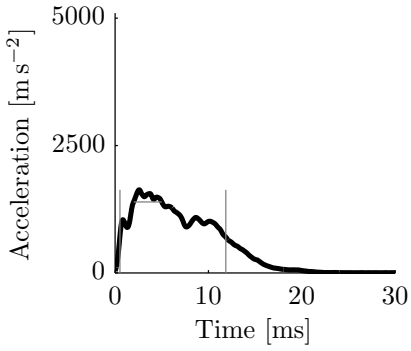

(e) Test 09030600 (A4C), HIC_∞ = 1760 (15), a_3 = 142.1 g (48).

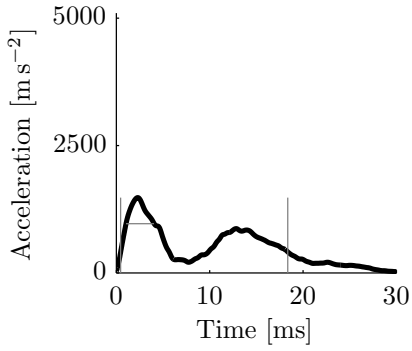

(f) Test 13120700 (A3C(cd)), HIC_∞ = 735 (22), a_3 = 98.5 g (68).

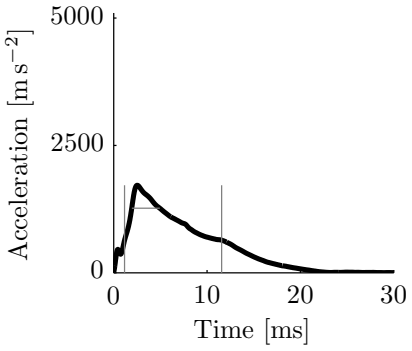

(g) Test 03050701 (A5C), HIC_∞ = 1284 (5), a_3 = 129.2 g (42).

Figure 7.8: Adult headform tests where $\mathbb{P}_{\text{HIC}}$ rank is lower than $\mathbb{P}_{a_m}$ rank. The number in brackets () indicates the $\mathbb{P}_{\text{IRF}}$ rank value.

Table 7.2: Tests with a lower $\mathbb{P}_{\text{HIC}}$ rank than $\mathbb{P}_{a_3}$ rank.

Test	Impact structure	Comment
	Child headform tests	
07080704	Above bonnet rib	Wide acceleration peak
18100700	Bonnet leading edge	Wide acceleration peak
25100703	Above bonnet catch	Wide acceleration peak
	Adult headform tests	
18010800	Above bonnet rib	Wide acceleration peak
02020601	Above bonnet rib	Triangle pulse
20090600	Windscreen surround	Triangle pulse
14120700	Above bonnet rib	Wide acceleration peak
09030600	Above firewall	Wide acceleration peak
13120700	Above bonnet rib	Wide acceleration peak
03050701	Base of windscreen	Triangle pulse

a higher $\mathbb{P}_{a_3}$ rank than $\mathbb{P}_{\text{HIC}}$ rank and that the measured acceleration is much greater than the a_3 value when the rank difference is the opposite. This means, for a particular impact velocity, stopping distance and coefficient of restitution, flatter and wider acceleration pulse shapes make a larger contribution to a_3 than they contribute to HIC.

7.3.3 Analysis of the pulse shapes that are discrepant between $\mathbb{P}_{\text{HIC}}$ and $\mathbb{P}_{a_3}$

In summary, two general pulse shape characteristics explain the discrepant ranks of $\mathbb{P}_{\text{HIC}}$ and $\mathbb{P}_{a_3}$. These are the width of the HIC_∞ evaluation window (Figure 7.5), and the average acceleration value during the 3 ms that the a_3 occurs (Figure 7.9). Each of these characteristics imply similar things about an impact.

Consider a test where the impact was against a very rigid structure. Its pulse shape would be narrow and its average acceleration during the time that the a_3 is evaluated would be much higher than the a_3. Each of these factors indicate a test that would have a high rank with $\mathbb{P}_{\text{HIC}}$ and a low rank with $\mathbb{P}_{a_3}$.

On the contrary, a test on a softer structure would have a smooth and long pulse shape. The average acceleration during the time that the a_3 is

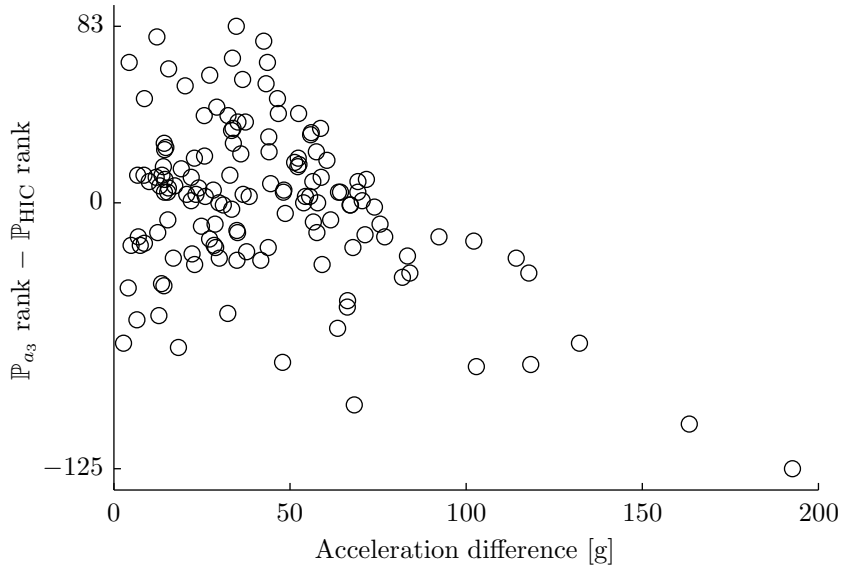

(a) Child headform tests.

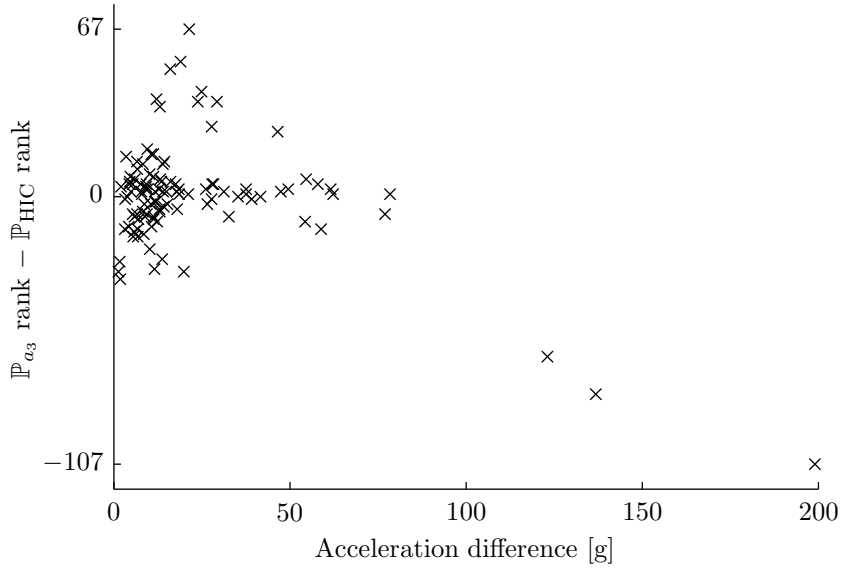

(b) Adult headform tests

Figure 7.9: Relationship between the difference in rank of $\mathbb{P}_{a_3}$ and $\mathbb{P}_{\text{HIC}}$ and the difference between the value of the a_3 and the mean value of acceleration during the 3 ms window of the a_3.

evaluated would be just higher than the a_3 value. Each of these factors point to a test that has a high rank with $\mathbb{P}_{a_3}$ and a low rank with $\mathbb{P}_{\text{HIC}}$.

This analysis has shown, when the effect of stopping distance, impact velocity and coefficient of restitution are factored out of the analysis, that a pulse shape thought to be ideal for the HIC_∞ — the front loaded triangle pulse — is not particularly suited to obtaining a low value of a_3. A designer, therefore, might try to avoid this type of pulse shape if the a_3 IRF were used instead of the HIC in a testing paradigm. A pulse shape with a very short duration peak, on the other hand, can be a good design for the a_3 IRF and a poor design for the HIC_∞. A structure with such a peak might be considered a good design if the a_3 is used as the IRF. These results confirm the observations made in Chapter 4.

7.4 Analysis of the discrepant pulse shapes between HIC and PVP

The tests with the most discrepant rankings according to $\mathbb{P}_{\text{HIC}}$ and $\mathbb{P}_{\text{PVP}}$ are identified in Figure 7.10 and Figure 7.11. Most discrepant tests with the Child headform have a higher ranking with $\mathbb{P}_{\text{HIC}}$ than with $\mathbb{P}_{\text{PVP}}$. Most of the discrepant tests with the Adult headform have a higher ranking with $\mathbb{P}_{\text{PVP}}$ than with $\mathbb{P}_{\text{HIC}}$.

7.4.1 Tests with a higher $\mathbb{P}_{\text{PVP}}$ rank than $\mathbb{P}_{\text{HIC}}$ rank

The tests with a higher $\mathbb{P}_{\text{PVP}}$ rank than $\mathbb{P}_{\text{HIC}}$ rank are shown in Figures 7.12 and 7.13. In these, and subsequent figures, the power of the impact, defined as $P(t)$ in Equation (3.21), is shown throughout the impact with a thin grey line. The resulting value of the PVP is the maximum value of this line. All these tests have a local peak in the acceleration occurring late in the impact pulse shape.

Table 7.3 summarises the important aspects of these pulse shapes. Two main types of pulse shape are identified as being discrepant. These pulse shapes are labelled 'Strong late acceleration' or 'Late rise in acceleration'. The main difference between these pulse shape types is the location of the

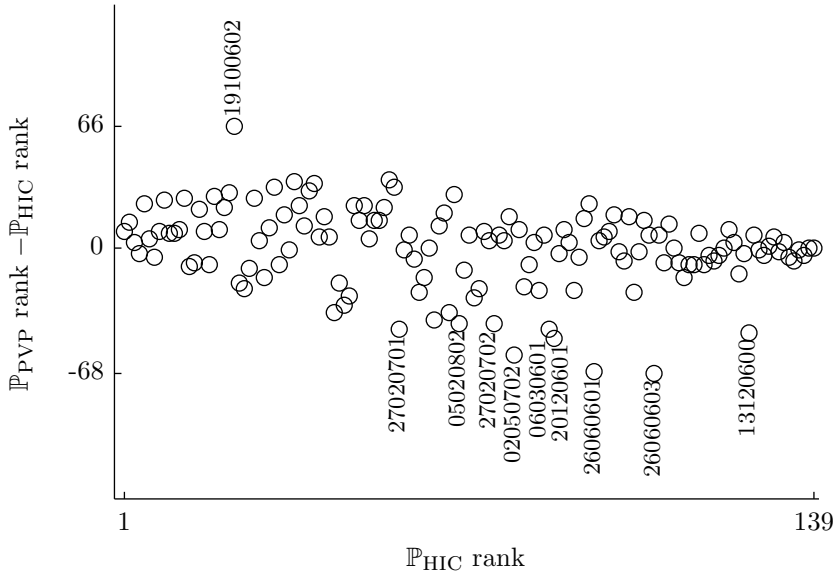

Figure 7.10: Child headform tests with discrepant ranking between $\mathbb{P}_{\text{HIC}}$ and $\mathbb{P}_{\text{PVP}}$.

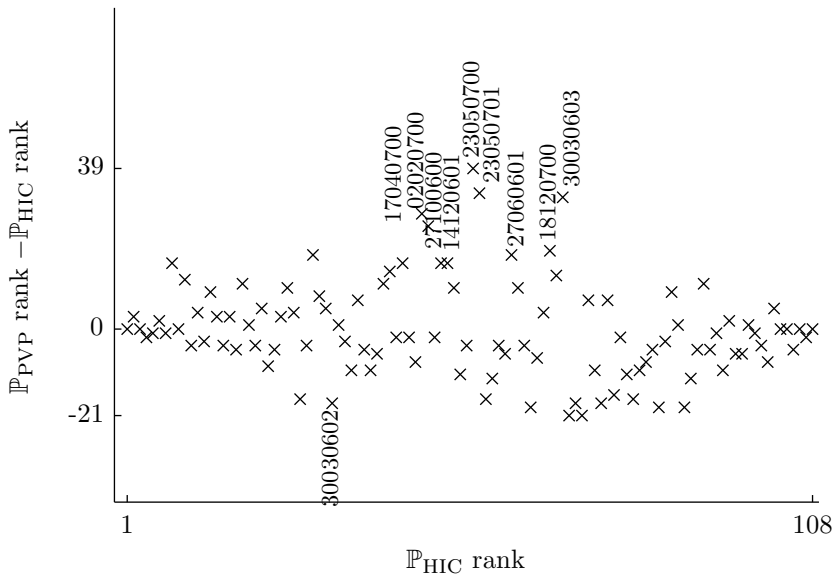

Figure 7.11: Adult headform tests with discrepant ranking between $\mathbb{P}_{\text{HIC}}$ and $\mathbb{P}_{\text{PVP}}$.

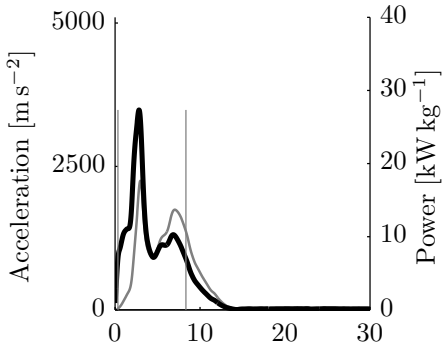

(a) Test 19100602 (C1B(b)),
HIC_∞ = 2246 (23),
PVP = 17.6 kW kg^{-1} (89).

Figure 7.12: Child headform test where $\mathbb{P}_{\text{HIC}}$ rank is lower than $\mathbb{P}_{\text{PVP}}$ rank. The number in brackets () indicates the $\mathbb{P}_{\text{IRF}}$ rank value.

Table 7.3: Tests that are discrepant and have a higher rank with $\mathbb{P}_{\text{PVP}}$ than with $\mathbb{P}_{\text{HIC}}$.

Test	Impact structure	Comment
	Child headform tests	
19100602	Wiper pivot	Late rise in acceleration
	Adult headform tests	
23050700	Above engine bolt	Strong late acceleration
23050701	Above engine bolt	Strong late acceleration
30030603	Above air intake	Late rise in acceleration
17040700	Above engine bolt	Strong late acceleration
02020700	Above engine bolt	Strong late acceleration
27060601	Above bonnet rib	Strong late acceleration
18120700	Above bonnet hinge	Late rise in acceleration
14120601	Above firewall	Strong late acceleration
27100600	Windscreen frame	Strong late acceleration

PVP in relation to the initial main peak in the acceleration. If the PVP is associated with a secondary peak it is labeled as a 'Strong late peak', and if the PVP is associated with the main peak in acceleration it is labeled 'Late rise in acceleration'. These two types of pulse shape have similar mechanisms for the discrepancy in ranking.

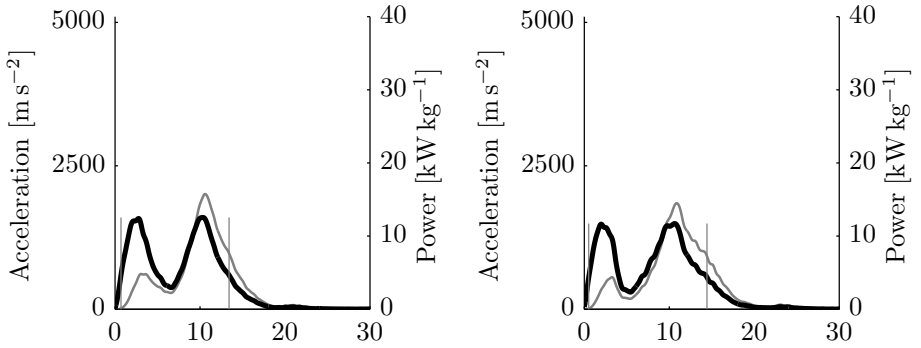

(a) Test 23050700 (A3C(cd)),
HIC_∞ = 1318 (55),
PVP = 15.8 kW kg^{-1} (94).

(b) Test 23050701 (A4C(cd)),
HIC_∞ = 1205 (56),
PVP = 14.5 kW kg^{-1} (89).

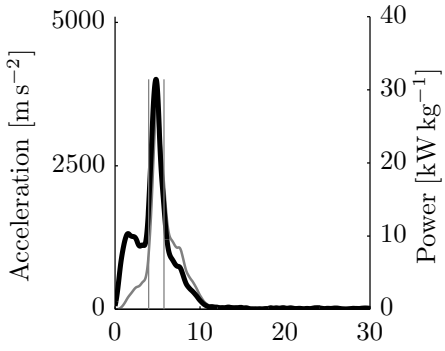

(c) Test 30030603 (A3A),
HIC_∞ = 2946 (69),
PVP = 28.9 kW kg^{-1} (101).

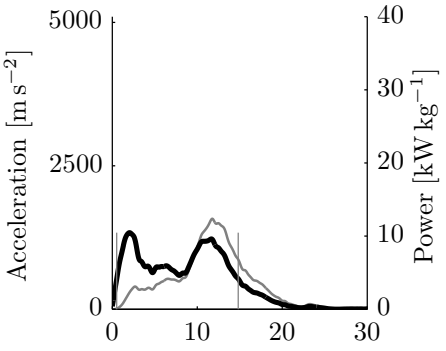

(d) Test 17040700 (A4D),
HIC_∞ = 1110 (47),
PVP = 12.4 kW kg^{-1} (75).

Figure 7.13: Adult headform tests where $\mathbb{P}_{\text{HIC}}$ rank is lower than $\mathbb{P}_{\text{PVP}}$ rank. The number in brackets () indicates the $\mathbb{P}_{\text{IRF}}$ rank value. Continued on the following page.

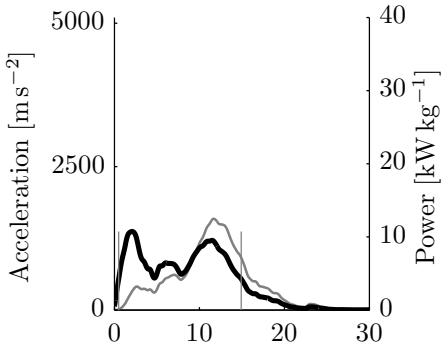

(e) Test 02020700 (A4D),
HIC_∞ = 1183 (48),
PVP = 12.5 kW kg^{-1} (73).

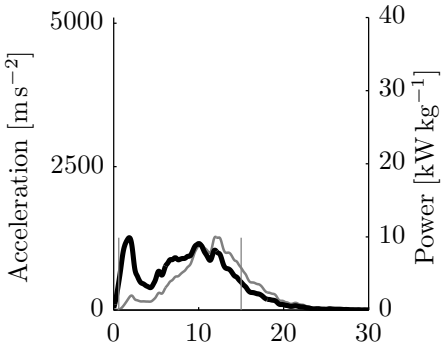

(f) Test 27060601 (A4C(c)),
HIC_∞ = 901 (61),
PVP = 10.0 kW kg^{-1} (79).

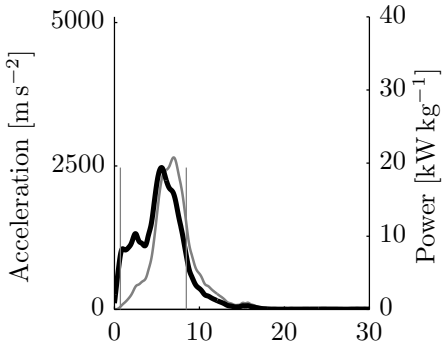

(g) Test 18120700 (A1A),
HIC_∞ = 2512 (67),
PVP = 20.8 kW kg^{-1} (86).

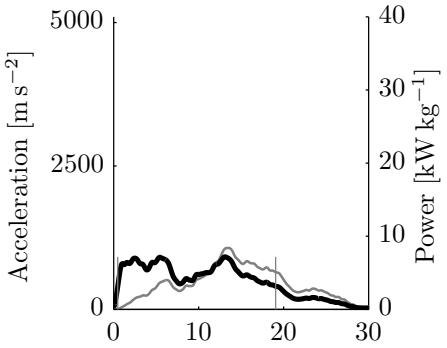

(h) Test 14120601 (A2D(cd)),
HIC_∞ = 726 (51),
PVP = 8.4 kW kg^{-1} (67).

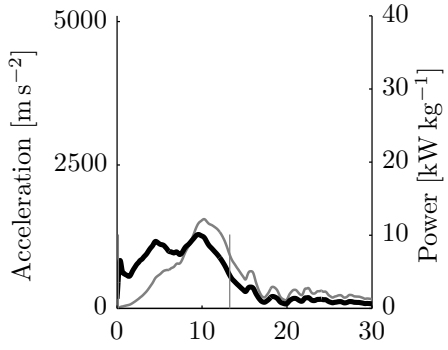

(i) Test 27100600 (A2C),
HIC_∞ = 1251 (50),
PVP = 12.2 kW kg^{-1} (66).

Figure 7.13: Adult headform tests where $\mathbb{P}_{\text{HIC}}$ rank is lower than $\mathbb{P}_{\text{PVP}}$ rank. The number in brackets () indicates the $\mathbb{P}_{\text{IRF}}$ rank value. Continued from previous page.

Pulse shapes with a late acceleration pulse

In most tests the higher ranking of $\mathbb{P}_{\text{PVP}}$ than with $\mathbb{P}_{\text{HIC}}$ is due to a strong late acceleration in the pulse shape. The strong late accelerations are mostly due to the headform interacting with the bonnet and then an under-bonnet structure, such as an engine bolt, later in the impact. In all these tests the strong late acceleration results in a second peak in PVP which has a higher value than the the peak in PVP associated with the first peak in acceleration.

The difference in ranking for these tests can be explained by considering the results of Chapter 4 where the theoretical pulse shapes were analysed. In that chapter a triangular pulse shape showed that the value of the PVP increased as the location of the apex of the triangle moved later into the impact (in Figure 4.7). The value of the HIC_∞, however, has been shown by Chou and Nyquist (1974) to remain constant regardless of the location of the apex in the impact sequence. The tests of this type can be considered to be the sum of an early peak triangle impact and a late peak triangle impact. The component with the late peak causes the PVP to have a high value. Meanwhile, the HIC_∞ is not accentuated by this late peak in acceleration as much as the PVP is accentuated.

Tests with a late rise in the acceleration

There are three tests that have a late rise in acceleration. In each of these tests the acceleration rises rapidly at the start of the impact, then flattens for a short time and then rises again toward a high peak in acceleration. The higher rank of $\mathbb{P}_{\text{PVP}}$ is caused by the distribution of the acceleration with time. For these tests, the peak in acceleration occurs later in the impact pulse shape than when the acceleration rises steadily towards its peak value. This additional time means that the PVP has a higher value than when the acceleration rises steadily (because the PVP is proportional to the acceleration times the integral of acceleration).

Table 7.4: Tests that are discrepant and have a lower rank with $\mathbb{P}_{\text{PVP}}$ than with $\mathbb{P}_{\text{HIC}}$.

Test	Impact structure	Comment
	Child headform tests	
26060603	Above bonnet ribs	Front loaded pulse
26060601	Above bonnet rib	Front loaded pulse
02050702	Above wiper pivot	Front loaded pulse
20120601	Above bonnet rib	Front loaded pulse
06030601	Above engine cover bolt	Front loaded pulse
27020701	Above bonnet rib	Front loaded pulse
05020802	Above bonnet rib	Front loaded pulse
27020702	Above bonnet rib	Front loaded pulse
13120600	Above bonnet rib	Front loaded pulse
	Adult headform tests	
30030602	Above bonnet rib	Front loaded pulse

7.4.2 Tests with a higher $\mathbb{P}_{\text{HIC}}$ rank than $\mathbb{P}_{\text{PVP}}$ rank

Nine tests with the Child headform were identified in the top 10 most discrepant tests with a higher ranking with $\mathbb{P}_{\text{HIC}}$ than with $\mathbb{P}_{\text{PVP}}$. These are shown in Figure 7.14. The one Adult headform test found is shown in Figure 7.15. Table 7.4 summarises the tests and the structures at which they were aimed. Each of the tests has a front loaded acceleration pulse shape.

The front loaded pulse shapes tend to produce low values of HIC for a given stopping distance (Wu and Beaudet, 2007). In Chapter 4 the front loaded triangle pulse shape was also shown to be a good candidate for a low value of PVP. In comparison with the other pulse shapes in the data set it appears that a front loaded pulse shape is more crashworthy according to PVP than it is according to HIC_∞.

The reason why these tests are ranked higher with $\mathbb{P}_{\text{HIC}}$ than with $\mathbb{P}_{\text{PVP}}$ can be found in the theory developed in Chapter 4. One of the findings of that chapter was that for a triangle pulse shape, the value of the PVP was dependent on the location of the peak in the acceleration in the pulse shape. An early peak resulted in a lower value of PVP. This, however, is not the case for the HIC_∞ which has no dependence on the location of the peak for

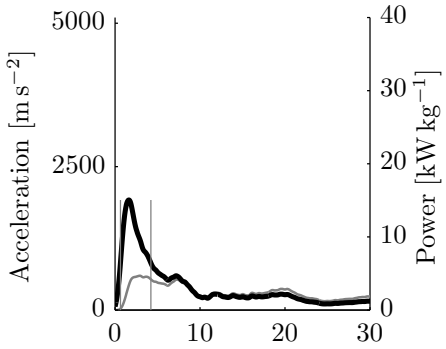

(a) Test 26060603 (C4B(ab)),
HIC_∞ = 817 (107),
PVP = 4.7 kW kg^{-1} (39).

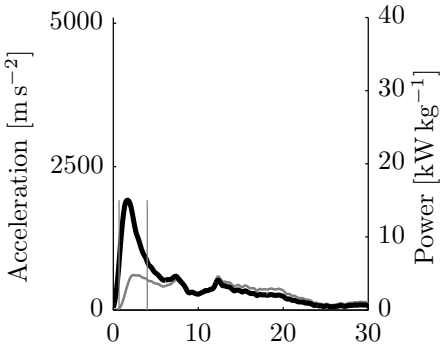

(b) Test 26060601 (C3A(ab)),
HIC_∞ = 817 (95),
PVP = 4.8 kW kg^{-1} (28).

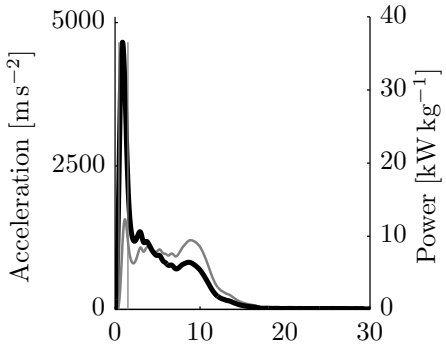

(c) Test 02050702 (C6A),
HIC_∞ = 2897 (79),
PVP = 12.3 kW kg^{-1} (21).

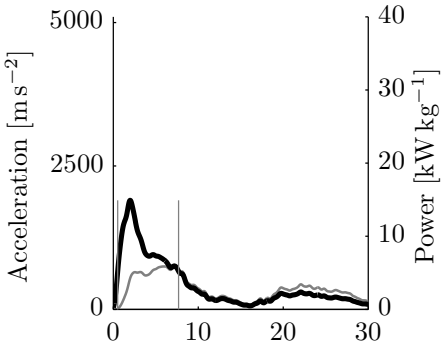

(d) Test 20120601 (C3A(ab)),
HIC_∞ = 976 (87),
PVP = 5.9 kW kg^{-1} (38).

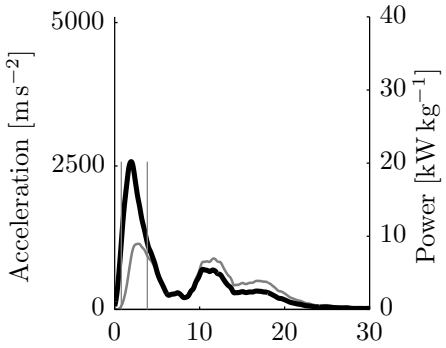

(e) Test 06030601 (C2B),
HIC_∞ = 1659 (86),
PVP = 9.0 kW kg^{-1} (42).

Figure 7.14: Child headform tests where $\mathbb{P}_{\text{HIC}}$ rank is higher than $\mathbb{P}_{\text{PVP}}$ rank. The number in brackets () indicates the $\mathbb{P}_{\text{IRF}}$ rank value. Continued on the following page.

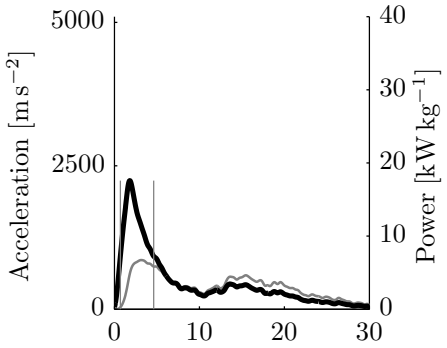

(f) Test 27020701 (C3A(ab)),
HIC$_\infty$ = 1209 (56),
PVP = 6.7 kW kg^{-1} (12).

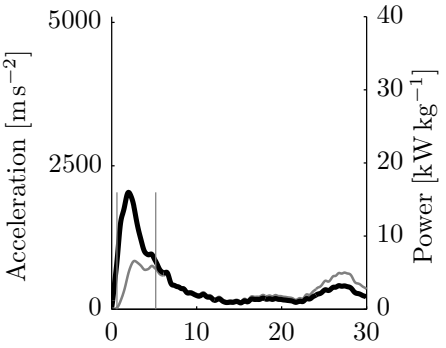

(g) Test 05020802 (C3A(ab)),
HIC$_\infty$ = 1094 (68),
PVP = 6.6 kW kg^{-1} (27).

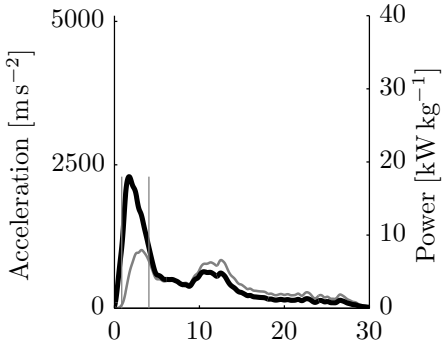

(h) Test 27020702 (C3C),
HIC$_\infty$ = 1396 (75),
PVP = 8.0 kW kg^{-1} (34).

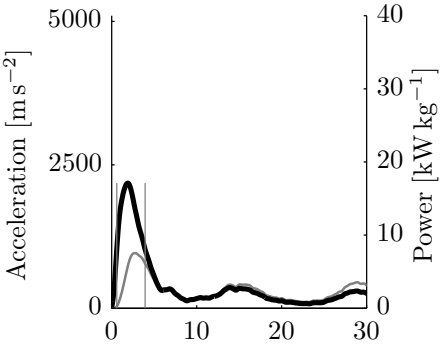

(i) Test 13120600 (C3B),
HIC$_\infty$ = 1339 (126),
PVP = 7.5 kW kg^{-1} (80).

Figure 7.14: Child headform tests where $\mathbb{P}_{\text{HIC}}$ rank is higher than $\mathbb{P}_{\text{PVP}}$ rank. The number in brackets () indicates the $\mathbb{P}_{\text{IRF}}$ rank value. Continued from previous page.

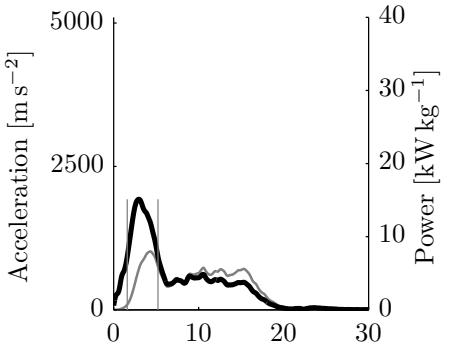

(a) Test 30030602 (A3D(cd)),
HIC_∞ = 1130 (33),
PVP = 8.0 kW kg^{-1} (15).

Figure 7.15: Adult headform test where $\mathbb{P}_{\text{HIC}}$ rank is higher than $\mathbb{P}_{\text{PVP}}$ rank. The number in brackets () indicates the $\mathbb{P}_{\text{IRF}}$ rank value.

a triangle pulse shape. The pulse shapes shown in Figure 7.14 have very early peaks in their acceleration.

7.4.3 Analysis of the differences between HIC_∞ and PVP

The tests that showed most difference between the HIC_∞ and the PVP can be characterised by the way the temporal distribution of the acceleration pulse shape was considered by the PVP. For instance, all the tests with a higher ranking of $\mathbb{P}_{\text{HIC}}$ than with $\mathbb{P}_{\text{PVP}}$ had acceleration pulse shapes that peaked early and then fell rapidly. While the tests with a lower ranking of $\mathbb{P}_{\text{HIC}}$ than with $\mathbb{P}_{\text{PVP}}$ all had significant parts of their acceleration occur in later parts of the impact sequence.

The difference between these two IRFs leads to an important question: what is the biomechanical effect of the location of the peaks in acceleration within an impact pulse? In Chapter 5 an early peak in the acceleration was shown to reduce the required stopping distance to achieve a particular level of an IRF. But it is beyond the scope of this thesis to determine what is the biomechanical effect of a difference in the temporal location of the acceleration.

These results also challenge the construction of HIC for pedestrian testing. In particular, it is not obvious which of HIC or PVP is the more biomechanically valid IRF. The PVP emphasises that impacts that occur later in the

sequence are less tolerable than impacts that occur earlier in the impact sequence, especially the impacts with rigid under-bonnet structures. It seems reasonable from an injury view point that a designer should minimise impacts with rigid structures. However it is not clear that an impact with a rigid structure that occurs late in the impact pulse would necessarily be more injurious than one that occurs early in the impact pulse as is suggested by the PVP. This discrepancy between the HIC and PVP warrants further investigation from an injury biomechanics point of view.

Important, in the context of this thesis, is that the use of PVP in a test protocol would discourage late peaks in the acceleration pulse shape. Late peaks, due to bottoming out (the bonnet deforming far enough that contact is made with an under-bonnet structure), would be penalised more with the PVP than it is with HIC. As a result, designs made for an assessment with PVP would be more likely to avoid bottoming out than those made for assessment with HIC.

7.5 Analysis of the discrepant pulse shapes between HIC and peak acceleration

The tests identified as being discrepant between the ranks of $\mathbb{P}_{\text{HIC}}$ and the ranks of $\mathbb{P}_{a_m}$ are shown in Figure 7.1 and Figure 7.2 for the tests performed with the Child headform and the Adult headform respectively. In each figure the difference rank of pulse shape contribution is cross plotted against the rank of $\mathbb{P}_{\text{HIC}}$. In subsection 7.5.1 the tests with a high $\mathbb{P}_{\text{HIC}}$ rank and a low $\mathbb{P}_{a_m}$ rank are investigated and in subsection 7.5.2 the tests with a low $\mathbb{P}_{\text{HIC}}$ rank and a high $\mathbb{P}_{a_3}$ rank are investigated. The tests investigated are those labeled in Figures 7.16 and 7.17.

7.5.1 Tests with a higher $\mathbb{P}_{\text{HIC}}$ rank than $\mathbb{P}_{a_m}$ rank

The pulse shapes within the top ten most discrepant tests with the Child headform, and with $\mathbb{P}_{a_m}$ ranked higher than $\mathbb{P}_{\text{HIC}}$, are shown in Figure 7.18. Each of these tests has a flat pulse shape between either end of the HIC evaluation window. There aren't any peaks in acceleration that dominate

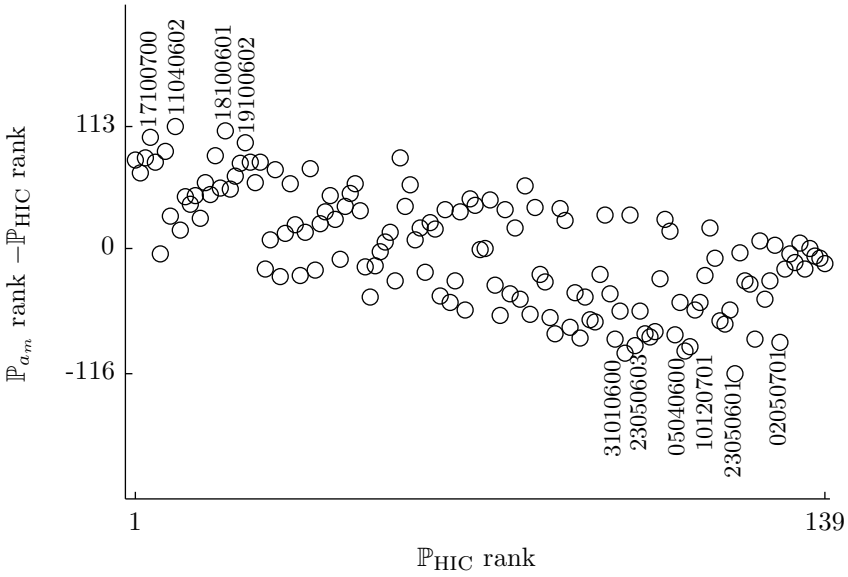

Figure 7.16: Child headform tests with discrepant ranking between $\mathbb{P}_{\text{HIC}}$ and $\mathbb{P}_{a_m}$.

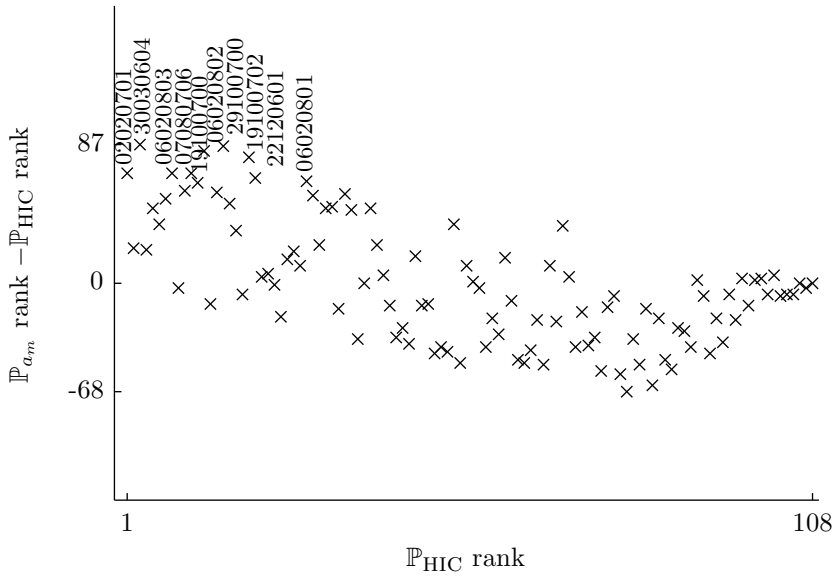

Figure 7.17: Adult headform tests with discrepant ranking between $\mathbb{P}_{\text{HIC}}$ and $\mathbb{P}_{a_m}$.

Table 7.5: Tests with a higher ranking of $\mathbb{P}_{\text{HIC}}$ than ranking of $\mathbb{P}_{a_m}$. Each of the pulse shapes is a flat pulse shape.

Test	Impact structure
Child headform tests	
23050601	Above bonnet rib
05040600	Above bonnet rib
31010600	Above weather strip
10120701	Edge of bonnet
23050603	Above bonnet rib
02050701	Above plenum

the appearance of these pulse shapes. In Chapter 4 it was shown that the square pulse shape was the most crashworthy pulse shape for the a_m from the theoretical pulse shapes examined in that chapter. These pulse shapes are examples of how a square pulse shape can be nearly achieved in a real test. There are no tests of this type with the Adult headform.

Table 7.5 summarises the location and identifies that the flat nature of the pulse shape is an important feature in each of these tests.

The value of the HIC functional evaluated at every value of t_1 and t_2 can be shown on a contour plot. Figure 7.19 shows, as an example of these flat pulse shapes, the contour plot of test 05040600. The maximum HIC for these flat pulse shapes occurs at the summit of a hill of HIC values. Any difference in the location of t_1 or t_2 for the evaluation window results in a much lower HIC value. This peak feature in the HIC contour plot of these pulse shapes will be contrasted with an extended ridge feature in the contour plot of the pulse shapes identified in the next section (shown in Figure 7.22).

7.5.2 Tests with a lower $\mathbb{P}_{\text{HIC}}$ rank than $\mathbb{P}_{a_m}$ rank

The tests with a lower $\mathbb{P}_{\text{HIC}}$ rank than $\mathbb{P}_{a_m}$ rank are shown in Figure 7.20 and Figure 7.21. Figure 7.20 shows the tests with the Child headform and Figure 7.21 shows the tests with the Adult headform. Table 7.6 summarises the important parts of each test.

Each of the tests shown in Figures 7.20 and 7.21 has two phases in its pulse shape. The first phase is a peak in acceleration that has a brief duration at

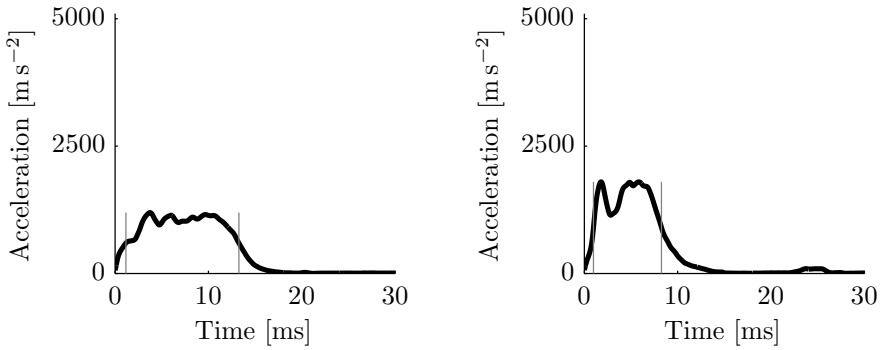

(a) Test 23050601 (C2D(cd)), HIC_∞ = 1255 (121), a_m = 122 g (5).

(b) Test 05040600 (C2C), HIC_∞ = 2155 (111), a_m = 183 g (16).

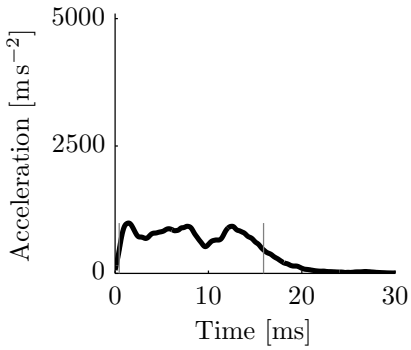

(c) Test 31010600 (C5D), HIC_∞ = 838 (99), a_m = 101 g (2).

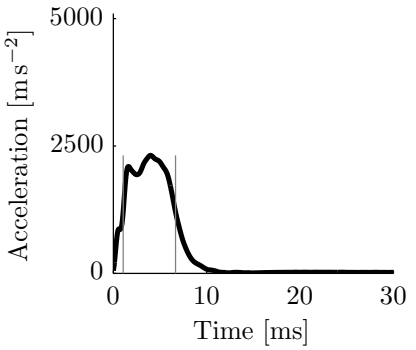

(d) Test 10120701 (C1C), HIC_∞ = 3358 (112), a_m = 236 g (21).

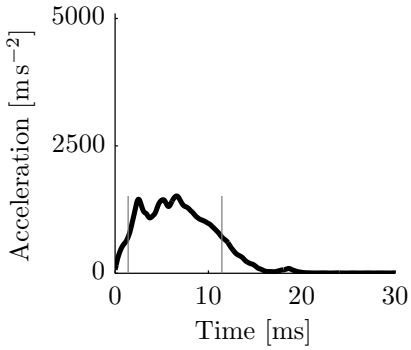

(e) Test 23050603 (C5D(cd)), HIC_∞ = 1604 (102), a_m = 155 g (11).

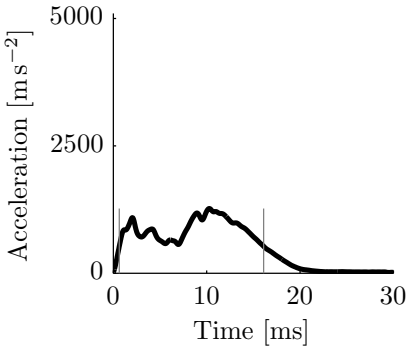

(f) Test 02050701 (C4B), HIC_∞ = 1182 (130), a_m = 130 g (43).

Figure 7.18: Child headform tests where $\mathbb{P}_{\text{HIC}}$ rank is higher than $\mathbb{P}_{a_3}$ rank. The number in brackets () indicates the $\mathbb{P}_{\text{IRF}}$ rank value.

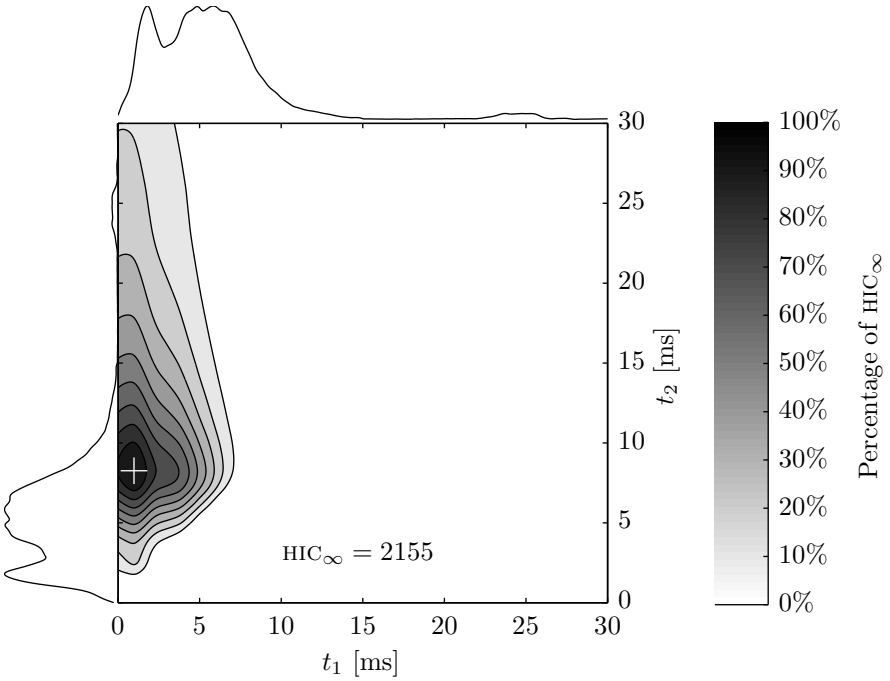

Figure 7.19: Contour plot of HIC for test 05040600. The peak HIC occurs at the time values indicated by the white cross.

the start of the impact. The second phase is a long duration of acceleration starting at a lesser value than the peak that either decreases in value over time or remains at a level value.

For pulse shapes of this type, the value of the HIC functional has an elongated ridge of near-maximum values, as shown in Figure 7.22. These near-maximum values occur when t_1 is before the start of the peak in acceleration, and t_2 anytime after the peak, during the second phase of the impact. This ridge of consistent near-maximum values of the HIC functional is in strong contrast with the localised region for the flat pulse shapes shown in the previous section.

These pulse shapes are consistent with those pulse shapes considered most crashworthy with HIC for standardised impact velocity and stopping distance. The early peak in acceleration during the first phase of the impact rapidly reduces the speed of the headform so that the remaining displacement occurs at a lower velocity and acceleration. The brief peak in accelera-

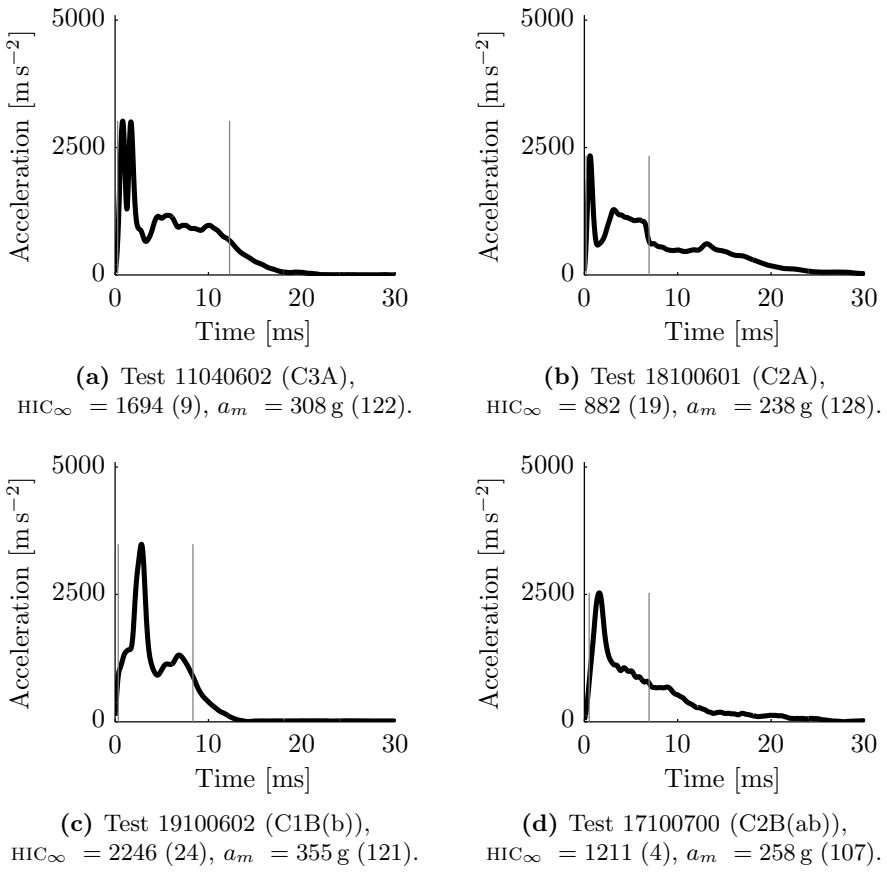

(a) Test 11040602 (C3A), HIC_∞ = 1694 (9), a_m = 308 g (122).

(b) Test 18100601 (C2A), HIC_∞ = 882 (19), a_m = 238 g (128).

(c) Test 19100602 (C1B(b)), HIC_∞ = 2246 (24), a_m = 355 g (121).

(d) Test 17100700 (C2B(ab)), HIC_∞ = 1211 (4), a_m = 258 g (107).

Figure 7.20: Child headform tests where $\mathbb{P}_{\text{HIC}}$ rank is lower than $\mathbb{P}_{a_m}$ rank. The number in brackets () indicates the $\mathbb{P}_{\text{IRF}}$ rank value.

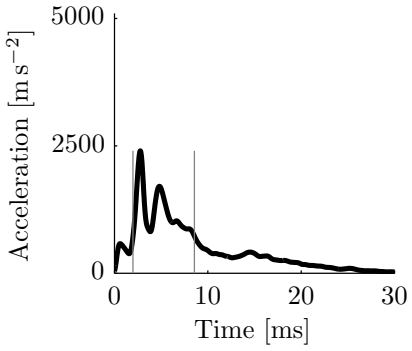

(a) Test 29100700 (A3C(cd)), HIC_∞ = 1133 (21), a_m = 245 g (102).

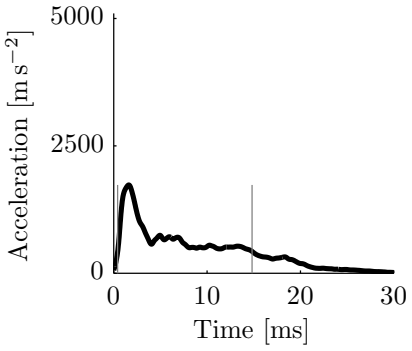

(b) Test 30030604 (A2D(d)), HIC_∞ = 651 (3), a_m = 177 g (90).

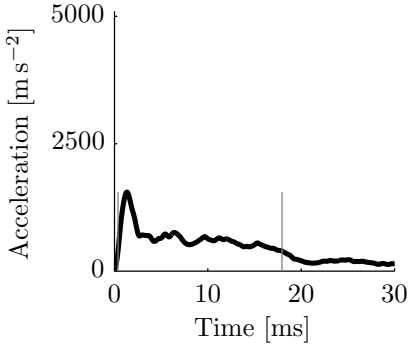

(c) Test 06020802 (A2D(cd)), HIC_∞ = 644 (16), a_m = 158 g (96).

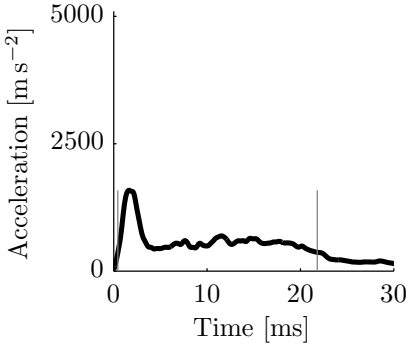

(d) Test 19100702 (A4D(acd)), HIC_∞ = 666 (4), a_m = 162 g (99).

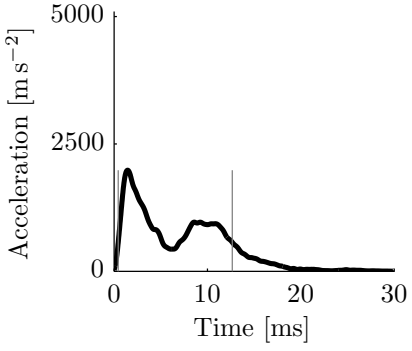

(e) Test 06020803 (A1D(d)), HIC_∞ = 1116 (11), a_m = 202 g (77).

Figure 7.21: Adult headform tests where $\mathbb{P}_{\text{HIC}}$ rank is lower than $\mathbb{P}_{a_m}$ rank. The number in brackets () indicates the $\mathbb{P}_{\text{IRF}}$ rank value. Continued on the facing page.

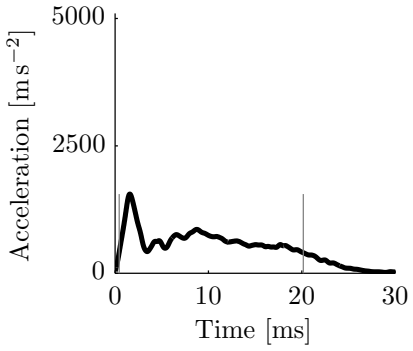

(f) Test 22120601 (A4D(cd)), HIC_∞ = 763 (13), a_m = 158 g (87).

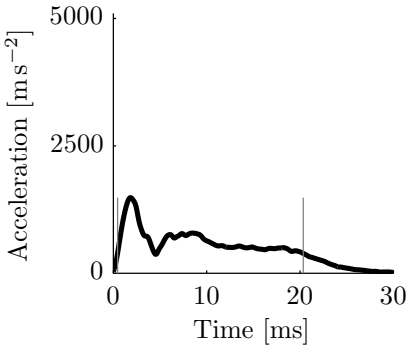

(g) Test 07080706 (A2D(bcd)), HIC_∞ = 705 (9), a_m = 151 g (80).

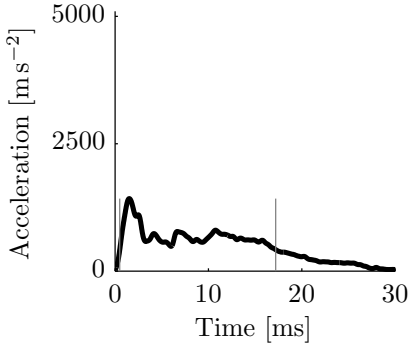

(h) Test 19100700 (A2D(cd)), HIC_∞ = 721 (14), a_m = 145 g (75).

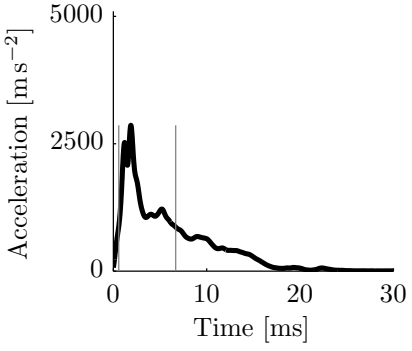

(i) Test 02020701 (A3B), HIC_∞ = 1592 (1), a_m = 292 g (70).

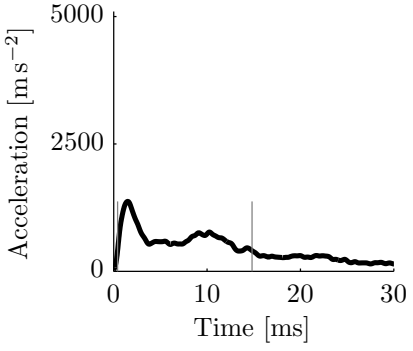

(j) Test 06020801 (A3C(cd)), HIC_∞ = 565 (33), a_m = 140 g (93).

Figure 7.21: Adult headform tests where $\mathbb{P}_{\text{HIC}}$ rank is lower than $\mathbb{P}_{a_m}$ rank. The number in brackets () indicates the $\mathbb{P}_{\text{IRF}}$ rank value. Continued from previous page.

Table 7.6: Tests with a lower ranking of $\mathbb{P}_{\mathrm{HIC}}$ than ranking of $\mathbb{P}_{a_m}$. All tests have an early peak in acceleration followed by a lower, flat or decreasing, period of acceleration.

Test	Impact structure
Child headform tests	
11040602	Wiper pivot
18100601	Wiper arm
19100602	Wiper pivot
17100700	Above bonnet rib
Adult headform tests	
29100700	Above wiper pivot
30030604	Above bonnet rib
06020802	Above bonnet rib
19100702	Above bonnet rib
06020803	Above bonnet rib
22120601	Above rear bonnet seal
07080706	Above bonnet rib
19100700	Above bonnet rib
02020701	Wiper pivot
06020801	Above bonnet rib

tion, however, causes the a_m to have a higher value than would be expected with flatter pulse shapes like those seen in the previous section.

7.5.3 Analysis of the differences between HIC and peak acceleration

Pulse shapes that are substantially flat, are discrepant with the $\mathbb{P}_{a_m}$ rank higher than the $\mathbb{P}_{\mathrm{HIC}}$ rank. Pulse shapes that have an early and brief peak in acceleration are discrepant with $\mathbb{P}_{a_m}$ rank higher than $\mathbb{P}_{\mathrm{HIC}}$ rank. These two pulse shape types are the only ones that were identified within the 10 most discrepant tests with both headforms.

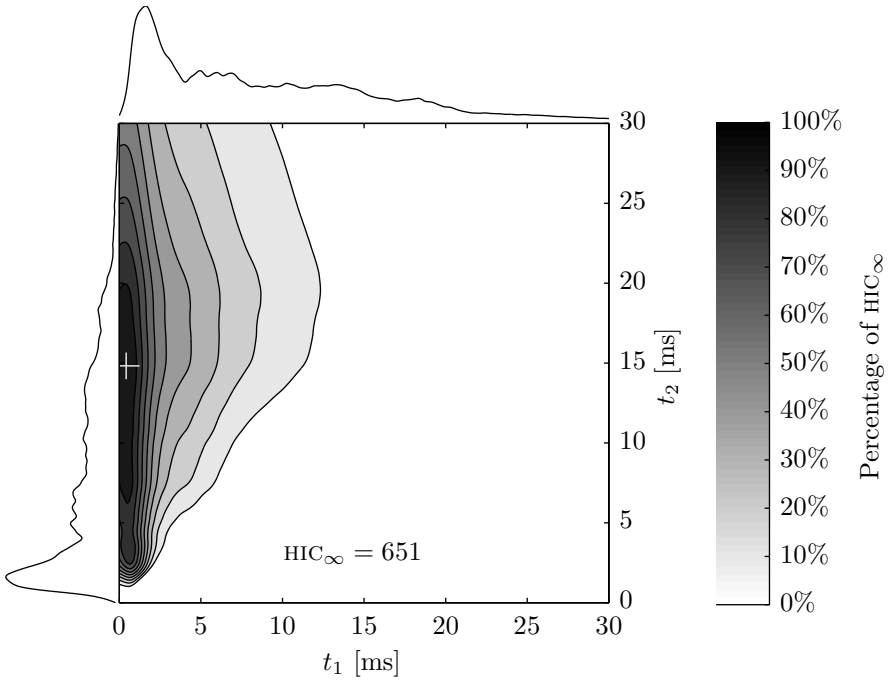

Figure 7.22: Contour plot of HIC for test 30030604. The peak HIC occurs at the time values indicated by the white cross.

7.6 Summary

In this chapter the important features of pulse shapes that lead to discrepancies between the HIC$_\infty$ pulse shape coefficient rank and the ranks of pulse shape coefficients of the other IRFs have been discussed. For each pair of IRFs, the tests identified had common characteristics that could be discussed. These provided insight into the types of acceleration pulse shapes that, for given stopping distance, impact velocity and coefficient of restitution, would be preferred over others in the data as ranked by various IRFs.

Two important observations were made from the discrepant tests with the $\mathbb{P}_{\text{HIC}}$ and $\mathbb{P}_{a_3}$ pair of IRFs that were then evaluated for the all tests in the data set. Each of the two could be used to predict the tests that would have discrepant values.

1. The duration of the HIC$_\infty$ evaluation window which identified tests that had narrow and tall acceleration segments.

2. The difference between the average acceleration of the pulse shape during the 3 ms and the a_3 value.

These two characteristics were shown to be related to each other during an impact.

Conceivably, if the a_3 was used to evaluate designs, a design may be produced that has a structure sufficiently rigid that the resulting high values of acceleration are finished so rapidly that the value of a_3 is very low. This, presumably, is not one of the intended features of the a_3 IRF and would be a poor result for safety. To that end, the HIC_∞ is a good IRF because it averages the acceleration over the pulse shape.

One important observation was made from the discrepant tests with the HIC_∞ and PVP pair of IRFs. This is the temporal distribution of the significant acceleration portions of the pulse shape.

Pulse shapes with one very early peak in acceleration had a lower rank with $\mathbb{P}_{\text{PVP}}$ while tests with a late peak in acceleration had a lower rank with $\mathbb{P}_{\text{HIC}}$. One consequence of using the PVP in a test protocol, then, would be that late peaks in acceleration, often caused by bottoming out, would be penalised more than if HIC were used in that test protocol. As a result, it may become a higher priority for designers to remove instances of bottoming out from their designs. At the same time, front loaded pulse shapes would be given even more priority if PVP were used as the IRF in a test protocol.

One important difference between the HIC_∞ and the a_m pair of IRFs was identified. Flat acceleration pulse shapes were noted as being discrepant with $\mathbb{P}_{a_m}$ ranked lower than $\mathbb{P}_{\text{HIC}}$ rank. Pulse shapes with an early and brief acceleration peak were identified as being discrepant with $\mathbb{P}_{\text{HIC}}$ ranked lower than $\mathbb{P}_{a_m}$ rank. Compared with HIC, the a_m encourages designs to have a flat acceleration pulse shape.

The main focus of this chapter, however, has been on the HIC IRF. The results have shown its properties as an IRF and these have been contrasted with the properties of the other IRFs. The HIC includes brief and dominating peaks in acceleration in its summary of pulse shape severity (unlike the a_3) and it does not emphasise the secondary acceleration or under-emphasise the

early acceleration (as PVP does). Whether these properties are strengths or weaknesses of the HIC is an area for biomechanical injury research.

It should be noted that these results are secondary to the broader analysis of crashworthiness made in other chapters. That analysis included the parameters of impact speed, stopping distance and coefficient of restitution. The secondary considerations of pulse shape types that each IRF finds preferable are subordinate to these other parameters. It is only when these parameters are factored into the analysis that the pulse shapes shown in this chapter are revealed. Nevertheless, the consequences coming from the choice of a particular IRF for a test protocol, intended or otherwise, should be understood. The way that different IRFs evaluate different pulse shapes, as shown in this chapter, is one of those consequences.

Chapter 8

Discussion, recommendations and conclusions

8.1 Summary

Much of the research addressing the severity of impacts to the head has centered around describing the mechanisms of injury and deriving an IRF that reflects these mechanisms. As concluded by Newman (1998):

> [This research] will no doubt continue as biomechanical engineers and others continue to search for ways to reduce the risk of brain injury.

It is assumed, that an IRF based on dummy kinematics can be found that correlates with the the mechanisms of injury (for example Marjoux et al., 2008). The validity of this assumption has been debated (Newman, 1980), but assuming such an IRF exists, then it can be used to differentiate between vehicle designs that are crashworthy and those that are not. This thesis has not concerned itself with the mechanisms of injury, but has concerned itself with the similarities and differences between several IRFs that are available for use with the dummies and headforms in current use. The basis for doing so is that differences in IRFs can only affect injury to the extent that they imply differences in vehicle design.

Several IRFs are used in various test protocols for automotive products and helmets including the HIC, a_m and a_3 (Hess et al., 1980; Newman, 1993). Of these, the HIC is the one most often used in vehicle testing applications. In addition, other IRFs that have been recently proposed such as the PVP (Neal-Sturgess et al., 2001) and the HIP (Newman et al., 2000b) are ready for use in test protocols once appropriate thresholds are agreed upon.

These more recent IRFs were proposed on the grounds of biofidelity. The HIP was proposed on the basis that is was a portrayal of the Wayne State Tolerance Curve that had a concise physical meaning, being the rate of change of kinetic energy (Newman et al., 2000b). The PVP was based on the principle of virtual power (Neal-Sturgess, 2002) applied to injury biomechanics. Because it was shown during the thesis that the PVP and the HIP were very similar only the PVP was extensively explored in the thesis.

Implicit in this quest for a better IRF has been the assumption that a better IRF will lead to better and changed designs, in respect of head protection. If this assumption does not hold then it would render this quest as rather

pointless because the final designs — the ones that could improve head injury outcomes in real injury crashes — would not change to become more crashworthy.

The properties of HIC have been extensively investigated by authors such as Chou and Nyquist (1974). Despite this, the equivalent properties of three other IRFs had hitherto not been investigated. Furthermore, the assumption that designs would change with different IRFs had not been adequately researched.

Consequently, the purpose of the thesis was to explore the hypothesis that designs would change with the choice of the currently available IRFs. A finding that the choice of IRF is an important determinant in the final design outcome would reinforce the need to invest time and resources into determining the best IRF to evaluate head injury and to then implement this IRF in important test protocols. Alternatively, finding that the choice of IRF does not substantially affect the design principles would suggest that these resources would be more appropriately spent on other aspects of test protocol development to improve safety. An intermediate finding between these two extremes would suggest an appropriate relative investment be made in determining the best IRF to evaluate head injury potential and to then implement this IRF in important test protocols.

The purpose of the thesis was met by:

1. determining the theoretical properties of various IRFs, and then

2. applying these theoretical results to tests that came from a real world test protocol.

Each of the IRFs are based on linear acceleration as this is the kinematic property that is measured in the pedestrian headform test used as the real world test protocol. Discussion of the limitations in restricting attention to linear acceleration is presented in Section 8.3.

The four specific aims of this thesis were described in Section 1.7. These aims and how they were met are summarised, in turn, in the following sections.

Table 8.1: Values of HIC, PVP_m, a_m and a_3 IRFs for various analytical pulse shapes. The HIC values are derived from Chou and Nyquist (1974). Identical to Table 4.11 on page 100.

Pulse	HIC	PVP	a_m	a_3
Half-sine	$\frac{0.4146}{g^{2.5}} {A_h}^{2.5} T_h$	$\frac{3\sqrt{3}}{4\,\pi} A_h^2\, T_h$	$\frac{A_h}{g}$	$\frac{A_h}{g} \cos\left(\frac{[1.5\,\text{ms}]\pi}{T_h}\right)$
Triangular	$\frac{0.2464}{g^{2.5}} {A_t}^{2.5} T_t$	$\frac{\sqrt{3}}{9\sqrt{1-k}} A_t^2 T_t$ (†) $\frac{k}{2} A_t^2 T_t$ (‡)	$\frac{A_t}{g}$	$\frac{A_t}{g}\left(1 - \frac{[3\,\text{ms}]}{T_t}\right)$
Square	$\frac{1}{g^{2.5}} {A_s}^{2.5} T_s$	$A_s^2 T_s$	$\frac{A_s}{g}$	$\frac{A_s}{g}$

†$0 \leq k \leq \frac{2}{3}$, ‡$\frac{2}{3} \leq k \leq 1$

8.1.1 Theoretical examination of each IRF

The initial focus of the thesis was the effect that the form of the acceleration pulse shape had on the value of each IRF. This was done on the basis that the pulse shape is the output measured from the structure being tested. Eight theoretical pulse shapes were used for this purpose and each was defined by its maximum acceleration A and its duration T. These were a square, a half-sine and six triangle pulse shapes. The triangle pulse shapes were differentiated by the position of their apex of acceleration, k, ranging from the very beginning of the pulse shape, $k = 0$, to the very end of the pulse shape, $k = 1$.

Importantly, the analytical values of each IRF for the theoretical pulse shapes were determined. These are summarised in Table 8.1. Most notable among these results is that the value of PVP increases as the apex of the triangle pulse shape moves further away from the beginning of the impact. This is in contrast to the other IRFs where the position of the apex has no bearing on the final value of the IRF for the triangle pulse shape for a given A and T.

To proceed further with the analysis, each pulse shape was made to be equivalent to all others by forcing each to have an identical stopping distance for a given impact velocity. Various rebound velocities for each pulse shape were considered by defining the coefficient of restitution that ranged between zero and one. Only those pulse shapes with a coefficient of restitution that was physically realistic were considered further in the analysis. Consequently with up to five different coefficients of restitution and eight pulse shapes

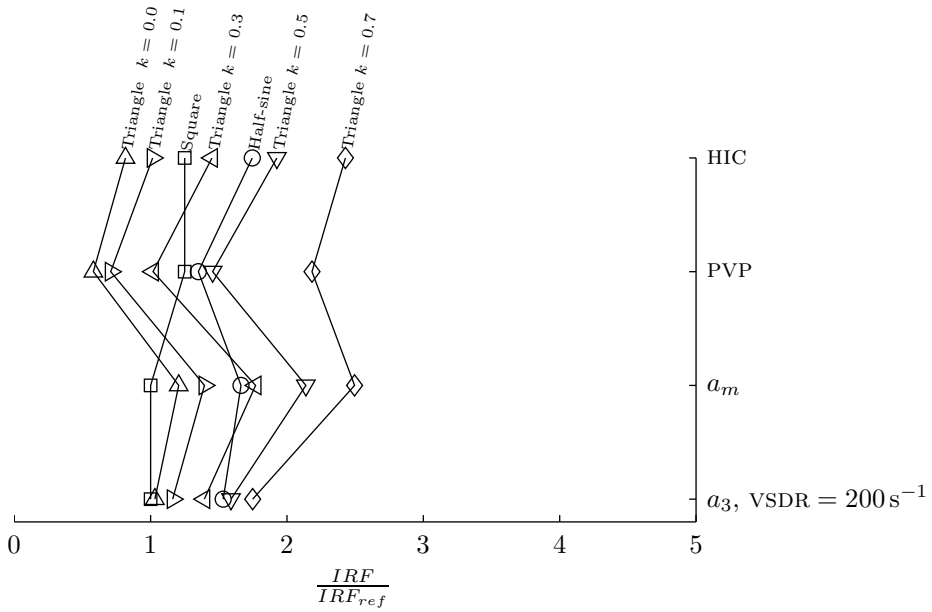

Figure 8.1: Comparison of relative effect of each pulse shape with $R = 0.25$, compared with a square pulse shape with $R = 0$, for each IRF.

the value of each IRF for 28 different impact scenarios was calculated and comparisons were made.

For the HIC and PVP IRFs, a triangle pulse shape with an early peak in acceleration was considered more crashworthy than any other pulse shape that was used for any given impact velocity and stopping distance. For both of these IRFs, all pulse shapes became more crashworthy as the coefficient of restitution decreased.

For the a_m IRF the square pulse shape was the most crashworthy pulse shape with the triangle pulse shapes with early acceleration peaks the next most crashworthy. The square pulse shape was also the most crashworthy pulse shape for the a_3 IRF as well, except where the ratio of the impact velocity and stopping distance was large, in which case the triangle with a late peak in acceleration was the most crashworthy. The relative effect of each pulse shape, with a coefficient of restitution equal to 0.25, for each IRF, is summarised in Figure 8.1. It is clear that a front loaded triangle pulse shape is a more crashworthy pulse shape for most IRFs.

The front loaded triangle pulse shape is the most crashworthy for most IRFs

because the early peak in acceleration rapidly reduces the velocity of the impactor at the start of the impact. In turn, this means that the impactor can traverse the remaining stopping distance with a lower level of acceleration than is possible with alternative pulse shapes. The constraint of a limited stopping distance makes this pulse shape more crashworthy than others. This is a realistic constraint to be considered in a design that has a limited deformation distance to manage the impact before contacting a more aggressive structure.

8.1.2 Effect of impact velocity, stopping distance and coefficient of restitution

The impact velocity, stopping distance and the coefficient of restitution also contribute to the value of each IRF and these were examined. It was shown, using results made available from the earlier analyses, that each IRF could be written as a power function of impact velocity, V, stopping distance, S, and coefficient of restitution, R, to a reasonable level of approximation. These power functions are shown in Equations (8.1) to (8.4).

$$\text{HIC} \propto V^4 S^{-1.5} (R+1)^1 \tag{8.1}$$

$$\text{PVP} \propto V^3 S^{-1} (R+1)^1 \tag{8.2}$$

$$a_3 \propto V^2 S^{-1} (R+1)^0 \tag{8.3}$$

$$a_m \propto V^2 S^{-1} (R+1)^0 \tag{8.4}$$

After taking the logarithm of both sides of these equations, a general form of Equations (8.1) to (8.4) can be obtained as shown in Equation (8.5).

$$\log(\text{IRF}) = p + m\log(V) + n\log(S) + q\log(R+1) \tag{8.5}$$

where m, n and q are unique coefficients for each IRF, and p accounts for the effect of pulse shape.

The data from 247 pedestrian headform tests were then used to determine the validity of the coefficients of this equation for each IRF in a real data set. 139 of these tests used a Child headform and 108 used an Adult headform. A linear regression was performed with this data for each headform, separately,

Table 8.2: Summary of data obtained from theory (bold) and regressions.

IRF	Headform	Coefficients $\log(V)$ m		$\log(S)$ n		$\log(R+1)$ q	
HIC	Child	**4**	4.9	**−1.5**	−1.8	**1**	0.5
	Adult		7.7		−1.9		1.1
PVP	Child	**3**	4.6	**−1**	−1.2	**1**	1.2
	Adult		5.4		−1.3		0.5
a_m	Child	**2**	1.6	**−1**	−0.9	**0**	−0.2
	Adult		2.6		−1.1		−0.6
a_3	Child	**2**	2.5	**−1**	−0.8	**0**	0.4
	Adult		5.3		−1.0		0.8

using Equation (8.5) as a theoretical basis for the linear regression. The coefficients from the linear regression were compared with the theoretical coefficients. This comparison is summarised in Table 8.2.

The best estimates for the coefficients of $\log(V)$ and $\log(R+1)$ are, in some cases, quite different than those predicted by the theory. For these parameters, however, there was only a small range of values used in the regression. Consequently, the confidence intervals of these estimates are broad and as a result the best estimates obtained from the regression are considered to be unreliable. On the other hand, because the range of values of $\log(S)$ in the data is much wider, the best estimates of the coefficient for this parameter are considered more reliable.

The values of the coefficient of $\log(S)$ are a little larger in magnitude than the predicted values. This differences were explained as due to the secondary, minor, peaks in the acceleration that are present in some tests tests in the data set. These secondary peaks in the acceleration were not modeled by the theoretical pulse shapes. The difference between the predicted value and the actual value for the coefficient of $\log(V)$ is also due to the difference in pulse shape between those used for the theoretical analysis and those in the data set.

For each of the regressions, the standard error of the residuals was used to

show that the unexplained variation in the regression could be adequately attributed to the variation in pulse shape in the real data.

At the conclusion of this section of the thesis, the relative contributions to the value of each IRF, apart from the pulse shape, had been identified. These other factors, namely the impact velocity, headform stopping distance, and coefficient of restitution are parameters which can be more or less controlled by the designer who is working with a particular test protocol or are specified by the test protocol. Aspects of the pulse shape may also be designed.

For the pedestrian headform test protocol, the designer has no real control over the impact speed, except to modify the angle of the bonnet which, in turn, modifies the normal impact velocity. In other test protocols, such as a full scale impact test for occupant protection, the designer could use other treatments to modify the impact velocity. An example of such a treatment could be a different restraint configuration to affect the velocity of the occupant.

Each IRF is affected differently by the impact velocity, headform stopping distance, and coefficient of restitution. The ratios of the relative contribution of each is different for each IRF. The HIC has a ratio of the contribution of impact velocity to the contribution of stopping distance to coefficient of restitution of $(4 : -1.5 : 1)$ which is different from PVP $(3 : -1 : 1)$, the a_m and the a_3 $(2 : -1 : 0)$. Consequently, a design that is subject to evaluation with HIC may evolve along a path that will differ from a design that is subject to some other IRF. This is because different design treatments will affect impact velocity, stopping distance and coefficient of restitution in slightly different ways. The optimal path for each IRF will adopt the treatment that lowers the IRF value the most. This will be subject to other constraints such as funding and time. However, despite these differences, the designs with each IRF will tend toward increased stopping distance and lowered impact velocity

8.1.3 Effect of the IRF on the testing result

In Chapters 6 and 7 the IRFs were compared with each other using tests from the data set. Initially this comparison occurred by considering all tests

in the data set together so that the comparison could be made statistically. This comparison was made in three different ways.

- The data was correlated using a Pearson correlation to show the raw correlation between each IRF.
- The IRFs were compared using a dichotomous classification of each test as either 'safe' or 'unsafe' with various pairs of IRFs.
- The ranking of data with each IRF was compared and correlated using a Spearman rank correlation.

The rank correlation method also provided a way to examine the pulse shape coefficient, $\mathbb{P}_{\text{IRF}}$, which is a measure of the contribution of the pulse shape to the value of the IRF for each test.

Linear correlation

Linear correlation is often used as a first step for analysis of correlation. Two correlations were performed for each pair of IRFs; one each from the data collected with each headform size. The correlation coefficients were similar for each headform. All of the IRFs were positively correlated. The square of the Pearson correlation coefficient ranged between 0.26 for the correlation between the a_m and a_3 IRFs and 0.91 for the correlation between the HIC_∞ and PVP IRFs. Each of the correlations was statistically significant.

In a real testing regime it is unlikely that data would be compared in this way. This is because the relationship between IRF value and injury risk is non-linear and an increase in IRF value of, say, three times does not necessarily indicate a commensurate increase in injury risk. As a result, tests in a data set are more likely to be compared using one of the other two methods that were considered.

'Safe' and 'unsafe' classification

An important function of an IRF is to discriminate between tests that are 'safe' and tests that are 'unsafe'. An important criterion that is used in automotive safety to identify a test as 'unsafe' is $\text{HIC} > 1000$.

Table 8.3: Summary of thresholds of each IRF that are conservative compared with HIC > 1000 in the data set of each headform.

Alternative IRF	Headform	Conservative threshold	Sens.	Spec.	PPV	NPV
PVP	Child	$6.6\,\mathrm{kW\,kg^{-1}}$	0.99	0.62	0.91	0.95
	Adult	$8.7\,\mathrm{kW\,kg^{-1}}$	0.94	0.76	0.88	0.88
a_3	Child	81.6 g	0.99	0.21	0.83	0.86
	Adult	95.2 g	0.96	0.79	0.89	0.91
a_m	Child	121 g	1.00	0.07	0.80	1.00
	Adult	126 g	0.94	0.34	0.73	0.76

A conservative criterion, was defined as one that, compared to HIC $= 1000$, was more likely to falsely classify a test as 'unsafe' than falsely classify a test as 'safe'. Using the tests in the data set, criteria using the other IRFs which are conservative were found. The thresholds for these conservative criteria are shown in Table 8.3.

These conservative thresholds were then compared with the thresholds found in the literature. The thresholds for a_m and PVP found in the literature tend to be more lenient than those shown in the table, while $a_3 = 80\,\mathrm{g}$ is similar to the threshold shown in the table.

As a result, it was argued that the choice of threshold is at least as important as the choice of IRF for a testing protocol.

By the definition used in this thesis, a conservative criteria is found when the value of the specificity of the alternate criterion is exceeded by the sensitivity and the PPV was exceeded by the NPV. Due to this definition, and the number of tests with HIC < 1000, the values of specificity of the alternate criteria, in some cases, are low. In particular the specificities of the criteria using a_3 (with the Adult headform) and a_m (with both headforms) are very low. These low values indicate the scatter of the data near these thresholds. As a result, many tests need to be classified as unsafe with the alternate criteria in order for the number tests classified as safe with the alternate criteria and unsafe with HIC > 1000 to be minimised.

Rank correlation

The tests could be ranked according to their IRF value. A rank correlation method was used to show that each IRF ranking is significantly correlated with the others. Spearman rank correlation coefficients, ρ, ranged between 0.598 for the rank correlation between the a_m and a_3 IRFs and 0.948 for the rank correlation between the HIC_∞ and PVP IRFs. This result was expected due to the effect of impact velocity, headform stopping distance and coefficient of restitution which was explored earlier in the thesis.

Rank correlation of pulse shape coefficients

The rank correlation method also provided an ideal way to explore the effect of the pulse shapes on the value of the IRF. The pulse shape coefficient, $\mathbb{P}_{\text{IRF}}$, for each test is obtained by subtracting the predicted effect of impact velocity and coefficient of restitution as well as the measured effect of stopping distance from the value of the IRF. The ranks of these pulse shape coefficients, for each IRF, were then compared. It was shown that the pulse shapes coefficients for HIC and PVP had a similar ranking. For the other pairs of IRFs, the ranks of pulse shape coefficients were more discrepant. For some of the cross plots of ranks involving the $\mathbb{P}_{a_m}$, negative correlation coefficients were found. This indicates that some crashworthy pulse shapes according to a_m are likely to be found uncrashworthy with an alternative IRF.

8.1.4 Comparison of individual discrepant tests

In this section the pulse shapes whose ranks were discrepant according to alternate IRFs were examined in detail. These tests were identified because they had discrepant rankings using the $\mathbb{P}_{\text{IRF}}$ values. The use of the ranks of $\mathbb{P}_{\text{IRF}}$ removed the effects of stopping distance, impact velocity and coefficient of restitution so that only the effect of pulse shape influenced the rankings.

Three pairs of $\mathbb{P}_{\text{IRF}}$ ranks were examined for discrepant tests. They were $\mathbb{P}_{\text{HIC}}$ and $\mathbb{P}_{a_3}$, $\mathbb{P}_{\text{HIC}}$ and $\mathbb{P}_{\text{PVP}}$ and $\mathbb{P}_{\text{HIC}}$ and $\mathbb{P}_{a_m}$. Several commonly occur-

ring features were observed in the pulse shapes of the discrepant tests and they were examined in detail.

The most discrepant pulse shapes between the $\mathbb{P}_{\text{HIC}}$ and $\mathbb{P}_{a_3}$ had a dominant feature which was a peak with a duration that was either slightly shorter or slightly longer than 3 ms. Tests whose feature was a short peak with a duration less than 3 ms had a higher ranking with $\mathbb{P}_{a_3}$ than with $\mathbb{P}_{\text{HIC}}$, and tests with a peak that was a little longer than 3 ms had a higher ranking with $\mathbb{P}_{\text{HIC}}$ than with $\mathbb{P}_{a_3}$. Keeping peaks shorter than 3 ms allows a designer to remove the impact energy 'for free', in that the IRF is not affected by such pulses.

The most discrepant pulse shapes between the $\mathbb{P}_{\text{HIC}}$ and the $\mathbb{P}_{\text{PVP}}$ were characterised by the position of the peaks of acceleration during the impact sequence. The tests that had late peaks in acceleration had higher rankings with $\mathbb{P}_{\text{PVP}}$ than with $\mathbb{P}_{\text{HIC}}$. The tests that had very early peaks in acceleration, had higher rankings with $\mathbb{P}_{\text{HIC}}$ than with $\mathbb{P}_{\text{PVP}}$. These results agreed with the theoretical predictions that were made in the earlier analysis of the PVP using the triangle pulse shape.

This highlights an important difference between the HIC and the PVP. That is the HIC is an averaged value, determined from the acceleration, while the PVP is the maximum value of the virtual power of the impact. As such, small changes in acceleration pulse shape, particularly later in the pulse shape, can have a minimal effect on an average quantity, like HIC but these can have a much larger effect on a quantity that chooses a maximum value, like PVP. The meaning of these differences, from a biofidelic point of view, remains open for investigation.

The most discrepant pulse shapes between $\mathbb{P}_{\text{HIC}}$ and $\mathbb{P}_{a_m}$ were those that were either flat pulse shapes, or pulse shapes with an early, brief, peak in acceleration which was bounded by a much larger HIC evaluation window. The flat pulse shapes, had lower ranks with $\mathbb{P}_{a_m}$, the pulse shapes with the brief peak in acceleration had lower ranks with $\mathbb{P}_{\text{HIC}}$. This reflects the same order of pulse shape crashworthiness for these two IRFs obtained from the theoretical pulse shape analysis and summarised in Figure 8.1.

Importantly, finding pulse shapes in the test data which are consistent with

the theoretical observations, makes the theoretical observations more tangible for anyone using those results.

8.2 Discussion

The thesis has concentrated on the aspects of a headform impact test that determine the value of an IRF. The thesis began and ended examining acceleration pulse shapes. In the first chapter, theoretical results were developed and in the last chapter real test data were examined. Between these analyses two further topics were studied. Firstly, there was analysis of impact velocity, stopping distance and coefficient of restitution. Secondly, there was analysis of the importance of an IRF in real testing scenarios.

These analyses were performed to examine how important the IRF is for determining final design outcomes reached as a result of a test protocol. To consider this question there are two perspectives that can be used: a macroscopic view of the trends in the data and a microscopic view of the details that exist within the data. In addition, several other factors which contribute to the final design were highlighted in the analysis. Each has a contribution to make to this final analysis and they are discussed below.

8.2.1 Macroscopic view of the trends

From a macroscopic viewpoint, the trend of the data is clear: a decrease in the value of one IRF is most likely to result in a decrease in the value of any alternative considered IRF. This trend has been explained through the contribution of several factors. In general, a decrease in the value of any IRF can be attributed to at least one of:

- an increase in stopping distance;
- a decrease in impact velocity;
- a decrease in coefficient of restitution; or
- a change in pulse shape so that the acceleration peak occurs earlier in the impact.

With this in mind, at a macroscopic level the choice of the IRF for a test protocol is relatively unimportant. Provided that designers are being challenged to meet targets for safety, then the range of strategies that they might adopt to meet those challenges, such as those listed above will be the same regardless of the IRF used.

8.2.2 Microscopic view of the detail

It is only once the detail of each IRF is considered that the differences among them emerge.

One difference is the relative importance of the impact velocity, stopping distance and coefficient of restitution on the value of each IRFs. This difference affects the ideal path of design improvements when only limited resources can be spent. For example, a designer may find that lowering the value of coefficient of restitution is a cost effective improvement if the design is being measured with HIC, but this would not be the case if it is being measured with a_m or a_3. Consequently, the evolution of design improvements will be different when different IRFs are being used for assessment.

Another difference is the effect of the pulse shape on the value of the IRF. Several examples of discrepant pulse shapes were shown in Chapter 7. The pulse shapes shown demonstrated that particular aspects of the pulse shapes are highlighted or ignored by the different IRFs. One example was the prominent acceleration features that were either just shorter than or just longer than 3 ms. These were ignored and highlighted respectively by the a_3. Another example is the very late acceleration peaks highlighted by the PVP. Consequently, design improvements focused on changing the pulse shape could be altered when different IRFs are used.

The differences between the details of each IRF will alter the strategies used by designers to improve their design depending on the IRF used in the test protocol.

Influence of the differences

There are two reasons why these microscopic differences between IRFs have only a limited influence on the design process. Firstly, it is unclear how important these differences are from an injury risk perspective; secondly, the design must normally affect a large area of possible impact sites.

Two impacts may have an identical value of an IRF but a different acceleration pulse shape or headform stopping distance. It is not clear if the probability of injury is changed for these impacts. Moreover, it is not clear to a designer whether it is more valuable to lower the value of an IRF by reducing the stopping distance or by reducing the coefficient of restitution or both. Consequently, until the relative importance to injury probability of stopping distance, impact velocity, coefficient of restitution, and pulse shape are elucidated, they cannot be treated differently from a design perspective.

Because of these problems that can make distinction between the IRFs difficult from a practical perspective, there is no real reason why one of these IRFs should be chosen over an alternative. An improvement in one IRF will normally lead to an improvement in an alternative IRF.

8.2.3 Other factors to consider

In addition to the effect of the IRF, this thesis has also highlighted other factors that should be considered in conjunction with the IRF. They are summarised below. They could be more important than the choice of IRF because they could have considerable influence on the result.

Choice of a threshold

It was shown that the choice of the threshold to form a criterion for an IRF is very important in distinguishing between 'unsafe' and 'safe' impacts. If the threshold is set at too high a value then too many impacts with be considered 'safe'. Consequently, the safety effect of the test protocol is likely to be negligible because most tests will be considered 'safe'. Alternatively, if the threshold is set at a value that is too low then the target value may be unattainable, or the cost to meet the target too high.

The target threshold should be set according to evidence based biomechanical thresholds. If this evidence does not exist, then, at a minimum, the threshold should not permit tests previously considered 'unsafe' to be considered as 'safe'. One way of ensuring an appropriate minimum threshold is chosen is to ensure that the threshold is conservative compared with a previously adopted criterion. A method for determining conservative thresholds was presented in this thesis.

Choice of the physical testing parameters

There are two main physical testing parameters that can affect the value of the IRF in the testing scenario. These are the mass of the impactor used in the test, and the velocity of the impactor for the test.

The relationship of each IRF with the impact velocity was derived theoretically and shown experimentally. The theoretical analysis showed that the value of HIC is proportional to the impact velocity to the power of four, the value of PVP is proportional to the impact velocity cubed and the value of a_m and a_3 is proportional to the impact velocity squared. Any change in the impact velocity used for the test protocol will accordingly affect the value of the IRF. Consequently, choice of impact velocity for a test protocol can be very influential in determining designs considered crashworthy. A structure subject to high impact velocities must allow for the deeper stopping distance.

The impact velocity is also determined by the impact angle. In the Euro NCAP pedestrian test protocol the firing angle is fixed relative to the ground. Consequently a bonnet which is perpendicular to this direction has to be designed to cope with this higher impact velocity. Conversely, a bonnet which is nearly parallel to the impact direction needs to cope with a much lower impact velocity.

In Chapter 3 a linear spring model was used to show that the maximum stopping distance of the headform was proportional to the square root of the mass of the headform. Consequently, a heavier headform needs a larger stopping distance than a lighter headform for both to have a similar IRF value. As a result, designs are formulated with the mass of the headform in mind.

These two physical testing parameters are determined as part of the design of the test protocol. Their judicious selection is an important aspect in determining the validity of a test protocol. If their selection is outside the range of normal impact values then this results in the test protocol becoming of low fidelity. On the other hand, if their values do not adequately capture the entire range of probable impact values then this also results in an ineffective test protocol. In a test protocol where a single mass and speed are defined for the test, then designers have an option to tune their design for this mass and speed. In a real impact, the mass and speed may be very different from those of the test protocol and as a result, the designs may be unsuitable because they are tuned only for the test mass and speed. The case for testing for pedestrian safety at different impact speeds was discussed by Hutchinson et al. (2011) and this may be one way of ensuring designs are not tuned to one particular set of impact conditions.

8.2.4 Summary

There is no doubt that there are some differences between the IRFs that have been trialled in this thesis. These differences are able to be found and quantified theoretically and verified experimentally. The most important of these differences is the effect of pulse shape on the value of each IRF. It is not evident, however, that these differences are large or important enough to make noticeable changes to the design outcomes as they have a lesser effect that of the impact velocity, stopping distance and coefficient of restitution.

To improve crashworthiness with any IRF considered here the headform stopping distance should be increased. This can be achieved by softening the impact structure and increasing the distance to stiffer structures, such as the engine, that are underneath it. Alternatively, the impact velocity should be reduced by changing the angle of the impact away from perpendicular. The HIC and PVP also suggest that the coefficient of restitution should also be reduced which could be achieved by increasing the permanent deformation caused by the impact.

Other items, that have a broader influence on the design outcomes than those cited as differences between the IRFs have also been identified. These include the threshold used to define a structure as ‘safe’ and the mass and

impact velocity of the impactors used in the test protocol. Appropriate selection of these items will also have a major effect on vehicle design and the consequent average risk posed by a design. As a result, sufficient attention should be given to these items because of the role they play in characterising a test protocol. This work should not be overshadowed by, and should be performed in concert with, research aimed at the design or selection of an IRF.

8.3 Discussion of the limitations and future work

The main limitation of this thesis is that it only considers, in-depth, four IRFs that are based on a measurement of linear acceleration. However, a significant part of research in head injury has focused on using an IRF that is not based on linear acceleration but is instead based on a rotational kinematic measurement such as rotational acceleration or change in rotational velocity. These were not considered here, however, because there are still many test protocols that use an IRF based on linear acceleration.

Analysing the effect of the IRFs based on rotational motion, on design outcomes, using similar techniques to those used in this thesis, would be an ideal topic for future research.

The rotational motion that was calculated for analysis of the stopping distance in this thesis could have been used for this purpose. However, there are important limitations of the test protocol as to the biofidelity of the measurement of angular motion in this test protocol. Fredriksson et al. (2007) demonstrated that a head-shaped, Hybrid III headform induced rotational motions in impacts scenarios where spherical headforms (like those used in the Euro NCAP protocol) did not. Furthermore, free flight headforms are not constrained by the influence of the torso and neck of the pedestrian, which could also contribute to the rotational motion of the impact device during the impact. Because the test protocol is not intended to produce a reliable biofidellic angular motion response to impact, it was not considered appropriate to examine this data in detail for the purposes of this study.

Another limitation of this thesis is that it did not consider the effect of the impact severity on injury risk. Instead, the crashworthiness of a design was

based entirely on the value of each IRF. The results of the thesis do raise several questions about the effect of the parameters that influence the value of each IRF on real world injury. In particular, it is not known how important the acceleration pulse shape is on injury response. It was shown in Chapter 4 and Chapter 7 that the pulse shape is important in determining the value of the IRF. It is also not known if the relationship of the IRFs with impact velocity, stopping distance and coefficient of restitution shown in Table 8.2 are valid in terms of real world injury or if they arise only because each IRF has been fitted to some measured injury data (the Wayne State Tolerance Curve described in Chapter 2). It may be desirable to conduct ethically responsible experiments, perhaps using an animal model, to examine the effect of pulse shape, impact velocity, stopping distance and coefficient of restitution on injury outcome, to resolve this problem.

The use of acceleration pulse shape as an indication of the properties of the impacted structure is another limitation. The acceleration pulse shape does not represent a contact model of impact — where material and geometric properties are used to determine acceleration as a function of displacement and velocity. Anyone who applies the results of this thesis to their application will need to experiment with the properties of their design to create their desired acceleration pulse shape.

8.4 Importance of this thesis for various stakeholders

This thesis has made advances in knowledge that have important ramifications for various stakeholders. These ramifications are discussed in the coming sections.

Regulatory and consumer testing organisations

Key stakeholders include those groups involved in developing test protocols for head injury safety. This thesis has demonstrated the differences between the IRFs based on linear acceleration. It has also shown that the ultimate design may not be dependent on the choice of IRF.

More importantly, this thesis has shown the importance of a correct selection of impact parameters, such as impact velocity and headform mass, as well as the appropriate selection of a threshold for the chosen IRF determine the final testing result. These parameters all affect the identification of tests that are considered 'safe'. The thesis has shown that emphasis should also be placed on these aspects of the test protocol.

Design engineers

From this thesis design engineers can be made aware of several properties of the IRFs that are an alternative to HIC. These properties include the effect that changes to pulse shape, impact stopping distance, impact velocity and coefficient of restitution have on each of these IRFs.

Members of the public

Members of the public can take heart from this thesis. Regardless of the IRF that is used to assess the product they are considering: vehicles, helmets, playgrounds or others, the final design would be similar whatever IRF was used for the testing. In particular, stopping distance will be made as large as possible. Consumers can be confident that, in this regard, an alternative choice of IRF would not have had a drastic influence on a determination of safety.

8.5 Conclusion

Returning to the original question, the choice of IRF can affect the design decisions in several ways and these have been shown throughout the thesis. From a broader perspective, however, these differences exist in conjunction with the other aspects of a test protocol. These other aspects, including the impact velocity of the test and the threshold set for safety, also offer an opportunity to improve safety of the products used by society than the choice of IRF. Consequently, commensurate resources should be dedicated to researching and improving the aspects of a test protocol that can make

the biggest difference to the products that are designed and tested for safety of the public.

Appendix A

Test results

The data for all headform tests are included in this chapter.

- Table A.1 includes the tests performed with the Child headform.
- Table A.2 includes the tests performed with the Adult headform.

Each test includes the pulse shape of the resultant linear acceleration. Each pulse shape is drawn on axes with identical horizontal and vertical scales. The horizontal axis shows the data recorded in the first 30 ms of the impact.

Table A.1: Summary of tests using Child headform.

Test ID	Bonnet Angle	V	S	R	Pulse shape	HIC_∞	PVP	a_3	a_m
01020600	18.8	10.49	0.037	0.19		4239	25.63	170	364
01020601	40.0	10.89	0.038	0.21		2621	15.99	172	286
01050700	30.1	10.91	0.061	0.15	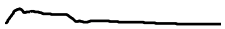	1093	8.64	115	150
02050700	30.1	10.93	0.066	0.26		1037	8.06	91	143
02050701	27.3	10.78	0.079	0.25		1182	11.67	107	130
02050702	36.8	10.99	0.037	0.22		2897	12.31	120	475
02060800	9.2	8.35	0.057	0.23	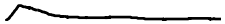	559	4.08	98	141
02060801	40.0	9.45	0.051	0.26		1306	10.63	130	143
02060802	11.7	8.47	0.047	0.25		820	6.42	89	135
05020800	6.9	9.61	0.048	0.32		988	8.22	117	212
05020801	10.6	9.94	0.046	0.25		1226	7.11	90	231
05020802	8.8	9.78	0.052	0.33		1094	6.60	106	208

Table A.1 – Child headform – continued from previous page.

Test ID	Bonnet Angle	V	S	R	Pulse shape	HIC_∞	PVP	a_3	a_m
05040600	18.5	10.50	0.045	0.25		2155	16.03	164	183
05040601	18.4	10.42	0.055	0.19		1127	9.13	103	167
05040602	14.3	10.18	0.028	0.32		4310	25.15	221	278
06020800	17.1	10.42	0.052	0.28		1246	9.48	115	144
06030600	12.0	10.00	0.046	0.26		1116	6.83	99	210
06030601	9.1	9.74	0.042	0.32	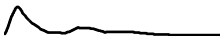	1659	8.97	121	263
06080700	10.7	9.85	0.058	0.21		711	4.60	88	184
06080701	11.7	9.99	0.059	0.18		699	6.05	87	183
06080702	18.0	10.44	0.058	0.30		843	6.59	91	187
06080703	9.6	9.81	0.053	0.32		1217	12.03	111	172
06120700	9.5	9.94	0.050	0.24		998	8.86	88	192
07030600	15.0	10.28	0.048	0.24		1402	9.01	117	185

Table A.1 – Child headform – continued from previous page.

Test ID	Bonnet Angle	V	S	R	Pulse shape	HIC_∞	PVP	a_3	a_m
07030601	8.2	9.69	0.047	0.36		1268	8.18	95	224
07030602	12.4	10.03	0.045	0.23	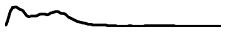	1463	11.81	108	182
07080704	11.2	9.98	0.052	0.28	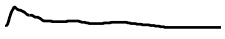	908	5.89	115	190
07120700	20.4	10.74	0.041	0.29		3338	19.98	199	285
08020800	10.6	9.85	0.047	0.27		1077	6.72	82	221
08030600	15.9	10.36	0.040	0.26		1790	12.26	114	246
08030601	13.4	10.12	0.027	0.33		4134	20.06	232	299
08120600	13.5	10.21	0.056	0.17	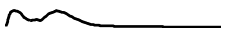	1240	11.79	112	155
08120601	10.5	9.90	0.058	0.27		1137	10.46	88	207
08120602	12.0	10.01	0.052	0.27	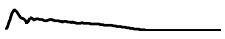	1105	7.30	90	192
08120603	5.5	9.41	0.036	0.27		2023	11.70	171	193
09050700	14.9	10.24	0.042	0.29		2234	15.27	167	199

Table A.1 – Child headform – continued from previous page.

Test ID	Bonnet Angle	V	S	R	Pulse shape	HIC_∞	PVP	a_3	a_m
09050701	12.5	10.05	0.067	0.31	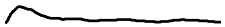	751	5.35	111	157
10040600	21.4	10.74	0.060	0.32		1070	9.44	101	172
10050700	13.8	10.15	0.059	0.29		813	6.33	103	175
10050701	20.3	10.60	0.049	0.37		2523	18.46	170	193
10080703	9.6	9.80	0.054	0.30		1126	10.04	119	157
10120700	9.7	9.97	0.057	0.26		819	5.87	79	183
10120701	12.5	10.12	0.033	0.31		3358	20.69	199	236
11040600	27.6	10.96	0.072	0.25		1691	15.48	141	194
11040601	28.0	10.92	0.052	0.31		2576	19.93	179	246
11040602	28.0	10.90	0.045	0.37		1694	11.50	95	308
11040603	20.9	10.59	0.056	0.31		1005	7.25	94	171
11040604	21.6	10.66	0.054	0.27		1300	10.30	100	170

Table A.1 – Child headform – continued from previous page.

Test ID	Bonnet Angle	V	S	R	Pulse shape	HIC_∞	PVP	a_3	a_m
11090600	16.8	10.37	0.058	0.24	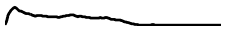	1161	8.96	104	166
11090601	17.2	10.40	0.061	0.26	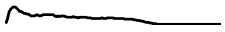	952	7.15	88	164
11090602	17.2	10.32	0.057	0.30	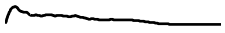	971	7.69	93	167
12090600	18.7	10.47	0.062	0.00		1037	7.79	100	159
12090601	16.3	10.30	0.049	0.27		1878	14.41	118	194
13120600	10.0	9.82	0.057	0.25		1339	7.54	119	222
13120601	16.0	10.36	0.057	0.08	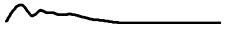	1014	7.35	83	169
13120602	10.9	9.97	0.060	0.17	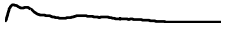	822	5.58	123	161
13120603	9.9	9.83	0.037	0.23	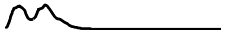	2264	18.70	106	226
15010800	40.0	11.11	0.036	0.27		4430	33.49	202	376
15050700	11.0	9.90	0.031	0.37		2986	18.54	180	236
15050701	16.6	10.33	0.060	0.24		918	7.89	84	149

Table A.1 – Child headform – continued from previous page.

Test ID	Bonnet Angle	V	S	R	Pulse shape	HIC_∞	PVP	a_3	a_m
15100700	40.0	11.15	0.033	0.23		3269	17.52	200	299
15110700	50.0	10.80	0.041	0.28		1965	12.13	160	193
15110701	50.0	10.81	0.041	0.26		2378	14.96	156	293
16010800	31.7	11.02	0.034	0.28		5087	32.10	206	360
16010801	25.8	10.86	0.029	0.32		5761	31.36	211	419
16100700	9.2	9.81	0.040	0.31		1537	7.99	133	240
16110700	36.5	11.10	0.034	0.27	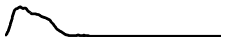	3781	18.70	208	274
16110701	32.0	11.02	0.052	0.31	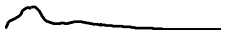	1505	11.96	131	213
16110702	32.5	11.03	0.046	0.21	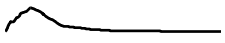	2014	13.36	171	220
16110703	31.3	10.97	0.043	0.26	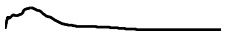	1916	12.85	150	204
17010801	9.2	9.72	0.040	0.29		1294	8.54	119	249
17010802	9.5	9.74	0.037	0.24	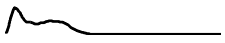	1719	11.43	113	248

Table A.1 – Child headform – continued from previous page.

Test ID	Bonnet Angle	V	S	R	Pulse shape	HIC_∞	PVP	a_3	a_m
17100600	33.0	11.23	0.074	0.22		1446	14.91	145	178
17100700	10.3	9.88	0.041	0.27		1211	6.68	107	258
17100701	40.0	11.10	0.042	0.29		2799	16.86	180	218
17100705	11.7	10.02	0.036	0.34		1762	11.65	123	242
18010700	39.0	11.21	0.033	0.30		4043	22.46	193	304
18010701	40.0	11.19	0.032	0.25		6201	34.80	167	481
18100600	40.3	11.14	0.073	0.31		969	9.10	89	316
18100601	36.5	11.17	0.067	0.20		882	7.25	109	238
18100700	40.0	11.16	0.039	0.41		2443	13.68	176	200
18120701	25.7	10.87	0.029	0.28		3454	17.10	198	350
19060800	40.0	11.20	0.061	0.24		2030	15.34	163	192
19060801	11.7	10.02	0.061	0.27		1110	8.46	98	138

Table A.1 – Child headform – continued from previous page.

Test ID	Bonnet Angle	V	S	R	Pulse shape	HIC_∞	PVP	a_3	a_m
19090600	41.0	10.99	0.060	0.20		2613	17.23	175	261
19090601	41.4	11.16	0.061	0.23		3305	22.03	207	256
19100600	40.0	11.13	0.092	0.25		775	8.68	78	122
19100601	33.0	11.11	0.084	0.21	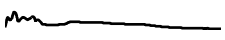	640	5.47	70	159
19100602	26.5	10.92	0.038	0.27		2246	17.64	122	355
20120600	13.7	10.11	0.051	0.34	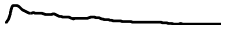	1015	7.24	104	176
20120601	10.4	9.81	0.056	0.24	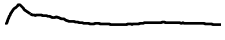	976	5.89	100	194
20120602	13.5	10.05	0.050	0.18		1021	6.52	106	209
21050700	10.1	9.84	0.049	0.31	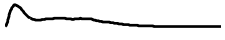	1010	7.73	81	203
21050701	7.7	9.56	0.042	0.27	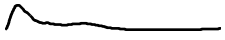	1341	7.52	114	229
21120600	9.9	9.71	0.047	0.23		1168	6.94	114	214
21120601	13.9	10.09	0.058	0.24		890	7.62	95	149

Table A.1 – Child headform – continued from previous page.

Test ID	Bonnet Angle	V	S	R	Pulse shape	HIC_∞	PVP	a_3	a_m
21120602	9.9	9.83	0.037	0.31		2609	17.28	154	263
22050600	45.5	10.98	0.063	0.30		3025	19.55	211	247
22050601	41.5	10.99	0.049	0.35		2200	17.84	139	197
22050602	38.5	10.98	0.051	0.22	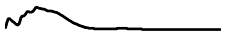	2216	15.68	166	208
22050700	9.4	9.76	0.049	0.26		1082	9.34	82	202
22050701	8.4	9.75	0.042	0.25		1135	6.63	121	187
22050702	10.2	9.87	0.036	0.29	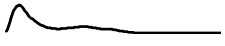	1831	9.72	133	260
22060600	16.0	10.36	0.054	0.12		1022	8.04	98	177
23020704	16.6	10.42	0.048	0.28		1803	14.18	141	168
23050600	78.4	8.27	0.034	0.50	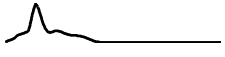	2326	16.78	98	351
23050601	56.0	10.47	0.065	0.26		1255	11.56	109	122
23050602	55.0	10.53	0.061	0.28		1259	10.66	112	164

Table A.1 – Child headform – continued from previous page.

Test ID	Bonnet Angle	V	S	R	Pulse shape	HIC_∞	PVP	a_3	a_m
23050603	51.2	10.64	0.055	0.30		1604	11.37	133	155
24050600	53.0	10.62	0.053	0.19		1686	12.45	149	193
24050601	82.8	7.69	0.040	0.43		605	5.30	87	110
24100702	10.9	9.87	0.057	0.34		738	4.95	98	183
25100700	12.9	10.02	0.051	0.31		829	6.45	100	200
25100701	28.8	10.92	0.047	0.29		3504	25.20	200	294
25100702	14.2	10.13	0.042	0.22		1991	15.39	136	236
25100703	27.9	10.90	0.037	0.27		2220	12.62	174	253
26020700	14.5	10.19	0.041	0.25		1507	9.50	134	207
26020701	9.2	9.76	0.036	0.40		2563	18.90	142	218
26050600	40.0	11.01	0.053	0.27		2100	17.81	116	317
26060600	10.0	9.84	0.059	0.14		923	7.90	89	215

Table A.1 – Child headform – continued from previous page.

Test ID	Bonnet Angle	V	S	R	Pulse shape	HIC_∞	PVP	a_3	a_m
26060601	11.6	9.93	0.065	0.17	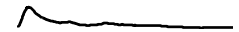	817	4.79	95	195
26060602	14.4	10.29	0.069	0.12		742	5.68	76	183
26060603	11.3	10.04	0.069	0.17		817	4.69	100	196
27020700	11.4	9.95	0.045	0.29		1191	6.64	111	221
27020701	10.4	9.83	0.048	0.30		1209	6.72	116	229
27020702	13.3	10.07	0.048	0.29		1396	7.95	117	234
27020703	16.4	10.32	0.050	0.32		1322	10.10	101	196
27060600	10.5	9.97	0.038	0.19		2430	16.60	188	225
27110700	14.2	10.19	0.060	0.34		742	6.40	76	179
27110701	16.7	10.41	0.051	0.20		1309	11.41	110	159
27110702	9.4	9.82	0.041	0.38		1348	9.49	100	212
27110703	14.2	10.22	0.059	0.33		756	5.52	77	183

Table A.1 – Child headform – continued from previous page.

Test ID	Bonnet Angle	V	S	R	Pulse shape	HIC_∞	PVP	a_3	a_m
28030600	9.5	9.82	0.028	0.29		2868	15.73	176	281
28050804	9.2	9.42	0.056	0.26		705	5.10	111	154
29010700	40.0	11.00	0.032	0.16		7178	36.02	145	514
29030600	8.2	9.74	0.037	0.20		1435	8.28	115	272
29030601	40.0	11.07	0.044	0.26		2318	14.72	167	206
29030602	40.0	11.05	0.030	0.18		3958	19.15	145	422
29030603	7.3	9.57	0.022	0.34		4786	23.89	251	306
29050800	10.3	9.60	0.057	0.22		657	5.53	87	172
29050801	11.7	9.78	0.048	0.29		1149	8.49	105	167
30010700	10.9	9.94	0.054	0.23		1131	9.05	110	134
30010701	10.3	9.87	0.041	0.28		1351	10.65	91	196
30010702	17.4	10.41	0.041	0.37		2375	16.12	149	185

Table A.1 – Child headform – continued from previous page.

Test ID	Bonnet Angle	V	S	R	Pulse shape	HIC_∞	PVP	a_3	a_m
30010703	29.5	10.98	0.039	0.29		5191	28.98	229	343
30040700	27.3	10.88	0.059	0.32		1151	7.99	110	151
30050800	40.0	9.33	0.036	0.26		1505	9.94	138	206
31010600	18.6	10.50	0.075	0.22		838	8.88	85	101

Table A.2: Summary of tests using Adult headform.

Test ID	Bonnet Angle	V	S	R	Pulse shape	HIC_∞	PVP	a_3	a_m
01020700	10.3	10.76	0.056	0.18		1562	13.60	134	175
02020600	8.4	10.66	0.091	0.15		520	5.08	75	98
02020601	12.8	10.96	0.076	0.20		718	6.54	104	137
02020602	9.1	10.81	0.080	0.10		690	5.64	101	125
02020700	7.5	10.66	0.069	0.31	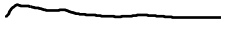	1183	12.48	104	140
02020701	33.6	10.88	0.042	0.26		1592	9.25	107	292
02020702	7.9	10.72	0.064	0.18		1378	12.39	123	140
02020703	7.1	10.64	0.056	0.24		1667	12.99	132	146
03010703	32.5	11.03	0.058	0.26		2111	15.01	148	168
03020600	14.3	10.91	0.085	0.13		584	6.02	84	133
03020601	5.5	10.64	0.050	0.19		1828	13.87	135	159
03050700	26.5	11.05	0.063	0.31		1846	13.32	154	178

Table A.2 – Adult headform – continued from previous page.

Test ID	Bonnet Angle	V	S	R	Pulse shape	HIC_∞	PVP	a_3	a_m
03050701	27.6	10.82	0.056	0.28		1284	8.25	129	175
03050702	27.6	11.02	0.066	0.25		1644	13.24	151	159
03060800	40.0	12.49	0.053	0.22		2402	14.28	166	245
03060801	9.2	11.03	0.070	0.18	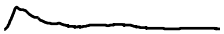	1219	7.08	121	210
03060802	40.0	12.51	0.061	0.24		3061	21.12	193	245
03060803	11.7	11.20	0.061	0.22		1465	10.05	115	212
05040603	8.4	10.70	0.069	0.30		1013	8.02	93	139
05040604	7.4	10.64	0.061	0.27		1500	12.65	129	156
06020801	7.9	10.76	0.092	0.20	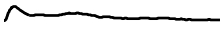	565	5.63	67	140
06020802	8.3	10.74	0.084	0.26	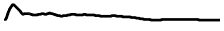	644	5.75	70	158
06020803	7.2	10.70	0.058	0.18		1116	9.68	101	202
06020804	39.7	10.66	0.089	0.28		959	10.18	101	116

Table A.2 – Adult headform – continued from previous page.

Test ID	Bonnet Angle	V	S	R	Pulse shape	HIC_∞	PVP	a_3	a_m
06040600	7.4	10.69	0.075	0.32		994	9.08	87	109
06040601	8.4	10.73	0.071	0.27	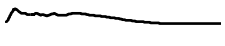	1028	8.71	83	138
07020800	40.9	10.62	0.090	0.28		876	9.02	89	97
07080705	7.9	10.68	0.079	0.25		862	7.72	83	136
07080706	7.8	10.69	0.078	0.27		705	6.04	71	151
08030602	32.1	10.98	0.059	0.25	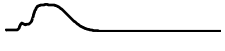	3261	19.05	207	239
08030603	32.5	10.94	0.060	0.29	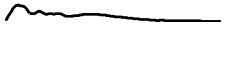	3675	22.36	228	251
08080700	7.9	10.71	0.070	0.23		796	6.73	76	154
08080701	33.6	10.87	0.088	0.33		1011	9.49	95	109
08080702	35.1	10.86	0.091	0.15		988	9.37	98	112
08120604	34.5	10.96	0.069	0.32		2797	20.04	193	208
09010700	8.8	10.92	0.090	0.19		826	7.64	80	108

Table A.2 – Adult headform – continued from previous page.

Test ID	Bonnet Angle	V	S	R	Pulse shape	HIC_∞	PVP	a_3	a_m
09030600	7.3	10.71	0.051	0.39		1760	12.15	142	166
09030601	7.0	10.72	0.046	0.34		2448	15.66	138	285
09030602	9.0	10.84	0.052	0.23		1680	12.61	116	189
09030603	31.0	10.94	0.069	0.24		3252	21.07	213	254
10050703	12.3	10.85	0.083	0.23	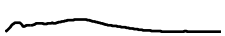	983	10.18	107	118
11050700	11.5	10.86	0.101	0.24		696	7.26	72	85
11050701	11.6	10.85	0.113	0.28		548	6.51	62	77
11120600	32.5	10.94	0.060	0.30		3247	20.60	200	268
12040600	30.7	11.01	0.072	0.21		1445	11.39	143	159
12040601	30.7	10.95	0.066	0.27		1609	11.78	130	183
12090602	27.9	10.98	0.072	0.28		1862	16.02	160	185
12090603	27.4	10.97	0.069	0.33		1633	13.11	134	153

Table A.2 – Adult headform – continued from previous page.

Test ID	Bonnet Angle	V	S	R	Pulse shape	HIC_∞	PVP	a_3	a_m
13050807	40.0	11.09	0.046	0.22		1992	11.93	152	220
13090600	20.5	11.06	0.045	0.27		1784	12.39	114	230
13120700	7.4	10.81	0.083	0.26	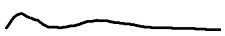	735	8.19	99	151
14050700	33.4	10.92	0.078	0.11		1082	9.62	122	144
14050701	32.6	10.86	0.073	0.27		1580	13.15	151	184
14050702	33.2	10.86	0.077	0.22		1000	8.86	109	130
14050800	9.2	9.81	0.062	0.19		910	5.75	116	174
14050801	10.3	9.90	0.059	0.19	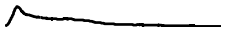	813	5.86	95	185
14050802	40.0	11.18	0.054	0.24	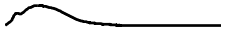	2121	14.39	166	189
14050803	11.7	10.10	0.051	0.28	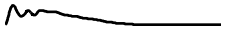	1299	9.53	111	181
14050804	40.0	11.11	0.050	0.37		1972	12.72	142	160
14120600	8.5	10.78	0.063	0.30		1643	15.09	147	162

Table A.2 – Adult headform – continued from previous page.

Test ID	Bonnet Angle	V	S	R	Pulse shape	HIC_∞	PVP	a_3	a_m
14120601	8.5	10.77	0.088	0.23		726	8.40	71	93
14120602	31.1	11.01	0.066	0.26		2953	20.19	191	215
14120603	33.3	10.87	0.064	0.30		1976	13.93	156	172
14120700	8.0	10.73	0.098	0.23		533	5.60	85	129
16010802	10.6	10.90	0.086	0.18		1085	12.79	118	147
17010800	11.1	10.95	0.072	0.14		1165	10.13	114	126
17040700	7.5	10.56	0.069	0.30		1110	12.37	103	136
17040701	10.3	10.80	0.058	0.20		1361	11.43	124	177
17120700	6.5	10.64	0.067	0.27		1463	13.04	120	137
17120701	6.5	10.60	0.072	0.23		1318	13.12	124	130
18010800	8.7	10.79	0.079	0.19	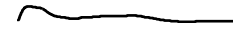	706	6.48	114	146
18010801	7.8	10.77	0.067	0.19		961	7.61	95	156

Table A.2 – Adult headform – continued from previous page.

Test ID	Bonnet Angle	V	S	R	Pulse shape	HIC_∞	PVP	a_3	a_m
18010802	10.5	10.91	0.042	0.18		3557	25.00	192	283
18060800	40.0	10.96	0.054	0.30		1496	10.54	129	165
18060801	9.2	9.69	0.074	0.24	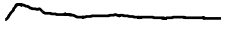	633	4.85	103	143
18100701	9.3	10.80	0.067	0.24		1067	9.21	97	123
18100702	9.3	10.65	0.064	0.27		1037	8.98	97	116
18120700	7.4	10.68	0.048	0.22		2512	20.77	168	252
19100700	9.6	10.59	0.077	0.29	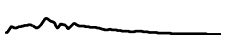	721	6.71	65	145
19100701	11.1	10.81	0.078	0.25	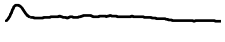	834	8.07	68	151
19100702	8.5	10.74	0.087	0.36	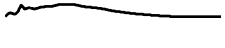	666	6.57	56	162
19100703	36.3	10.85	0.079	0.31		1079	8.99	108	118
19100704	34.6	10.82	0.072	0.29		1166	9.33	109	127
19110700	47.8	10.21	0.051	0.21		2172	15.94	157	181

Table A.2 – Adult headform – continued from previous page.

Test ID	Bonnet Angle	V	S	R	Pulse shape	HIC_∞	PVP	a_3	a_m
19110701	47.8	10.19	0.046	0.33		2993	19.35	199	209
20090600	44.0	10.41	0.068	0.24		740	5.73	105	145
22050703	6.7	10.61	0.078	0.26		929	8.94	84	143
22120600	9.7	10.72	0.069	0.26	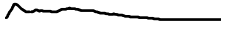	996	8.93	87	147
22120601	8.2	10.69	0.079	0.31		763	6.82	73	158
23050700	7.2	10.67	0.065	0.26		1318	15.75	110	163
23050701	7.1	10.64	0.068	0.28		1205	14.49	110	152
25050600	45.4	10.26	0.067	0.29		1803	13.49	153	199
25050601	46.6	10.11	0.073	0.34		1374	11.02	122	130
26100700	11.7	10.69	0.075	0.26		928	9.47	94	132
27060601	7.9	10.74	0.080	0.18		901	10.01	92	129
27060602	8.1	10.77	0.065	0.14		4026	34.79	54	410

Table A.2 – Adult headform – continued from previous page.

Test ID	Bonnet Angle	V	S	R	Pulse shape	HIC_∞	PVP	a_3	a_m
27060603	8.5	10.74	0.061	0.17		2829	27.14	103	330
27060604	8.4	10.74	0.066	0.24	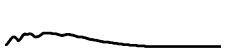	1207	9.90	105	129
27100600	31.0	11.05	0.069	0.21		1251	12.20	108	131
27100601	30.2	11.02	0.088	0.23		889	8.48	87	116
28020700	9.0	10.75	0.075	0.25		877	8.39	79	139
28020701	8.3	10.71	0.080	0.31		822	7.28	78	151
28020702	9.2	10.76	0.076	0.27	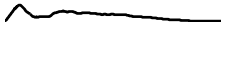	800	7.33	73	145
28060600	7.3	10.67	0.079	0.16	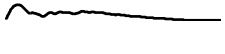	733	7.11	84	112
28060601	35.0	10.94	0.061	0.18	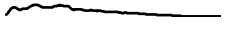	3621	26.93	188	303
28090600	28.0	11.10	0.066	0.28	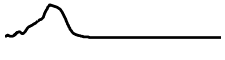	1747	13.41	134	185
28110700	29.7	11.24	0.068	0.30		2635	20.65	181	204
28110701	30.6	11.12	0.065	0.31		2504	17.99	178	191

Table A.2 – Adult headform – continued from previous page.

Test ID	Bonnet Angle	V	S	R	Pulse shape	HIC_∞	PVP	a_3	a_m
29100700	8.5	10.63	0.061	0.25		1133	8.67	97	245
29100701	8.5	10.62	0.082	0.30		779	7.33	80	129
29100702	26.9	11.16	0.063	0.28		1692	12.48	131	139
29100703	26.6	11.14	0.074	0.23		1704	14.42	134	164
30030600	8.0	10.61	0.067	0.13		1090	10.51	106	190
30030601	6.7	10.61	0.068	0.20		1046	10.51	99	130
30030602	8.1	10.65	0.062	0.14		1130	7.99	121	197
30030603	6.7	10.60	0.042	0.15	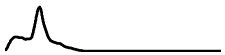	2946	28.89	113	409
30030604	7.9	10.70	0.072	0.15	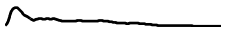	651	5.14	72	177
30060600	33.6	11.00	0.062	0.15		2593	17.89	184	250
31030600	7.4	10.67	0.035	0.20		3962	23.19	211	329
31030601	6.4	10.63	0.029	0.23	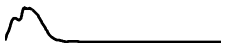	4620	26.08	204	319

Appendix B

Derivation of theoretically realistic triangle pulse shapes

B.1 Deformation at the end of the impact is less than zero

It was claimed in Equation (4.28) that the triangle pulse shapes that have a negative deformation at the conclusion of the impact had the following property.

$$R \leq \frac{(k+1)}{(2-k)} \tag{B.1}$$

This was derived by calculating the crush at $t = T$ for a general triangular impact and seeking those with $s(T) \leq 0$.

At the beginning of the impact the headform zero displacement

$$s(0) = 0 \tag{B.2}$$

and an impact velocity

$$v(0) = V = -\frac{AT}{2(1+R)}. \tag{B.3}$$

The acceleration of the triangle pulse shape from the beginning of the impact until the apex of the acceleration pulse shape at $t = kT$ is

$$a(t) = \frac{At}{kT}. \tag{B.4}$$

Up to the apex of the pulse shape the velocity is

$$v(t \leq kT) = \int_0^{kT} a(t).dt + v(0) \tag{B.5}$$

$$= \frac{A\,t^2}{2\,T\,k} - \frac{A\,T}{2\,R+2}. \tag{B.6}$$

At the apex of pulse shape the velocity is

$$v(kT) = \frac{A\,T\,k}{2} - \frac{A\,T}{2\,R+2}. \tag{B.7}$$

The displacement of the headform into the hood surface at the apex is

$$s(kT) = \int_0^{kT} v(t \leq kT).dt + 0 \tag{B.8}$$

$$= \frac{A\,T^2\,k\,\left(k + R\,k - 3\right)}{6\,R+6} \tag{B.9}$$

After the apex of the pulse shape the acceleration is

$$a(t) = \frac{A\,\left(T-t\right)}{T\,\left(1-k\right)}. \tag{B.10}$$

The velocity of the headform after the apex of the pulse shape is

$$v(kT \leq t < T) = \int_{kT}^{t} a(t).dt + v(kT) \tag{B.11}$$

$$= \int_{kT}^{t} \frac{A\,\left(T-t\right)}{T\,\left(1-k\right)}.dt + \frac{A\,T\,k}{2} - \frac{A\,T}{2\,R+2} \tag{B.12}$$

$$= \frac{A\,\left(T-t\right)^2}{2\,T\,\left(k-1\right)} + \frac{A\,R\,T}{2\,R+2}. \tag{B.13}$$

Consequently, the displacement of the headform at the end of the impact at

$t = T$ is

$$s(T) = \int_{kT}^{T} v(kT \leq t < T).dt + s(kT) \tag{B.14}$$

$$= -\frac{A\,T^2\ (k - 2\,R + R\,k + 1)}{6\,R + 6} \tag{B.15}$$

The solutions to Equation (B.15) for which $s(T) \leq 0$ are found when

$$0 \geq s(T) \tag{B.16}$$

$$0 \geq -\frac{A\,T^2\ (k - 2\,R + R\,k + 1)}{6\,R + 6} \tag{B.17}$$

As both AT^2 and $6R + 6$ are positive definite, these can be factored out of the equation.

$$0 \geq -\left(k - 2\,R + R\,k + 1\right) \tag{B.18}$$

$$0 \geq 2\,R - k - R\,k - 1 \tag{B.19}$$

$$0 \geq -R\ (k - 2) - (k + 1) \tag{B.20}$$

$$R\ (k - 2) \geq -(k + 1) \tag{B.21}$$

$$R \leq \frac{-(k + 1)}{(k - 2)} \tag{B.22}$$

Leading to the required relationship

$$R \leq \frac{(k + 1)}{(2 - k)}. \tag{B.23}$$

Triangle pulse shapes that do not have this property have a positive crush at $t = T$, indicating that the hood is accelerating the headform after the headform has bounced back beyond the natural position of the hood. These are considered to be unrealistic.

B.2 Peak acceleration occurs before time of maximum stopping distance.

It is also considered unrealistic for a pulse shape to have a peak in acceleration after it has reached its maximum stopping distance.

The time of the peak acceleration of the triangle pulse shape is given by Equation (B.24)

$$t^* = kT \tag{B.24}$$

The time of the maximum crush for the triangle pulse shape is given by Equation (B.25).

$$\hat{t} = T - T(1-k)\sqrt{\frac{R}{(R+1)(1-k)}} \tag{B.25}$$

Equation (4.30) is calculated by setting $t^* \leq \hat{t}$ and solving Equation (B.25) for R.

$$kT \leq T - T(1-k)\sqrt{\frac{R}{(R+1)(1-k)}} \tag{B.26}$$

$$k \leq 1 - (1-k)\sqrt{\frac{R}{(R+1)(1-k)}} \tag{B.27}$$

$$\frac{(k-1)}{(1-k)} \geq \sqrt{\frac{R}{(R+1)(1-k)}} \tag{B.28}$$

$$\frac{(k-1)^2}{(1-k)^2} \geq \frac{R}{(R+1)(1-k)} \tag{B.29}$$

$$-(k-1) \geq \frac{R}{R+1} \tag{B.30}$$

$$(k-1)(R+1) \leq -R \tag{B.31}$$

$$kR + k - 1 \leq 0 \tag{B.32}$$

$$R \leq \frac{1-k}{k} \tag{B.33}$$

Equation (B.33) shows the relationship necessary for the apex of the triangle pulse shape to occur before the time of the maximum stopping distance.

Appendix C

Assumption that HIC_∞ and HIC_{15} are the same

In this thesis the HIC_∞ has been used instead of the HIC_{15} in all the theoretical analysis because these IRFs have been assumed to be sufficiently similar that their differences are negligible in this data set. This assumption was made because the HIC_{15} added the confounding factor of pulse duration to the theoretical analysis. This could be easily avoided by using the HIC_∞ variant. In this section, attention is turned to quantifying the similarities between these two IRFs so that this claim can be validated.

Figure C.1 shows that the correlation between these two IRFs is high. The correlation statistic is $r^2 > 0.9990$ for both headform sizes. This is expected because the duration of most tests is less than 15 ms. The figure also shows that the differences between these IRFs only occur at low values of HIC as this is the only place where equality between the HIC_∞ and HIC_{15} is not maintained.

The value of the HIC_{15} is found by determining the maximum value of the HIC over an evaluation window with a maximum duration of 15 ms. If the maximum duration of that evaluation window is increased, as it is for the HIC_∞, then the maximum value of the functional can either have the same value (in which case the evaluation window will be the same size) or increase in value if a new evaluation window is found with a larger value of the HIC functional. As a result, the $HIC_\infty \geq HIC_{15}$.

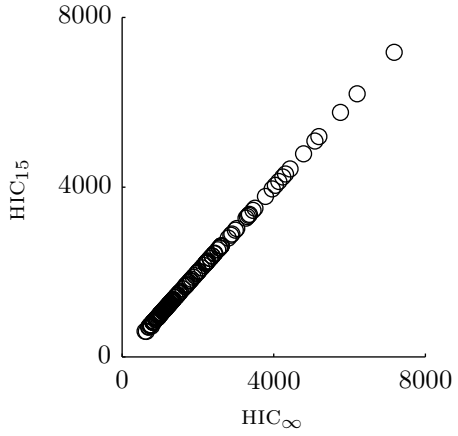

(a) Tests with Child headform ($r^2 = 1.0000, p < .001$).

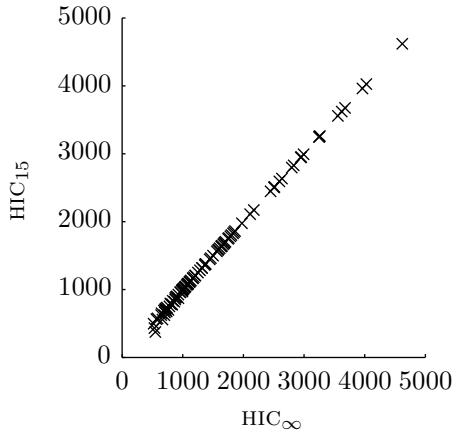

(b) Tests with Adult headform. ($r^2 = 0.9993, p < .001$).

Figure C.1: Correlation of HIC_∞ with HIC_{15}.

There are two important arguments that are needed to demonstrate that the differences between the HIC_∞ and the HIC_{15} are minor. Firstly, the proportion of tests with different values of $\text{HIC}_\infty$and HIC_{15} are small and secondly, that the difference between these two IRFs, when it exists, is small in value.

Just eight of the 139 tests done with the Child headform have $\text{HIC}_\infty > \text{HIC}_{15}$ and 24 of the 108 tests with the Adult headform have $\text{HIC}_\infty > \text{HIC}_{15}$. All tests with different values of HIC_{15} and HIC_∞ have low values of both HIC_{15} and HIC_∞. All , except three tests with tests with different values of HIC_{15} and HIC_∞ have values of HIC_∞ and HIC_{15} less than 1000. All three of these tests with $\text{HIC}_\infty > 1000$ were performed with the Child headform and each of these three tests also had $\text{HIC}_{15} > 1000$.

The mean increase of the HIC value for the eight tests with the Child headform is 17 HIC units and the mean increase in HIC value for the 24 tests with the Adult headform is 51 HIC units. The test with the Child headform with the largest increase in HIC ($\text{HIC}_\infty - \text{HIC}_{15} = 50$) has $\text{HIC}_\infty = 775$. The test with the Adult headform with the largest increase in HIC ($\text{HIC}_\infty - \text{HIC}_{15} = 173$) has $\text{HIC}_\infty = 548$. The tests with the highest HIC_∞ value with a difference between HIC_∞ and HIC_{15} has $\text{HIC}_\infty = 1182$ with the Child headform (this test has $\text{HIC}_{15} = 1179$) and $\text{HIC}_\infty = 994$ (from $\text{HIC}_{15} = 972$) for the Adult headform.

Of the 32 tests with different values of HIC_∞ and HIC_{15}, just one has a HIC_{15} evaluation window that is less than 15 ms. This test was with the Adult headform, had a HIC_{15} evaluation window of 4.46 ms and a HIC_∞ evaluation window of 21.9 ms. This was test 14120700 and is shown in Figure C.2. The large difference in evaluation window sizes is a result of the substantial peak in acceleration that occurred outside the 15 ms window necessary for it to be included in the HIC_{15} calculation.

The 32 tests where $\text{HIC}_\infty > \text{HIC}_{15}$ are shown in Figure C.3. The tests with the largest difference between HIC_∞ and HIC_{15} also have the lowest values of HIC_{15} as is shown in Figure C.3(a). The tests with the largest difference between HIC_∞ and HIC_{15} also have the largest increase in duration of the evaluation window as is shown in Figure C.3(b).

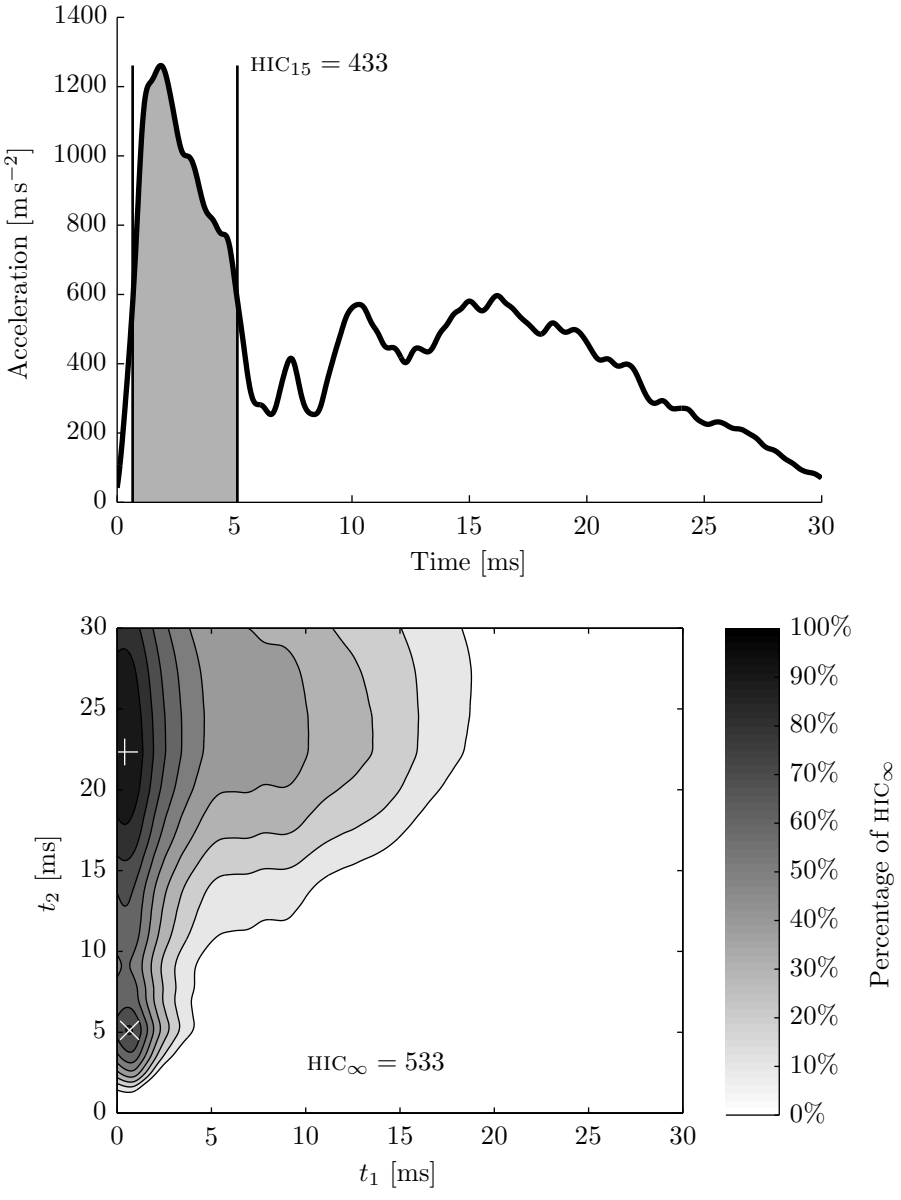

Figure C.2: Locations of the HIC_∞ (+) and HIC_{15} (×) evaluation windows for test 14120700.

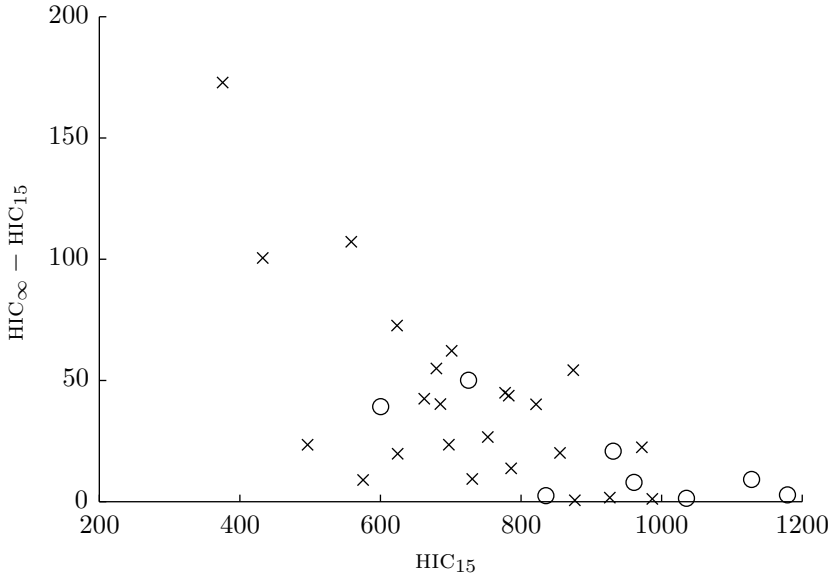

(a) The change in HIC and the HIC_{15} value.

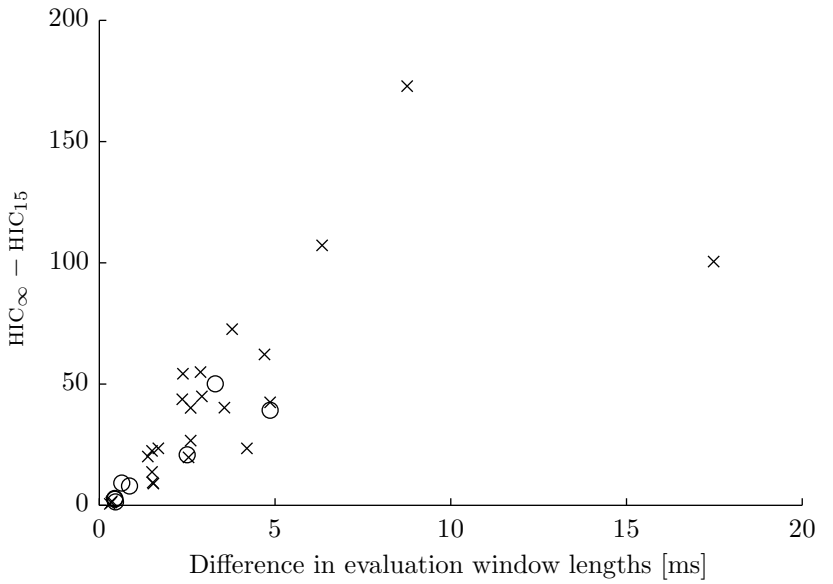

(b) The change in HIC because of an increase in available evaluation window length.

Figure C.3: Examination of aspects of all of the tests that have $\text{HIC}_\infty > \text{HIC}_{15}$. Child headform tests are shown with circles, Adult headform tests are shown with crosses.

Overall, these results show that the difference between the HIC_{∞} and the HIC_{15} is minimal in this dataset. When there is change, there is a small increase in the value of HIC and the change only occurs for values of HIC_{15} that are already low. Consequently, there appears to be little reason why the HIC_{∞} IRF should not be used instead of the HIC_{15} IRF for the analysis of this dataset.

The similarity between the HIC_{∞} and the HIC_{15} in this dataset does not necessarily mean that this relationship is generally true. In datasets where long impacts are usual, or in testing regimes where the head acceleration is subject to other forces not coming from an impact (such as forces due to attachment to the torso in a full dummy testing device) this similarity cannot be assumed without first testing this assumption.

Appendix D

Comparison between rotational acceleration and linear acceleration based IRFs

This thesis is dedicated to investigating the properties of head injury IRFs that are based on linear acceleration. As noted in Chapters 1 and 2, IRFs based on rotational motion have also been studied for decades. The most important of these are peak rotational acceleration and peak change in rotational velocity. An analysis of these IRFs, comparing them with the linear IRFs, whilst acknowledging the limitations of doing this, is made in this Appendix, thus using the data to its most reasonable extent.

Analysis of the two main IRFs that use rotational kinematics was not performed in this thesis for two main reasons. First, the angular acceleration and velocity are not measured directly during each test but are instead estimated using the method described by Searson and Anderson (2008). While this data has been substantiated using the high speed film made of each impact and the method has been confirmed using a MADYMO simulation, it was not directly measured. Therefore, it should be, and is, treated with caution. Second, because only the linear acceleration measured by the headform was compared to the results of cadaver testing (Glaeser, 1991) there is no evidence that the pedestrian impact testing protocol used to collect this data accurately models the angular kinematics experienced by a pedestrian in a real impact. Last, there is evidence to suggest that the spherical headform used provides different rotational kinematics than non-spherical,

human-like Hybrid III headform (Fredriksson et al., 2007). Consequently, there is little reason to believe that the rotational motions that occur in the headform, measured in this data, are biofidelic.

However, comparisons between the rotational IRFs and the linear IRFs can be made because these motions exist and have been estimated. These comparisons are made here, noting those limitations of this data previously described.

D.1 Peak rotational acceleration

The peak rotational acceleration is the absolute maximum rotational acceleration estimated using the Searson and Anderson (2008) method for determining the kinematics of the headform during a pedestrian impact test. Figures D.1 and D.2 show how the peak rotational acceleration estimated for each impact compares with the linear acceleration IRFs for the tests with the Child and Adult headform respectively. Tables D.1 and D.2 quantify these results with the square of the Pearson correlation coefficient. All correlations have a magnitude less than 0.1. There is no association between the IRFs based on linear acceleration and the peak angular acceleration for tests of this type.

The peak angular acceleration, however, is related to the angle of impact. This is shown in Figure D.3. An impact that is perpendicular to the surface has a complementary impact angle of zero degrees, as was defined in Figure 3.9 on page 50. Perpendicular impacts have less peak rotational acceleration than impacts at a greater complementary impact angles. These are positively correlated and have squared Pearson correlation coefficient values greater than 0.3.

To determine the interaction effects of complementary impact angle and each linear acceleration IRF, a multiple linear regression model was developed. This model showed that peak rotational acceleration had a weak positive correlation with linear acceleration IRFs, but this was only significant ($p > .01$) for the HIC, a_3 and a_m, and only with the Child headform data. However, the peak angular acceleration was significantly and positively influenced by the complementary impact angle in all circumstances.

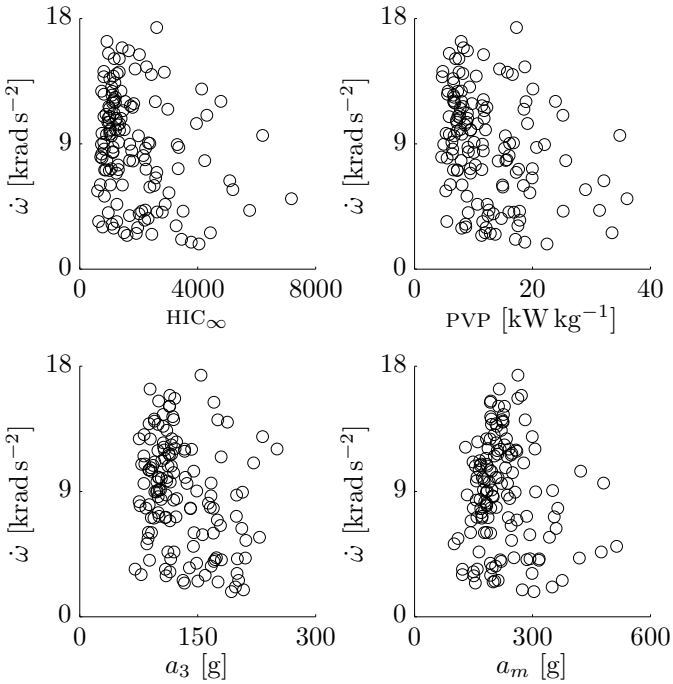

Figure D.1: Comparison of peak rotational acceleration ($\dot{\omega}$) with the linear acceleration based IRFs. Child headform tests.

Table D.1: Square of Pearson correlation coefficient (r^2) for correlations shown in Figure D.1.

HIC$_\infty$	PVP	a_3	a_m
0.0660	0.0991	0.0804	0.0108

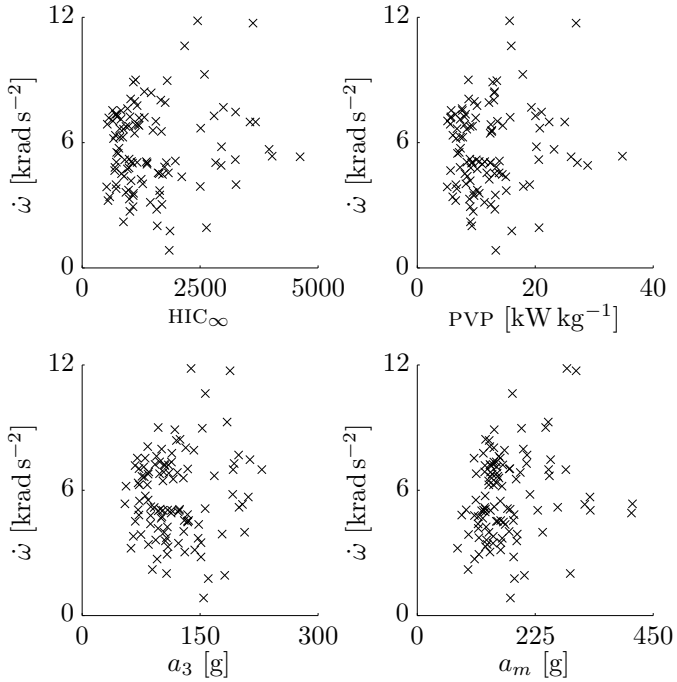

Figure D.2: Comparison of peak rotational acceleration ($\dot{\omega}$) with the linear acceleration based IRFs. Adult headform tests.

Table D.2: Square of Pearson correlation coefficient (r^2) for correlations shown in Figure D.2.

HIC$_\infty$	PVP	a_3	a_m
0.0143	0.0111	0.0057	0.0339

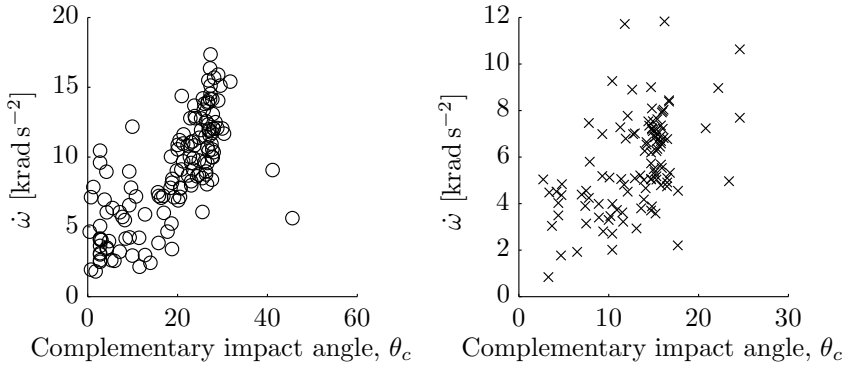

(a) Child headform. $r^2 = 0.5235$. **(b)** Adult headform. $r^2 = 0.2587$.

Figure D.3: Effect of complementary impact angle on peak angular acceleration.

This demonstrates that peak angular acceleration has a strong association with the angle of impact but has a lesser relationship with the linear IRFs.

D.2 Peak change in rotational velocity

The peak change in rotational velocity is the maximum absolute value of angular velocity calculated using the Searson and Anderson (2008) method for determining the kinematics of the headform during a pedestrian impact test. Figures D.4 and D.5 show how the peak change in rotational velocity, estimated for each impact, compares with the linear acceleration IRFs for the tests with the Child and Adult headforms respectively. There is a negative correlation between the linear IRFs and the peak change in rotational velocity. Higher values of each IRF indicate lower peak changes in rotational velocity. Tables D.3 and D.4 quantify the association using the square of the Pearson correlation coefficient.

The peak rotational velocity is also correlated with the angle of impact for the data with both headforms. These are shown in Figure D.6.

Multiple linear regression models were developed to predict the peak change in rotational velocity using both the complementary impact angle, and the value of each linear IRF. In each model the peak change in rotational velocity was significantly ($p < .01$) and positively correlated with impact angle, and significantly ($p < .01$) and negatively correlated with each linear acceleration based IRF.

D.3 Discussion

There are limitations that affect the interpretation of the IRFs based on rotational acceleration that are determined from this data. These limitations include the biofidelity the test for replicating the kinematics of a pedestrian's head and the acknowledgement that the rotational data was estimated, rather than measured. Nevertheless, an analysis correlating the IRFs based on rotational acceleration with the IRFs based on linear acceleration has been completed.

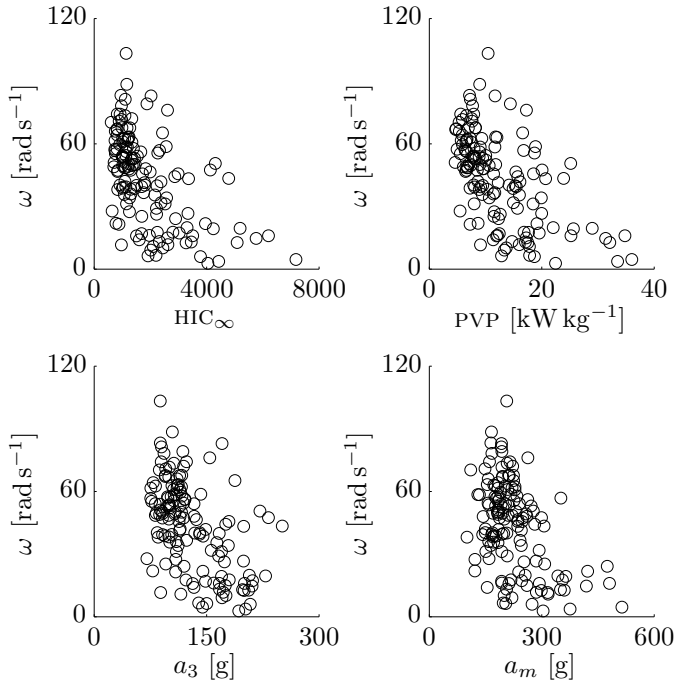

Figure D.4: Comparison of peak change in rotational velocity (ω) with the linear acceleration based IRFs. Child headform tests.

Table D.3: Square of Pearson correlation coefficient (r^2) for correlations shown in Figure D.4.

HIC$_\infty$	PVP	a_3	a_m
0.3027	0.3296	0.2679	0.2061

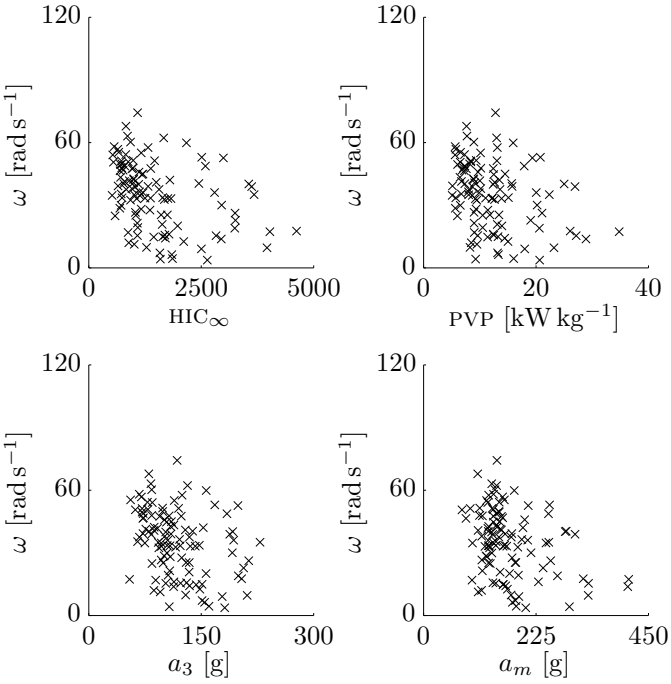

Figure D.5: Comparison of peak change in rotational velocity (ω) with the linear acceleration based IRFs. Adult headform tests.

Table D.4: Square of Pearson correlation coefficient (r^2) for correlations shown in Figure D.5.

HIC$_\infty$	PVP	a_3	a_m
0.1335	0.1071	0.1175	0.0874

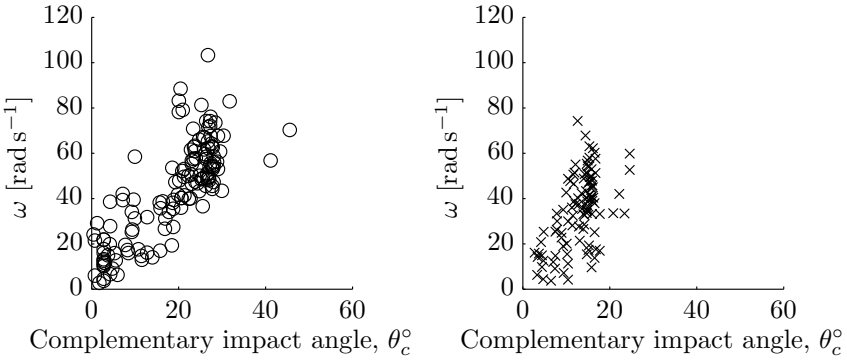

(a) Child headform.$r^2 = 0.6419$. **(b)** Adult headform.$r^2 = 0.3102$.

Figure D.6: Effect of impact angle on peak rotational acceleraton.

There are three main highlights from this analysis. First, the peak rotational acceleration is not correlated with any of the linear acceleration based IRFs. Second, the change in rotational velocity is weakly and negatively correlated with each of the linear acceleration based IRFs. And third, the complementary impact angle is positively correlated with both the peak rotational acceleration and the change in rotational velocity.

These three highlights point to the major design change that would be expected if an IRF based on rotational motion were used, instead of an IRF based on linear acceleration; that is, the impact surfaces would be designed to be perpendicular to the impact direction. While this would reduce the values of the IRFs based on rotational accelerations it would also have a negative safety benefit if the impact were to be measured with one of the linear acceleration IRFs. Consequently, there is a contradiction between the design philosophies that would be encouraged if test locations were assessed based on linear acceleration or rotational acceleration.

This contradiction is reliant on the test procedure being biofidelic for both linear and rotational accelerations. Because the test procedure used to collect this data has not been validated for rotational kinematics it may not yield meaningful results. Consider an alternative test scenario in which each test location is tested at multiple test speeds. At each location, it is known higher impact speeds will result in higher values of the linear acceleration IRFs; but it is also likely that the higher speeds will result in higher values of the rotational acceleration and change in rotational velocity. Consequently there may be positive correlation between these two types of IRF at each test location if variable impact speeds were used. It is not possible, with this data set, to observe the correlation that might occur with the test scenario just described because the impact velocity was fixed. This type of positive correlation was shown in Funk et al. (2008). With an alternative test scenario like this, designs which minimise linear acceleration based IRFs may also minimise rotational acceleration based IRFs. As a result the results shown here should not be generalised until the test procedure has been demonstrated to be biofidelic for both linear and rotational kinematics. This, in turn, limits the meaningfulness of discussing these results in a broader context, so this discussion is not undertaken.

Appendix E

Comparison of the PVP and HIP

The formulae used to calculate HIP and PVP are similar because they multiply an acceleration by the integral of that acceleration, but they do this in slightly different ways. These two formulae are shown in the following equations.

$$\text{PVP} = \max\left[a \int_0^t a.dt\right] \tag{E.1}$$

$$\text{HIP} = \max\left[\sum_{i=1}^{3} C_i a_i(t) \int_0^t a_i dt + \sum_{k=1}^{3} W_k \dot{\omega}_k \int_0^t \dot{\omega}_k dt\right] \tag{E.2}$$

where a is the total acceleration, a_i is the acceleration in each individual axis j, and $\dot{\omega}_i$ is the rotational acceleration in each axis k. C_i and W_k are constants (typically C_i is the mass and W_k is the moment of inertia on each axis). The Searson and Anderson (2008) method for calculating the rotational acceleration only calculates it in one dimension that is not aligned with any linear axes, so the formula that is used in this data set is:

$$\text{HIP} = \max\left[\sum_{i=1}^{3} C a_j(t) \int_0^t a_i dt + W \dot{\omega} \int_0^t \dot{\omega} dt\right] \tag{E.3}$$

where C is the mass of the headform, W is the moment of inertia of the headform and $\dot{\omega}$ is the rotational acceleration of the headform calculated using the Searson and Anderson (2008) method.

There are three obvious differences between the formulae in Equations (E.1) and (E.3). They are:

1. The HIP uses separate acceleration traces from each orthogonal axis but the PVP uses the resultant acceleration.
2. Each of the accelerations on these orthogonal axes is multiplied by the mass of the headform in the HIP.
3. The HIP includes rotational and linear acceleration components whereas the PVP only includes linear acceleration components.

This section will show that the second item is the most influential of these differences. The others have a negligible effect for the tests in this data set.

The correlation of all tests with the PVP and HIP IRFs are shown in Figure E.1. The IRFs are highly correlated with each headform size, but the lines of correlation for each headform size differ. The main features in this figure are the two straight lines, each one consisting of all tests with each headform size. This shows that the main differences between the HIP and the PVP can be associated with the differences between the headform (mainly the difference in mass). Within each of these lines, however, there is little variation ($r^2 > 0.99$) indicating that the effects of the other differences between the PVP and the HIP mentioned in the above list, including the effect of rotational motion, are of minor consequence on the evaluation of the impact for the tests in this data set.

This analysis also shows that for the components of rotational motion to make any noticeable effect on the assessment of crashworthiness then they must be given an appropriate weighting. Using the moment of inertia as a weighting factor, as is done with the HIP, means that the angular kinematics component of the HIP makes no more than a negligible difference when compared to the PVP.

The slope obtained from the linear approximation of the regression line for the data from each headform is shown with Figure E.1. For each set of data the slope is approximately equal to the mass of each headform. The slope

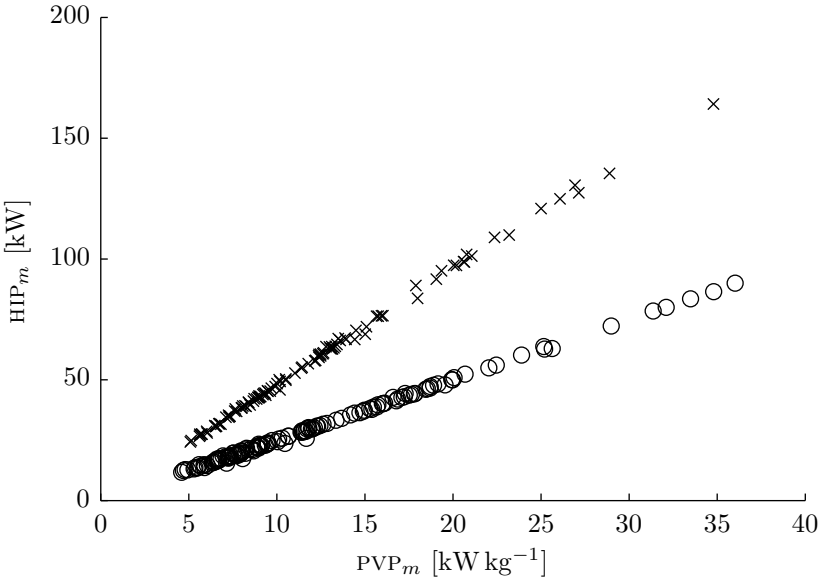

Figure E.1: Correlation of HIP with PVP. Tests with the Child headform shown with circles ($r^2 = 0.9985, p < .001$, slope = 2.4984), tests with the Adult headform shown with crosses ($r^2 = 0.9987, p < .001$, slope = 4.7875).

for the tests with the Child headform is 2.4984 which is within 0.1% of the 2.5 kg headform mass, and the slope for the tests with the Adult headform is 4.7875 which is within 0.2% of the 4.8 kg headform mass. This slope is predicted by comparing the formulation for PVP and the formulation for HIP. The HIP includes mass coefficients, but the PVP does not. Figure E.2 shows that a 1-1 relationship exists between the PVP and the ratio of the HIP and headform mass.

The relationship shown in Figure E.2 suggests that an equation relating the PVP and the HIP can be found in Equation (E.4).

$$\text{PVP} = \text{HIP} \div \text{Mass} \tag{E.4}$$

Equation (E.4) is used in Chapter 6 to provide a threshold for a criterion to use with PVP based on a criterion using HIP.

The coefficients for the HIP do not necessarily have to equal the mass of the headform. Newman et al. (2000b) originally proposed that the constants for the HIP could be determined to tune the power index (as HIP was described)

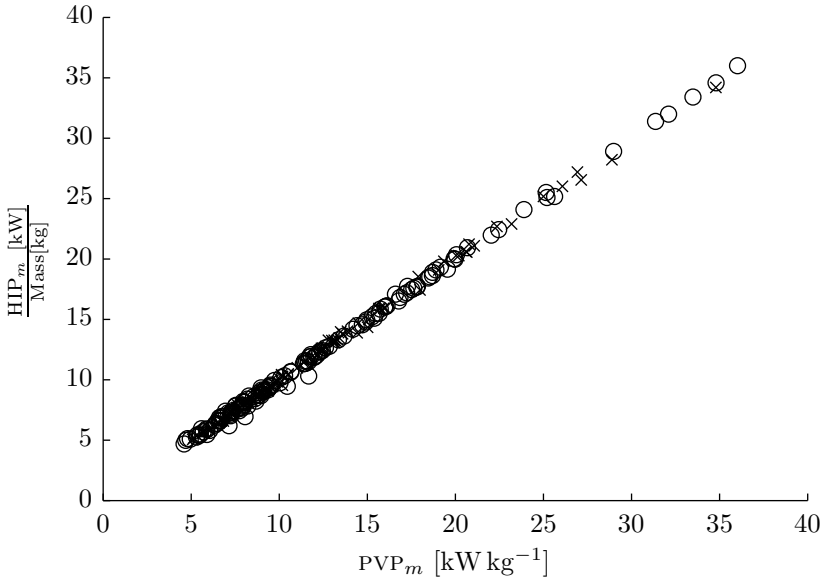

Figure E.2: Correlation of the ratio of HIP and headform mass with PVP. Tests with the Child headform shown with circles ($r^2 = 0.9985, p < .001$, slope = 0.9994), tests with the Adult headform shown with crosses ($r^2 = 0.9987, p < .001$, slope = 0.9974).

to any observed injury data and a different coefficient was permitted for each axis. However, the mass and moment of inertia have been used in subsequent analyses of the HIP (such as in Jiang et al., 2010; Marjoux et al., 2008; Newman et al., 2000b).

To the author's knowledge, the HIP is the only IRF that has such a dependence on mass. Its presence in the formulation for HIP raises interesting biofidelic questions about its appropriateness that have not yet received any attention in the literature. All known publications that have used the HIP have used a head mass (either finite element or dummy) of 4.5 kg (Jiang et al., 2010; Marjoux et al., 2008; Newman et al., 2000a). None of the inquiries has asked whether the injury response to a common acceleration pulse shape depends on the head mass. Neal-Sturgess (2002) deliberately chose to formulate the PVP as a specific, mass independent, quantity, on the basis that this was hypothesised by Waller (1985) to be the important factor for the severity of injury. Newman et al. (2000a) took an alternative view suggesting that absolute power was the important parameter. Addressing this issue is not within the scope of this thesis because it requires biome-

chanical injury data from a range of head sizes. The presence of this effect is mentioned here as an opportunity for further investigation using data from reconstructed impacts or from animal experimentation.

Appendix F

Contingency tables

In Table 6.4, the results of several contingency tables are used. Those contingency tables are provided here. In addition the the values of Sensitivity, Specificity, Positive Predictive Value (PPV) and Negative Predictive Value (NPV) of the alternate criteria, compared with HIC $>$ 1000, are shown graphically over a range of thresholds.

F.1 HIC with PVP

Table F.1: Contingency table comparing $\text{HIC}_\infty > 1000$ with $\text{PVP} > 6.6\,\text{kW}\,\text{kg}^{-1}$. Child headform tests.

		$\text{HIC}_\infty > 1000$		*Total*
		Safe	Unsafe	
$\text{PVP} > 6.6\,\text{kW}\,\text{kg}^{-1}$	Safe	18	1	19
	Unsafe	11	109	120
Total		29	110	139

Sensitivity $= 0.99\ (0.94, 1.00)$, Specificity $= 0.62\ (0.42, 0.79)$,
PPV $= 0.91\ (0.84, 0.95)$, NPV $= 0.95\ (0.72, 1.00)$,
$\chi^2 = 72.75$, $\phi = 0.72$.

Table F.2: Contingency table comparing $\text{HIC}_\infty > 1000$ with $\text{PVP} > 8.7\,\text{kW}\,\text{kg}^{-1}$. Adult headform tests.

		$\text{HIC}_\infty > 1000$		*Total*
		Safe	Unsafe	
$\text{PVP} > 8.7\,\text{kW}\,\text{kg}^{-1}$	Safe	29	4	33
	Unsafe	9	66	75
Total		38	70	108

Sensitivity $= 0.94\ (0.85, 0.98)$, Specificity $= 0.76\ (0.59, 0.88)$,
PPV $= 0.88\ (0.78, 0.94)$, NPV $= 0.88\ (0.71, 0.96)$,
$\chi^2 = 57.86$, $\phi = 0.73$.

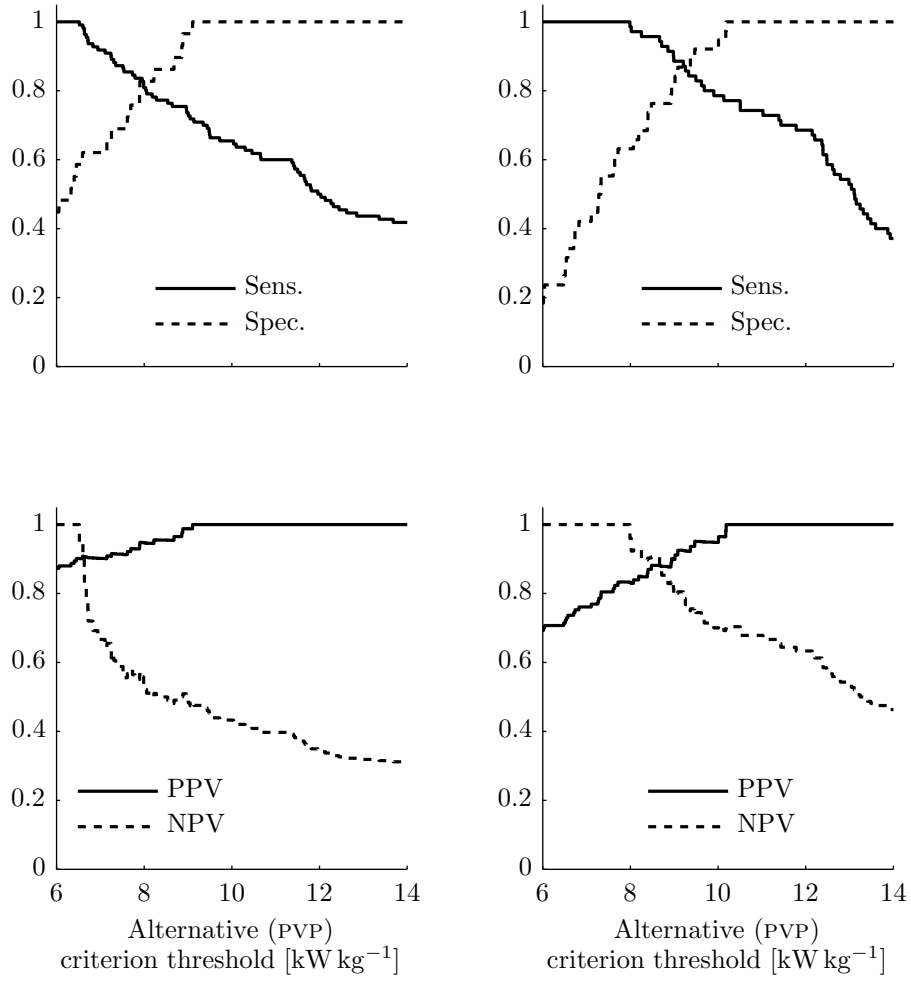

(a) Child headform tests.

(b) Adult headform tests.

Figure F.1: Sensitivity, Specificity, PPV and NPV of an alternate criteria at a range of thresholds of PVP, compared with reference $\text{HIC}_\infty > 1000$ criterion.

F.2 HIC with 3 millisecond clip

Table F.3: Contingency table comparing $\text{HIC}_\infty > 1000$ with $a_3 > 81.6$. Child headform tests.

		$\text{HIC}_\infty > 1000$		*Total*
		Safe	Unsafe	
$a_3 > 81.6\,\text{g}$	Safe	6	1	7
	Unsafe	23	109	132
Total		29	110	139

Sensitivity $= 0.99\ (0.94, 1.00)$, Specificity $= 0.21\ (0.09, 0.40)$,
PPV $= 0.83\ (0.75, 0.88)$, NPV $= 0.86\ (0.42, 0.99)$,
$\chi^2 = 18.78$, $\phi = 0.37$.

Table F.4: Contingency table comparing $\text{HIC}_\infty > 1000$ with $a_3 > 95.2\,\text{g}$. Adult headform tests.

		$\text{HIC}_\infty > 1000$		*Total*
		Safe	Unsafe	
$a_3 > 95.2\,\text{g}$	Safe	30	3	33
	Unsafe	8	67	75
Total		38	70	108

Sensitivity $= 0.96\ (0.87, 0.99)$, Specificity $= 0.79\ (0.62, 0.90)$,
PPV $= 0.89\ (0.80, 0.95)$, NPV $= 0.91\ (0.75, 0.98)$,
$\chi^2 = 64.70$, $\phi = 0.77$.

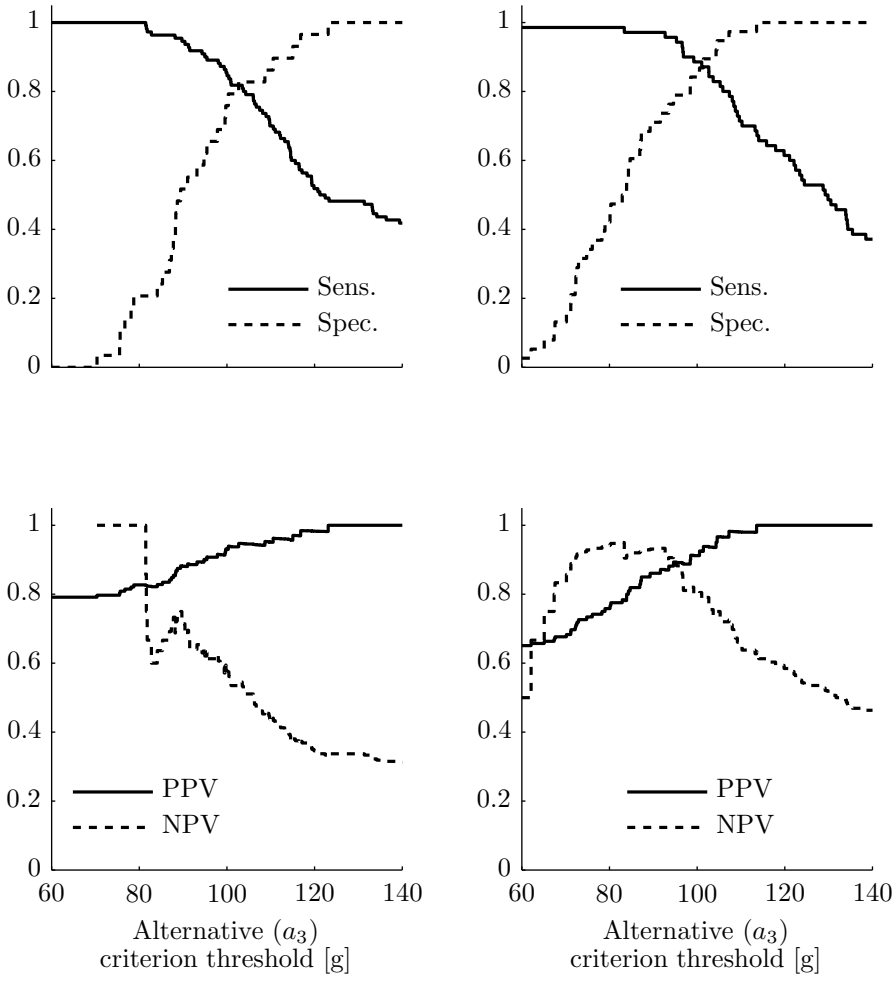

(a) Child headform tests.

(b) Adult headform tests.

Figure F.2: Sensitivity, Specificity, PPV and NPV of an alternate criteria at a range of thresholds of a_3, compared with reference $\text{HIC}_\infty > 1000$ criterion.

F.3 HIC with peak acceleration

Table F.5: Contingency table comparing $\text{HIC}_\infty > 1000$ with $a_m > 121\,\text{g}$. Child headform tests.

		$\text{HIC}_\infty > 1000$		*Total*
		Safe	Unsafe	
$a_m > 121\,\text{g}$	Safe	2	0	2
	Unsafe	27	110	137
Total		29	110	139

Sensitivity $= 1.00\ (0.96, 1.00)$, Specificity $= 0.07\ (0.01, 0.24)$,
PPV $= 0.80\ (0.72, 0.86)$, NPV $= 1.00\ (0.20, 1.00)$,
$\chi^2 = 7.70$, $\phi = 0.24$.

Table F.6: Contingency table comparing $\text{HIC}_\infty > 1000$ with $a_m > 126\,\text{g}$. Adult headform tests.

		$\text{HIC}_\infty > 1000$		*Total*
		Safe	Unsafe	
$a_m > 126\,\text{g}$	Safe	13	4	17
	Unsafe	25	66	91
Total		38	70	108

Sensitivity $= 0.94\ (0.85, 0.98)$, Specificity $= 0.34\ (0.20, 0.51)$,
PPV $= 0.73\ (0.62, 0.81)$, NPV $= 0.76\ (0.50, 0.92)$,
$\chi^2 = 15.08$, $\phi = 0.37$.

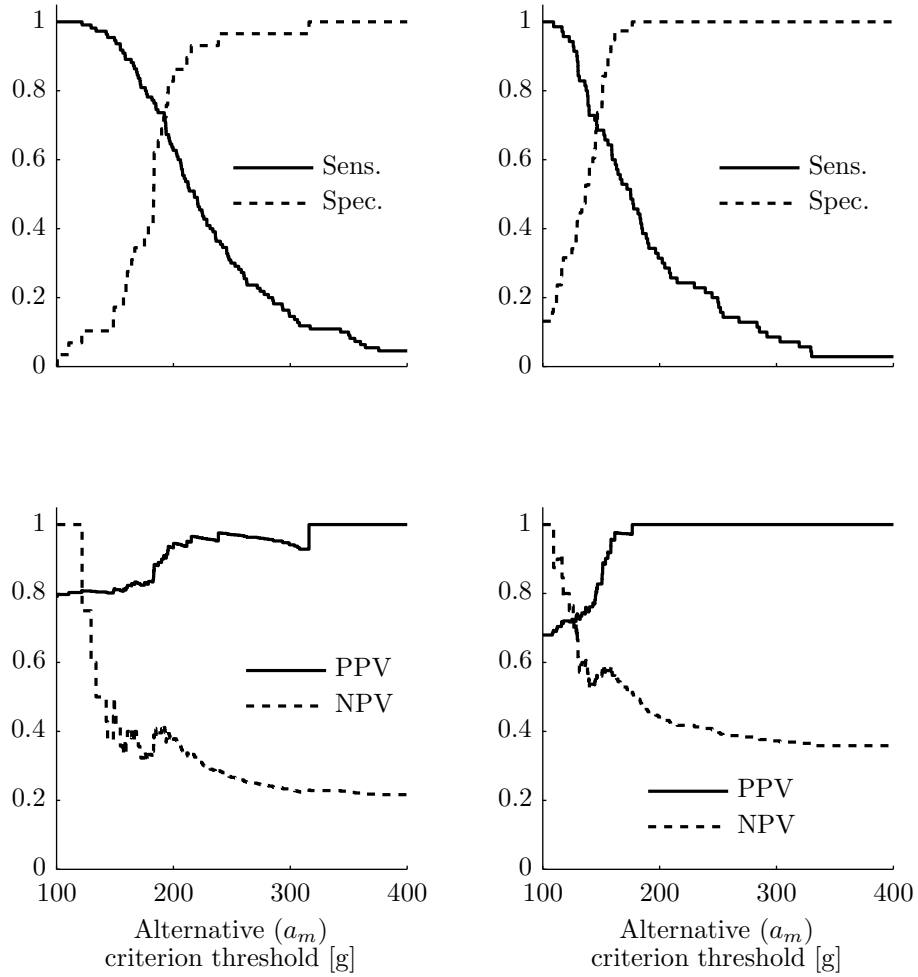

(a) Child headform tests.

(b) Adult headform tests.

Figure F.3: Sensitivity, Specificity, PPV and NPV of an alternate criteria at a range of thresholds of a_m, compared with reference $\text{HIC}_\infty > 1000$ criterion.

Bibliography

Aare, M. and Halldin, P. (2003). A new laboratory rig for evaluating helmets subject to oblique impacts. *Traffic Injury Prevention*, 4(3):240–248.

Aare, M., Kleiven, S., and Halldin, P. (2004). Injury tolerances for oblique impact helmet testing. *International Journal of Crashworthiness*, 9(1):15–23.

Anderson, R. (2005). Accuracy of speed measurements using the LSMD in crash testing applications. Technical report, Center for Automotive Safety Research, Adelaide.

Anderson, R. and McLean, J. (2005). Biomechanics of closed head injury. In Reilly, P. and Bullock, R., editors, *Head injury: pathophysiology and management*, pages 26–40. Hodder Arnold, London, 2nd edition.

Bayly, P., Cohen, T., Leister, E., Ajo, D., Leuthardt, E., and Genin, G. (2005). Deformation of the human brain induced by mild acceleration. *Journal of Neurotrauma*, 22(8):845–856.

Belingardi, G., Scattina, A., and Gobetto, E. (2009). Development of an hybrid hood to improve pedestrian safety in case of vehicle impact. In *Proceedings of the 17th International Technical Conference on the Enhanced Safety of Vehicles*, Washington DC. National Highway Traffic Safety Administration.

Boggess, B. M. and Foreman, G. G. (2007). Mass-based considerations for head injury protection development. In *Proceedings of the twentieth International Technical Conference on the Enhanced Safety of Vehicles*, Washington DC. National Highway Traffic Safety Administration.

Bowman, B. M. (1994). Analytical considerations of HIC in relation to the proposed new FMVSS 201. Technical Report UMTRI-94-40, University of Michigan, Transportation Research Institute, Ann Arbor.

Chou, C. C. and Nyquist, G. W. (1974). Analytical studies of the head injury criterion. SAE Paper 740082, SAE International, Warrendale.

Deck, C. and Willinger, R. (2008). Improved head injury criteria based on head FE model. *International Journal of Crashworthiness*, 13(6):667–678.

Deck, C. and Willinger, R. (2009). The current state of the human head finite element modelling. *International Journal of Vehicle Safety*, 4(2):85112.

DiLorenzo, F. A. (1976). Power and bodily injury. SAE Paper 760014, SAE International, Warrendale.

EEVC (2003). Improved test methods to evaluate pedestrian protection afforded by passenger cars (December 1998 with September 2002 updates). EEVC Working Group 17 Report, European Enhanced Vehicle-safety Committee, Brussels, Belgium.

Euro NCAP (2004). Pedestrian testing protocol. Testing Protocol Version 4.1, European New Car Assesment Programme, Brussels, Belgium.

Feng, Y., Abney, T. M., Okamoto, R. J., Pless, R. B., Genin, G. M., and Bayly, P. V. (2010). Relative brain displacement and deformation during constrained mild frontal head impact. *Journal of The Royal Society Interface*, 7(53):1677 –1688.

FMVSS 201 (2008). Occupant protection in interior impact. Code of Federal Regulations Title 49, Pt 571.201. 2008 ed.

FMVSS 208 (2008). Occupant crash protection. Code of Federal Regulations Title 49, Pt 571.208, Department of Transport. 2008 ed.

Fredriksson, R., Zhang, L., Bostrm, O., and Yang, K. (2007). Influence of impact speed on head and brain injury outcome in vulnerable road user impacts to the car hood. SAE Paper 2007-22-0007, SAE International, Warrendale.

Funk, J. R., Cormier, J. M., Bain, C. E., Guzman, H., and Bonugli, E. (2008). Relationship between linear and rotational head acceleration in various activities. In *Biomedical Sciences Instrumentation*, Copper Mountain, Colorado. ISA.

Gadd, C. W. (1961). Criteria for injury potential. In *Impact acceleration stress: A symposium*, pages 141–144. National Academy of Sciences - National Research Council, Washington DC.

Gadd, C. W. (1966). Use of weighted-impulse criterion for estimating injury hazard. SAE Paper 660793, SAE International, Warrendale.

Geddes, D. M., Cargill, R. S., and LaPlaca, M. C. (2003). Mechanical stretch to neurons results in a strain rate and magnitude-dependent increase in plasma membrane permeability. *Journal of Neurotrauma*, 20:1039–1049. 10.

Geddes-Klein, D., Schiffman, K., and Meaney, D. (2006). Mechanisms and consequences of neuronal stretch injury in vitro differ with the model of trauma. *Journal of neurotrauma*, 23(2):193204.

Gennarelli, T. A., Thibault, L. E., Tomei, G., Wiser, R., Graham, D., and Adams, J. (1987). Directional depedence of axonal brain injry due to centroidal and non-centroidal acceleration. SAE Paper 872197, SAE International, Warrendale.

Glaeser, K. P. (1991). Development of a head impact test procedure for pedestrian protection. In *Proceedings of The Thirteenth International Technical Conference on Experimental Safety Vehicles*, page 302309, Washington. National Highway Traffic Safety Administration.

Goldsmith, W. (1981). Current controversies in the stipulation of head injury criteria. *Journal of Biomechanics*, 14(12):883–884.

Got, C., Patel, A., Fayon, A., Tarri, C., and Walfisch, G. (1978). Results of experimental head impacts on cadavers: the various data obtained and their relations to some measured physical parameters. SAE Paper 780887, SAE International, Warrendale.

Gurdjian, E. S., Lissner, H. R., Evans, F. G., Patrick, L. M., and Hardy, W. G. (1961). Intracranial pressure and acceleration accompanying head impacts in human cadavers. *Surgery, Gynecology & Obstetrics*, 113:185–190. PMID: 13709837.

Gurdjian, E. S., Lissner, H. R., Latimer, F. R., Haddad, B. F., and Webster, J. E. (1953). Quantitative determination of acceleration and intracranial pressure in experimental head injury; preliminary report. *Neurology*, 3(6):417.

Gurdjian, E. S., Roberts, V. L., and Thomas, L. M. (1966). Tolerance curves of acceleration and intracranial pressure and protective index in experimental head injury. *The Journal of Trauma*, 6(5):600–604.

Gurdjian, E. S., Webster, J. E., and Lissner, H. R. (1950). The mechanism of skull fracture. *Radiology*, 54(3):313 –339.

Hardy, W. N., Foster, C. D., Mason, M. J., Yang, K. H., King, A. I., and Tashman, S. (2001). Investigation of head injury mechanisms using neutral density technology and high-speed biplanar x-ray. SAE Paper 2001-22-0016, SAE International, Warrendale. 45th Stapp Car Crash Conference.

Hardy, W. N., Khalil, T. B., and King, A. I. (1994). Literature review of head injury biomechanics. *International Journal of Impact Engineering*, 15(4):561–586.

He, S. X., Devilbiss, T., and Angamuthu, R. (2000). A design methodology for interior components to comply with FMVSS 201 head impact requirement. SAE Paper 2000-01-0638, SAE International, Warrendale.

Helps, Y., Henley, G., and Harrison, J. (2008). Hospital separations due to traumatic brain injury, Australia 200405. AIHW Injury research and statistics series 45, Australian Institute of Health and Welfare, Canberra.

Hess, R. L., Weber, K., and Melvin, J. W. (1980). Review of literature and regulation relating to head impact tolerance and injury criteria. Technical Report UM-HSRI-80-52-1, Highway Safety Research Institute, The University of Michigan, Ann Arbor.

Hodgson, V. R. and Thomas, L. (1972). Effect of long duration impact on the head. SAE Paper 720956, SAE International, Warrendale.

Holbourn, A. H. S. (1943). Mechanics of head injuries. *The Lancet*, 242(6267):438–441.

Hutchinson, J., Kaiser, M. J., and Lankarani, H. M. (1998). The head injury criterion (HIC) functional. *Applied Mathematics and Computation*, 96:1–16.

Hutchinson, T. P., Searson, D., Anderson, R. W., Dutschke, J. K., Ponte, G., and van den Berg, A. L. (2011). Protection of the unhelmeted head against blunt impact: The pedestrian and the car bonnet. In *Proceedings of the 2011 Road Safety Researchers, Policing and Education Conference*, Perth. Government of Western Australia.

Jiang, C., Neal-Sturgess, C. E., and Hu, Y. (2010). Kinematics simulation and head injury analysis for rollovers using MADYMO. *International Journal of Crashworthiness*, 15(5):505–515.

Kaleto, H. A., Mangum, H. W., Lee, P., and Schick, M. (2007). Overview of federal motor vehicle safety standard (FMVSS) 202A - head restraints: Methodology and equipment for the dynamic test. SAE Paper 2007-01-0703, SAE International, Warrendale.

Kang, H.-S., Willinger, R., Diaw, B. M., and Chinn, B. (1997). Validation of a 3D anatomic human head model and replication of head impact in motorcycle accident by finite element modeling. SAE Paper 973339, SAE International, Warrendale.

Kerkeling, C., Schfer, J., and Thompson, G. M. (2005). Structural hood and hinge concepts for pedestrian protection. In *Proceedings of the 19th International Technical Conference Enhanced Safety of Vehicles*, Washington DC. National Highway Traffic Safety Administration.

King, A. I., Yang, K. H., Zhang, L., Hardy, W., and Viano, D. C. (2003). Is head injury caused by linear or angular acceleration. In *Proceedings of International Research Conference on the Biomechanics of Impacts*, page 112.

Kleiven, S. (2002). *Finite element modeling of the human head*. PhD thesis, Department of Aeronautics, Royal Institute of Technology, Stockholm, Sweden.

Kleiven, S. (2003). Influence of impact direction on the human head in prediction of subdural hematoma. *Journal of neurotrauma*, 20(4):365379.

Kleiven, S. (2006). Evaluation of head injury criteria using a finite element model validated against experiments on localized brain motion, intracerebral acceleration, and intracranial pressure. *International Journal of Crashworthiness*, 11(1):6579.

Kroman, A., Kress, T., and Porta, D. (2011). Fracture propagation in the human cranium: A retesting of popular theories. *Clinical Anatomy*, 24(3):309–318.

LaPlaca, M. C., Lee, V., and Thibault, L. (1997). An in vitro model of traumatic neuronal injury: loading rate-dependent changes in acute cytosolic calcium and lactate dehydrogenase release. *Journal of Neurotrauma*, 14(6):355368.

Lemaitre, J. and Chaboche, J.-L. (1994). *Mechanics of Solid Materials*. Cambridge University Press.

Lim, G. G., Chou, C. C., Patel, R. N., Shahab, S. A., and Patel, P. J. (1995). Estimating the minimum space to meet federal interior head impact requirements. SAE Paper 950333, SAE International, Warrendale.

Lissner, H. R., Lebow, M., and Evans, F. G. (1960). Experimental studies on the relation between acceleration and intracranial pressure changes in man. *Surgery, gynecology & obstetrics*, 111:329–338.

Liu, Q., Xia, Y., Zhou, Q., and Wang, J. T. (2009). Design analysis of a sandwich hood structure for pedestrian protection. In *21st International Technical Conference of the Enhanced Safety of Vehicles*, Washington. National Highway Traffic Safety Administration.

Loong, T.-W. (2003). Understanding sensitivity and specificity with the right side of the brain. *British Medical Journal*, 327(7417):716.

Margulies, S. S. and Thibault, L. E. (1992). A proposed tolerance criterion for diffuse axonal injury in man. *Journal of Biomechanics*, 25(8):917–923.

Marjoux, D., Baumgartner, D., Deck, C., and Willinger, R. (2008). Head injury prediction capability of the HIC, HIP, SIMon and ULP criteria. *Accident Analysis & Prevention*, 40(3):1135–1148.

McLean, A. J. (1993). Understanding head impact tolerance as an aid in injury prevention. In Nakamura, N., Hashimoto, T., and Yasue, M., editors, *Recent Advances in Neurotraumatology*, pages 27–29. Springer-Verlag, Tokyo.

McLean, A. J. (1995). Brain injury without head impact? *Journal of Neurotrauma*, 12(4):621625.

Melvin, J. and Evans, F. (1971). A strain energy approach to the mechanics of skull fracture. SAE Paper 710871, SAE International, Warrendale. 15th Stapp Car Crash Conference.

Mertz, H. J. (1993). Anthropomorphic test devices. In Nahum, A. M. and Melvin, J., editors, *Accidental injury: biomechanics and prevention*, pages 66–84. Springer-Verlag, New York.

Mertz, H. J., Prasad, P., and Nusholtz, G. (1996). Head injury risk assessment for forehead impacts. SAE Paper 960099, SAE International, Warrendale.

Neal-Sturgess, C. E. (2002). A thermomechanical theory of impact trauma. *Proceedings of the Institution of Mechanical Engineers, Part D: Journal of Automobile Engineering*, 216(11):883895.

Neal-Sturgess, C. E., Hassan, A., and Cuerden, R. (2001). The relationship of AIS to peak virtual power. In *Proceedings of the 45th Annual Scientific Conference of the Association for the Advancement of Automotive Medicine*, Barrington. Association for the Advancement of Automotive Medicine.

Newcombe, R. G. (1998). Two-sided confidence intervals for the single proportion: comparison of seven methods. *Statistics in Medicine*, 17(8):857872.

Newman, J. A. (1980). Head injury criteria in automotive crash testing. SAE Paper 801317, SAE International, Warrendale.

Newman, J. A. (1986). A generalized model for brain injury threshold (GAMBIT). In *Proceedings of 1986 International IRCOBI Conference on the Biomechanics of Impacts*, Bron, France. International Research Council on Biokinetics of Impacts.

Newman, J. A. (1993). Biomechanics of human trauma: Head protection. In Nahum, A. M. and Melvin, J., editors, *Accidental injury: biomechanics and prevention*. Springer-Verlag, New York.

Newman, J. A. (1998). Kinematics of head injury. In Yoganandan, N., editor, *Frontiers in head and neck trauma: clinical and biomechanical*, pages 200–214. IOS Press, Burke, Virginia.

Newman, J. A., Barr, C., Beusenberg, M., Fournier, E., Shewchenko, N., Welbourne, E., and Withnall, C. (2000a). A new biomechanical assessment of mild traumatic brain injury part 2-results and conclusions. In *Proceedings of the 2000 International IRCOBI conference on the biomechanics of impact*, Bron, France. International Research Council on Biomechanics of Impacts.

Newman, J. A., Shewchenko, N., and Welbourne, E. (2000b). A proposed new biomechanical head injury assessment function - the maximum power index. SAE Paper 2000-01-SC16, SAE International, Warrendale.

Newstead, S., Cameron, M., and Watson, L. (2012). Vehicle safety ratings estimated from police reported crash data: 2012 update. Technical Report 313, Monash University Accident Research Centre, Monash, Victoria.

NFPA 1971 (2007). Protective ensembles for structural fire fighting and proximity fire fighting. Technical report, National Fire Protection Association.

Ommaya, A. K. and Hirsch, A. E. (1971). Tolerances for cerebral concussion from head impact and whiplash in primates. *Journal of Biomechanics*, 4(1):13–21.

Ommaya, A. K., Thibault, L. E., and Bandak, F. A. (1994). Mechanisms of impact head injury. *International Journal of Impact Engineering*, 15(4):535–560.

Onusic, H. (1995). HIC (Head injury criterion) and SI (Severity index) of impacts with different pulse shapes. *International Journal of Vehicle Design*, 16(2/3):194202.

Pinecki, C. and Zeitouni, R. (2007). Technical solutions for enhancing the pedestrian protection. In *20th International Technical Conference on the Enhanced Safety of Vehicles*, Washington DC. National Highway Traffi c Safety Administration.

Prasad, P. and Mertz, H. J. (1985). The position of the united states delegation to the ISO working group 6 on the use of HIC in the automotive environment. SAE Paper 851246, SAE International, Warrendale.

R Development Core Team (2010). *R: A Language and Environment for Statistical Computing*. R Foundation for Statistical Computing, Vienna, Austria. ISBN 3-900051-07-0.

Sabet, A., Christoforou, E., Zatlin, B., Genin, G., and Bayly, P. (2008). Deformation of the human brain induced by mild angular head acceleration. *Journal of biomechanics*, 41(2):307315.

SAE (1980). Human tolerance to impact conditions as related to motor vehicle design. SAE Information Report J885 APR80, SAE International, Warrendale.

SAE (2003). Instrumentation for impact test-part 1-electronic instrumentation (J211). Technical standard, SAE International, Warrendale.

Schwarz, D., Bachem, H., and Opbroek, E. (2004). Comparison of steel and aluminum hood with same design in view of pedestrian head impact. SAE Paper 2004-01-1605, SAE International, Warrendale.

Searson, D. and Anderson, R. (2008). Pedestrian impact testing: Modelling the effect of head-form mass and speed. In *Australasian Road Safety Research, Policing and Education Conference*, Adelaide, Australia. South Australia. Department for Transport, Energy and Infrastructure.

Shahbeyk, S., Kamalan, A., and Osanlou, M. (2003). A comparative study on vehicle aluminum and steel hood assemblies. *International Journal of Crashworthiness*, 8(4):367–374.

Simms, C. and Wood, D. (2009). *Pedestrian and Cyclist Impact: A Biomechanical Perspective*, volume 166 of *Solid Mechanics and its Applications*. Springer.

Stalnaker, R. L., Burke, W. V., and Hines, M. H. (1997). Translational energy criteria: A validation study for non-fracture head impacts. SAE Paper 973337, SAE International, Warrendale.

Stalnaker, R. L., Lin, C. A., and Guenther, D. A. (1985). The application of the new mean strain criterion (NMSC). In *Proceedings of the 1985 International IRCOBI/AAAM Conference on the Biomechanics of Impacts*, Bron, France. International Research Council on Biokinetics of Impacts.

Standards Australia (1996). Playground surfacing - specifications, requirements and test method. AS/NZS 4422:1996, Standards Australia, Sydney.

Stapp, J. P. (1961). Human tolerance to severe, abrupt acceleration. In Gauer, O. H. and Zuidema, G. D., editors, *Gravitational Stress in Aerospace Medicine*. J. & A. Churchill Ltd., London.

Takhounts, E., Ridella, S., Hasija, V., Tannous, R., Campbell, J., Malone, D., Danelson, K., Stitzel, J., Rowson, S., and Duma, S. (2008). Investigation of traumatic brain injuries using the next generation of simulated injury monitor (SIMon) finite element head model. *Stapp Car Crash Journal*, 52:131.

Takhounts, E. G., Eppinger, R. H., Campbell, J. Q., Tannous, R. E., Power, E. D., and Shook, L. S. (2003). On the development of the SIMon finite element head model. SAE Paper 2003-22-0007, SAE International, Warrendale.

Untaroiu, C., Shin, J., Crandall, J., and Crino, S. (2006). Development and validation of a headform impactor finite element model with application to vehicle hood design for pedestrian protection. Michigan, USA.

Untaroiu, C. D., Shin, J., and Crandall, J. R. (2007). A design optimization approach of vehicle hood for pedestrian protection. *International Journal of Crashworthiness*, 12(6):581589.

Versace, J. (1971). A review of the severity index. SAE Paper 710881, SAE International, Warrendale.

Waller, J. A. (1985). *Injury Control: A Guide to the Causes and Prevention of Trauma*. Lexington Books, Lexington, Mass.

Willinger, R., Kopp, C. M., and Cesari, D. (1991). Brain tolerance in the frequency field. In *Proceedings of the 13th International Conference on Experimental Safety Vehicles*, Washington DC. National Highway Traffi c Safety Administration.

World Health Organisation (1992). *International Statistical Classification of Diseases and Related Health Problems — 10th Revision (ICD-10)*. World Health Organisation, Geneva, Switzerland.

Wu, J. and Beaudet, B. (2007). Optimization of head impact waveform to minimize HIC. SAE Paper 2007-01-0759, SAE International, Warrendale.

Yoganandan, N., Pintar, F. A., Sances, A., Walsh, P. R., Ewing, C. L., Thomas, D. J., and Snyder, R. G. (1995). Biomechanics of skull fracture. *Journal of Neurotrauma*, 12:659–668.

Zar, J. H. (1972). Significance testing of the spearman rank correlation coefficient. *Journal of the American Statistical Association*, 67(339):578–580.